Title
The Masses and Orbital Dynamics of Exoplanets

Author
Weiss, Lauren Michelle

Publication Date
2016

Peer reviewed|Thesis/dissertation

The Masses and Orbital Dynamics of Exoplanets

By

Lauren Michelle Weiss

A dissertation submitted in partial satisfaction of the

requirements for the degree of

Doctor of Philosophy

in

Astrophysics

in the

Graduate Division

of the

University of California, Berkeley

Committee in charge:

Geoffrey W. Marcy, Chair
Eugene Chiang
Gibor Basri
Michael Manga

Spring 2016

The Masses and Orbital Dynamics of Exoplanets

Abstract

The Masses and Orbital Dynamics of Exoplanets

by

Lauren Michelle Weiss

Doctor of Philosophy in Astrophysics

University of California, Berkeley

Geoffrey W. Marcy, Chair

We live in a golden era of exoplanet discovery and characterization. Since its launch in 2009, the *Kepler* Mission has discovered over 4000 exoplanets, enabling detailed studies of their physical and orbital properties. These include empirical studies of the prevalence of planets of various sizes and orbital distances. In some of the *Kepler* systems, the compositions of the planets have been determined. Other studies include empirical, analytical, and numerical constraints on the formation and evolution of planetary systems.

This thesis focuses on two aspects of the *Kepler* revolution. The first focus is on the masses and densities of small planets. Planets smaller than Neptune span a variety of compositions. Some of them are rocky and potentially habitable. The diversity of compositions among sub-Neptunes offers clues to planet formation and evolution. To determine the compositions of small planets, it is necessary to compute bulk densities from measurements of the planet radii and masses. While *Kepler* has determined the radii of thousands of planets, only a handful of the small planets are amenable to mass measurement techniques. Using the results from two mass measurement techniques, called the radial velocity (or Doppler) method and the transit timing variation method, a detailed study of the masses and compositions of more than 65 small planets was conducted. This study determined empirical relationships that describe the average masses and densities of exoplanets smaller than Neptune as a function of planet radius. Such exoplanets achieve a peak bulk density of 7.6 grams per cubic centimeter at a physical size of 1.5 times the radius of Earth. This peak density corresponds to a rocky composition; rocky planets smaller than 1.5 Earth radii are less compressed and less dense, whereas planets larger than 1.5 Earth radii have thick envelopes composed of volatile gases that lower their bulk densities.

The second focus of this thesis is on the masses and orbital dynamics of planets in multi-planet systems. Multi-planet systems represent the end-states of planet formation. Their orbital dynamics and planet compositions are a fossil record of how they arrived at their present configurations. The systems studied herein include 3 multi-planet systems: KOI-94, Kepler-10, and Kepler-11. KOI-94 is a system of 4 planets including a warm Jovian

world. Kepler-10 contains a scorched rocky planet, a cooler gas-enveloped world, and a likely third planet. Kepler-11 has six small planets with fluffy hydrogen-rich envelopes, all contained within the equivalent orbital distance of Venus. Measurements of the compositions and orbital dynamics of these planets offer valuable steps toward characterizing the possible formation and evolutionary histories of these planetary systems.

I dedicate this dissertation to the people who look upward.

Contents

List of Figures

List of Tables

Acknowledgments

In the words of Isaac Newton, I have stood on the shoulders of giants. Geoff Marcy: thank you for being my Ph.D. advisor, my tallest giant, my biggest cheerleader, and my mentor. You taught me what it means to be a scientist. I will always remember the time I complained that mass-radius work was too easy because it simply involved drawing a straight line through a collection of data, and you countered, "That's what Hubble did." I cannot imagine what my life would be like without the past five years of fun and challenging scientific inquiry with you. Thank you a hundred times for being here for me.

Andrew Howard: thank you for being my second Ph.D. advisor, mentor, and longtime teammate. Your gentleness and generosity are infinite. When times got hard, you picked up our team–including me–and guided us to the light at the end of the tunnel. You have always helped me see where I want to be in the future. Howard Isaacson: thank you for always being there, whether for an unexpected night on Keck or a team celebration. Your loyalty means so much to me. To the rest of the California Planet Search collaboration, especially Erik Petigura, BJ Fulton, Lea Hirsch, and Evan Sinukoff: thank you for being a team of champions.

Bob Kibrick and Brad Holden: you are rock stars. You stayed awake more nights than seem humanly possible, missing sleep and evening engagements. On the nights you intended to sleep, you picked up the phone when I called after midnight to report that the APF was stuck, broken, or possibly on fire. You developed critical software for basic telescope operations, such as acquiring and guiding on a star and focusing the telescope. You continued to do these difficult things long past the point that an ordinary human would have given up. Thank you for being awesome!

To the rest of the APF techs, including Kyle Lanclos, Will Deich, and Matt Radovan: thank you for your dedication and creativity in troubleshooting the APF engineering, hardware, and software problems we encountered.

To my thesis committee members Gibor Basri, Eugene Chiang, and Michael Manga: thank you for these past few years of your guidance and wisdom. Our conversations have opened doors for me.

All of my other teachers, including Dr. Craxton, Mrs. Eiselen, Mr. Whitman, Mr. Kinsman, Mr. McKinney, Mr. Bobin, Mrs. Munch, Mr. Quinlisk, Mrs. Shuffelton, Howard Georgi, Jenny Hoffman, Doug Finkbeiner, David Charbonneau, Vladimir Strelnitski, Simon Hodgkin, Ramesh Narayan, Michael Woods-Vasey, Chris Stubbs, Peter Bol, Marjorie Garber,

James Wood, and Sabrina Sadique: thank you for the time you spent teaching me the vast majority of what I know, from elementary physics to how to write a good story.

My parents: thank you for having me and encouraging me to be anything I could dream of being (except a Broadway actress). My friends: thank you for keeping me sane. I'm counting on you to keep the good times coming.

Three years of my PhD studies were supported by the National Science Foundation through Grant DGE 1106400. I am thankful to the NSF, President Obama, and the American taxpayers for making this possible.

I owe huge thanks to Ken and Gloria Levy, who generously donated the funds for two years of my PhD studies. Thank you also for contributing the Levy spectrometer to the Automated Planet Finder, which I used for this thesis.

Thank you to the staff at Lick Observatory and the W. M. Keck Observatory who made the hundreds of observations within this thesis possible. Thank you also to the California tax payers, the University of California, and Google for supporting Lick Observatory.

I wish to extend special thanks to those of Hawai'ian ancestry on whose sacred mountain of Mauna Kea I have been privileged to be a guest. Without your generous hospitality, the Keck observations presented herein would not have been possible.

This dissertation was typeset using the ucastrothesis LaTeX template.

1

Introduction

> *"Then Humankind was born. Either the creator god, source of a better world, seeded it from the divine, or the newborn earth just drawn from the highest heavens still contained fragments related to the skies, so that Prometheus, blending them with streams of rain, moulded them into an image of the all-controlling gods. While other animals look downwards at the ground, he gave human beings an upturned aspect, commanding them to look towards the skies, and, upright, raise their face to the stars. So the earth, that had been, a moment ago, uncarved and imageless, changed and assumed the unknown shapes of human beings."*
>
> – Ovid, *Metamorphoses* (tr. A. S. Kline)

A defining feature of humanity is our desire to know our origin. Thousands of years ago, Ovid laid the literary foundation of a worldview that we are now reacquring through the scientific method. Today, we know that humans and the precious things of Earth are "fragments related to the skies:" we are made of the elements manufactured in the hearts of stars and blown wayward in supernovae's kisses to the universe.

It is my privilege to use my "upturned aspect" to investigate how the fragments of the heavens assemble into planets. Hydrogen is the most common element, comprising 74% of the atomic makeup of the universe by mass; helium comprises an additional 24%. Yet these elements account for very little of the mass of Earth. How do the universe's trace amounts of carbon, oxygen, nitrogen, silicon, magnesium, and iron coalesce to form planets? What is the variety of different planets that the universe can assemble? Which conditions give rise to planets like the Earth?

We live in a golden age for understanding the formation of Earth. In the past two decades, scientists have discovered over 4000 exoplanets–planets orbiting stars other than the sun (Mullally et al. 2015). With the advent of exoplanet science, we have stumbled upon an immense astrophysical laboratory. The thousands of exoplanets available for characterization allow robust statistical studies of the total population of planets. The sizes, masses, compositions, and orbital dynamics of these planets represent the outcomes of planet formation. Each planetary system is one realization of planet formation; each can be compared to

our own solar system.

1.1 Theories of Planet Formation and Evolution

Before the discovery of the first exoplanet, scientists were already working toward a theory of planet formation that could adequately reproduce our own solar system. How did Jupiter and Saturn get so big, while Earth and the terrestrial planets remained so small? Can these rules of planet formation simulate the formation of Neptune and Uranus as well as the inner planets? Did the planets of the solar system all form at the same time, or at different times? Did they form where they are today (in situ), or did they "migrate" to their present locations? Below I review some highlights from planet formation theory.

Core accretion is the idea that planets gradually grow from gentle collisions of non-volatile material in the circumstellar disk. Planet formation begins with the aggregation of dust grains into larger rocky material. The rocky material can eventually become massive enough to gravitationally accrete gas from the circumstellar disk, if the gas in the disk is still present and the core is large enough. Lissauer & Stewart (1993), Pollack et al. (1996), Goldreich et al. (2004), and others have made detailed predictions about the growth rate of solids in the disk. If the solids accrete rapidly enough to achieve "runaway accretion," they quickly form a massive ($\sim$ 10 Earth mass) planetary core that has a sufficient mass and cross-sectional area to capture a large amount of gas from the disk, resulting in a planet with more mass in gas than in solids (i.e. a Jovian world). While alternative theories to core accretion might explain some of the most massive giant planets and brown dwarfs, core accretion is the only detailed physical prediction at this time that can explain planets smaller than Jupiter.

Gas-induced disk migration describes the mechanisms in which the gas in the circumstellar disk influences the orbits of planets. The gas exchanges energy and angular momentum with the proto-planets embedded in it, moving the proto-planets inward or outward from their initial locations. Whether the planet moves inward or outward depends sensitively on the planet mass and the gradients in the circumstellar disk. This is a gradual process that occurs over a timescale of many orbits.

Planets can also migrate by gravitationally interacting with each other. Interactions can be rapid near-collisions ("planet-planet scattering"), or they can be more gradual perturbations over hundreds of orbits. These migration mechanisms can produce distinctive architectures. Planets migrating at different rates can become trapped in a mean motion resonance, a low-energy state in which the orbital periods of the planets have an integer ratio (Murray & Dermott 2000; Yu & Tremaine 2001). Therefore, bodies in mean motion resonances are a hallmark of migration (although not all migration results in mean motion resonance architectures). The Kozai-Lidov mechanism is an oscillatory process in which two bodies with a large mutual inclination (> 40 degrees) swap angular momentum, undergoing huge changes in eccentricity and inclination. Systems in which large mutual inclinations and/or eccentricities exist today might have arrived at their present architectures through

this mechanism.

1.2 Exoplanets: Large to Small, Hot to Cold, Few to Many

This section chronicles the major milestones in exoplanet science. Each milestone was either a major challenge to planet formation, or a major triumph of planet detection techniques.

1.2.1 Milestones from the Doppler technique

The Doppler (or radial velocity) technique is a method which attempts to measure the motion of a star due to the gravitational pull of an orbiting planet. Stellar motion along the line of sight is detected through changes in the Doppler shift of the star's visible-light spectrum. This technique allows the characterization of the planet's projected mass ($m \sin i$), orbital period, and eccentricity.

Using the Doppler method, Mayor & Queloz (1995) made the first discovery of an exoplanet orbiting a hydrogen-burning star. This planet was 51 Pegasi b, a Saturn-mass planet orbiting its star in just 4 days. Marcy & Butler (1995) confirmed the existence and planetary nature of 51 Peg b. Early models of core accretion theory predicted that it is difficult to form a Jupiter-mass planet inside the snow line. How did 51 Peg b arrive not only inside the snow line, but at such an awesomely close distance to its star? This planet, and subsequently discovered hot Jupiters, posed a challenge for planet formation theory that remains unsolved.

Since the discovery of 51 Peg b, the capability of the Doppler technique to detect planets has extended to planets at longer orbital periods and lower masses. Marcy & Butler (1996) discovered 70 Virginis, a Jupiter-mass planet that took a full 117 days to orbit its star and with an orbital eccentricity of 0.4. The discovery of this cool, eccentric Jupiter demonstrated that exoplanets could be found at long orbital periods. A few years later, Marcy et al. (2000) discovered two sub-Saturn mass planets with the Doppler method, demonstrating the capability to detect low-mass planets.

As Doppler surveys continued, evidence for single stars hosting multiple exoplanets emerged. Butler et al. (1999) discovered the first system of multiple exoplanets around the star Upsilon Andromedae. These three planets have orbital periods of 4, 242, and 1269 days, and they ranged in mass from 0.7 - 4 times the mass of Jupiter. How did these Jovian-mass planets come to orbit so close to their star, all well within the distance that Jupiter orbits our own sun? Their moderate eccentricities suggest a dynamically active past. Two years later, Marcy et al. (2001) discovered two exoplanets in mean motion resonance around GJ 876. Although mean motion resonance has been observed and studied among the minor bodies of our solar system, none of the solar system planets currently reside in

first-order mean motion resonances with each other. A mean motion resonance architecture is interpreted as clear evidence of a history of migration.

1.2.2 The transiting planet revolution

At the turn of the millennium, a new technique revolutionized the discovery and characterization of exoplanets. Henry et al. (2000) and Charbonneau et al. (2000) observed the known hot, Jupiter-mass planet, HD 209258 b, transit its star. As the planet transited its star, blocking some starlight, the change in brightness of the star allowed a precise determination of the radius of the planet compared to the radius of the star. Combining the radius of the planet with the mass of the planet, which was known from Doppler studies, allowed a determination of the planet's density and an inference of its composition. This discovery ushered an era of prolific surveys for transiting Jovian worlds. The detected transiting planets were then studied with the Doppler technique to determine their masses, densities, and compositions.

In 2009, the *Kepler* spacecraft launched, heralding an explosion of exoplanet discoveries through the transit method. During its four-year mission, *Kepler* discovered planets large and small, in short and long orbital periods (Borucki et al. 2011; Batalha et al. 2013; Burke et al. 2015; Mullally et al. 2015). The exquisite quality of the photometry and *Kepler* team analysis pipeline produce high-fidelity planet candidates; the vast majority of the candidates are real planets (Morton & Johnson 2011) The most recent headcount of *Kepler* planet candidates is 4696 (Mullally et al. 2015).

The enormous haul of planets from *Kepler* enabled unprecedented statistical studies of exoplanets. Howard et al. (2012), Petigura et al. (2013a), Fressin et al. (2013), Petigura et al. (2013b), Burke et al. (2015), and others computed the prevalence of planets of various sizes and orbital periods based on the observed population in the *Kepler* data. This is not as simple as counting the number of planets of various properties, because correction factors must be applied to account for (1) the probability of transit given the system geometry and (2) the probability of transit detection given the complex photometric noise and the sensitivity of the data analysis pipeline. The major results of these population studies are that small planets are more common than large planets. Half of sun-like stars have a planet the size of Neptune or smaller within an orbital period of of 100 days, whereas only 1.6% have Jupiter-size planets in the same orbital space. Thus, 51 Peg b and the other early discoveries of hot Jupiters represent a rare outcome of planet formation, but small planets are very common. The abundance of small, close-in planets directly contradicts the prediction in Ida & Lin (2004) that the details of planet formation and migration should produce a dearth of small planets close to their stars. A particularly noteworthy result from Petigura et al. (2013b) is that small planets are just as common at long orbital periods (100-200 days) as they are at moderate orbital periods (10-50 days). Therefore, it is possible to cautiously extrapolate to Earth's orbital distance. Petigura et al. (2013b) calculated that 20% of sun-like stars have a planet 1 to 2 times the size of Earth in an orbit receiving 1/4 to 4 times as much stellar irradiation as the Earth does. This was the first computation of the fraction of stars that

bear potentially Earth-like planets.

Also common in the *Kepler* haul are systems with multiple exoplanets; *Kepler* has found more than 700 planets residing in 340 multi-planet systems (Lissauer et al. 2014; Rowe et al. 2014, , see Figure 1.1). Because the transit probability rapidly decreases with increasing orbital distance, most of the planets discovered by *Kepler* are close to their stars, including most members of multi-planet systems. Fabrycky et al. (2014) catalogued the architectures of many of these compact planetary systems (Figure 1.2). An example system is Kepler-11, which has six small, transiting planets with orbital periods ranging from 10 to 118 days; all six planets would fit within the orbit of Venus if they were transplanted to our own solar system. The planets are not in mean motion resonances with each other. How did the planets arrive in such a compact non-resonant architecture? Either a finely tuned migration scenario is necessary to explain how the planets did not become trapped in resonances, or the planets formed in situ.

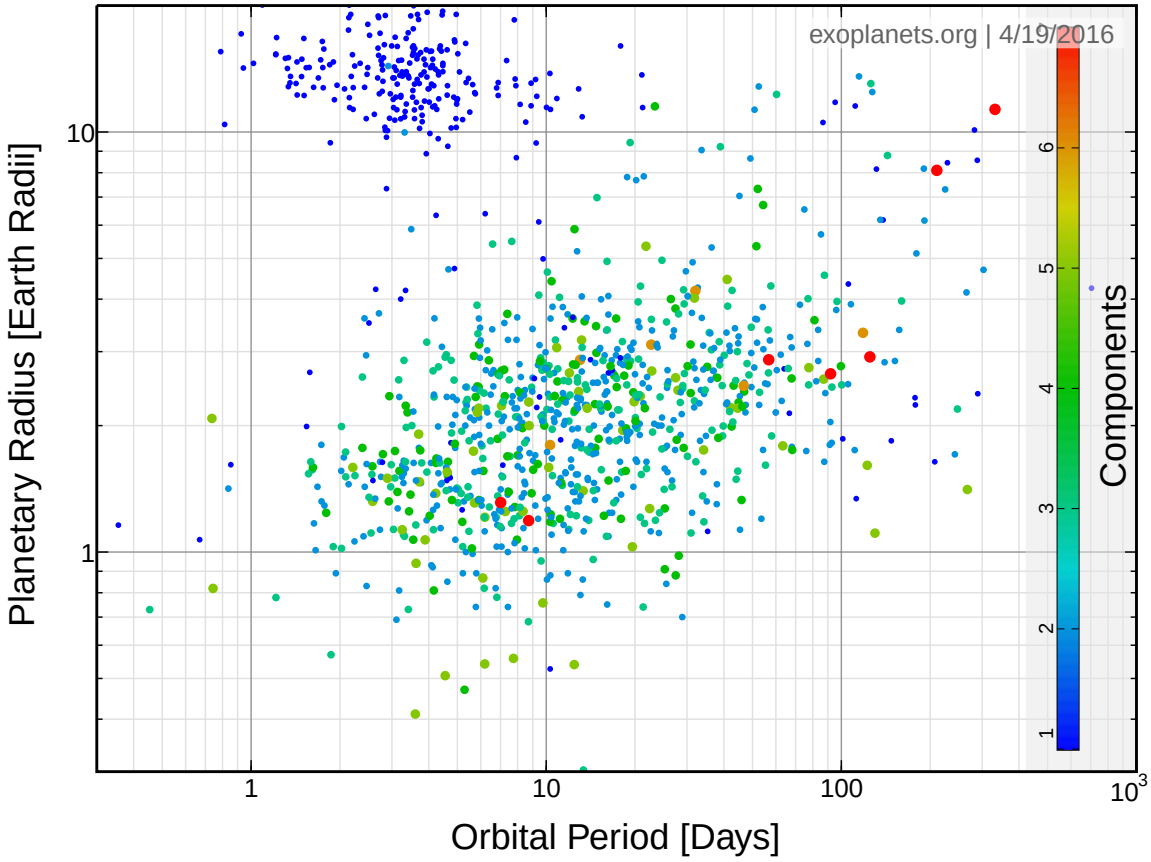

Figure 1.1: Confirmed planets as a function of orbital period and radius. The majority of the planets smaller than 4 Earth radii were discovered by *Kepler*. The point color (and point size for clarity) correspond to the total number of planets in the system. The majority of planets smaller than 4 Earth radii are in multi-planet systems.

The architecture of the Kepler-11 planets is so compact that the planets gravitationally perturb each other's orbits. These orbital perturbations are detectable as transit timing variations–the relatively early or late timing of some transits with respect to a clockwork-like, non-perturbed orbit (Agol et al. 2005). The transit timing variations of the planets in Kepler-11 are tens of minutes. It is possible to reproduce the observed transit timing variations by forward-modeling the gravitational interactions of the planets with a classical Newtonian N-body integrator. With this method, Lissauer et al. (2011) measured the masses of the planets and found that the Kepler-11 planets have very low masses and densities relative to other planets of their size. Other analyses, including Sanchis-Ojeda et al. (2013), Jontof-Hutter et al. (2014), Kipping et al. (2014), and Jontof-Hutter et al. (2015) have used transit timing variations to measure planet masses in similarly compact systems. So far, the majority of planets in compact multi-planet systems have bulk densities that are abnormally low compared to planets is less compact architectures. What is the causal connection between the compact system architecture and the low densities of the planets?

Planets can undergo compositional changes after they form. One example of a planet sculpted after formation is Kepler-10 b, which orbits its star in less than one day, has an equilibrium temperature of 2100 Kelvin, and has a mass and radius consistent with a rocky composition (Batalha et al. 2011). Kepler-10 b and a handful of other small planets at orbital periods shorter than 15 days have rocky compositions, despite masses as high as 5 Earth masses. At longer orbital periods, planets of these same masses are larger, meaning they have lower densities that require a thick hydrogen envelope over the rocky core. Lopez et al. (2012) explored how X-ray and UV radiation from the star can partially or completely photo-evaporate the hydrogen envelope. The photo-evaporation mechanism reproduces the observed hot, high-mass rocky planet cores while preserving the warm and cool Neptune-sized planets. However, the efficiency factor controlling what fraction of stellar energy does the work of photo-evaporation is a free parameter that must be tuned to match observations. Moreover, the evaporative efficiency might depend on detailed properties of the host star. Thus, it is difficult to predict the orbital distances at which photo-evaporation will no longer strip or significantly reduce a planet's gaseous envelope. Also, additional processes, such as the heavy bombardment of planets with asteroids, might contribute to the removal of planetary envelopes.

1.3 A Summary of Continuing Questions

What physical processes govern the transformation of rocky cores into gas-rich planets? How and where can planets lose their gaseous envelopes? Why are most multi-planet systems in non-resonant rather than resonant architectures? How do planets form in the compactly spaced systems of multiple, low-density planets we observe from *Kepler*? What physics sculpt the relationship between the masses, compositions, and orbital spacings of the planets in multi-planet systems?

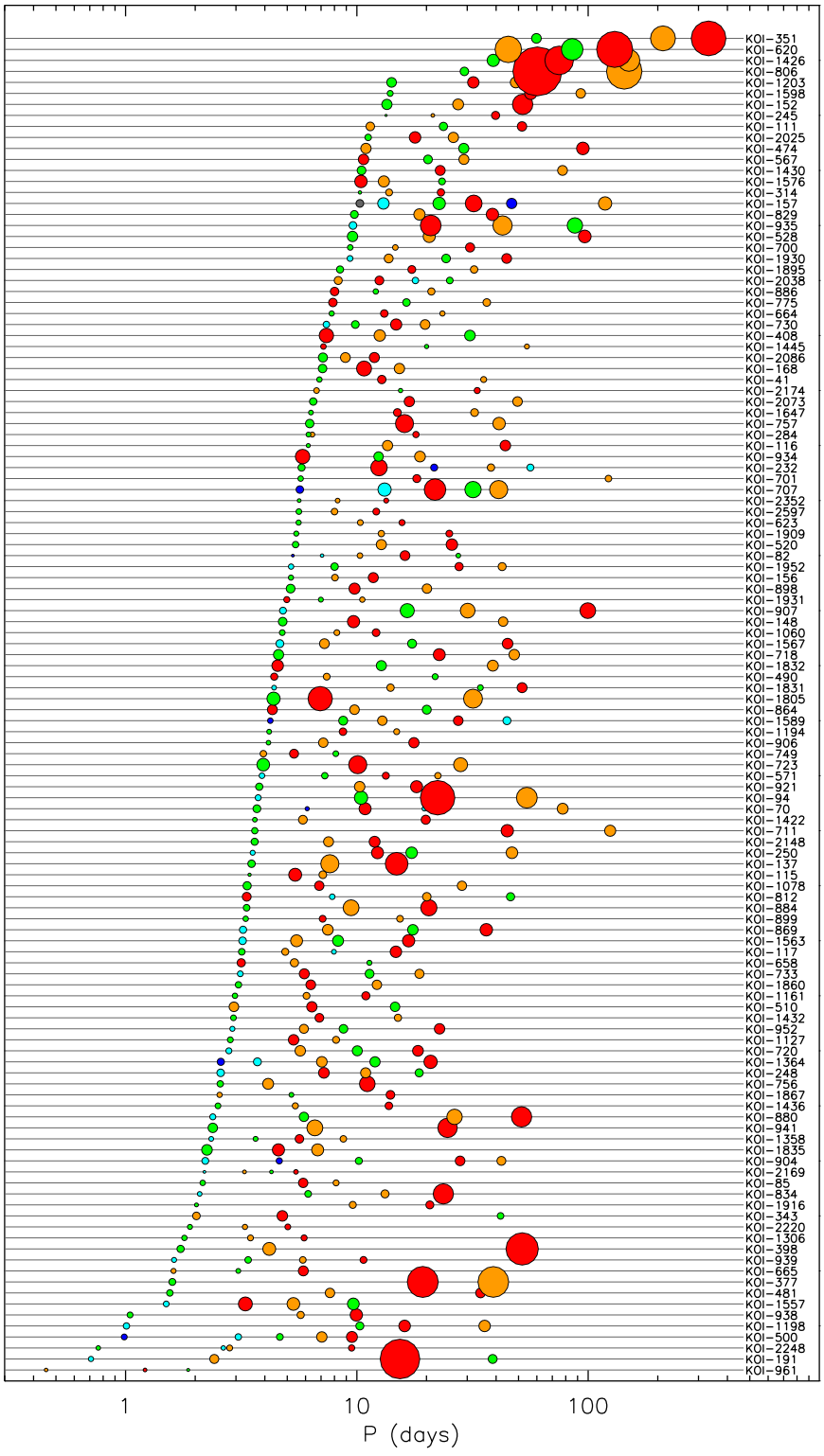

Figure 1.2: The architectures of compact systems of multiple planets discovered by *Kepler*. Reproduced with permission from Fabrycky et al. (2014).

1.4 Plan

In this thesis, I explore both individual planetary systems and patterns in the broader exoplanet population that provide key clues to the questions above. Chapter 2 characterizes KOI-94, a system of four exoplanets, in detail. Three of these planets are smaller than Neptune, one is the size of Jupiter, and they are all closer to their star than Mercury is to the sun. For the Jupiter-sized planet, and for other exoplanets larger than Saturn, a robust empirical relationship between the planet size, planet mass, and the stellar irradiation on the planet is established. Chapter 3 establishes empirical relationships between the masses and sizes of 65 planets smaller than Neptune. This study sought to answer whether small planets are scaled-up rocky worlds, scaled-down Neptunes, or something else. A break in the compositional distribution of small planets is discovered at 1.5 times the planetary radius of Earth: no planets larger than this size are rocky; whereas a large proportion of the planets smaller than this size are rocky. Chapter 4 returns to an individual planetary system, Kepler-10, which contains two small planets. New data corroborate the rocky composition of the smaller planet (Kepler-10 b), find that the larger planet (Kepler-10 c) is not rocky, and discover evidence for a third planet in the system. Chapter 5 delves into the orbital dynamics of Kepler-11, a six-planet system with very low-density planets packed close to their star. Chapter 6 details the development and automation of the Automated Planet Finder, a telescope dedicated to hunting for planets around nearby stars. This chapter also describes an ongoing program to look for additional planets in bright stars already known to host multiple planets.

2

The Mass of KOI-94d and a Relation for Planet Radius, Mass, and Incident Flux

A version of this chapter was previously published in the Astrophysical Journal (Weiss, L. M., Marcy, G. W., Rowe, J. F., et al. 2013, The Astrophysical Journal, 768, 14).

We measure the mass of a modestly irradiated giant planet, KOI-94d. We wish to determine whether this planet, which is in a 22-day orbit and receives 2700 times as much incident flux as Jupiter, is as dense as Jupiter or rarefied like inflated hot Jupiters. KOI-94 also hosts at least 3 smaller transiting planets, all of which were detected by the *Kepler* Mission. With 26 radial velocities of KOI-94 from the W. M. Keck Observatory and a simultaneous fit to the *Kepler* light curve, we measure the mass of the giant planet and determine that it is not inflated. Support for the planetary interpretation of the other three candidates comes from gravitational interactions through transit timing variations, the statistical robustness of multi-planet systems against false positives, and several lines of evidence that no other star resides within the photometric aperture. We report the properties of KOI-94b ($M_{\rm p}= 10.5 \pm 4.6 M_\oplus$, $R_{\rm p}= 1.71 \pm 0.16 R_\oplus$, P = 3.74 days), KOI-94c ($M_{\rm p}= 15.6^{+5.7}_{-15.6} M_\oplus$, $R_{\rm p}= 4.32 \pm 0.41 R_\oplus$, P = 10.4 days), KOI-94d ($M_{\rm p}= 106 \pm 11 M_\oplus$, $R_{\rm p}= 11.27 \pm 1.06 R_\oplus$P = 22.3 days), and KOI-94e ($M_{\rm p}= 35^{+18}_{-28} M_\oplus$, $R_{\rm p}= 6.56 \pm 0.62 R_\oplus$, P = 54.3 days). The radial velocity analyses of KOI-94b and KOI-94e offer marginal ($> 2\sigma$) mass detections, whereas the observations of KOI-94c offer only an upper limit to its mass. Using the KOI-94 system and other planets with published values for both mass and radius (138 exoplanets total, including 35 with $M_{\rm p} < 150 M_\oplus$), we establish two fundamental planes for exoplanets that relate their mass, incident flux, and radius from a few Earth masses up to ten Jupiter masses: $\frac{R_{\rm p}}{R_\oplus} = 1.78 \left(\frac{M_{\rm p}}{M_\oplus}\right)^{0.53} \left(\frac{F}{\rm erg\,s^{-1}\,cm^{-2}}\right)^{-0.03}$ for $M_{\rm p} < 150 M_\oplus$, and $\frac{R_{\rm p}}{R_\oplus} = 2.45 \left(\frac{M_{\rm p}}{M_\oplus}\right)^{-0.039} \left(\frac{F}{\rm erg\,s^{-1}\,cm^{-2}}\right)^{0.094}$ for $M_{\rm p} > 150 M_\oplus$. These equations can be used to predict the radius or mass of a planet.

2.1 Introduction

One of the most pressing problems in exoplanetary physics is the anomalously large radii of close-in transiting gas giant planets. These hot Jupiters have radii larger than predicted by standard models of giant planet cooling and contraction (for reviews, see Fortney & Nettelmann 2010; Baraffe et al. 2010). Some mechanism, or a variety of mechanisms, prevents planets from contracting, resulting in the observed inflated planetary radii. The reasons for the radius anomaly for these planets could be tied to their formation and subsequent orbital evolution to close-in orbits, where the planets are subject to extremes of both tidal and radiative forcing. Mechanisms to explain the large radii of the planets have tried to tap the vast energy sources available in tidal or radiative forcing. It is critical to build up a large sample size of transiting giant planets, at a variety of orbital distances and incident fluxes, to better understand the physics that leads to the radius anomaly.

Miller & Fortney (2011) pointed out that all transiting giant planets receiving less incident flux than 2×10^8 erg s^{-1} cm^{-2} do not appear inflated, meaning that they are all smaller in radius than expected for pure H/He objects. Miller & Fortney (2011) estimated the masses of heavy elements contained within that relatively cool sample of 16 planets (at that time). Demory & Seager (2011) extended this work to *Kepler* gas giant candidate planets, and also found a lack of inflated candidates beyond this same critical flux level, 2×10^8 erg s^{-1} cm^{-2}. This incident flux is approximately equal to an equilibrium temperature of 1000 K, for a zero Bond albedo and planet-wide redistribution of absorbed stellar flux. The detailed study of giant planets receiving less than 2×10^8 erg s^{-1} cm^{-2} in incident flux will serve as a useful contrast against the population of inflated giant planets that receive higher levels of incident flux.

To probe the underlying physical processes that cause the observed diversity of planetary densities, we need to both expand our sample and to test links between the planets' physical properties and their orbital properties. The first part of the paper focuses on expanding our sample. We measure the mass of a modestly irradiated giant planet or "warm Jupiter," KOI-94d, in order to calculate its density and place constraints on its interior structure. We wish to determine whether this planet, which is in a 22.3-day orbit and receives 2675 times as much incident flux as Jupiter (just a bit below the "critical" flux limit described above), is more similar to the bloated hot Jupiters or the cooler non-inflated gas giants, like our own Jupiter.

In addition to the warm Jupiter, KOI-94 hosts at least 3 smaller planets, all of which were detected through transit signatures in the photometry from the *Kepler* Mission. Hirano et al. (2012) note the planet-planet eclipse that occurs in this system, which allows a detailed analysis of the planets' orbital dynamics. The multiplicity of this system presents an opportunity to examine the architecture of a closely packed system with a warm Jupiter. Using Keck-HIRES radial velocities (RVs), we measure the mass of the warm Jupiter. We obtain marginal mass measurements of two other planets in the system and an upper limit to the mass of the fourth. Coupled with the mass of the giant planet we obtain from RVs, transit timing variations (TTVs) in the photometry allow an additional check of the RV

masses obtained in this work.

In the second part of this paper, we investigate how the mass and incident flux of a planet relate to the planet's radius. Enoch et al. (2012) and Kane & Gelino (2012) have done similar work, but here we include many more low-mass planets (down to 3 $M_{\oplus}$), allowing us to probe the mass-radius-flux relation at lower masses than in either of those papers.

This chapter is structured as follows: Section 2.2 reviews mechanisms for inflating giant planets, 2.3 presents observations of KOI-94, 2.4 describes the analyses used to derive planet masses, 2.5 argues for the planetary status of all four transiting candidates of KOI-94 2.6 describes the composition of KOI-94d, 2.7 presents the radius-mass-incident flux relations for exoplanets and discusses possible interpretations, and 2.8 summarizes.

2.2 Inflation Mechanisms

A menagerie of radius inflation mechanisms have been proposed to explain the large radii of hot Jupiters. The most recent reviews, now becoming slightly out of date, are in Fortney & Nettelmann (2010) and Baraffe et al. (2010). Without going into detail here on any one mechanism, we classify possible explanations into three groups: incident flux-driven mechanisms, tidal mechanisms, and delayed contraction.

Some inflation mechanisms are driven by incident flux from the parent star, also called insolation, whereby a small fraction of the absorbed stellar flux is transported by a physical mechanism much deeper into the atmosphere, near or past the radiative-convective boundary. These mechanisms are discussed in a variety of papers: weather layer kinetic energy transport (Showman & Guillot 2002; Showman & Guillot 2002), Ohmic dissipation (Batygin & Stevenson 2010; Perna et al. 2010), thermal tides (Arras & Socrates 2010), and mechanical greenhouse (Youdin & Mitchell 2010). These mechanism would in general affect all close in giant planets to some degree, with the strength of the effect waning at lower insolation levels. Diversity in planetary mass, planetary heavy element masses, and planetary temperature would lead to a range of inflated radii. For reference, the time-averaged incident flux on a planet is:

$$\langle F \rangle = \sigma T_{\rm eff}^4 \frac{R_\star^2}{4\pi a^2} \sqrt{\frac{1}{1-e^2}}, \tag{2.1}$$

where $R_\star$ is the stellar radius, $T_{\rm eff}$ is the effective stellar temperature, a is the semi-major axis, and e is the orbital eccentricity.

Another class of solutions are tidal interactions between the host star and planet, in particular, eccentricity damping. Coupled tidal and planetary structure evolution has been calculated by a number of authors (Bodenheimer et al. 2001; Gu et al. 2003; Ibgui & Burrows 2009; Miller et al. 2009; Ibgui et al. 2010; Leconte et al. 2010). The emerging view, in particular advanced by Leconte et al. (2010) who used the most detailed tidal evolution equations, is that since radius inflation via orbital eccentricity damping is a transient phenomenon, it cannot be the "universal" radius inflation mechanism. Radius inflation by tidal heating is a short-lived phenomenon, but the average system age is several Gyr. However, in

certain circumstances, including when a nonzero orbital eccentricity is maintained by outside forcing, tidal heating can inflate giant planet radii for as long as the forcing lasts. The tidal power on a planet scales like:

$$\dot{E} = \frac{63}{4} \frac{(2\pi)^5}{G} \frac{R_{\rm p}^5}{Q'_P} \frac{e^2}{P^5} \tag{2.2}$$

where $\dot{E}$ is the power, $R_{\rm p}$ is the planetary radius, G is Newton's gravitational constant, Q'_P is the tidal dissipation factor, and P is the orbital period (rewritten from Equation 1 in Ibgui et al. 2010, using Kepler's Third Law). Two advantages of rewriting this equation are that (1) orbital period, rather than semi-major axis, is an observable, and (2) this formulation of the equation does not depend on stellar mass.

For completeness, we mention that delayed planetary contraction, due either to higher than anticipated atmospheric opacities (Burrows et al. 2007) or interior barrier to convection (Chabrier & Baraffe 2007) are another class of solutions which could contribute somewhat to larger radii. However, neither of these ideas should depend on proximity to the parent star, which should clearly be a feature of the correct solution(s).

2.3 Observations

In this section, we present photometry from the *Kepler* Space Telescope, as well as data from the ground-based techniques of adaptive optics imaging, speckle imaging, and spectroscopy. Transits of the planet candidates were identified in the *Kepler* light curves in Batalha et al. (2013) and Borucki et al. (2012). In §4, we describe our method for simultaneously fitting the photometry and radial velocities derived from time-series spectroscopy. Here, we present adaptive optics imaging, speckle imaging, and spectroscopy of KOI-94. These observations rule out various instances of a nearby, stellar companion that could masquerade as a transiting planet, or possible false-positive scenarios, as discussed in §5.

2.3.1 *Kepler* Space Telescope

KOI-94 is on the edge of one of the chips of the *Kepler* CCD (see Figure 2.1), so when the spacecraft rotates, the CCD loses the part of its field of view containing KOI-94. This causes two-quarter long gaps in the light curve.

Nonetheless, the *Kepler* pipeline, as described in Batalha et al. (2013), has found 4 transiting planet candidates associated with KOI-94 (see Figure 2.2). The light curve is phase-folded around their transit centers in Figure 2.3. In summary, they are a super-Earth (KOI-94b) in a 3.7-day orbit, a mini-Neptune or super-Earth (KOI-94c) in a 10-day orbit, a Jupiter-size planet (KOI-94d) in a 22-day orbit, and a Neptune-size planet (KOI-94e) in a 54-day orbit. The Kepler Input Catalog (KIC) ascribes an effective temperature of 6217 K and a radius of 1.238 $R_\odot$to KOI-94, resulting in planetary radii of 1.41 $R_\oplus$, 3.44 $R_\oplus$, 9.26 $R_\oplus$, and 5.48 $R_\oplus$for planets b, c, d, and e, respectively. Our analysis of the stellar

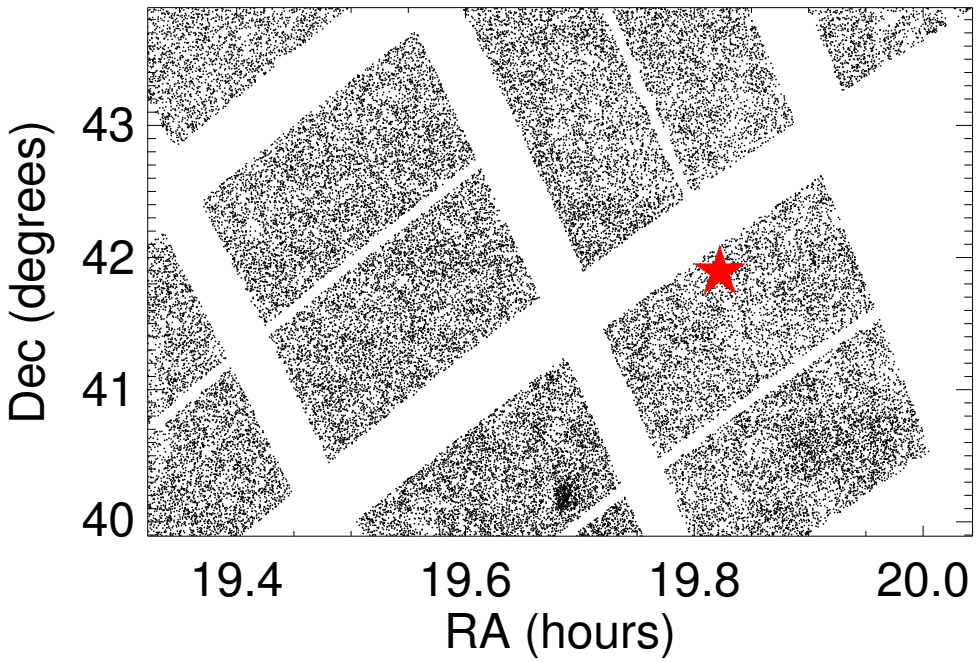

Figure 2.1: A section of the *Kepler* footprint. Each point is a *Kepler* target. The red five-pointed star marks the location of KOI-94.

spectrum, which finds different values for the stellar temperature and radius and therefore for the planet radii, is described in §4.

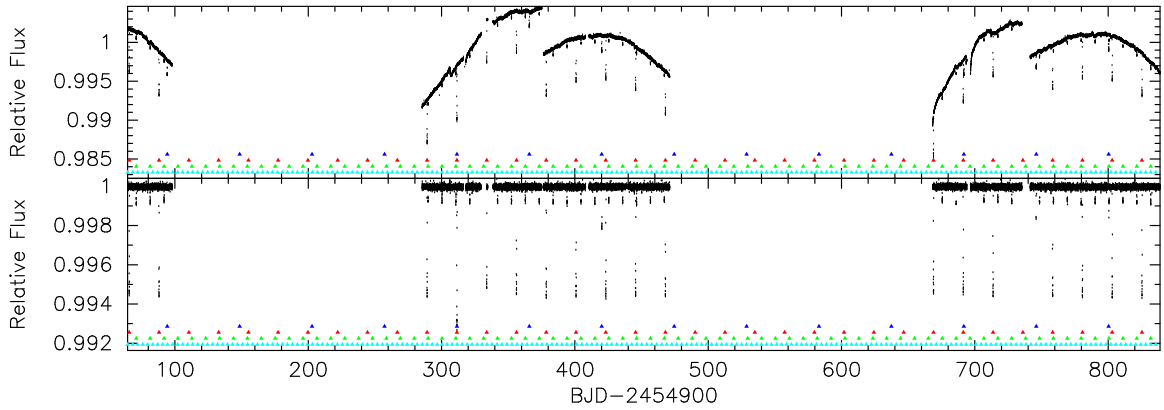

Figure 2.2: The top panel shows the aperture photometry long cadence (30 minute) light-curve. No corrections have been applied to the photometric measurements. The bottom panel shows the detrended light-curve. The data were detrended by applying a 2-day median filter. Observations that occurred during a planetary transit were excluded from the calculation of the median. The triangles indicate when transits occurred for planets b, c, d, and e with corresponding colours of cyan, green, red and blue.

2.3.2 Adaptive Optics

KOI-94 was observed with near-infrared adaptive optics on 2009 Nov 08 using ARIES on the MMT (Adams et al. 2012). Images were obtained in both J and Ks, and reveal no companions closer than 7.5″ ($\Delta_J = 2.5$, $\Delta_{Ks} = 2$; see Figure 2.4). The image FWHM was 0.23 in Ks and 0.43 in J. We can place a limit on undetected companions of $\Delta_J = 2.2$ and $\Delta_{Ks} = 3.4$ at 0.5″, $\Delta_J = 4.6$ and $\Delta_{Ks} = 5.9$ at 1.0″, and $\Delta_J = 8.7$ and $\Delta_{Ks} = 9.1$ at 4.0″(and beyond). Any additional companions that would dilute the transit light curve and change the planet parameters are constrained to be faint or very close to the star.

2.3.3 Speckle Imaging

Speckle imaging of KOI-94 was obtained on the night of 19 June 2010 UT and the night of 23 Oct 2010 using the two-color DSSI speckle camera at the WIYN 3.5-m telescope on Kitt Peak. The speckle camera simultaneously obtained 5000 (3000) 40 msec images on 19 June (23 Oct) in filters: V (center = 5620Å, width = 400Å) , R (center = 6920Å, width = 400Å) and I (center = 8880Å, width = 400Å). These data were reduced and processed to produce a final reconstructed speckle image for each filter. Figure 2.5 shows the reconstructed R band image. North is up and East is to the left in the image and the "cross" pattern seen in the image is an artifact of the reconstruction process. The details of the two-color speckle

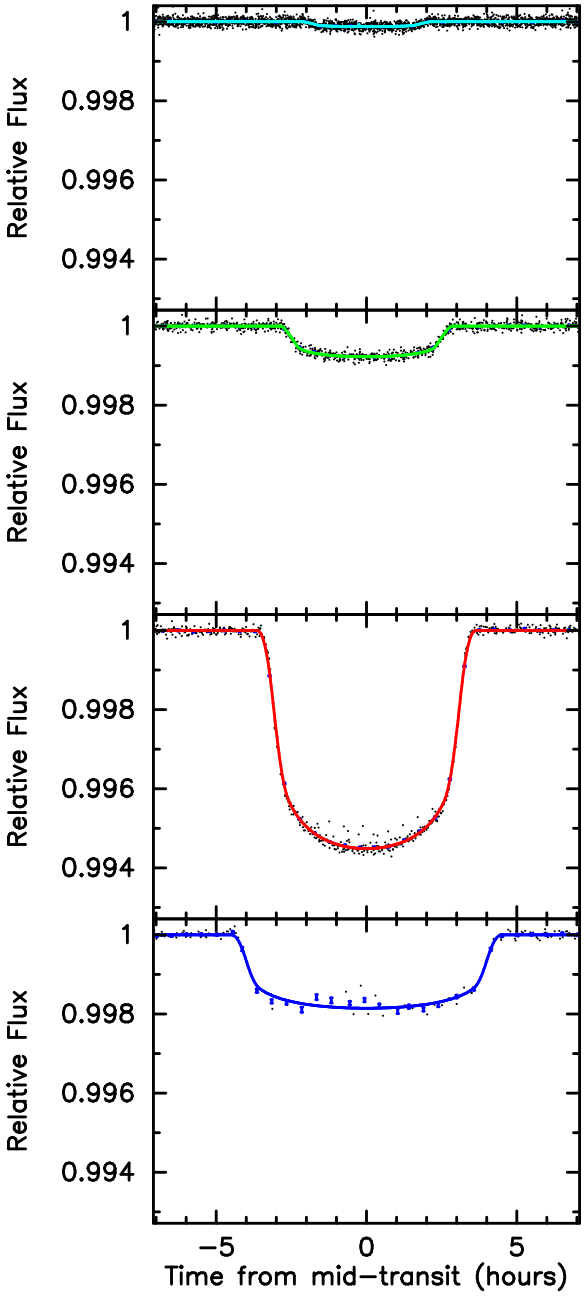

Figure 2.3: The top panel shows the photometric observations phased to the orbital period of planet b with the best fit transit model overlaid. The transit models for planets c, d and e have been removed. The transit times have been corrected for transit-timing variations. The next three panels show the transit lightcurves centred on planets c, d, and e respectively. As in the upper panel, the best fit models for other transiting planet have been removed and corrected for transit timing variations. The colors of the overlaid models match the identification used in Figure 2.2.

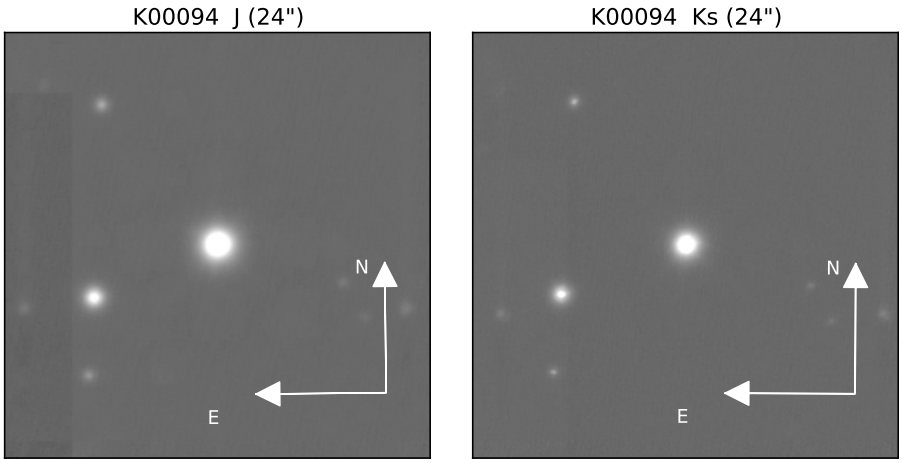

Figure 2.4: Adaptive optics image of KOI-94 (center) in J and Ks. The closest companion is 7.5″ away. All of the objects in the frame are stars except for the spot in the bottom left, which is an artifact.

camera observations and the *Kepler* follow-up observing program are presented in Howell et al. (2011).

On both occasions, the speckle data for this R=12.5 star allow detection of a companion star within the approximately 2.76 × 2.76″ box centered on the target. The speckle observation can detect, or rule out, companions between 0.05″ and 1.5″ from KOI-94. The June 2010 speckle image was obtained with the WIYN telescope during relatively poor native seeing near 1.0″, while the Oct 2010 observations made during good seeing, 0.6″. We found no companion star within the speckle image separation detection limits to a delta magnitude limit of ∼4 mag in the R band, 2 mag in the V band, and 3.4 mag in the I band.

2.3.4 Spectroscopy

We obtained time-series spectroscopy of KOI-94 on the W. M. Keck I telescope with the HIRES echelle spectrometer through an iodine cell. Most of the observations occurred between May and August 2012, but our earliest observation was 2009-12-07. We rejected spectra with fewer than 4000 ADU (8760 photons), since these low-signal spectra resulted in large (> 6 m/s) radial velocity errors. We also excluded spectra taken during a transit of KOI-94d to avoid confusion from the Rossiter-McLaughlin effect. This yielded 26 spectra that we deemed suitable for RV analysis, as presented in Table 2.1. We also obtained a spectrum of KOI-94 without the iodine cell as a template for RV analysis and for characterizing the star (see Section 2.4)).

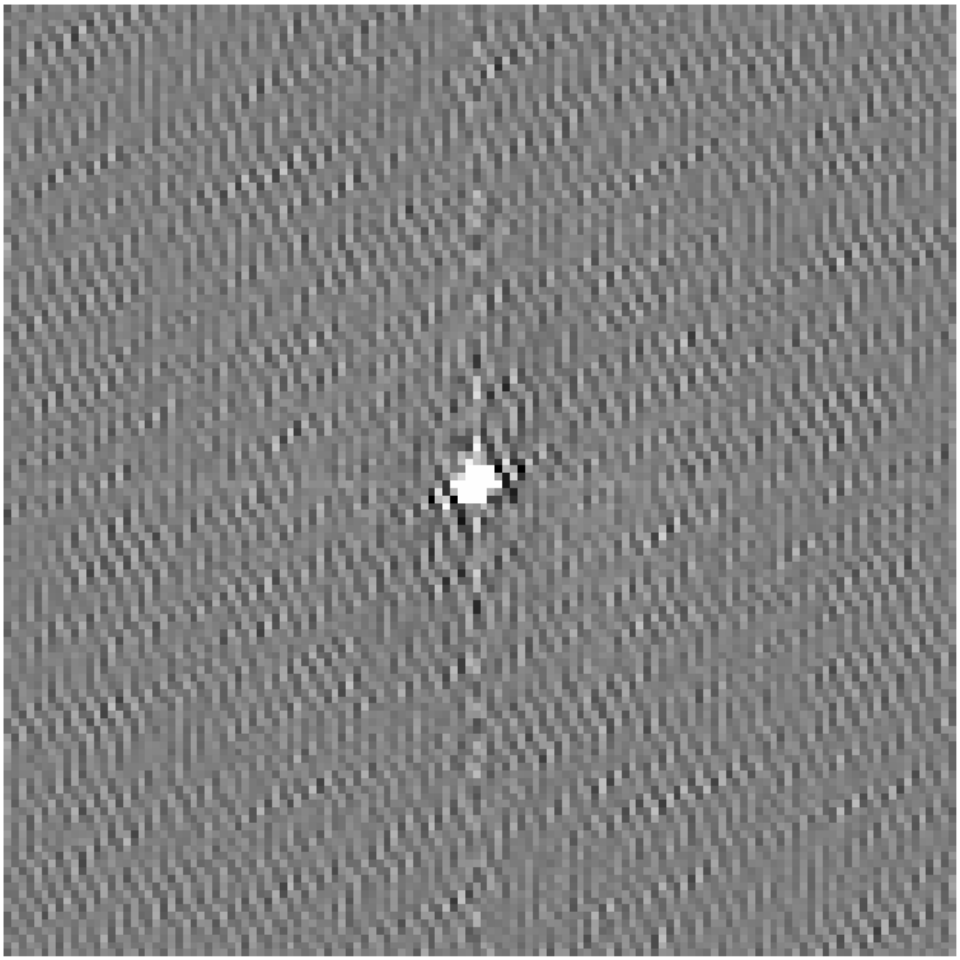

Figure 2.5: Speckle image obtained 2012-10-23 at the WIYN telescope at 692 nm. The image spans $2.76'' \times 2.76''$.

Table 2.1: Spectroscopic Observations

JD - 2440000.0	Photons	RV (m/s)	Error (m/s; Jitter = 3.0)
15172.768	9351	−9.6	6.1
16076.070	11709	27.0	5.5
16100.047	23095	14.2	5.0
16109.929	23065	−13.5	5.0
16111.048	22920	−16.8	5.0
16113.043	22594	−14.9	5.0
16114.077	14484	−17.0	6.0
16115.074	21584	−5.0	5.0
16116.054	23041	8.1	4.8
16134.015	22973	−9.2	4.9
16135.095	23592	−9.7	4.7
16139.015	22594	6.8	4.5
16140.813	22370	3.8	5.0
16144.100	20178	20.3	5.2
16144.796	23330	14.6	4.6
16146.057	18774	18.5	4.9
16147.972	22642	2.5	4.7
16149.091	15395	−13.8	5.0
16149.752	22918	6.1	4.5
16149.766	22629	−6.7	4.6
16150.065	19204	−2.6	4.8
16150.079	19162	−5.6	4.8
16150.094	18323	−10.1	4.9
16151.075	22791	−10.0	5.2
16164.001	23183	23.0	4.9
16173.925	21904	−10.7	5.1

Note. — Observations with low signal-to-noise (fewer than 8760 photons) were not used in our analysis and are omitted from this table. Photon counts are averaged over all pixels.

Note that one observation, on JD 16135.095, occurred during a transit of planet e. To see whether this datum affected our mass results, we tried removing it and repeating the circular analysis described in Section 2.4.2. Removing the datum changed the masses of the planets by $\sim .01\sigma$, and so we can safely ignore the effects of this datum on our analysis of the planetary system.

We determined the radial velocity of KOI-94 in each iodine spectrum based on the spectrum's Doppler shift. We used the lab-frame iodine lines that the iodine cell superimposes on the stellar spectrum to calibrate velocities to an instrumental precision of 3 $\mathrm{m\,s^{-1}}$(although stellar jitter introduces additional errors). This technique is described in further detail in Howard et al. (2011).

2.4 Planet and Stellar Properties from Radial Velocities, Photometry and Spectra

We use radial velocity measurements of KOI-94 to determine the mass of planet d, marginal mass detections of planets e and b, and an upper limit on the mass of planet c. A plot of radial velocity versus time and a four-planet circular fit is shown in Figure 2.6.

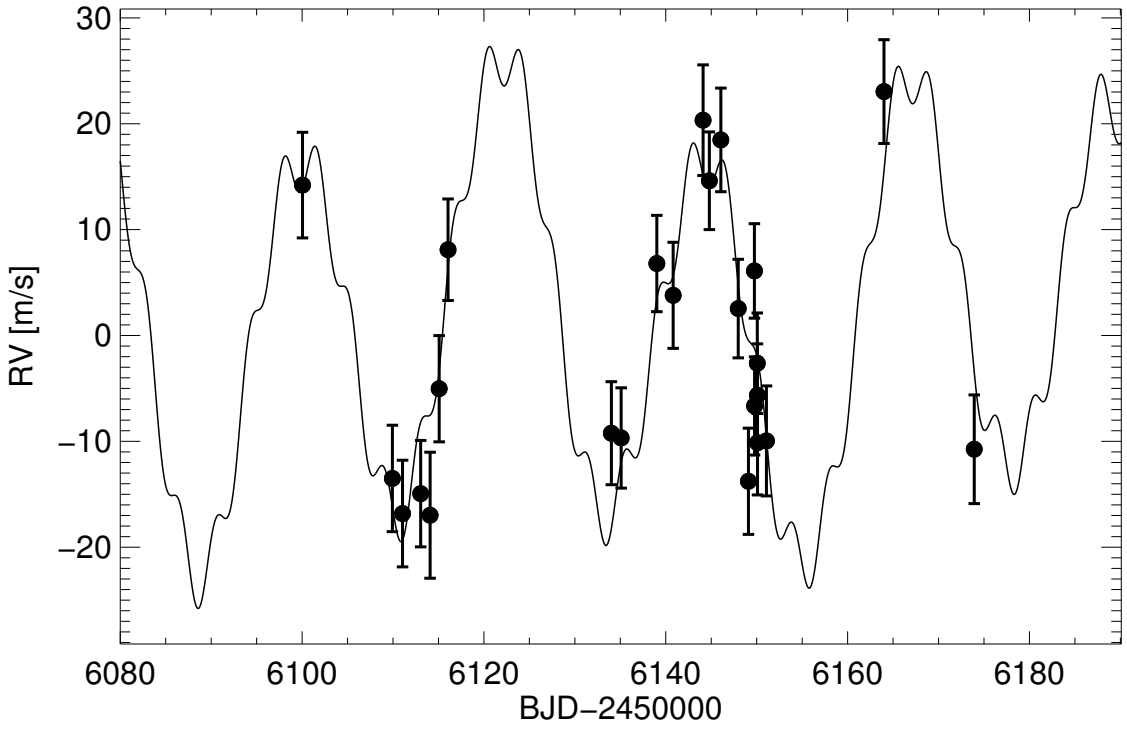

Figure 2.6: Radial velocity versus time from May 2012 onward. Black points are data with 1σ errors (assuming a stellar jitter of 3.0 m/s); a circular four-planet fit is superimposed.

We fit the RVs with three models, each of which provides an interesting interpretation of the system. The first model has only one planet (the giant) in a circular orbit. This is because the giant planet dominates the RVs, and so it is useful to compare a four-planet solution to a simpler one-planet solution. In our second model, all four planets are in circular orbits. Because KOI-94 is a closely-packed system, we do not expect large eccentricities of the planets, so we want to verify that a solution allowing eccentricities is not significantly different from a circular solution. In our third and most sophisticated model, we fit for all four planets in eccentric orbits while simultaneously fitting the light curve.

2.4.1 Circular Orbit Solutions

Here we compare the results of the one-planet and four-planet circular orbital solutions. For the one-planet fit, we find $K = 16.3\,\mathrm{m\,s^{-1}}$, producing a reduced χ^2 of 1.97. The data and phase-folded, one-planet circular fit are shown in Figure 2.7.

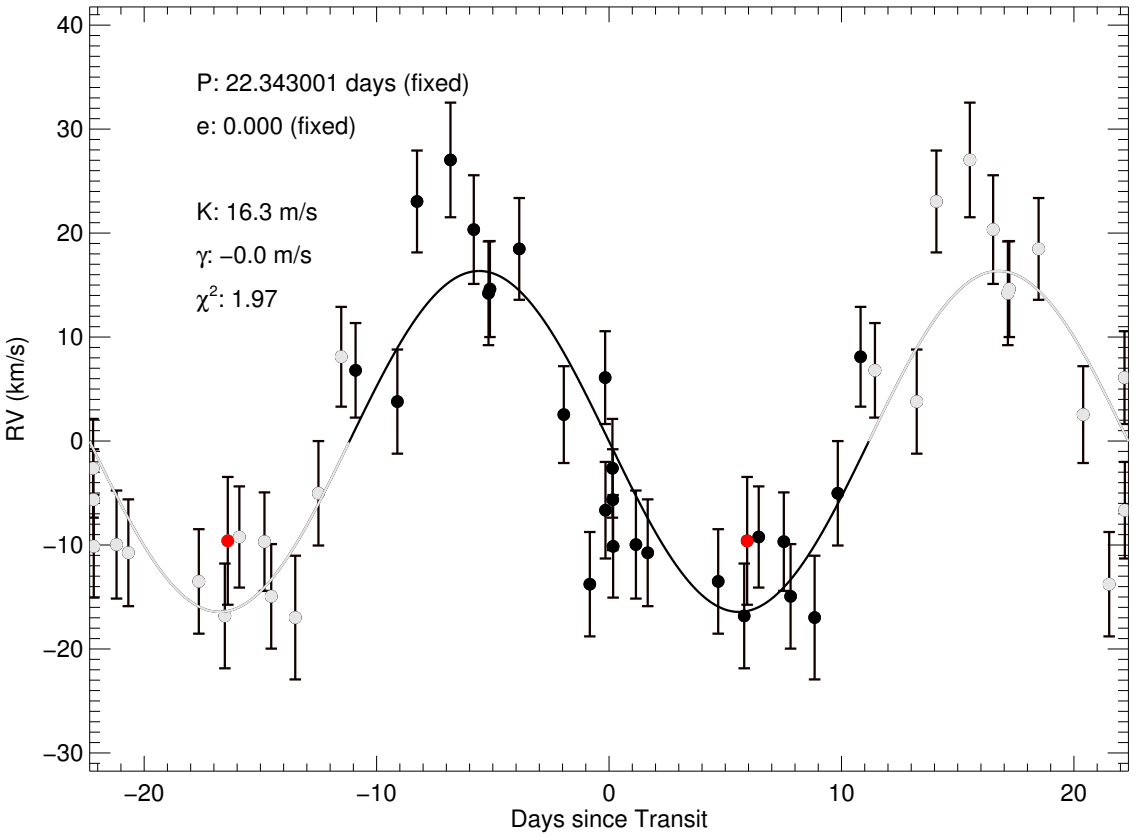

Figure 2.7: A one-planet, circular fit to the RVs, phase-folded to the period of KOI-94d. The black points are the data (error bars are 1σ), and the black line is the circular one-planet fit to the data. The gray points and fit are time-shifted repetitions of the black data points and fit. The red point is the oldest data point (2009); all other data are from summer 2012.

In the four-planet circular model, the center-of-mass velocity γ of the system and the semi-amplitude K_n of each planet n are allowed to vary, allowing 5 degrees of freedom; all other orbital parameters are fixed. We augmented the photon-noise errors by 3.0 $\mathrm{m\,s^{-1}}$in quadrature to account for the stellar jitter. The best four-planet fit had a reduced χ^2 of 1.60. The best-fit radial velocity components from the four planets are shown in Figure 2.8.

Because the stellar jitter is unknown, we recalculated this fit, varying the stellar jitter to achieve $\chi^2 = 1$ (this yielded a jitter of 5.0 $\mathrm{m\,s^{-1}}$). The RV semi-amplitudes achieved in this fit were consistent with those assumed for a stellar jitter of 3.0 $\mathrm{m\,s^{-1}}$: the semi-amplitude

Table 2.2: Planet parameters for circular orbits of KOI-94.

Parameter	Value
Circular Keplerian Fit: KOI-94b	
Center-of-mass velocity γ ($\mathrm{m\,s^{-1}}$)	1.76 ± 1.4
Orbital semi-amplitude K ($\mathrm{m\,s^{-1}}$)	3.2 ± 1.7
Mass M_p ($M_\oplus$)	9.2 ± 4.9
Density ρ_p ($\mathrm{g\,cm^{-3}}$)	9.0 ± 4.7
Circular Keplerian Fit: KOI-94c	
Orbital semi-amplitude K ($\mathrm{m\,s^{-1}}$)	1.6 ± 1.3
Mass M_p ($M_\oplus$)	6.5 ± 6.3
Density ρ_p ($\mathrm{g\,cm^{-3}}$)	0.46 ± 0.37
Circular Keplerian Fit: KOI-94d	
Orbital semi-amplitude K ($\mathrm{m\,s^{-1}}$)	19.68 ± 2.19
Mass M_p ($M_\oplus$)	102 ± 11.4
Density ρ_p ($\mathrm{g\,cm^{-3}}$)	0.380 ± 0.042
Circular Keplerian Fit: KOI-94e	
Orbital semi-amplitude K ($\mathrm{m\,s^{-1}}$)	5.25 ± 2.04
Mass M_p ($M_\oplus$)	36.6 ± 14.4
Density ρ_p ($\mathrm{g\,cm^{-3}}$)	0.690 ± 0.268

Note. — The best fit parameters for four planets in circular Keplerian orbits, after adopting stellar parameters and orbital ephemerides from the eccentric solution described in Section 2.4.2 (see Table 2.3).

for KOI-94d and KOI-94e changed by less than half a percent, and the semi-amplitudes for KOI-94b and KOI-94c fell within the 1σ errors. We also note that because these are circular fits, the difference in χ^2 between a model with a stellar jitter of $3.0\mathrm{m\,s^{-1}}$ and $5.0\mathrm{m\,s^{-1}}$ could arise from planetary eccentricities that are excluded from the model. Therefore, we assume a stellar jitter of $3.0\ \mathrm{m\,s^{-1}}$ and adopt the resulting parameters for the 4-planet circular solution, which are reported in Table 2.2.

We assessed the errors in K_n with a Markov Chain Monte Carlo (MCMC) analysis of 1 chain of 10^7 trials using the Metropolis-Hastings algorithm. Figure 2.9 shows the posterior likelihood distributions. The corresponding planet mass (M_p) and density (ρ_p) distributions (which are calculated from the orbital period and planet radius) are also shown. These parameters are reported in Table 2.2.

To calculate the probability of a non-detection in RVs for each planet, we assume a Gaussian posterior distribution and calculate the fraction of trials that would have occurred for masses at or below zero, had we not imposed a positive definite value for K_n. We calculate the following probabilities of a non-detection via RVs: 0.04 for planet b, 0.14 for planet c, 5×10^{-19} for planet d, and 0.007 for planet e. However, these estimates of the non-detection probability are smaller than the true probability of non-detection because of the Lutz-Kelker bias, especially for planet c.

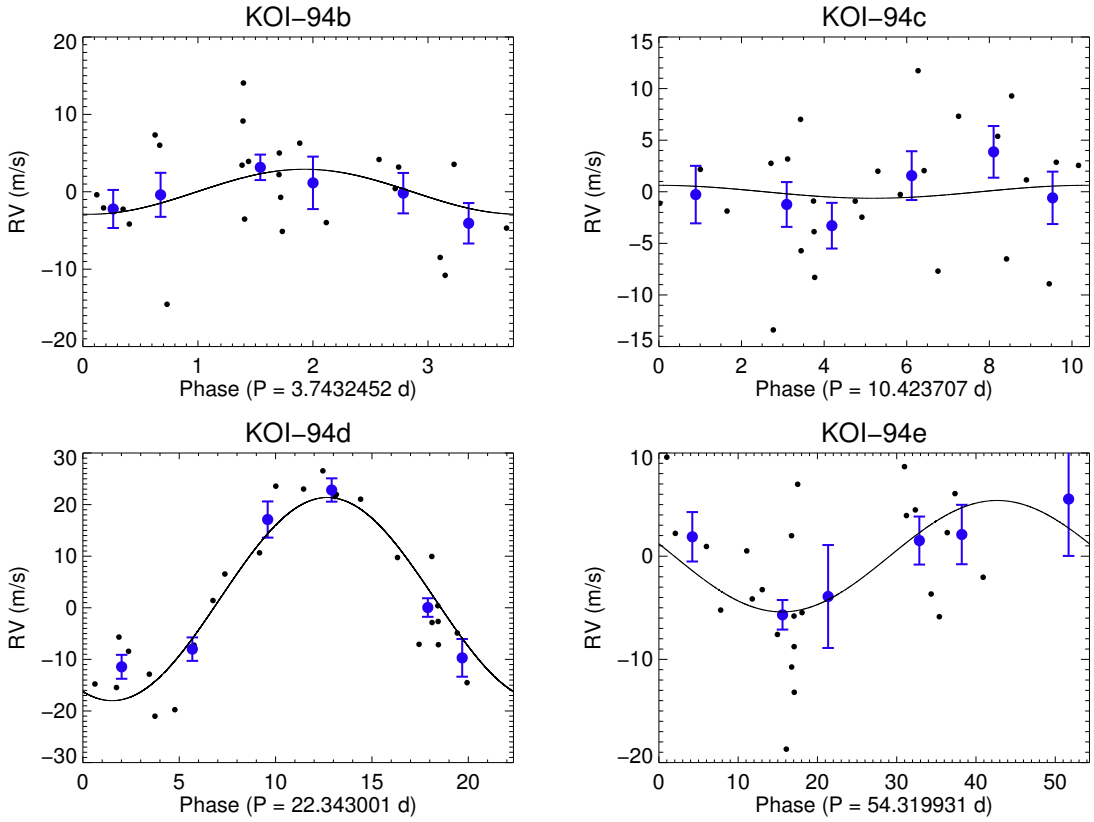

Figure 2.8: Radial velocity components from a four-planet circular fit. Each panel shows the radial velocity signature from one planet. The black line is the model fit; the black points are the RV data minus the model RVs from the other three planets. The blue points are the binned RVs. We chose the number of bins by rounding up the square root of the number of observations, creating 6 bins of equal spacing in phase. The error bars are the uncertainty in the mean of the data in each bin. The reduced χ^2 of this fit is 1.60. The RVs provide a 9σ detection of KOI-94d, a 2.5σ detection of KOI-94e, a 2σ detection of KOI-94b and an upper limit on the mass of KOI-94c.

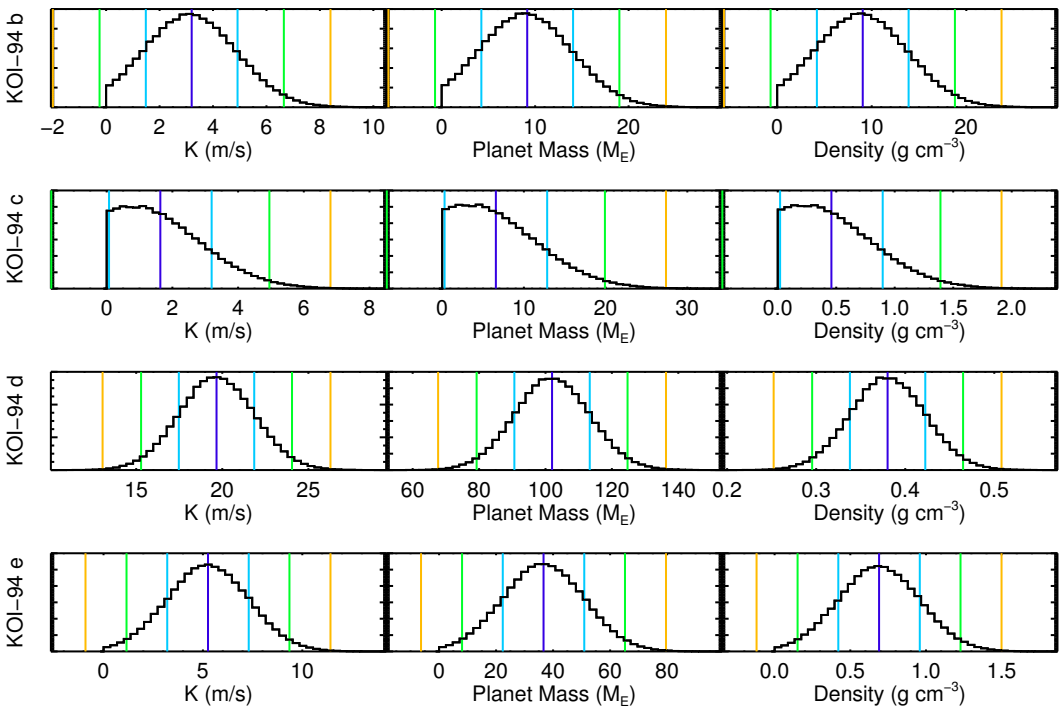

Figure 2.9: Posterior distributions for the four-planet circular fit. From left to right: likelihoods of K, M_P, and ρ_P for (top to bottom) KOI-94b, KOI-94c, KOI-94d, and KOI-94e. The median, 1σ, 2σ, and 3σ likelihoods are over-plotted in dark blue, cyan, green, and orange. To account for the positive definite bias of the likelihood distribution, σ is measured above the median only; lower bounds are reflections of the upper bounds (i.e., a symmetric distribution is assumed). This enables a quantitative estimate of the number of trials consistent with a non-detection via RVs. Note that the best-fit values are obtained by minimizing χ^2; the posterior distributions are used only for estimating uncertainties. The best-fit values and uncertainties for the circular orbits are presented in Table 2.2.

Limiting Outer Planets

The absence of a significant change in the radial velocity of the star between our earliest and most recent measurements strongly limits the possibility of a massive outer companion. To quantify this, we computed a circular, four-planet orbit solution in which we allowed a linear trend in the radial velocity as a free parameter and used an MCMC analysis to explore the likelihood of a given linear velocity trend. Over a two-year baseline, the median trend was -0.0125 ± 0.0063 m s^{-1} per day, which corresponds to a 3σ upper limit of -6.9 m s^{-1} per year. In the style of Winn et al. (2010), we compute the mass of an outer perturber based on the stellar acceleration, $\dot{\gamma}$, assuming the planet induces Newtonian gravitational acceleration on the star and in the limit $M_{\rm p} \ll M_\star$: $\dot{\gamma} = GM_{\rm p}/a^2$. To induce a stellar acceleration $\dot{\gamma}$ of -6.9 m s^{-1} per year via Newtonian gravity, an outer perturber would need to satisfy

$$\frac{M_{\rm p} \sin i}{M_{\rm J}} \left(\frac{a}{10 \text{ AU}} \right)^{-2} = 3.9, \tag{2.3}$$

where i is the inclination of the planet's orbital plane with respect to the line of sight and $M_{\rm J}$ is the mass of Jupiter. Thus, with a significance of 3σ, we can rule out companions more massive than 3.9 $M_{\rm J}$ within 10 AU or more massive than 1.0 $M_{\rm J}$ within 5 AU.

2.4.2 Eccentric Orbit Solution

The four-planet fit in which we allow eccentricities to float is the most versatile model. This model has the advantage of simultaneously fitting the light curve and the RVs, which measures $\rho_\star$ (thus refining $M_\star$ and $R_\star$). As demonstrated below, the values for planet masses in this model agree with the planet masses determined in the circular orbital solution to within 1σ, and so we adopt the parameters from the eccentric solution for the rest of this work.

The *Kepler* photometry and Keck radial velocities were simultaneously fit with an orbital model. The model has the following free parameters: mean stellar density ($\rho_\star$), scaled planetary radius ($r_n/R*$), impact parameter (b_n), orbital period (P_n), center of transit time ($T_{c,n}$), radial velocity amplitude (K_n), eccentricity (e_n) and argument of pericenter (w_n) via esinw_n and ecosw_n. A photometric and radial velocity zero point were also included. The number (n=1,2,3,4) corresponds to the parameters for planet b,c,d and e respectively. The transit model uses the quadratic formulae of Mandel & Agol (2002). Limb-darkening coefficients were fixed in the models to 0.3236 and 0.3052 as determined from the grid of Claret & Bloemen (2011). The orbits are modeled with non-interacting Keplerians.

A best-fit model was initially computed by minimizing χ^2 with a Levenberg-Marquardt style algorithm. This model was used to measure TTVs and to seed an MCMC analysis of the model parameter space. TTVs were determined by fitting for each individual transit, fixing all parameters except T_c to their best-fit values. An updated best-fit model was then computed using the TTVs to produce a better phased transit for each planet. The time-series were corrected by computing time-corrections based on a linear-interpolation of the TTVs.

Posterior distributions for each model parameter were determined with an MCMC-style algorithm. This model has been described in Gautier III et al. (2012) and Borucki et al. (2012), the only difference is that the TTV measurements are included and fixed to their best-fit values. Four Markov-chains were calculated each with a length of 10^6. The first 10% of each chain was discarded as burn-in. The median and $\pm 1\sigma$ percentiles were calculated for each model parameter and reported in Table 2.3.

Stellar Properties

We used the template spectrum (without iodine) to determine the effective temperature ($T_{\rm eff}$= 6182 ± 58), surface gravity ($\log g$= 4.181 ± 0.066), and metallicity ([Fe/H]= +0.0228 ± 0.0020) of KOI-94 through the Spectra Made Easy (SME) analysis technique described in Valenti & Piskunov (1996). Applying the evolutionary constraints of the Yi et al. (2001) model isochrones and the simultaneous solution of the lightcurve and RVs, we determine the mass ($M_\star = 1.277 \pm 0.050$) and radius ($R_\star = 1.52 \pm 0.14$) of KOI-94. The stellar properties are presented in Table 2.3.

Properties of KOI-94d from the Eccentric Orbit Solution

We detect KOI-94d with 9σ confidence with the RVs. The eccentric orbit analysis gives a mass of $106 \pm 11 M_\oplus$. This mass is marginally consistent with the mass reported by Hirano et al. (2012), who found $M_{\rm p} = 73 \pm 25\ M_\oplus$.

2.4.3 Planet Masses from Transit Timing Variations.

We observe coherent TTVs for KOI-94c and KOI-94d which are presented in Figure 2.11. TTVs usually indicate gravitational interactions between adjacent pairs of planets; such interactions allow us to refine the mass estimates of these planets.

We use the prescription of Equations 8 and 9 from Lithwick et al. (2012) to predict the anti-correlated TTV signals produced during the interaction of planets c and d between 650 and 800 days. Assuming zero eccentricity for both planets and ignoring factors of order unity, we calculate

$$V = P \frac{\mu'}{\pi j^{(2/3)} (j-1)^{(1/3)} \Delta} \tag{2.4}$$

$$V' = P' \frac{\mu}{\pi j (j-1)^{(1/3)} \Delta} \tag{2.5}$$

where μ is the ratio of the inner planet mass to the stellar mass, μ' is the ratio of the outer planet mass to the stellar mass, V is the predicted semi-amplitude of the complex TTV signal for the inner planet, and V' is the predicted semi-amplitude of the complex TTV signal for the outer planet. Δ, which is given by

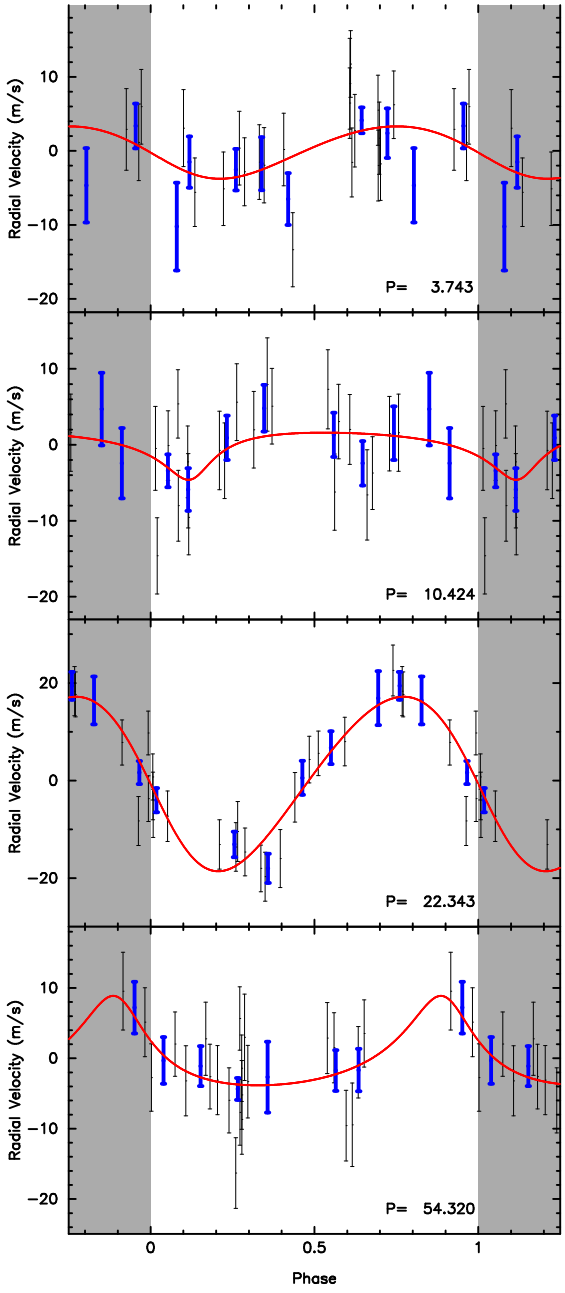

Figure 2.10: Radial velocity components from the four-planet eccentric fit in which the photometry and radial velocities were fit simultaneously. Each panel shows the radial velocity signature from one planet (top to bottom: b, c, d, e). The red line is the model fit; the black points are the RV data minus the model RVs from the other three planets. The blue points are the binned RVs; their error bars the uncertainty in the mean. The shaded regions show phase-shifted repetitions of the data and fit.

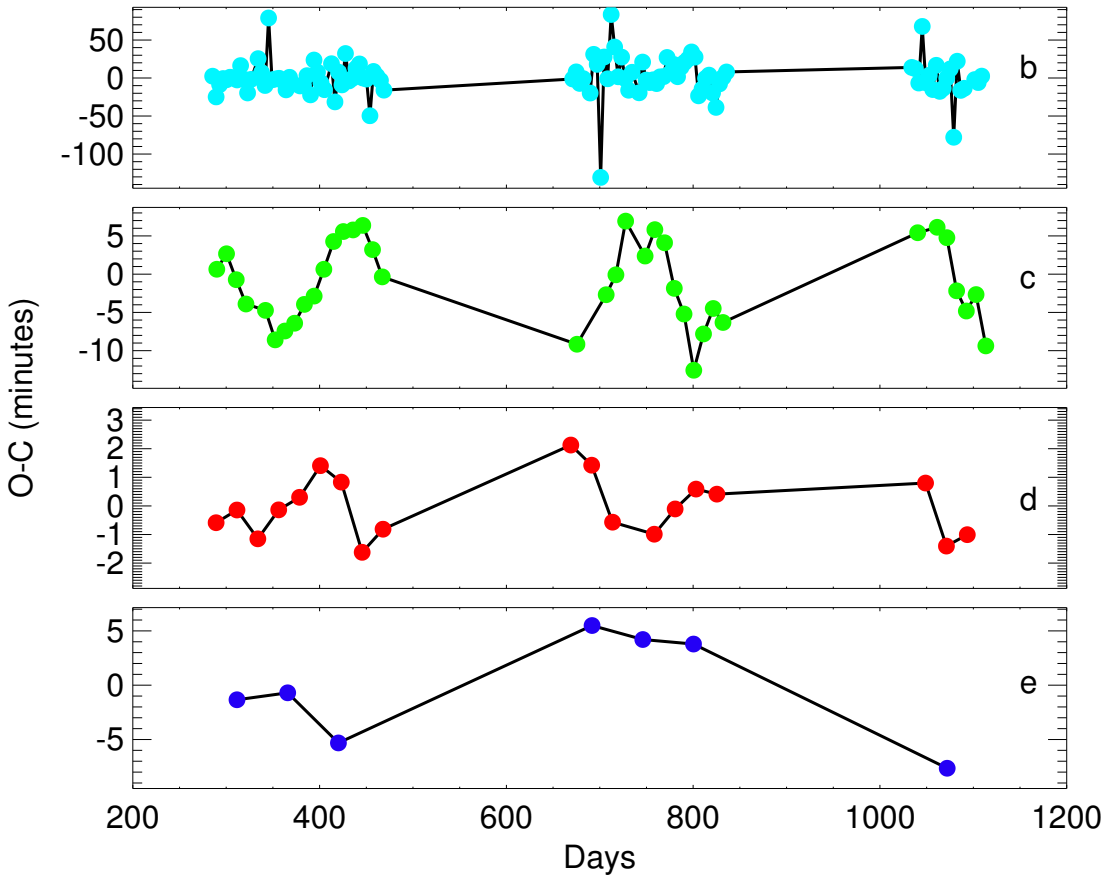

Figure 2.11: Observed Transit Timing Variations in Q1-Q12 for (top to bottom) KOI-94b, KOI-94c, KOI-94d, and KOI-94e, with the same color scheme as Figures 2.2 and 2.3. The y-axis of each plot shows the difference between the observed transit time (O) and the transit time expected for a periodic orbit (C). Days are in JD−2454900. The errors are smaller than the point size. We excluded one 5.5σ outlier in the O-C measurements for planet c at 686 days. There is a section between days 650 and 800 in which the TTVs of planets c and d are anti-correlated, indicating a possible gravitational interaction.

$$\Delta = \frac{P'}{P}\frac{j-1}{j} - 1 \tag{2.6}$$

is the fractional departure from a $j : j-1$ mean motion resonance.

Using the values for the orbital periods of planets c and d, for which the closest first-order mean motion resonance is 2:1, we calculate $\Delta = 0.074$. Using the SME-determined mass of the star and the RV-determined planet masses, we calculate $V = 7$ minutes and $V' = 1.7$ minutes. These values agree with the observed TTV interaction in Figure 2.11, for which the TTV amplitudes of planets c and d appear to be about 7 and 1 minutes, respectively.

2.4.4 Dynamical Stability

We investigate the long-term stability of the KOI-94 system. We integrate the orbits of all four planets using the built-in hybrid symplectic/Bulirsch-Stoer integrator, part of the Mercury software package (Chambers 1999). We use the orbital and physical parameters of the four planets detailed in Table 2.3. The mean anomalies are derived from the best-fit joint radial-velocity solution. We define in the following a non-stable system when a close encounter between a given body and one of the four others occurs, within their common Hill radius. In a first set of 1-Myr integrations, fifteen eccentricity values for each planet are randomly drawn from the normal distribution $N(e, \sigma_e^2)$, where e is the best-fit orbital eccentricity and σ_e is the 1σ eccentricity uncertainty. Eighty percent of these integrations yield close encounters between the two innermost planets b and c. Closer inspection of the results reveal that the proximity of b and c put stringent constraints on their orbital eccentricity, only allowing values less than or equal to the best-fit values for the system to be stable.

In a second set of ten integrations, all planets are restricted to circular orbits with masses drawn from their normal distributions, in a similar manner as for orbital eccentricity in the previous step. All integrations with circular orbits resulted in stable systems, showing that varying planetary masses within their 1σ uncertainty has a negligible influence on the dynamical stability of the system, if orbits are kept circular.

More detailed dynamical analyses of the KOI-94 system would determine an upper limit on orbital eccentricity for the b and c components. This would however imply arbitrary assumptions on planetary masses, which would not completely exclude configurations with large orbital eccentricities. A possible resolution would be to precisely determine the planetary masses of the close-in components, either through additional RV observations or an N-body analysis of the TTV signals from these planets.

2.5 Support for the Existence of the Planets

In this work, we sought to measure the mass of the warm Jupiter KOI-94d to determine how the planet compared to the population of hot Jupiters. We simultaneously fit the *Kepler*

light curve and 26 RVs from Keck/HIRES to measure the mass of KOI-94d with a statistical significance of 9σ. We also sought to measure the masses of the other three transiting planet candidates in KOI-94 in order to better understand the architecture of this planetary system. Our RV measurements of KOI-94 measure the masses of the other planets with signficances of less than 3σ (see Tables 2.2 and 2.3). However, other observations we have made support the interpretation of KOI-94 as a system with four transiting planets. We describe support for the planetary interpretation of the candidates below. We defer our discussion of the comparison of KOI-94d to other Jupiter-size planets to the next section.

We report the properties of planets KOI-94b ($M_{\rm p}= 10.5 \pm 4.6 M_{\oplus}$, $R_{\rm p}= 1.71 \pm 0.16 R_{\oplus}$), KOI-94c ($M_{\rm p}= 15.6^{+5.7}_{-15.6} M_{\oplus}$, $R_{\rm p}= 4.32 \pm 0.41 R_{\oplus}$), KOI-94d ($M_{\rm p}= 106 \pm 11 M_{\oplus}$, $R_{\rm p}= 11.27 \pm 1.06 R_{\oplus}$), and KOI-94e ($M_{\rm p}= 35^{+18}_{-28} M_{\oplus}$, $R_{\rm p}= 6.56 \pm 0.62 R_{\oplus}$). Although the fidelity of the *Kepler* candidates is very high ($90-95\%$ according to Morton & Johnson 2011, see Fressin et al. (in prep) for an estimate of fidelity as a function of planetary radius), false positives do exist among the *Kepler* planet candidates in the form of background eclipsing binaries, hierarchical triples, and other configurations of stars that result in the dilution of the eclipse signal, allowing it to masquerade as a planetary transit. The large size of *Kepler* pixels renders *Kepler* particularly vulnerable to bound companion stars with a large planet, such as a Neptune- or Jupiter-size planet, mimicking the transit signal of an Earth-size planet. To show that a planetary interpretation is superior to the interpretation of these various false positive signals, we outline the various measurements and statistical properties of the KOI-94 system that support the hypothesis of four transiting planets.

2.5.1 Radial Velocities from KOI-94d

The eccentric orbit solution of the RVs and light curve yield a semi-amplitude of 18.3 ± 1.5 $\mathrm{m\,s^{-1}}$ with a 22.3 day period for KOI-94d. Similarly, the four-planet circular orbit solution yields a semi-amplitude of 19.68 ± 2.19 $\mathrm{m\,s^{-1}}$ to the RVs. The agreement between the circular and eccentric values for the semi-amplitude of KOI-94d underscores the robustness of this measurement.

At a 22-day period, a semi-amplitude of 18.3 ± 1.5 $\mathrm{m\,s^{-1}}$ is consistent with the orbit of a planet around a star. A binary star system in 22-day period would have a velocity semi-amplitude of hundreds of kilometers per second. The width of the spectral lines is consistent with a stellar rotation speed of 8 $\mathrm{kms^{-1}}$, which is at least an order of magnitude smaller than the orbital speed of a such a binary system. Thus, we rule out the possibility of an eclipsing binary false positive in a 22-day orbital period for KOI-94d. This supports the interpretation of KOI-94d as a planet. As discussed below, the planetary status of KOI-94d strengthens the case that the other transiting candidates are also planets.

2.5.2 Observed TTV signature between KOI-94c and KOI-94d

The apparent anti-correlation in the TTVs between planets c and d from 700-800 days (see Figure 2.11 suggests that these bodies are dynamically interacting, i.e. that KOI-94c is

also a planet. Our order-of-magnitude treatment of the TTV signatures indicates that the interacting bodies are of planetary masses, although the mass estimates are too low by a factor of 5.

2.5.3 No Evidence of Another Star

The adaptive optics images show no evidence of companions as close as 0.5″ from KOI-94 within 2 magnitudes in the J band or 3.4 magnitudes in the Ks band. Similarly, the speckle imaging shows no evidence of companions as close to KOI-94 as 0.6″ within 4 magnitudes in the R band. Also, the 3σ upper limit on an RV trend of $\dot{\gamma} = 6.9\ \mathrm{m\,s^{-1}}$ per year between fall 2009 and fall 2012 rules out a Jupiter-mass or more massive companion within 5 AU.

The detection of a second stellar spectrum in the spectrum of KOI-94 would indicate background or companion star. We searched for the spectrum of a second star in the iodine-free HIRES spectrum of KOI-94. To fit the spectrum of the primary star (KOI-94), we used a library of over 700 observed spectra from Keck HIRES that span $T_{\rm eff}$: $3266\,\mathrm{K} - 7258\,\mathrm{K}$, $\log g : 1.46 - 5.0$, and [Fe/H]:$-1.47 - +0.56$. We found the spectrum from this library with the least squares difference from the spectrum of KOI-94 (with similar results to the SME analysis) and subtracted this spectrum. We then compared the residual spectrum to each spectrum in the stellar library. The deepest minimum in χ^2 between the residual spectrum and another star from the library was 2σ at $-59.2\mathrm{km\,s^{-1}}$; however, there were many other 2σ solutions for that spectrum. We did not detect a second stellar spectrum with $> 1\%$ of the observed brightness of KOI-94 and a relative radial velocity of at least $\sim 8\,\mathrm{km\,s^{-1}}$ with $> 2\sigma$ significance. This technique is sensitive only to neighboring stars within 0.4″, the half-width of the slit of the HIRES spectrometer.

2.5.4 Low False Positive Rate in Multi-Planet Systems

Lissauer et al. (2012) uses statistical arguments to calculate the false positive fraction in multi-planet systems. Given the observed number of *Kepler* targets n_t, the number of *Kepler* planet candidates n_c, the number of *Kepler* multi-planet systems with i planet candidates $n_{m,i}$, and the planet fidelity P (or single candidate false positive rate $1 - P$), the fraction of systems with four planet candidates that we expect to consist of one false positive and three true planets ($\mathrm{P_{1FP}}$) is equivalent to the probability that a false positive is lined up behind a system that already has three true planets. The number of false positives among the candidate transiting planets is $(1-P)n_c$, and the fraction of those aligned with apparent i-planet systems is $n_{m,i}/n_t$. Thus,

$$\mathrm{P_{1FP}} = \frac{(1-P)n_c\frac{n_{m,4}}{n_t}}{n_{m,4}} = \frac{(1-P)n_c}{n_t}. \tag{2.7}$$

Adopting the values $n_t = 160171$ from Lissauer et al. (2012) and $n_c = 2300$ from Batalha et al. (2013), and assuming $P = 0.9$ (in accordance with Morton & Johnson 2011), we

calculate

$$P_{1FP} = 0.0014.$$

The probability that 2, 3, etc. planet candidates are all false positives (un-associated eclipsing binaries that all happen to align behind KOI-94 within 0.5″) is orders of magnitude smaller and can be ignored. The low false positive probability is definitive of planethood even without the other arguments presented in this section.

2.5.5 Rossiter-McLaughlin Measurement During the Transit of KOI-94d

Hirano et al. (2012) measured the Rossiter-McLaughlin (RM) effect during transit of KOI-94d. They observed a clear RM signal that, when measured considering a transit depth of $R_p/R_\star = 0.06856 \pm 0.00012$, implied a projected stellar rotation of $V \sin I_s = 8.01 \pm 0.73 \mathrm{km\,s^{-1}}$, which is in good agreement with their spectroscopically determined value of $7.33 \pm 0.32 \mathrm{km\,s^{-1}}$ and our SME analysis. This constitutes evidence for the planetary status of KOI-94d. Albrecht et al. (2013) also measured and modeled the RM effect during the same transit of KOI-94dand obtained results that agreed with Hirano et al. (2012).

Modeling of the transit durations, including ingress and egress, of the KOI-94 transit candidates indicate small inclinations with respect to the line of sight (see the inclinations in Table 2.3. Hirano et al. (2012) measure a projected mutual inclination between planets d and e of $\delta = -1.5°$ during a mutual transit event, indicating that these bodies are coplanar. That these planets are aligned with the stellar spin axis strengthens the argument for their planetary status. Recent work by Fabrycky & Kepler Science Team (2012) shows that many *Kepler* multi-planetary systems are coplanar, so it is likely that planets b and c are coplanar with planets d and e.

2.6 Constraints on the Composition of KOI-94d

The goal of this work was to measure the mass of the giant planet, KOI-94d, and determine whether its bulk density was consistent with that of an inflated or a cold Jupiter.

We have modeled the thermal evolution and contraction of planet d using the methods described in Fortney et al. (2007) and Miller & Fortney (2011). This model assumes no extra heat source from the star. Including uncertainties in the system age, planet mass, planet radius, orbital semi-major axis, and heavy element distribution within the planet (see Miller & Fortney 2011) we estimate that $18 \pm 6\ M_\oplus$ of heavy elements are contained within the planet. This is very similar to estimates for Saturn (Saumon & Guillot 2004). Based on the [Fe/H] of the parent star determined from our SME analysis of the spectrum, we estimate that the metals mass-fraction of planet d (Z_{planet}) is 11 ± 4 times that of the parent star. This metallicity enhancement, at this planet mass, agrees well with other "warm Jupiter" planets studied by Miller & Fortney (2011).

We use state of the art thermal evolution models for giant planets to establish that the bulk density of the planet is fully consistent with a non-inflated planet, and it is indeed enhanced in heavy elements compared to its parent star, in a manner similar to Saturn. We can furthermore compare KOI-94d to other planets by creating mass-radius and mass-density plots for all planets with measured radius and mass (see Figure 2.12). These plots demonstrate the dependence of planetary radius (and density) on mass and incident flux.

2.7 The Radius-Mass-Incident Flux Relation

In this section, we examine empirical relations between the radius, mass and incident flux of exoplanets, including the KOI-94 system. We discuss possible physical interpretations of these relations and suggest avenues of future theoretical investigation.

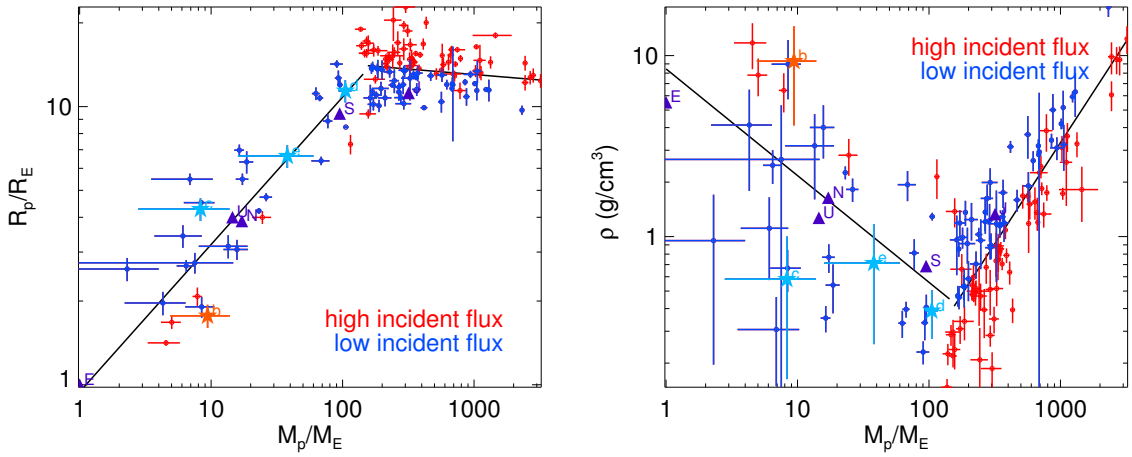

Figure 2.12: All planets with measured mass, radius, incident flux, and uncertainties therein, as listed in exoplanets.org (Wright et al. 2011, see Table 2.4). KOI-94 planets are plotted as five-pointed stars; Solar system planets are plotted as triangles. **Left:** Planet radius vs. planet mass. We divide the planets into two populations: those with higher-than-median incident flux (red), and those with lower-than-median incident flux (blue) The Solar system planets (purple) all receive less than the median incident flux; KOI-94 planets c, d, and e (cyan) receive less than the median incident flux, while KOI-94b (orange) receives more than the median incident flux. For $M_{\rm p} > 150 M_{\oplus}$, higher incident flux correlates with larger planetary radius. For $M_{\rm p} < 150 M_{\oplus}$, higher incident flux ($F$) correlates with smaller planetary radius. The best-fit planes for $M_{\rm p} < 150 M_{\oplus}$ and for $M_{\rm p} > 150 M_{\oplus}$ are shown at the median flux $F = 8.6 \times 10^8$ erg s^{-1} cm^{-2}. **Right:** Planet density vs. planet mass. The coloring is the same as in the left panel, and the density fits for $M_{\rm p} < 150 M_{\oplus}$and for $M_{\rm p} > 150 M_{\oplus}$are shown at the median flux. For $M_{\rm p} > 150 M_{\oplus}$, higher incident flux correlates with lower bulk density. For $M_{\rm p} < 150 M_{\oplus}$, higher incident flux correlates with higher bulk density. We determine empirical relations (see text) between $\log(M_{\rm p})$, $\log(F)$, and each $\log(R_{\rm p})$ and $\log(\rho_{\rm p})$ for $M_{\rm p} > 150 M_{\oplus}$ and $M_{\rm p} < 150 M_{\oplus}$.

This population of planets was compiled from exoplanets.org (Wright et al. 2011), which was queried on September 27, 2012. Our selection criteria were that the mass and radius of the planet were measured, and that errors in these measurements were reported, that the effective temperature and radius of the star were measured with errors reported, and that the semi-major axis was measured with errors reported. This resulted in the sample of 138 exoplanets listed in Table 2.4.

The methods for determining the radius, mass, and incident flux of the planets in Table 2.4 were as follows: All the planets transit, and so their radius measurement was based on transit depth as determined within a self-consistent model of the observed light curve. For many of these planets, the uncertainty in planet radius is dominated by the uncertainty in stellar radius. The masses of the planets were measured by one of two methods: the majority were measured as $M_{\rm p}{\rm sin}i$ based on the radial velocity of the star; however, in several *Kepler* systems of multiple planets, TTVs aided (Cochran et al. 2011, Kepler-18) or provided the sole means (Lissauer et al. 2011, Kepler-11) of planetary mass calculation. Uncertainties in the planet mass stem from uncertainties in the stellar mass, uncertainties in the RV semi-amplitude K for low-mass planets, and uncertainties in the TTV analysis. The incident flux for each planet was calculated using Equation 2.1, so uncertainties in the incident flux relate to uncertainties in stellar effective temperature, stellar radius, and semi-major axis.

There is a break in the mass-radius relation at $\sim$150 $M_{\oplus}$ (see Figure 2.12). We chose 150 $M_{\oplus}$ as the break based on a visual inspection of the mass-radius and mass-density diagrams. In determining the relation between planet radius, planet mass, and incident flux, we consider planets more or less massive than 150 $M_{\oplus}$ separately. Our sample included 35 planets with $M_{\rm p}<$ 150 $M_{\oplus}$ and 103 planets with $M_{\rm p}>$ 150 $M_{\oplus}$. All four planets in the KOI-94 system are included in the low-mass population.

To determine how incident flux affects radius, we calculated the time-averaged incident flux on each exoplanet from Equation 2.1. We divided the population into the "high incident flux" half (those with incident fluxes larger than the median incident flux, $F_m = 8.6 \times 10^8 {\rm erg\,s^{-1}\,cm^{-2}}$), and the "low incident flux" half. These are shown in Figure 2.12 as the red (high flux) and blue (low flux) sets of points. For planets with $M_{\rm p} > 150 M_{\oplus}$, the planets that receive high incident flux are systematically larger than planets that receive low incident flux.

We performed a similar test to determine how the orbital period affects radius (see Figure 2.13). We divided the exoplanet population into those with lower than the median orbital period of 3.52 days (red, "short period") and higher than the median orbital period (blue, "long period"). Planet radius does not correlate with orbital period.

Using the KOI-94 system and all other exoplanets with published values for both mass and radius, we establish two fundamental planes for exoplanets that relate their mass, incident flux, and radius from a few Earth masses up to ten Jupiter masses. We fit two planes between

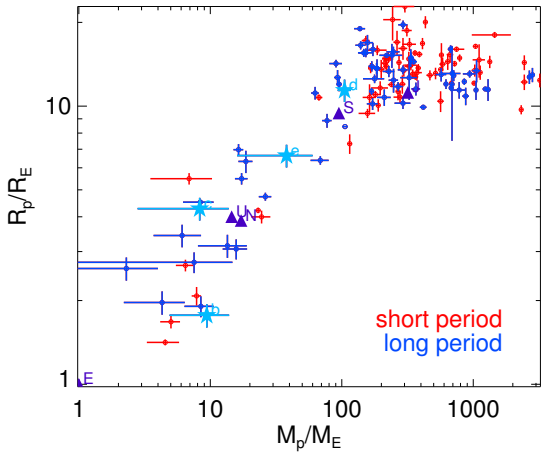

Figure 2.13: Planet radius vs. planet mass (same Figure 2.12, but with a different coloring scheme). We divide the planets into those with lower-than-median orbital periods (red) and those with higher-than-median orbital periods (blue). The Solar System planets (purple) and KOI-94 planets b, c, d, and e (cyan) all have longer than the median period. Orbital period does not correlate with planet radius.

$\log(R_\mathrm{p})$, $\log(M_\mathrm{p})$, and $\log(F)$, one in each mass regime. The resulting relations are:

$$\frac{R_\mathrm{p}}{R_\oplus} = 1.78 \left(\frac{M_\mathrm{p}}{M_\oplus}\right)^{0.53} \left(\frac{F}{\mathrm{erg\,s^{-1}\,cm^{-2}}}\right)^{-0.03} \quad \text{for } M_\mathrm{p} < 150 M_\oplus \tag{2.8}$$

and

$$\frac{R_\mathrm{p}}{R_\oplus} = 2.45 \left(\frac{M_\mathrm{p}}{M_\oplus}\right)^{-0.039} \left(\frac{F}{\mathrm{erg\,s^{-1}\,cm^{-2}}}\right)^{0.094} \quad \text{for } M_\mathrm{p} > 150 M_\oplus \tag{2.9}$$

For completeness, we also fit two planes between $\log(\rho_\mathrm{p})$, $\log(M_\mathrm{p})$, and $\log(F)$:

$$\frac{\rho_\mathrm{p}}{\mathrm{g\,cm^{-3}}} = 1.30 \left(\frac{M_\mathrm{p}}{M_\oplus}\right)^{-0.60} \left(\frac{F}{\mathrm{erg\,s^{-1}\,cm^{-2}}}\right)^{0.09} \quad \text{for } M_\mathrm{p} < 150 M_\oplus \tag{2.10}$$

and

$$\frac{\rho_\mathrm{p}}{\mathrm{g\,cm^{-3}}} = 0.48 \left(\frac{M_\mathrm{p}}{M_\oplus}\right)^{1.10} \left(\frac{F}{\mathrm{erg\,s^{-1}\,cm^{-2}}}\right)^{-0.28} \quad \text{for } M_\mathrm{p} > 150 M_\oplus \tag{2.11}$$

Table 2.4 lists the mass, radius, incident flux, orbital period, and reference for the planets used to calculate these fits. We include the Solar system planets in Figure 2.12 for reference, although these planets were not used to generate the fits in Equations 2.8−2.11. Slice through the planes at the median incident flux is shown as black lines in Figure 2.12.

These planes were calculated by fitting a plane to the measurements of $\log M_{\rm p}$, $\log R_{\rm p}$, and $\log F$ in each mass regime, with equal weight for each point. To see how the uncertainties in $M_{\rm p}$, $R_{\rm p}$, and F influenced the fit, we did 1000 trials in which we varied each measurement of $M_{\rm p}$, $R_{\rm p}$, and F based on a Gaussian distribution with the 1σ uncertainties reported for that planet to create a posterior distribution of coefficients. The median and average values for the posterior distribution of the coefficients were consistent with the coefficients of the original fit. If we write Equations 2.8 and 2.9 more generally as $\log(R_{\rm p}/R_\oplus) = A + B\log(M_{\rm p}/M_\oplus) + C\log(F/{\rm erg\,s^{-1}\,cm^{-2}})$, the 1σ uncertainties in the coefficients for Equation 2.8 (i.e. for $M_{\rm p} < 150 M_\oplus$) are $A = 0.25 \pm 0.185$, $B = 0.53 \pm 0.052$, and $C = -0.03 \pm 0.017$. The 1σ uncertainties in the coefficients for Equation 2.9 (i.e. for $M_{\rm p} > 150 M_\oplus$) were $A = 0.39 \pm 0.053$, $B = -0.039 \pm 0.0096$, and $C = 0.094 \pm 0.0055$. Thus, the dependence of radius on mass for low-mass planets is significant at 10σ, and the dependence of radius of flux for high-mass planets is significant at 17σ. The downward slope of radius versus mass for giant planets is detected at a significance of 4σ, and the downward slope of radius versus flux for small planets is uncertain.

For $M_{\rm p} < 150 M_\oplus$, the RMS scatter of the radius is $1.41 R_\oplus$ and the RMS scatter of the density is $2.69 {\rm g\,cm^{-3}}$. Considering that the average radius of a planet in this mass regime is $6.72 R_\oplus$ and the average uncertainty in planet radius in this mass regime is $0.34 R_\oplus$(i.e. 5% of the typical planet radius), the RMS scatter of radii for $M_{\rm p} < 150 M_\oplus$ is large compared to the uncertainties in measurements of planet radii. For $M_{\rm p} > 150 M_\oplus$, the RMS scatter of the radius is $1.15 R_\oplus$ and the RMS scatter of the density is $1.48 {\rm g\,cm^{-3}}$. Considering that the average uncertainty in planet radius for $M_{\rm p} > 150 M_\oplus$ is $0.76 R_\oplus$, the RMS scatter is comparable to the uncertainty in planet radius in this mass regime. Interpretations of the RMS scatter in each mass regime is discussed in Section 2.7.1.

Note than for $M_{\rm p} < 150 M_\oplus$, radius depends strongly on mass ($R_{\rm p} \propto M_{\rm p}^{0.52}$) and very weakly on incident flux ($R_{\rm p} \propto F^{-0.03}$). For $M_{\rm p} > 150 M_\oplus$, the dependence is reversed: $R_{\rm p} \propto M_{\rm p}^{-0.04}$, and $R_{\rm p} \propto F^{0.09}$. Since mass has little effect on radius for giant planets, the incident flux is the most important factor in predicting planet radius.

In light of the very clear dependence of giant planet radius on incident flux, and the possibility of a dependence of low-mass planet radius on incident flux, we wanted to examine the relations between incident flux and planet radius in greater detail. The top panel of Figure 2.14 shows planet radius as a function of incident flux for the low-mass and high-mass planets. The scatter in radius of the low-mass planets can be attributed to the strong dependence of planetary radius on mass for $M_{\rm p} < 150 M_\oplus$. However, the relation between the radii of giant planets and the incident flux is clear in this plot because the dependence of planet radius on mass is very small for $M_{\rm p} > 150 M_\oplus$.

It appears that for planets with $M_{\rm p} < 150 M_\oplus$, the planets receiving high incident flux are systematically smaller than planets receiving low incident flux. To examine the validity of

this correlation, we plotted the residuals to the relation $R_p \propto M_p^{0.52}$ as a function of incident flux (see the bottom panel of Figure 2.14). We found that the residuals only weakly depend on incident flux, but that there is a visible downward trend. Thus the suggestion that low-mass planets with high incident flux are smaller remains unclear. Future characterization of low-mass planets receiving varying amounts of incident flux will help elucidate this relation, if it exists.

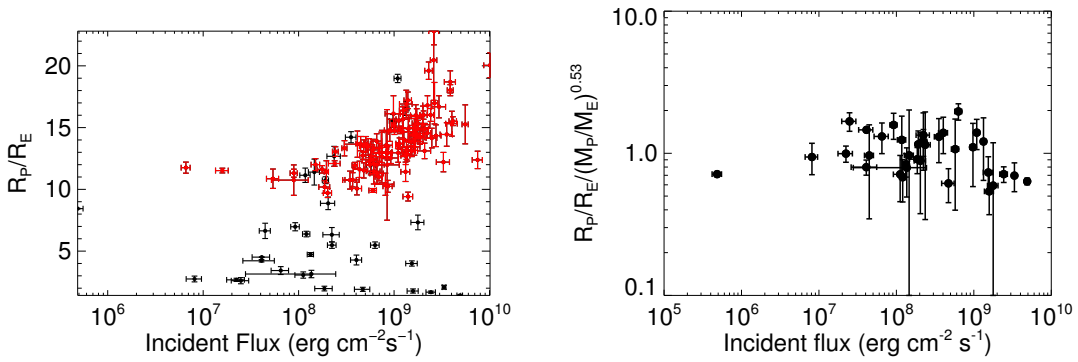

Figure 2.14: Left: All planets with measured mass, radius, and incident flux, as listed in exoplanets.org (see Table 2.4). The black points are planets with $M_p < 150 M_\oplus$, and the red points are planets with $M_p > 150\ M_\oplus$. For the giant planets, planet radius increases with incident flux. For low-mass planets, incident flux does not correlate with planet radius. This is because planet radius scales with planet mass more strongly than with incident flux for low-mass planets, whereas incident flux is the primary factor in determining the radii of high-mass planets (see Equation 2.9). Right: Planet radius, divided by dependence on planet mass according to Equation 2.8, versus incident flux for $M_p < 150 M_\oplus$. The best fit to the data suggests a slight trend toward lower radius at higher incident flux, although the data are also consistent with no correlation between incident flux and planet radius.

2.7.1 Interpretation of the Radius-Mass-Incident Flux Relations

We consider the KOI-94 system in the context of other planets with published values for both mass and radius. We quantify these trends in two fundamental planes (see Equations 2.8−2.9) for exoplanets that relate their mass, incident flux, and radius from a few Earth masses up to ten Jupiter masses. These equations demonstrate that for low-mass planets, mass is much more important than flux in predicting a planet's radius, whereas for high-mass planets, incident flux is more important for predicting the radius of a giant planet than the planet mass.

For low-mass planets, inverting Equation 2.8 predicts the planet's mass given its radius and incident flux. The small coefficient for mass for $M_p > 150 M_\oplus$ indicates that it is difficult to predict the mass of a giant planet given its radius and incident flux.

The small RMS scatter in radius for giant planets ($\delta R_{\rm p} = 1.15\ R_\oplus$) compared to the typical uncertainty in radius ($\sigma_{R_{\rm p}} = 0.76 R_\oplus$) suggests that our model of mass and incident flux affecting the radius of giant planets is appropriate and that other factors, such as orbital period and metallicity, play a small part, if any.

For low-mass planets, the high RMS scatter ($\delta R_{\rm p} = 1.41\ R_\oplus$) compared to uncertainties in the radius ($\sigma_{R_{\rm p}} = 0.34 R_\oplus$) indicates that additional physics might play a role in determining radius. In particular, the composition of low-mass planets could strongly affect planetary radius. Planets on the low-mass branch could have compositions ranging from mostly hydrogen/helium (e.g. Saturn) to mostly water (Charbonneau et al. 2009, e.g. GJ 1214 b) to mostly rock (Batalha et al. 2011, e.g. Kepler 10b). The equations of state of these materials are quite different, allowing a planet of $10 M_\oplus$ to vary by a factor of 5 in radius depending on its composition, in theory. Despite the potentially large range in compositions at a given mass, the low-mass fundamental plane works reasonably well: extrapolating this relation to Earth, we predict $R_{\rm p} = 1.15 R_\oplus$.

Planetary composition might be described in part by the mass-radius relation. For low-mass planets, the exponential dependence of $R_{\rm p}$ on $M_{\rm p}$ is higher than expected. For a body of constant density (for instance, a rocky planet, if we ignore compressibility), we expect $R_{\rm p} \propto M_{\rm p}^{1/3}$. For low-mass planets, the observed relation, $R_{\rm p} \propto M_{\rm p}^{0.52}$, is steeper. This steep increase in radius with mass cannot be explained by the compressibility of material, since compressibility would cause less increase in radius with increasing mass. The extra increase in radius per unit mass suggests a compositional gradient. Within the low-mass regime ($M_{\rm p} < 150 M_\oplus$), higher-mass planets might have an increased admixture of volatiles. This is supported by observations in our own solar system; Uranus, Neptune and Saturn have a larger fraction of volatiles than Earth and Venus.

In the giant planet population ($M_{\rm p} > 150\ M_\oplus$), the decline in radius with increasing mass corresponds to the onset of electron degeneracy as an important component of the planet's pressure along with Coulomb forces. For a body supported by electron degeneracy pressure, we expect $R_{\rm p} \propto {M_{\rm p}}^{-1/3}$. The dependence of $R_{\rm p} \propto {M_{\rm p}}^{-0.04}$, which is measured with a significance of 4σ, indicates that Coulomb forces still play a significant role in supporting high-mass planets.

In planetary modeling, 150 $M_\oplus$ occurs where the mass-radius relation for model planets (e.g. Fortney et al. 2007) begins to gradually flatten out. It is marked by waning relative importance of electrostatic forces which alone lead to $R \sim M^{1/3}$, and the gradual onset of degeneracy pressure, which for complete degeneracy leads to $R \sim M^{-1/3}$. In an approximate way, 150 $M_\oplus$ can be thought of as the start of the broad maximum in this curve that leads to radius being nearly independent of mass for giant planets and brown dwarfs (Zapolsky & Salpeter 1969).

The reversal of the correlation between $R_{\rm p}$ and F at 150 $M_\oplus$ is an interesting feature of the exoplanet population. The current population of observed planets can be sculpted to some degree by evaporative mass loss (Baraffe et al. 2004, 2006; Hubbard et al. 2007; Lopez et al. 2012). X-ray and UV (XUV) photons can drive mass-loss of hydrogen/helium planetary atmospheres, and in the energy-limited escape model (e.g., Erkaev et al. 2007),

the mass loss rate depends inversely on the planet density and linearly with the incident XUV flux. Planets with masses near $\sim$150 $M_\oplus$ are those that have low bulk densities (see Figure 2.12) are and generally more susceptible to atmospheric mass loss. Under extreme XUV irradiation, some rare planets may migrate from just above 150 $M_\oplus$ to below.

Unlike the incident flux on a planet, the orbital period of a planet does not correlate with planet radius. This suggests that the mechanism that maintains the inflated radii of giant planets is driven by the incident flux rather than by tidal forces via eccentricity damping. However, because the eccentricities of many planets are poorly constrained, it is difficult to calculate the tidal power deposited in the planet. The uncertainty in the heat dissipation timescale further complicates our analysis, since we cannot determine how long ago various planets might have been in sufficiently eccentric orbits for tidal forcing to inflate them. Regardless, a planet's radius is more strongly correlated with the incident flux it receives than its orbital period. Future studies of warm Jupiters and hot Jupiters with various orbital periods and eccentricities will help elucidate the role of potential interior heating mechanisms. However, the goodness of fit between the radius, mass, and incident flux for giant planets suggests that the current role of tidal heating (or any other inflation mechanism that is not driven by incident flux) is quite small.

There are only 9 low-mass planets out of 35 that receive more than the median incident flux and 9 that have shorter than the median orbital period, whereas the population of giant planets is more evenly split. Howard et al. (2012) find that the occurrence of giant planets is smaller than the occurrence of small planets at orbital periods less than 10 days, suggesting that the hot Jupiters in this work are over-represented. The over-abundance of hot Jupiters compared to hot Neptunes in this sample could be due to historic observational bias of hot Jupiters, since the detection of Neptune-size and smaller planets from the ground was infrequent before the *Kepler* Mission. Measuring the masses of Neptune-size and smaller planets that receive high incident flux is necessary to probe the radius-mass-incident flux relation for low-mass planets.

2.7.2 Comparison to Previous Work

The idea of searching for correlations between planetary radius, mass, incident flux, and other measurable planetary and stellar parameters is not novel; as mentioned in §1, Enoch et al. (2012) and Kane & Gelino (2012) sought empirical relations between the properties of planets and their host stars. Here, we incorporate an additional year's worth of planet discoveries and mass determinations, especially for Kepler planets. There are additional differences between our work and theirs, and we highlight how this study differs from previous work.

The primary difference between Enoch et al. (2012) and the work presented here is that Enoch et al. (2012) study 16 planets within orbital periods of 10 days and with masses between 0.1 and 0.5 $M_{\rm J}$, whereas here we study 35 planets with masses below 150 $M_\oplus$ (0.5 $M_{\rm J}$). Whereas Enoch et al. (2012) consider three mass regimes of planets ($0.1 < M_{\rm p} < 0.5M_{\rm J}$, $0.5M_{\rm J} < M_{\rm p} < 2.0M_{\rm J}$, $2.0M_{\rm J} < M_{\rm p} < 12M_{\rm J}$), here, we only consider two regimes

($M_{\rm p} < 150 M_{\oplus}$, $150 M_{\oplus} < M_{\rm p} < 13 M_{\rm J}$). With the additional transiting planets included here, we do not see evidence for three mass domains.

However, we find that fits to the data incorporating only mass and incident flux predict the radius of a planet as well as the fits described in Enoch et al. (2012). Enoch et al. (2012) find an average absolute deviation in the predicted radius from the true radius of 0.11 $R_{\rm J}$ (1.23 $R_{\oplus}$) across all three of their mass regimes, whereas we find a mean absolute difference of 1.41 for $M_{\rm p} < 150 M_{\oplus}$and 1.15 for $M_{\rm p} > 150 M_{\oplus}$, or 1.23 $R_{\oplus}$, over the whole sample. Incorporating the orbital period of the planet, the stellar metallicity, and the stellar age does not significantly improve the accuracy of the predicted planetary radius.

The slope of the mass-radius fit for $M_{\rm p} < 150 M_{\oplus}$ reported here, 0.53 $\pm$0.0052, is only 1.5σ different from the value of 0.45 reported in Enoch et al. (2012) for planets with $M_{\rm p} < 0.5 M_{\rm J}$. Our slope of the mass-radius fit for the high-mass planets, -0.039 , falls between the values for middle- and high-mass regimes in Enoch et al. (2012), 0 and -0.09.

Kane & Gelino (2012) used a similar prescription to our method to obtain a mass-radius relation. They fit a power law between the mass and radius of low-mass planets. However, they assumed that giant planet radius was constant with planet mass (at one Jupiter radius). Furthermore, they did not consider the effects of incident flux on planetary radius in either mass regime.

2.8 Conclusions

1. **The KOI-94 system** In this paper, we presented 26 radial velocity measurements of KOI-94 obtained on Keck/HIRES. These measurements confirm the giant planet KOI-94d and strongly support the existence of other transiting planets in the system.

   (a) **Properties of Planet KOI-94d** The mass is $106 \pm 11 M_{\oplus}$. The radius is $11.27 \pm 1.06 R_{\oplus}$. The density is $0.363 \pm 0.101 \mathrm{g\,cm^{-3}}$. The planet is enriched in metals by a factor of 11 ± 4 with respect to the parent star. The mass of heavy elements, or "metals," in the planet is 18 ± 6 $M_{\oplus}$.

   (b) **Properties of Planets KOI-94b, KOI-94c, KOI-94e** These planets were detected at significance of less than 3σ in the radial velocity data. The radial velocity detections of planets e and b are marginal ($> 2\sigma$), whereas the radial velocity measurements of planet c are consistent with a non-detection to 1σ. More RVs and a numerical analysis of the TTVs are needed to better characterize these planets. However, the TTVs, multiplicity of the system, lack of evidence for another star, RM effect during the transit of KOI-94d and coplanarity of these objects strongly suggest that these candidates are planets.

   (c) **Dynamical Stability of the KOI-94 System** The system is dynamically stable on a 1 Myr timescale for a variety of configurations, including circular orbital solutions. Although some eccentric solutions are stable, the best-fit solution considered in this work is unstable due to close encounters of planets b and c.

(d) **No Massive Outer Perturbers** The non-detection of a trend in radial velocity, the lack of spectral features from a second star to 1% of the brightness of KOI-94within 0.4″, and the non-detection of a companion outside 0.5″(in both AO and speckle imaging) rule out large, outer companions.

2. **Radius-Mass-Incident Flux Relation** Using the KOI-94 system and other exoplanets (138 exoplanets total) with published values and uncertainties for planet mass, radius, and incident flux, we establish two fundamental planes for exoplanets that relate planet radius, planet mass, and incident flux between 2 and 3000 $M_\oplus$ in Equations 2.8−2.11. The slope of the mass-radius relation for low-mass planets suggests that as low-mass planets increase in mass, the admixture of volatiles increases. Although the plane for for $M_\mathrm{p} > 150 M_\oplus$ fits the giant planets very well, a higher RMS compared to uncertainties in radius (400%) for the low-mass planets suggests that additional physics, such as the composition of heavy elements, might contribute to the radii of these planets.

Acknowledgments

This project was possible thanks to NASA's *Kepler* Mission, which provided the photometry of KOI-94 and identified it as a target worthy of follow-up. The authors thank the *Kepler* Team as a whole, and also a few individuals for their specific roles: Bill Borucki and David Koch for designing the mission, and Natalie Batalha for leadership in the scientific analysis of the *Kepler* planetary candidates.

LMW thanks Yoram Lithwick for helpful conversations and assistance in interpreting the TTV data.

LMW is financially supported by the National Science Foundation Graduate Research Fellowship Program, Grant DGE 1106400.

Spectra of KOI-94 were obtained at the W. M. Keck Observatory. The authors wish to extend special thanks to those of Hawai'ian ancestry on whose sacred mountain of Mauna Kea we are privileged to be guests. Without their generous hospitality, the Keck observations presented herein would not have been possible.

Table 2.3: Star and planet parameters for the KOI-94 system.

Parameter	Value	Notes
Transit and orbital parameters: KOI-94b		
Orbital period P (days)	3.743208 ± 0.000015	A
Midtransit time E (BJD)	2454964.6175 ± 0.0021	A
Scaled semimajor axis $a/R_\star$	7.25 ± 0.59	A
Scaled planet radius $R_\mathrm{p}/R_\star$	0.01031 ± 0.00014	A
Impact parameter b	0.088 ± 0.072	A
Orbital inclination i (deg)	89.30 ± 0.57	A
Orbital semi-amplitude K ($\mathrm{m\,s^{-1}}$)	3.3 ± 1.4	B
Orbital eccentricity e	0.25 ± 0.17	B
Center-of-mass velocity γ ($\mathrm{m\,s^{-1}}$)	2.1 ± 1.4	B
Transit and orbital parameters: KOI-94c		
Orbital period P (days)	10.423648 ± 0.000016	A
Midtransit time E (BJD)	$2454971.00870 \pm 0.00103$	A
Scaled semimajor axis $a/R_\star$	14.3 ± 1.2	A
Scaled planet radius $R_\mathrm{p}/R_\star$	0.02599 ± 0.00047	A
Impact parameter b	0.41 ± 0.018	A
Orbital inclination i (deg)	88.36 ± 0.75	A
Orbital semi-amplitude K ($\mathrm{m\,s^{-1}}$)	$3.5^{+1.3}_{-3.5}$	B
Orbital eccentricity e	0.43 ± 0.23	B
Transit and orbital parameters: KOI-94d		
Orbital period P (days)	22.3429890 ± 0.0000067	A
Midtransit time E (BJD)	$2454965.74052 \pm 0.00015$	A
Scaled semimajor axis $a/R_\star$	23.8 ± 1.9	A
Scaled planet radius $R_\mathrm{p}/R_\star$	0.068016 ± 0.000080	A
Impact parameter b	0.055 ± 0.051	A
Orbital inclination i (deg)	89.871 ± 0.123	A
Orbital semi-amplitude K ($\mathrm{m\,s^{-1}}$)	18.3 ± 1.5	B
Orbital eccentricity e	0.022 ± 0.038	B
Transit and orbital parameters: KOI-94e		
Orbital period P (days)	54.32031 ± 0.00012	A
Midtransit time E (BJD)	2454994.2379 ± 0.0012	A
Scaled semimajor axis $a/R_\star$	43.1 ± 3.5	A
Scaled planet radius $R_\mathrm{p}/R_\star$	0.03960 ± 0.00024	A
Impact parameter b	0.18 ± 0.11	A
Orbital inclination i (deg)	89.76 ± 0.15	A
Orbital semi-amplitude K ($\mathrm{m\,s^{-1}}$)	$4.5^{+2.3}_{-3.5}$	B
Orbital eccentricity e	0.019 ± 0.23	B

Table 2.3 (cont'd): Star and planet parameters for the KOI-94 system.

Parameter	Value	Notes
Observed stellar parameters		
Effective temperature $T_{\rm eff}$(K)	6182 ± 58	C
Spectroscopic gravity $\log g$(cgs)	4.181 ± 0.066	C
Metallicity [Fe/H]	$+0.0228 \pm 0.0020$	C
Projected rotation $v \sin i$(km s^{-1})	7.3 ± 0.5	C
Fundamental Stellar Properties		
Mass $M_\star(M_\odot)$	1.277 ± 0.050	D
Radius $R_\star(R_\odot)$	1.52 ± 0.14	D
Surface gravity $\log g_\star$ (cgs)	4.181 ± 0.066	D
Luminosity $L_\star$ ($L_\odot$)	3.01 ± 0.60	D
Kepler Magnitude K_p (mag)	12.2	D
Age (Gyr)	3.16 ± 0.39	D
Planetary parameters: KOI-94b		
Mass $M_{\rm p}$ ($M_\oplus$)	10.5 ± 4.6	B,C,D
Radius $R_{\rm p}$ ($R_\oplus$)	1.71 ± 0.16	A,B,C,D
Density $\rho_{\rm p}$ (g cm^{-3})	10.1 ± 5.5	A,B,C,D
Orbital semi-major axis a (AU)	0.05119 ± 0.00067	E
Incident Flux F (erg s^{-1} cm^{-2})	1.58×10^9	A,C
Equilibrium temperature $T_{\rm eq}$ (K)	1486	F
Planetary parameters: KOI-94c		
Mass $M_{\rm p}$ ($M_\oplus$)	$15.6^{+5.7}_{-15.6}$	B,C,D
Radius $R_{\rm p}$ ($R_\oplus$)	4.32 ± 0.41	A,B,C,D
Density $\rho_{\rm p}$ (g cm^{-3})	$0.91^{+0.36}_{-0.91}$	A,B,C,D
Orbital semi-major axis a (AU)	0.1013 ± 0.0013	E
Incident Flux F (erg s^{-1} cm^{-2})	4.03×10^8	A,C
Equilibrium temperature $T_{\rm eq}$ (K)	1012	F
Planetary parameters: KOI-94d		
Mass $M_{\rm p}$ ($M_\oplus$)	106 ± 11	B,C,D
Radius $R_{\rm p}$ ($R_\oplus$)	11.27 ± 1.06	A,B,C,D
Density $\rho_{\rm p}$ (g cm^{-3})	0.363 ± 0.101	A,B,C,D
Orbital semi-major axis a (AU)	0.1684 ± 0.0022	E
Incident Flux F (erg s^{-1} cm^{-2})	1.46×10^8	A,C
Equilibrium temperature $T_{\rm eq}$ (K)	806	F
Planetary parameters: KOI-94e		
Mass $M_{\rm p}$ ($M_\oplus$)	35^{+18}_{-28}	B,C,D
Radius $R_{\rm p}$ ($R_\oplus$)	6.56 ± 0.62	A,B,C,D
Density $\rho_{\rm p}$ (g cm^{-3})	$0.60^{+0.26}_{-0.56}$	A,B,C,D

Table 2.3 (cont'd): Star and planet parameters for the KOI-94 system.

Parameter	Value	Notes
Orbital semi-major axis a (AU)	0.3046 ± 0.0040	E
Incident Flux F ($\mathrm{erg\,s^{-1}\,cm^{-2}}$)	4.46×10^8	A,C
Equilibrium temperature T_{eq} (K)	584	F

Note. — A: Based primarily on an analysis of the photometry,
B: Based on a joint analysis of the photometry and radial velocities,
C: Based on an analysis by D. Fischer of the Keck/HIRES template spectrum using SME (Valenti & Piskunov 1996),
D: Based on the Yale-Yonsei isochrones (Yi et al. 2001) and the results from A, B, and C,
E: Based on Newton's revised version of Kepler's Third Law and the results from D,
F: Calculated assuming Bond albedos of 0.3 (b; Earth), 0.4 (c; Neptune), 0.34 (d; Jupiter), and 0.4 (e; Neptune) and complete redistribution of heat for reradiation.

Table 2.4: Exoplanets with Measured Mass and Radius

Name	$M_{\rm p}$ ($M_{\oplus}$)	$R_{\rm p}$ ($R_{\oplus}$)	Incident Flux (erg s^{-1} cm^{-2})	Period (days)	First Ref.	Orbit Ref.
55 Cnc e	7.862	2.078	3.34E+09	0.737	McArthur et al. (2004)	Demory et al. (2011)
CoRoT-1 b	327.284	16.685	2.96E+09	1.509	Barge et al. (2008)	Barge et al. (2008)
CoRoT-10 b	875.699	10.862	5.39E+07	13.241	Bonomo et al. (2010)	Bonomo et al. (2010)
CoRoT-11 b	746.274	16.013	2.04E+09	2.994	Gandolfi et al. (2010)	Gandolfi et al. (2010)
CoRoT-12 b	292.131	16.125	9.86E+08	2.828	Gillon et al. (2010)	Gillon et al. (2010)
CoRoT-13 b	416.654	9.910	5.99E+08	4.035	Cabrera et al. (2010)	Cabrera et al. (2010)
CoRoT-14 b	2445.485	12.205	3.29E+09	1.512	Tingley et al. (2011)	Tingley et al. (2011)
CoRoT-17 b	781.832	11.422	1.32E+09	3.768	Tingley et al. (2011)	Tingley et al. (2011)
CoRoT-18 b	1108.075	14.669	1.23E+09	1.900	Hébrard et al. (2011)	Hébrard et al. (2011)
CoRoT-19 b	352.115	14.445	1.72E+09	3.897	Guenther et al. (2012)	Guenther et al. (2012)
CoRoT-2 b	1041.197	16.405	1.27E+09	1.743	Alonso et al. (2008)	Alonso et al. (2008)
CoRoT-4 b	228.008	13.325	3.02E+08	9.202	Moutou et al. (2008); Aigrain et al. (2008)	Moutou et al. (2008)
CoRoT-5 b	147.002	15.542	9.74E+08	4.038	Rauer et al. (2009)	Rauer et al. (2009)
CoRoT-6 b	938.715	13.057	2.43E+08	8.887	Fridlund et al. (2010)	Fridlund et al. (2010)
CoRoT-7 b	5.021	1.677	2.43E+09	0.854	Queloz et al. (2009); Léger et al. (2009)	Queloz et al. (2009)
CoRoT-8 b	68.673	6.383	1.21E+08	6.212	Bordé et al. (2010)	Bordé et al. (2010)
CoRoT-9 b	268.099	11.758	6.59E+06	95.274	Deeg et al. (2010)	Deeg et al. (2010)
GJ 1214 b	6.468	2.675	2.23E+07	1.580	Charbonneau et al. (2009)	Carter et al. (2011)
GJ 436 b	23.105	4.218	4.09E+07	2.644	Butler et al. (2004)	Maness et al. (2007)
HAT-P-1 b	169.196	13.908	6.58E+08	4.465	Bakos et al. (2007a)	Bakos et al. (2007a)
HAT-P-11 b	26.231	4.725	1.33E+08	4.888	Bakos et al. (2010)	Bakos et al. (2010)
HAT-P-12 b	66.997	10.739	1.91E+08	3.213	Hartman et al. (2009)	Hartman et al. (2009)
HAT-P-13 b	272.394	14.344	1.67E+09	2.916	Bakos et al. (2009)	Winn et al. (2010)
HAT-P-14 b	710.648	12.877	1.37E+09	4.628	Torres et al. (2010)	Torres et al. (2010)
HAT-P-15 b	620.231	12.004	1.51E+08	10.864	Kovács et al. (2010)	Kovács et al. (2010)
HAT-P-16 b	1335.623	14.434	1.58E+09	2.776	Buchhave et al. (2010)	Buchhave et al. (2010)
HAT-P-17 b	168.493	11.310	8.91E+07	10.339	Howard et al. (2012)	Howard et al. (2012)
HAT-P-18 b	62.675	11.142	1.17E+08	5.508	Hartman et al. (2011a)	Hartman et al. (2011a)
HAT-P-19 b	92.889	12.676	2.36E+08	4.009	Hartman et al. (2011a)	Hartman et al. (2011a)
HAT-P-2 b	2819.241	12.956	1.10E+09	5.633	Bakos et al. (2007c)	Pál et al. (2010)
HAT-P-20 b	2316.734	9.708	2.02E+08	2.875	Bakos et al. (2011)	Bakos et al. (2011)
HAT-P-21 b	1296.160	11.466	6.12E+08	4.124	Bakos et al. (2011)	Bakos et al. (2011)
HAT-P-22 b	683.741	12.094	6.12E+08	3.212	Bakos et al. (2011)	Bakos et al. (2011)
HAT-P-23 b	666.163	15.318	4.03E+09	1.213	Bakos et al. (2011)	Bakos et al. (2011)
HAT-P-24 b	217.977	13.908	1.63E+09	3.355	Kipping et al. (2010)	Kipping et al. (2010)
HAT-P-26 b	18.640	6.327	2.23E+08	4.235	Hartman et al. (2011c)	Hartman et al. (2011c)
HAT-P-27 b	195.955	11.623	4.34E+08	3.040	Anderson et al. (2011b)	Anderson et al. (2011b)
HAT-P-28 b	199.536	13.572	8.27E+08	3.257	Buchhave et al. (2011a)	Buchhave et al. (2011a)
HAT-P-29 b	247.580	12.396	5.70E+08	5.723	Buchhave et al. (2011a)	Buchhave et al. (2011a)
HAT-P-3 b	189.327	10.067	4.08E+08	2.900	Torres et al. (2007)	Torres et al. (2008)
HAT-P-30 b	225.996	15.005	1.63E+09	2.811	Johnson et al. (2011)	Johnson et al. (2011)
HAT-P-31 b	689.358	11.982	8.46E+08	5.005	Kipping et al. (2011)	Kipping et al. (2011)
HAT-P-32 b	302.182	22.810	2.62E+09	2.150	Hartman et al. (2011b)	Hartman et al. (2011b)
HAT-P-33 b	243.556	20.458	2.60E+09	3.474	Hartman et al. (2011b)	Hartman et al. (2011b)
HAT-P-34 b	1059.600	13.404	7.35E+08	5.453	Bakos et al. (2012)	Bakos et al. (2012)
HAT-P-35 b	335.047	14.915	1.41E+09	3.647	Bakos et al. (2012)	Bakos et al. (2012)
HAT-P-36 b	584.539	14.154	2.49E+09	1.327	Bakos et al. (2012)	Bakos et al. (2012)
HAT-P-37 b	372.996	13.191	6.01E+08	2.797	Bakos et al. (2012)	Bakos et al. (2012)
HAT-P-4 b	213.416	14.266	1.87E+09	3.057	Kovács et al. (2007)	Kovács et al. (2007)
HAT-P-5 b	335.490	14.042	1.27E+09	2.788	Bakos et al. (2007b)	Bakos et al. (2007b)
HAT-P-6 b	336.749	14.893	1.78E+09	3.853	Noyes et al. (2008)	Noyes et al. (2008)
HAT-P-7 b	572.656	15.262	5.57E+09	2.205	Pál et al. (2008)	Winn et al. (2009)
HAT-P-8 b	411.052	16.797	2.24E+09	3.076	Latham et al. (2009)	Latham et al. (2009)
HAT-P-9 b	246.817	15.677	1.24E+09	3.923	Shporer et al. (2009)	Shporer et al. (2009)
HD 149026 b	114.882	7.323	1.78E+09	2.876	Sato et al. (2005)	Carter et al. (2009)
HD 17156 b	1049.670	11.422	1.95E+08	21.217	Fischer et al. (2007)	Barbieri et al. (2009)
HD 189733 b	363.454	12.743	4.71E+08	2.219	Bouchy et al. (2005)	Bouchy et al. (2005)
HD 209458 b	219.181	15.218	9.93E+08	3.525	Henry et al. (2000); Charbonneau et al. (2000)	Torres et al. (2008)
HD 80606 b	1236.479	11.522	1.59E+07	111.437	Naef et al. (2001)	Moutou et al. (2009)
KOI-135 b	1027.001	13.437	1.63E+09	3.024	Borucki et al. (2011)	Bonomo et al. (2012)
KOI-196 b	156.857	9.417	1.40E+09	1.856	Borucki et al. (2011)	Santerne et al. (2011)
KOI-204 b	324.519	13.885	1.51E+09	3.247	Borucki et al. (2011)	Bonomo et al. (2012)
KOI-254 b	162.563	10.750	8.91E+07	2.455	Borucki et al. (2011)	Johnson et al. (2012)
KOI-428 b	691.836	13.101	1.54E+09	6.873	Santerne et al. (2011)	Santerne et al. (2011)
Kepler-10 b	4.539	1.415	4.88E+09	0.837	Batalha et al. (2011)	Batalha et al. (2011)
Kepler-11 b	4.298	1.968	1.86E+08	10.304	Lissauer et al. (2011)	Lissauer et al. (2011)
Kepler-11 c	13.500	3.147	1.36E+08	13.025	Lissauer et al. (2011)	Lissauer et al. (2011)
Kepler-11 d	6.100	3.427	6.50E+07	22.687	Lissauer et al. (2011)	Lissauer et al. (2011)
Kepler-11 e	8.401	4.515	4.11E+07	31.996	Lissauer et al. (2011)	Lissauer et al. (2011)
Kepler-11 f	2.298	2.607	2.48E+07	46.689	Lissauer et al. (2011)	Lissauer et al. (2011)
Kepler-12 b	137.283	18.980	1.09E+09	4.438	Borucki et al. (2011)	Fortney et al. (2011)
Kepler-14 b	2671.703	12.721	1.32E+09	6.790	Borucki et al. (2011)	Buchhave et al. (2011b)
Kepler-15 b	210.532	10.750	3.45E+08	4.943	Borucki et al. (2011)	Endl et al. (2011)
Kepler-16 b	105.833	8.441	4.84E+05	228.776	Borucki et al. (2011)	Doyle et al. (2011)

Table 2.4 (cont'd): Exoplanets with Measured Mass and Radius

Name	M_p ($M_\oplus$)	R_p ($R_\oplus$)	Incident Flux (erg s^{-1} cm^{-2})	Period (days)	First Ref.	Orbit Ref.
Kepler-17 b	788.004	14.893	2.10E+09	1.486	Borucki et al. (2011)	Désert et al. (2011)
Kepler-18 b	6.900	5.484	6.32E+08	3.505	Borucki et al. (2011)	Cochran et al. (2011)
Kepler-18 c	17.299	5.484	2.24E+08	7.642	Borucki et al. (2011)	Cochran et al. (2011)
Kepler-18 d	16.399	6.973	9.21E+07	14.859	Borucki et al. (2011)	Cochran et al. (2011)
Kepler-20 b	8.474	1.906	4.70E+08	3.696	Borucki et al. (2011)	Gautier et al. (2012)
Kepler-20 c	15.734	3.064	1.12E+08	10.854	Borucki et al. (2011)	Gautier et al. (2012)
Kepler-20 d	7.528	2.745	8.12E+06	77.612	Borucki et al. (2011)	Gautier et al. (2012)
Kepler-4 b	24.544	3.998	1.54E+09	3.213	Borucki et al. (2010)	Borucki et al. (2010)
Kepler-5 b	672.699	16.024	2.42E+09	3.548	Koch et al. (2010)	Koch et al. (2010)
Kepler-6 b	212.739	14.815	1.16E+09	3.235	Dunham et al. (2010)	Dunham et al. (2010)
Kepler-7 b	139.127	16.550	1.33E+09	4.886	Latham et al. (2010)	Latham et al. (2010)
Kepler-8 b	186.158	15.890	1.73E+09	3.523	Jenkins et al. (2010)	Jenkins et al. (2010)
OGLE-TR-182 b	325.603	12.653	7.45E+08	3.979	Pont et al. (2008)	Pont et al. (2008)
OGLE-TR-211 b	240.675	15.229	2.01E+09	3.677	Udalski et al. (2008)	Udalski et al. (2008)
OGLE2-TR-L9 b	1453.828	18.028	3.89E+09	2.486	Snellen et al. (2009)	Snellen et al. (2009)
Qatar-1 b	346.352	13.034	8.45E+08	1.420	Alsubai et al. (2011)	Alsubai et al. (2011)
TrES-1 b	239.152	11.948	3.88E+08	3.030	Alonso et al. (2004)	Alonso et al. (2004)
TrES-2 b	381.607	13.706	1.14E+09	2.471	O'Donovan et al. (2006)	O'Donovan et al. (2006)
TrES-4 b	292.473	19.607	2.31E+09	3.554	Mandushev et al. (2007)	Mandushev et al. (2007)
TrES-5 b	565.109	13.538	1.09E+09	1.482	Mandushev et al. (2011)	Mandushev et al. (2011)
WASP-1 b	263.078	16.976	2.65E+09	2.520	Collier Cameron et al. (2007)	Simpson et al. (2011a)
WASP-10 b	1013.770	12.094	2.38E+08	3.093	Christian et al. (2009)	Christian et al. (2009)
WASP-11 b	171.543	10.190	1.87E+08	3.722	West et al. (2009a); Bakos et al. (2009)	West et al. (2009a)
WASP-12 b	432.432	20.044	1.01E+10	1.091	Hebb et al. (2009)	Maciejewski et al. (2011)
WASP-13 b	152.357	15.554	1.12E+09	4.353	Skillen et al. (2009)	Skillen et al. (2009)
WASP-14 b	2444.754	14.344	2.75E+09	2.244	Joshi et al. (2009)	Joshi et al. (2009)
WASP-15 b	172.613	15.990	1.69E+09	3.752	West et al. (2009b)	West et al. (2009b)
WASP-16 b	267.695	11.287	6.64E+08	3.119	Lister et al. (2009)	Lister et al. (2009)
WASP-17 b	156.828	16.909	1.34E+09	3.735	Anderson et al. (2010)	Anderson et al. (2010)
WASP-18 b	3206.179	12.385	7.50E+09	0.941	Hellier et al. (2009b)	Hellier et al. (2009b)
WASP-19 b	360.211	15.520	4.13E+09	0.789	Hebb et al. (2010)	Hellier et al. (2011)
WASP-2 b	288.782	11.993	6.47E+08	2.152	Collier Cameron et al. (2007)	Charbonneau et al. (2007)
WASP-21 b	95.431	11.982	5.75E+08	4.322	Bouchy et al. (2010)	Bouchy et al. (2010)
WASP-22 b	177.678	12.541	9.25E+08	3.533	Maxted et al. (2010a)	Maxted et al. (2010a)
WASP-23 b	277.208	10.772	3.69E+08	2.944	Triaud et al. (2011)	Triaud et al. (2011)
WASP-24 b	346.738	14.557	2.22E+09	2.341	Street et al. (2010)	Simpson et al. (2011a)
WASP-25 b	183.847	13.661	5.06E+08	3.765	Enoch et al. (2011)	Enoch et al. (2011)
WASP-26 b	323.366	14.781	9.03E+08	2.757	Smalley et al. (2010)	Smalley et al. (2010)
WASP-29 b	77.261	8.869	2.04E+08	3.923	Hellier et al. (2010)	Hellier et al. (2010)
WASP-3 b	639.396	14.445	3.56E+09	1.847	Pollacco et al. (2008)	Tripathi et al. (2010)
WASP-31 b	152.339	17.211	1.40E+09	3.406	Anderson et al. (2011a)	Anderson et al. (2011a)
WASP-32 b	1129.221	13.213	1.35E+09	2.719	Maxted et al. (2010b)	Maxted et al. (2010b)
WASP-34 b	185.399	13.661	4.13E+08	4.318	Smalley et al. (2011)	Smalley et al. (2011)
WASP-35 b	227.906	14.781	1.01E+09	3.162	Enoch et al. (2011)	Enoch et al. (2011)
WASP-36 b	721.220	14.210	1.89E+09	1.537	Smith et al. (2012)	Smith et al. (2012)
WASP-37 b	570.041	12.989	7.01E+08	3.577	Simpson et al. (2011b)	Simpson et al. (2011b)
WASP-38 b	854.794	12.250	5.49E+08	6.872	Barros et al. (2011)	Barros et al. (2011)
WASP-39 b	90.367	14.221	3.54E+08	4.055	Faedi et al. (2011)	Faedi et al. (2011)
WASP-4 b	388.827	15.352	1.77E+09	1.338	Wilson et al. (2008)	Wilson et al. (2008)
WASP-41 b	296.362	13.437	5.35E+08	3.052	Maxted et al. (2011)	Maxted et al. (2011)
WASP-43 b	564.470	10.414	8.11E+08	0.813	Hellier et al. (2011)	Hellier et al. (2011)
WASP-48 b	312.807	18.700	3.88E+09	2.144	Enoch et al. (2011)	Enoch et al. (2011)
WASP-5 b	516.398	13.112	2.09E+09	1.628	Anderson et al. (2008)	Anderson et al. (2008)
WASP-50 b	467.967	12.911	8.54E+08	1.955	Gillon et al. (2011)	Gillon et al. (2011)
WASP-6 b	165.697	13.706	4.46E+08	3.361	Gillon et al. (2009)	Gillon et al. (2009)
WASP-7 b	292.162	10.246	8.60E+08	4.955	Hellier et al. (2009a)	Hellier et al. (2009a)
WASP-8 b	679.482	11.623	1.76E+08	8.159	Queloz et al. (2010)	Queloz et al. (2010)
XO-1 b	291.903	13.504	4.82E+08	3.942	McCullough et al. (2006)	McCullough et al. (2006)
XO-2 b	180.056	11.007	6.93E+08	2.616	Burke et al. (2007)	Burke et al. (2007)
XO-5 b	366.286	11.534	4.82E+08	4.188	Burke et al. (2008)	Burke et al. (2008)
KOI-94 b	9.400	1.770	1.58E+09	3.743	Borucki et al. (2011)	Weiss et al. (2013)
KOI-94 c	8.300	4.280	4.03E+08	10.424	Borucki et al. (2011)	Weiss et al. (2013)
KOI-94 d	105.000	11.400	1.46E+08	22.343	Borucki et al. (2011)	Weiss et al. (2013)
KOI-94 e	38.000	6.640	4.46E+07	54.320	Batalha et al. (2013)	Weiss et al. (2013)
Earth	1.000	1.000	1.07E+06	365.250		
Jupiter	317.817	11.198	3.97E+04	4336.069		
Saturn	95.027	9.440	1.17E+04	10833.641		
Uranus	14.535	4.003	2.91E+03	30730.951		
Neptune	17.147	3.879	1.19E+03	60157.796		

3

The Mass-Radius Relation for 65 Exoplanets Smaller than 4 Earth Radii

A version of this chapter was previously published in the Astrophysical Journal Letters (Weiss, L. M., & Marcy, G. W. 2014, The Astrophysical Journal, 783, L6).

We study the masses and radii of 65 exoplanets smaller than $4R_\oplus$ with orbital periods shorter than 100 days. We calculate the weighted mean densities of planets in bins of 0.5 $R_\oplus$ and identify a density maximum of 7.6 $\mathrm{g\,cm^{-3}}$at 1.4 $R_\oplus$. On average, planets with radii up to $R_\mathrm{p} = 1.5R_\oplus$ increase in density with increasing radius. Above 1.5 $R_\oplus$, the average planet density rapidly decreases with increasing radius, indicating that these planets have a large fraction of volatiles by volume overlying a rocky core. Including the solar system terrestrial planets with the exoplanets below 1.5 $R_\oplus$, we find $\rho_\mathrm{p} = 2.43{+}3.39\,(R_\mathrm{p}/R_\oplus)\,\mathrm{g\,cm^{-3}}$ for $R_\mathrm{p} < 1.5R_\oplus$, which is consistent with rocky compositions. For $1.5 \leq R_\mathrm{p}/R_\oplus < 4$, we find $M_\mathrm{p}/M_\oplus = 2.69\,(R_\mathrm{p}/R_\oplus)^{0.93}$. The RMS of planet masses to the fit between 1.5 and 4 $R_\oplus$ is 4.3 $M_\oplus$ with reduced $\chi^2 = 6.2$. The large scatter indicates a diversity in planet composition at a given radius. The compositional diversity can be due to planets of a given volume (as determined by their large H/He envelopes) containing rocky cores of different masses or compositions.

3.1 Introduction

The Kepler Mission has found an abundance of planets with radii $R_{\rm p} < 4R_{\oplus}$ (Batalha et al. 2013); the most recent head-count indicates 3206 planet candidates in this size range (NASA exoplanet Archive, queried 15 Jan. 2014), most of which are real (Morton & Johnson 2011). Although there are no planets between the size of Earth and Neptune in the solar system, occurrence calculations that de-bias the orbital geometry and completeness of the Kepler survey find that planets between the size of Earth and Neptune are common in our galaxy, occurring with orbital periods between 5 and 50 days around 24% of stars (Petigura et al. 2013b). However, in many systems, it is difficult to measure the masses of such small planets because the gravitational acceleration these planets induce on their host stars or neighboring planets is challenging to detect with current telescopes and instruments. We cannot hope to measure the masses of all planets in this size range discovered by Kepler. Obtaining measurements of the masses of a subset of these planets and characterizing their compositions is vital to understanding the formation and evolution of this population of planets.

Many authors have explored the relation between planet mass and radius as a means for understanding exoplanet compositions and as a predictive tool. Seager et al. (2007) predict the mass-radius relationship for planets of various compositions. The mass-radius relation in Lissauer et al. (2011), which is commonly used in literature to translate between planet masses and radii, is based on fitting a power law relation to Earth and Saturn only. Other works, such as Enoch et al. (2012); Kane & Gelino (2012); Weiss et al. (2013), determine empirical relations between mass and radius based on the exoplanet population.

Recent mass determinations of small planets motivate a new empirical mass-radius relation. Restricting the empirical mass-radius relation to small exoplanets will improve the goodness of fit, allowing better mass predictions and enabling a superior physical understanding of the processes that drive the mass-radius relation for small planets.

One challenge in determining a mass-radius relation for small planets is the large scatter in planet mass. At $2R_{\oplus}$, planets are observed to span a decade in density, from less dense than water to densities comparable to Earth's. This scatter could result from measurement uncertainty or from compositional variety among low-mass exoplanets.

In this paper, we investigate mass-radius relationships for planets smaller than 4 Earth radii. We explore how planet composition–rocky versus rich in volatiles– influences the mass-radius relationship. We also investigate the extent to which system properties contribute to the scatter in the mass-radius relation by examining how these properties correlate with the residuals of the mass-radius relation.

3.2 Selecting Exoplanets with Measured Mass and Radius

We present a judicious identification of small transiting planets with masses or mass upper limits measured via stellar radial velocities (RVs) or numerically modeled transit timing variations (TTVs). The only selection criterion was that the exoplanets have $R_{\rm p} < 4R_{\oplus}$ and either a mass determination, a marginal mass determination, or a mass upper limit. There were no limits on stellar type, orbital period, or other system properties.

We include all 19 planets smaller than $4R_{\oplus}$ with masses vetted on exoplanets.org, as of January 13, 2013. Twelve of these masses are determined by RVs, but the masses of four Kepler-11 planets, Kepler-30 b, and two Kepler-36 planets are determined by TTVs (Lissauer et al. 2013; Sanchis-Ojeda et al. 2012; Carter et al. 2012). We include five numerically-determined planet masses from TTVs not yet on exoplanets.org: three KOI-152 (Kepler-79) planets (Jontof-Hutter et al. 2014), and two KOI-314 planets (Kipping et al. 2014). We also include all 40 transiting planets with RV follow-up in Marcy et al. (2014) that are smaller than $4R_{\oplus}$, and the RV-determined mass of KOI-94 b (Weiss et al. 2013), none of which yet appear on exoplanets.org.

55 Cnc e, Corot-7 b, and GJ 1214 b have been studied extensively, and we had to choose from the masses and radii reported in various studies. For 55 Cnc e, we use $M_{\rm p} = 8.38 \pm 0.39$, $R_{\rm p} = 1.990 \pm 0.084$ (Endl et al. 2012; Dragomir et al. 2014); for Corot-7 b, we use $M_{\rm p} = 7.42 \pm 1.21$, $R_{\rm p} = 1.58 \pm 0.1$ (Hatzes et al. 2011), and for GJ 1214 b, we use $M_{\rm p} = 6.45 \pm 0.91$, $R_{\rm p} = 2.65 \pm 0.09$ (Carter et al. 2011). Histograms of the distributions of planet radius, mass, and density are shown in Figure 3.1, and the individual measurements of planet mass and radius are listed in Table 3.1.

The exoplanets all have $P < 100$ days. This is because the transit probability is very low for planets at long orbital periods and because short-period planets are often favored for RV and TTV studies.

3.2.1 Inclusion of Mass Non-Detections

For small exoplanets, uncertainties in the mass measurements can be of order the planet mass. Although one might advocate for only studying planets with well-determined ($> 3\sigma$) masses, imposing a significance criterion will bias the sample toward more massive planets at a given radius. This bias is especially pernicious for small planets, for which the planet-induced RV signal can be small ($\sim 1 {\rm m\,s^{-1}}$) compared to the noise from stellar activity ($\sim 2 {\rm m\,s^{-1}}$) and Poisson photon noise ($\sim 2 {\rm m\,s^{-1}}$). We must include the marginal mass detections and non-detections in order to minimize bias in planet masses at a given radius.

Marcy et al. (2014) employ a new technique for including non-detections. They allow a negative semi-amplitude in the Keplerian fit to the RVs and report the peak and 68^{th} percentiles of the posterior distribution of the semi-amplitude. The posterior distribution peak often corresponds to a "negative" planet mass, although the wings of the posterior distribution encompass positive values. Although planets cannot have negative masses in nature,

Table 3.1: Exoplanets with Masses or Mass Upper Limits and $R_{\rm p} < 4R_\oplus$

Name	Per (d)	Mass ($M_\oplus$)	Radius ($R_\oplus$)	Flux[A] ($F_\oplus$)	First Ref.	Mass, Radius Ref.
[B]55 Cnc e	0.737	8.38±0.39	1.990±0.084	2400	McArthur et al. (2004)	Endl et al. (2012), Dragomir et al. (2014)
CoRoT-7 b	0.854	7.42±1.21	1.58±0.1	1800	Queloz et al. (2009), Léger et al. (2009)	Hatzes et al. (2011)
GJ 1214 b	1.580	6.45±0.91	2.65±0.09	17	Charbonneau et al. (2009)	Carter et al. (2011)
HD 97658 b	9.491	7.87±0.73	2.34±0.16	48	Howard et al. (2011)	Dragomir et al. (2013)
Kepler-10 b	0.837	4.60±1.26	1.46±0.02	3700	Batalha et al. (2011)	Batalha et al. (2011)
[C]Kepler-11 b	10.304	1.90±1.20	1.80±0.04	130	Lissauer et al. (2011)	Lissauer et al. (2013)
[C]Kepler-11 c	13.024	2.90±2.20	2.87±0.06	91	Lissauer et al. (2011)	Lissauer et al. (2013)
[C]Kepler-11 d	22.684	7.30±1.10	3.12±0.07	44	Lissauer et al. (2011)	Lissauer et al. (2013)
[C]Kepler-11 f	46.689	2.00±0.80	2.49±0.06	17	Lissauer et al. (2011)	Lissauer et al. (2013)
Kepler-18 b	3.505	6.90±3.48	2.00±0.10	460	Borucki et al. (2011)	Cochran et al. (2011)
Kepler-20 b	3.696	8.47±2.12	1.91±0.16	350	Borucki et al. (2011)	Gautier et al. (2012)
Kepler-20 c	10.854	15.73±3.31	3.07±0.25	82	Borucki et al. (2011)	Gautier et al. (2012)
Kepler-20 d	77.612	7.53±7.22	2.75±0.23	6.0	Borucki et al. (2011)	Gautier et al. (2012)
[C]Kepler-30 b	29.334	11.3±1.4	3.90 ±0.20	21	Borucki et al. (2011)	Sanchis-Ojeda et al. (2012)
[C]Kepler-36 b	13.840	4.46±0.30	1.48±0.03	220	Borucki et al. (2011)	Carter et al. (2012)
[C]Kepler-36 c	16.239	8.10±0.53	3.68±0.05	180	Carter et al. (2012)	Carter et al. (2012)
Kepler-78 b	0.354	1.69±0.41	1.20±0.09	3100	Sanchis-Ojeda et al. (2013)	Howard et al. (2013)
Kepler-100 c	12.816	0.85±4.00	2.20±0.05	210	Borucki et al. (2011)	Marcy et al. (2014)
Kepler-100 b	6.887	7.34±3.20	1.32±0.04	470	Borucki et al. (2011)	Marcy et al. (2014)
Kepler-100 d	35.333	-4.36±4.10	1.61±0.05	56	Borucki et al. (2011)	Marcy et al. (2014)
Kepler-93 b	4.727	2.59±2.00	1.50±0.03	220	Borucki et al. (2011)	Marcy et al. (2014)
Kepler-102 e	16.146	8.93±2.00	2.22±0.07	17	Borucki et al. (2011)	Marcy et al. (2014)
Kepler-102 d	10.312	3.80±1.80	1.18±0.04	31	Borucki et al. (2011)	Marcy et al. (2014)
Kepler-102 f	27.454	0.62±3.30	0.88±0.03	8.3	Borucki et al. (2011)	Marcy et al. (2014)
Kepler-102 c	7.071	-1.58±2.00	0.58±0.02	51	Borucki et al. (2011)	Marcy et al. (2014)
Kepler-102 b	5.287	0.41±1.60	0.47±0.02	78	Borucki et al. (2011)	Marcy et al. (2014)
Kepler-94 b	2.508	10.84±1.40	3.51±0.15	210	Borucki et al. (2011)	Marcy et al. (2014)
Kepler-103 b	15.965	14.11±4.70	3.37±0.09	120	Borucki et al. (2011)	Marcy et al. (2014)
Kepler-106 c	13.571	10.44±3.20	2.50±0.32	84	Borucki et al. (2011)	Marcy et al. (2014)
Kepler-106 e	43.844	11.17±5.80	2.56±0.33	16	Borucki et al. (2011)	Marcy et al. (2014)
Kepler-106 b	6.165	0.15±2.80	0.82±0.11	240	Borucki et al. (2011)	Marcy et al. (2014)
Kepler-106 d	23.980	-6.39±7.00	0.95±0.13	43	Borucki et al. (2011)	Marcy et al. (2014)
Kepler-95 b	11.523	13.00±2.90	3.42±0.09	180	Borucki et al. (2011)	Marcy et al. (2014)
Kepler-109 b	6.482	1.30±5.40	2.37±0.07	440	Borucki et al. (2011)	Marcy et al. (2014)
Kepler-109 c	21.223	2.22±7.80	2.52±0.07	95	Borucki et al. (2011)	Marcy et al. (2014)
Kepler-48 b	4.778	3.94±2.10	1.88±0.10	170	Borucki et al. (2011)	Marcy et al. (2014)
Kepler-48 c	9.674	14.61±2.30	2.71±0.14	230	Borucki et al. (2011)	Marcy et al. (2014)
Kepler-48 d	42.896	7.93±4.60	2.04±0.11	14	Borucki et al. (2011)	Marcy et al. (2014)
Kepler-79 b	13.4845	10.9±6.70	3.47±0.07	160	Borucki et al. (2011)	Jontof-Hutter et al. (2014)
Kepler-79 c	27.4029	5.9±2.10	3.72±0.08	63	Borucki et al. (2011)	Jontof-Hutter et al. (2014)
Kepler-79 e	81.0659	4.1±1.15	3.49±0.14	15	Borucki et al. (2011)	Jontof-Hutter et al. (2014)
Kepler-113 c	8.925	-4.60±6.20	2.19±0.06	51	Borucki et al. (2011)	Marcy et al. (2014)
Kepler-113 b	4.754	7.10±3.30	1.82±0.05	64	Borucki et al. (2011)	Marcy et al. (2014)
Kepler-25 b	6.239	9.60±4.20	2.71±0.05	670	Borucki et al. (2011)	Marcy et al. (2014)
Kepler-37 d	39.792	1.87±9.08	1.94±0.06	7.7	Borucki et al. (2011)	Marcy et al. (2014)
Kepler-37 c	21.302	3.35±4.00	0.75±0.03	16	Borucki et al. (2011)	Marcy et al. (2014)
Kepler-37 b	13.367	2.78±3.70	0.32±0.02	37	Borucki et al. (2011)	Marcy et al. (2014)
Kepler-68 b	5.399	5.97±1.70	2.33±0.02	380	Borucki et al. (2011)	Marcy et al. (2014)
Kepler-68 c	9.605	2.18±3.50	1.00±0.02	220	Borucki et al. (2011)	Marcy et al. (2014)
Kepler-96 b	16.238	8.46±3.40	2.67±0.22	74	Borucki et al. (2011)	Marcy et al. (2014)
Kepler-131 b	16.092	16.13±3.50	2.41±0.20	72	Borucki et al. (2011)	Marcy et al. (2014)
Kepler-131 c	25.517	8.25±5.90	0.84±0.07	29	Borucki et al. (2011)	Marcy et al. (2014)
Kepler-97 b	2.587	3.51±1.90	1.48±0.13	850	Borucki et al. (2011)	Marcy et al. (2014)
Kepler-98 b	1.542	3.55±1.60	1.99±0.22	1600	Borucki et al. (2011)	Marcy et al. (2014)
Kepler-99 b	4.604	6.15±1.30	1.48±0.08	90	Borucki et al. (2011)	Marcy et al. (2014)
[D]Kepler-406 b	2.426	4.71±1.70	1.43±0.03	710	Borucki et al. (2011)	Marcy et al. (2014)
[D]Kepler-406 c	4.623	1.53±2.30	0.85±0.03	290	Borucki et al. (2011)	Marcy et al. (2014)
Kepler-407 b	0.669	0.06±1.20	1.07±0.02	3600	Borucki et al. (2011)	Marcy et al. (2014)
Kepler-409 b	68.958	2.69±6.20	1.19±0.03	6.2	Borucki et al. (2011)	Marcy et al. (2014)
KOI-94 b	3.743	10.50±4.60	1.71±0.16	1200	Batalha et al. (2013)	Weiss et al. (2013)
KOI-1612.01	2.465	0.48±3.20	0.82±0.03	1700	Borucki et al. (2011)	Marcy et al. (2014)
KOI-314 b	13.78164	3.83±1.5	1.61±0.16	6.8	Borucki et al. (2011)	Kipping et al. (2014)
KOI-314 c	23.08933	1.01±0.42	1.61±0.16	3.39	Borucki et al. (2011)	Kipping et al. (2014)

[A]Incident stellar flux is calculated as $F/F_\oplus = (R_\star/R_\odot)^2(T_{\rm eff}/5778{\rm K})^4 a^{-2}\sqrt{1/(1-e^2)}$, where a is the semi-major axis in A.U. and e is the eccentricity. Typical errors are 10%.

[B]Mass is from Endl et al. (2012), radius is from Dragomir et al. (2014). The density is calculated from these values.

[C]Planet mass determined by TTVs of a neighboring planet.

[D]Planet mass and density updated based on additional RVs.

random fluctuations in the RVs from noise can produce a velocity curve that is low when it should be high, and high when it should be low, mimicking the RV signature of a planet 180° out of phase with the transit-determined ephemeris. Since the planetary ephemeris is fixed by the transit, Marcy et al. (2014) allow these cases to be fit with a negative semi-amplitude solution in their MCMC analysis. Reporting the peak of the posterior distribution is statistically meaningful because there are also cases where the fluctuations in RVs from the random noise happen to correlate with the planetary signal, artificially increasing the planet mass. We include non-detections (as negative planet masses and low-significance positive planet masses) to avoid statistical bias toward large planet masses at a given radius.

Including literature values, which typically only report planet mass if the planet mass is detected with high confidence, slightly biases our sample toward higher masses at a given radius. We include the literature values to provide a larger sample of exoplanets.

3.3 The Mass-Radius Relations

In Figure 3.2, we show the measured planet densities and planet masses for $R_{\rm p} < 4R_{\oplus}$. In addition, we show the weighted mean planet density and mass in bins of 0.5 $R_{\oplus}$. The weighted mean densities and masses guide the eye, demonstrating how the ensemble density and mass change with radius. We also include the solar system planets. Examining the solar system terrestrial planets and the weighted mean density at 1.5 $R_{\oplus}$, we see that planet density increases with increasing radius up to 1.5 $R_{\oplus}$. For planets between 1.0 and 1.5 $R_{\oplus}$, the weighted mean density achieves a maximum at $7.6 \pm 1.2 \mathrm{g\,cm^{-3}}$, and the weighted center of the bin is at 1.4 $R_{\oplus}$. Above 1.5 $R_{\oplus}$, planet density decreases with increasing radius. The break in the density-radius relation motivates us to explore different empirical relations for planets smaller and larger than 1.5 $R_{\oplus}$.

Exoplanets smaller than 1.5 $R_{\oplus}$ mostly have mass uncertainties of order the planet mass, except for Kepler-10 b, Kepler-36 b, Kepler-78 b, and Kepler-406 b (KOI-321 b). Because there are so few planets with well-determined masses in this regime, we include the terrestrial solar system planets (Mercury, Venus, Earth, Mars) in a fit to the planets smaller than 1.5 $R_{\oplus}$. We impose uncertainties of 20% in their masses and 10% in their radii so that the solar system planets will contribute to, but not dominate, the fit. Because the solar system planets appear to satisfy a linear relation between density and radius, we choose a linear fit to planet density vs. radius. We find:

$$\rho_{\rm p} = 2.43 + 3.39 \left(\frac{R_{\rm p}}{R_{\oplus}} \right) \mathrm{g\,cm^{-3}}. \tag{3.1}$$

Transforming the predicted densities to masses via

$$\frac{M_{\rm p}}{M_{\oplus}} = \left(\frac{\rho_{\rm p}}{\rho_{\oplus}} \right) \left(\frac{R_{\rm p}}{R_{\oplus}} \right)^3 \tag{3.2}$$

and calculating the residuals with respect to the measured planet masses, we obtain reduced $\chi^2 = 1.3$, RMS=2.7 $M_{\oplus}$.

For exoplanets satisfying $1.5 \leq R_{\rm p}/R_\oplus < 4$, we calculate an empirical fit to their masses and radii, yielding:

$$\frac{M_{\rm p}}{M_\oplus} = 2.69 \left(\frac{R_{\rm p}}{R_\oplus}\right)^{0.93} \tag{3.3}$$

with reduced $\chi^2 = 3.5$ and RMS=4.7 $M_\oplus$. We exclude Uranus and Neptune from this fit because they differ from the exoplanets in our sample. Most of the exoplanets in our sample have $P < 50$ days, and so we do not expect them to resemble Uranus and Neptune, which have orbital periods of tens of thousands of days.

The empirical density- and mass-radius relations and their goodness of fit are summarized in Table 3.2. Below, we discuss the implications of these relations for planet compositions.

3.4 Implications for Planet Compositions

3.4.1 Interpretation of the Density-Radius and Mass-Radius Relations

The peak of the density-radius relation at 1.5 $R_\oplus$ and 8 g cm^{-3} is consistent with the Seager et al. (2007) prediction for the density of a 1.5 $R_\oplus$ Earth-composition planet. The density peak at 1.5 $R_\oplus$ is also consistent with the division between rocky and non-rocky planets determined in Rogers (2015) through Bayesian modeling and MCMC analysis. Following the Seager et al. (2007) prediction for the density of an Earth-composition (67.5% $MgSiO_3$, 32.5% Fe) planet, we see a predicted increase in planet density with increasing planet radius. This is because rock is slightly compressible, causing an increase in density with increasing planet radius. Because the compression of rock is slight, we could, in principle, take a first-order Taylor expansion to the equation of state of a rocky planet and approximate that density increases linearly with radius; this is consistent with our empirical, linear density-radius fit. If the exoplanets in this regime are indeed rocky, our inclusion of the solar system planets is justified because the orbital period (out to Earth's orbit) and incident flux on a rocky planet should have very little effect on that planet's mass and radius. Equation 3.1 and the density-radius relation from Seager et al. (2007) are both consistent with the interpretation that planets smaller that 1.5 $R_\oplus$ are rocky, but Equation 3.1 has advantages in that it (a) is empirical, and (b) passes closer to Earth, Venus, and Mars, which are known to be rich in silicon and magnesium (unlike Mercury, which is iron-rich). Additional and more precise, mass measurements for planets smaller than 1.5 $R_\oplus$ are necessary to hone the density-radius relation below 1.5$R_\oplus$ and examine any scatter about the relation.

For planets between 1.5 and 4 $R_\oplus$, the weighted mean density decreases with increasing planet radius, making these planets inconsistent with a rocky composition. The decrease in density must be due to an increasing fraction of volatiles, which we argue must be at least partially in the form of H/He envelopes. The gentle rise in planet mass with increasing radius indicates a substantial change in volume (from 3.4 to 64 times the volume of Earth) for very little change in mass (from 4 to 10 Earth masses; see Figure 3.2). A water layer

alone cannot explain this enormous change in volume for so little added mass; lightweight gas must be present in increasing quantities with increasing planetary radius. We can do a thought experiment: if exoplanets at 4 $R_\oplus$ (which have densities of about 1 g cm^{-3}) are made entirely of water, what distinguishes them from the 1.5 $R_\oplus$ planets whose compositions are likely rocky? We see no empirical evidence in the weighted mean density vs. radius that would suggest a shift between planets that do have rocky cores at 1.5 $R_\oplus$, and planets that do not have rocky cores at 4 $R_\oplus$. Moreover, planet formation theory makes it very likely that water content will be accompanied by at least a comparable amount of silicates and iron-nickel. The smooth decline in the weighted mean density from 1.5 to 4 $R_\oplus$ seems more consistent with the accumulation of lightweight gaseous envelopes upon rocky cores.

3.4.2 Scatter about the Relations

The moderate reduced χ^2 (6.3) to the mass-radius relation between 1.5 and 4 $R_\oplus$ indicates that measurement errors do not explain the variation in planet mass at a given radius. Only a diversity of planet compositions at given radius explains the large scatter in planet mass. Perhaps the mass diversity at a given radius results from different core masses in planets with large gaseous envelopes (as argued in Lopez & Fortney 2014); the size of the planet is determined by the fraction of gas, but the mass is determined by the size of the rocky core. In addition, water layers between the rocky cores and gaseous envelopes could help account for the scatter in mass at a given radius.

3.4.3 Previous Studies of the Mass-Radius Relation

Lissauer et al. (2011), Enoch et al. (2012), Kane & Gelino (2012), and Weiss et al. (2013) suggest that the mass-radius relation is more like $M_\mathrm{p} \propto R_\mathrm{p}^2$ for small exoplanets. However, these studies include Saturn or Saturn-like planets at the high-mass end of their "small planet" populations. Such planets are better described as part of the giant planet population and are not useful in determining an empirical mass-radius relation of predictive power for small exoplanets.

In a study of planets with $M_\mathrm{p} < 20 M_\oplus$, Wu & Lithwick (2013) find $M_\mathrm{p}/M_\oplus = 3 R_\mathrm{p}/R_\oplus$ in a sample of 22 pairs of planets that exhibit strong anti-correlated TTVs in the *Kepler* data. Our independent assessment of 65 exoplanets, 52 of which are not analyzed in Wu & Lithwick (2013), is consistent with this result for planets larger than $1.5 R_\oplus$. Wu & Lithwick (2013) note that a linear relation between planet mass and radius is dimensionally consistent with a constant escape velocity from the planet (i.e. $v_\mathrm{esc}^2 \sim M_\mathrm{p}/R_\mathrm{p}$). The linear mass-radius relation might result from photo-evaporation of the atmospheres of small planets near their stars (Lopez et al. 2012).

3.4.4 Masses from TTVs are Lower than Masses from RVs

We have included planets with masses determined by TTVs in Table 3.1, Figure 3.2 and the mass-radius relations. The TTV masses included in this work are the result of dynamical modeling that reproduces the observed TTV signatures in the Kepler light curve. Planets with TTV-determined masses are marked with superscript c in Table 3.1. In Figure 3.2, the TTV planets are shown as orange points; they are systematically less massive than the RV-discovered planets of the same radii (also see Jontof-Hutter et al. 2014). A T-test comparing the residual masses from the RVs to the TTVs results in a two-tailed P-value of 0.03, indicating the two samples, if drawn from the same distribution, would be this discrepant 3% of the time. An empirical fit between only the RV-determined planet masses and their radii for $1.5 < R_{\rm p}/R_{\oplus} < 4$ yields a similar solution to equation 3.3, but predicts slightly higher masses and less scatter of the residuals: $M_{\rm p}/M_{\oplus} = 4.87\,(R_{\rm p}/R_{\oplus})^{0.63}$, reduced $\chi^2 = 2.0$.

The systematic difference between the TTV and RV masses is unlikely to stem from a bias in the RVs. Either the TTVs are systematically underestimating planet masses (possibly because other planets in the system damp the TTVs), or compact systems amenable to detection through TTVs have lower-density planets than non-compact systems (e.g. the Kepler-11 system, Lissauer et al. 2013). That Wu & Lithwick (2013) also find $M_{\rm p}/M_{\oplus} \approx 3\,(R_{\rm p}/R_{\oplus})$ suggests that the TTV masses might be reliably systematically lower, although Wu & Lithwick (2013) use analytic rather than numerical methods to estimate planet masses.

3.4.5 Absence of Strong Correlations to Residuals

We investigate how the residual mass correlates with various orbital properties and physical properties of the star. The residual mass is the measured minus predicted planet mass at a given radius. The quantities we correlate against are: planet orbital period, planet semi-major axis, the incident flux from the star on the planet, stellar mass, stellar radius, stellar surface gravity, stellar metallicity, stellar age, and stellar velocity times the sine of the stellar spin axis inclination (which are obtained through exoplanets.org or the papers cited in Table 3.1). In these data, the residual mass does not strongly correlate with any of these properties.

We find possible evidence of a correlation between residual planet mass and stellar metallicity for planets smaller than $4R_{\oplus}$. The Pearson R-value of the correlation is 0.25, resulting in a probability of 7% that the residual planet mass and stellar metallicity are not correlated, given the residual masses and metallicities. However, given that we looked for correlations among 9 pairs of variables, the probability of finding a 93.6% confidence correlation in any of the 9 trials due to random fluctuation is $1 - 0.936^9 = 0.45$, meaning there is only a 55% chance that the apparent metallicity correlation is real.

Table 3.2: Empirical Mass-Radius and Density-Radius Relations

Planet Size	Equation	Reduced χ^2	RMS
[a] $R_\mathrm{p} < 1.5 R_\oplus$	$\rho_\mathrm{p} = 2.43 + 3.39 \left(\frac{R_\mathrm{p}}{R_\oplus}\right) \mathrm{g\,cm^{-3}}$	1.3	2.7 $M_\oplus$
$1.5 \leq R_\mathrm{p}/R_\oplus < 4$	$\frac{M_\mathrm{p}}{M_\oplus} = 2.69 \left(\frac{R_\mathrm{p}}{R_\oplus}\right)^{0.93}$	6.2	4.3 $M_\oplus$

[a]Including terrestrial solar system planets Mercury, Venus, Earth, and Mars.

3.5 Conclusions

The weighted mean exoplanet density peaks at approximately 1.4 $R_\oplus$ and 7.6 $\mathrm{g\,cm^{-3}}$ which is consistent with an Earth-composition planet. Planet density increases with radius up to 1.5 $R_\oplus$, but above 1.5 $R_\oplus$, planet density decreases with planet radius. Planets smaller than $1.5 R_\oplus$ are consistent with a linear density-radius relation, and are also consistent with the Seager et al. (2007) Earth composition curve. Above $1.5 R_\oplus$, the decrease in planet density with increasing radius can only be due to the inclusion of volatiles, and so planets larger than 1.5 $R_\oplus$ are generally inconsistent with a purely rocky composition. Among planets larger than $1.5 R_\oplus$, the gentle rise in planet mass with increasing radius indicates a substantial change in radius for very little change in mass, suggesting that lightweight H/He gas is present in increasing quantities with increasing planetary radius.

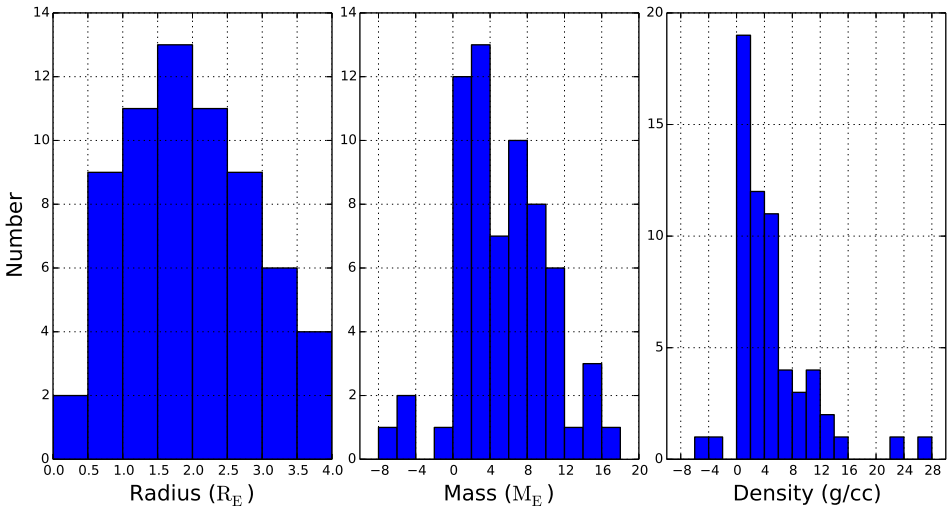

Figure 3.1: Histograms of exoplanet radii, masses, and densities for the 65 exoplanets smaller then 4 Earth radii with measured masses or mass upper-limits. Extreme density outliers Kepler-37 b, Kepler-100 d, Kepler-106 c, and Kepler-131 c are excluded from the density histogram for clarity, but are included in Table 1 and the fits.

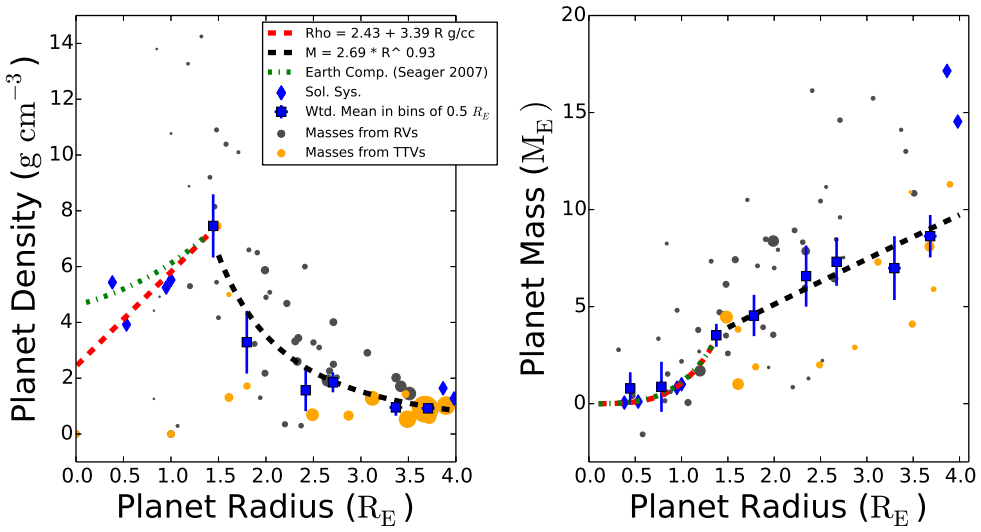

Figure 3.2: Left: Density vs. radius for 65 exoplanets. Gray points have RV-determined masses; orange points have TTV-determined masses, and the point size corresponds to $1/\sigma(\rho_{\rm p})$. The blue squares are weighted mean densities in bins of 0.5 $R_\oplus$, with error bars representing $\sigma_i/\sqrt{N_i}$, where σ_i is the standard deviation of the densities and N_i is the number of exoplanets in bin i. We omit the weighted mean densities below 1.0 $R_\oplus$ because the scatter in planet densities is so large that the error bars span the range of physical densities (0 to 10 g cm^{-3}). The blue diamonds indicate solar system planets. The red line is an empirical density-radius fit for planets smaller than $1.5R_\oplus$, including the terrestrial solar system planets. The green line is the mass-radius relation from Seager et al. (2007) for planets of Earth composition (67.5% $MgSiO_3$, 32.5% Fe). The increase in planet density with radius for $R_{\rm p} < 1.5R_\oplus$ is consistent with a population of rocky planets. Above 1.5 $R_\oplus$, planet density decreases with planet radius, indicating that as planet radius increases, so does the fraction of gas. Right: Mass vs. radius for 65 exoplanets. Same as left, but the point size corresponds to $1/\sigma(M_{\rm p})$, and the blue squares are the weighted mean masses in bins of $0.5R_\oplus$, with error bars representing $\sigma_i/\sqrt{N_i}$, where σ_i is the standard deviation of the masses and N_i is the number of exoplanets in bin i. The black line is an empirical fit to the masses and radii above 1.5 $R_\oplus$; see equation 3.3. The weighted mean masses were not used in calculating the fit. Some mass and density outliers are excluded from these plots, but are included in the fits.

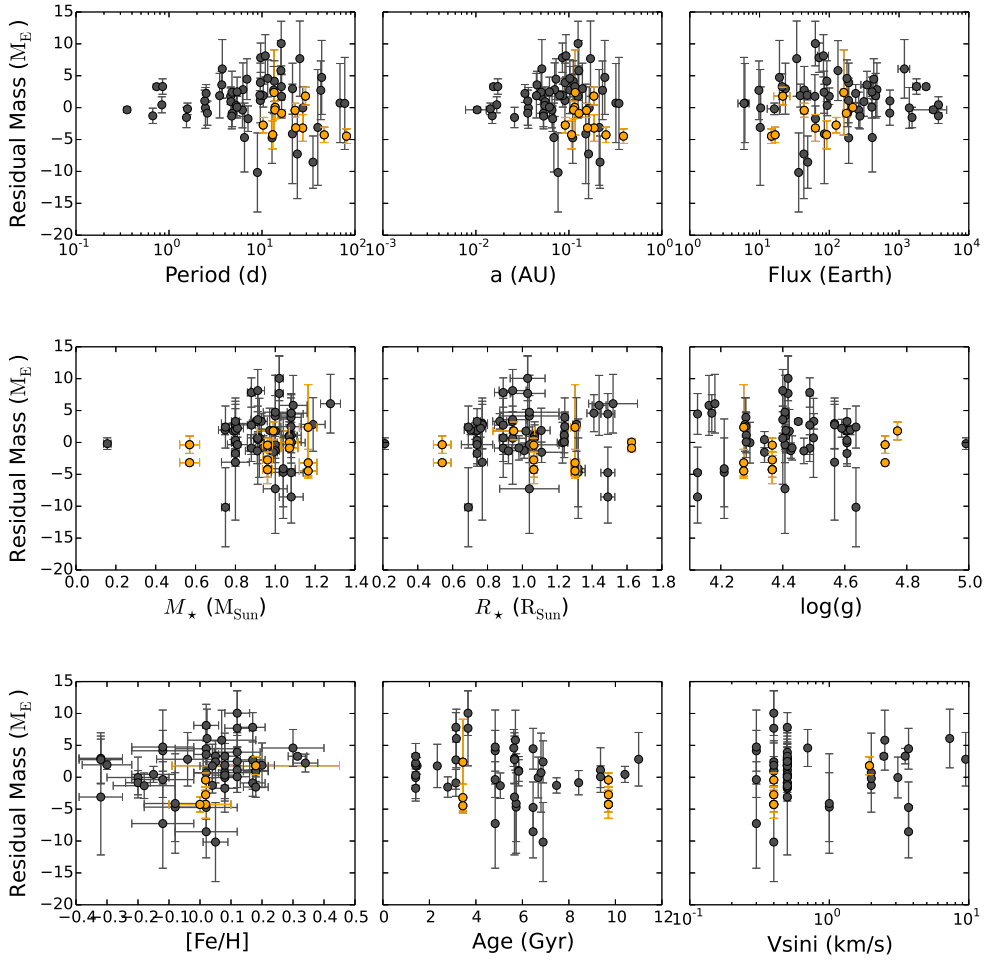

Figure 3.3: Mass residuals (measured minus the mass predicted from equations 3.1 - 3.3) versus (top left to bottom right): planet orbital period, planet semi-major axis, incident stellar flux, stellar mass, stellar radius, surface gravity, metallicity (compared to solar), stellar age, and stellar $v\sin i$. Error bars are 1σ uncertainties, and the orange points are residuals of the TTV-determined masses. None of the residuals show a significant correlation, although more mass measurements might elucidate a correlation with metallicity.

4

Revised Masses and Densities of the Planets around Kepler-10

A version of this chapter was previously published in the Astrophysical Journal (Weiss, L. M., Rogers, L. A., Isaacson, H. T., et al. 2016, ApJ, 819, 83).

Determining which small exoplanets have stony-iron compositions is necessary for quantifying the occurrence of such planets and for understanding the physics of planet formation. Kepler-10 hosts the stony-iron world Kepler-10b, and also contains what has been reported to be the largest solid silicate-ice planet, Kepler-10c. Using 220 radial velocities (RVs), including 72 precise RVs from Keck-HIRES of which 20 are new from 2014-2015, and 17 quarters of *Kepler* photometry, we obtain the most complete picture of the Kepler-10 system to date. We find that Kepler-10b ($R_{\rm p} = 1.47\ R_\oplus$) has mass $3.72 \pm 0.42\ M_\oplus$ and density 6.46 ± 0.73 g cm^{-3}. Modeling the interior of Kepler-10b as an iron core overlaid with a silicate mantle, we find that the iron core constitutes 0.17 ± 0.11 of the planet mass. For Kepler-10c ($R_{\rm p} = 2.35\ R_\oplus$) we measure mass $13.98 \pm 1.79\ M_\oplus$ and density 5.94 ± 0.76 g cm^{-3}, significantly lower than the mass computed in Dumusque et al. (2014, $17.2 \pm 1.9\ M_\oplus$). Our mass measurement of Kepler-10c rules out a pure stony-iron composition. Internal compositional modeling reveals that at least 10% of the radius of Kepler-10c is a volatile envelope composed of hydrogen-helium (0.2% of the mass, 16% of the radius) or super-ionic water (28% of the mass, 29% of the radius). However, we note that analysis of only HIRES data yields a higher mass for planet b and a lower mass for planet c than does analysis of the HARPS-N data alone, with the mass estimates for Kepler-10 c being formally inconsistent at the 3σ level. Moreover, dividing the data for each instrument into two parts also leads to somewhat inconsistent measurements for the mass of planet c derived from each observatory. Together, this suggests that time-correlated noise is present and that the uncertainties in the masses of the planets (especially planet c) likely exceed our formal estimates. Transit timing variations (TTVs) of Kepler-10c indicate the likely presence of a third planet in the system, KOI-72.X. The TTVs and RVs are consistent with KOI-72.X having an orbital period of 24, 71, or 101 days, and a mass from 1-7 $M_\oplus$.

4.1 Introduction

The thousands of high-fidelity planet candidates between 1 and 4 Earth radii discovered by the *Kepler* Mission (Borucki et al. 2011; Batalha et al. 2013; Burke et al. 2014; Rowe et al. 2014; Mullally et al. 2015), though absent from our solar system, are abundant in orbital periods < 100 days around Sun-like stars (Petigura et al. 2013a; Fressin et al. 2013; Petigura et al. 2013b). To understand the formation of these common planets, we must constrain their compositions. Are they terrestrial, or are they "water worlds" that are primarily water by volume, or are they stony-iron cores overlaid with thick, hydrogen-rich envelopes of volatiles?

In the last few years, the exoplanet community has measured the masses of dozens of small exoplanets, enabling the study of the compositions of individual planets and the identification of several stony-iron super-Earths. Corot-7 b ($R_{\rm p} = 1.58 \pm 0.10 R_{\oplus}$, $M_{\rm p} = 5.37 \pm 1.02\ M_{\oplus}$; Bruntt et al. 2010; Haywood et al. 2014) and Kepler-10 b ($R_{\rm p} = 1.46 \pm 0.034\ R_{\oplus}$, $M_{\rm p} = 4.56 \pm 1.23\ M_{\oplus}$; Batalha et al. 2011) were the first stony-iron planets discovered. Carter et al. (2012) used transit timing variations to determine the mass of Kepler-36 b from orbital perturbations it induced on neighboring planet Kepler-36 c. At the time of writing, Kepler-36 b has the best-determined mass and density of the known rocky exoplanets ($M_{\rm p} = 4.56 \pm 1.23$, $\rho_{\rm p} = 8.8 \pm 2.5 {\rm g\,cm^{-3}}$). Howard et al. (2013), Pepe et al. (2013), and Grunblatt et al. (2015) measured the mass of the Earth-density planet Kepler-78 b ($R_{\rm p} = 1.20 \pm 0.09 R_{\oplus}$, $M_{\rm p} = 1.87 \pm 0.26 M_{\oplus}$, $\rho_{\rm p} = 6.0 \pm 1.7 {\rm g\,cm^{-3}}$), the closest Earth-analog in terms of planet mass, radius, and density, although it is far too hot to support life as we know it.

However, some small planets have definitively non-rocky surfaces and require hydrogen-helium envelopes to explain their low bulk densities. For instance, three of the six planets orbiting Kepler-11 are smaller than 4 $R_{\oplus}$ and have densities lower than 1.0 ${\rm g\,cm^{-3}}$ (Lissauer et al. 2011; Lissauer et al. 2013). Likewise, two of four the planets orbiting Kepler-79 (a.k.a. KOI-152) are smaller than 4 $R_{\oplus}$ and have densities lower than 1.0 ${\rm g\,cm^{-3}}$ (Jontof-Hutter et al. 2014). In an intensive *Kepler* follow-up campaign spanning 4 years, Marcy et al. (2014) measured or constrained the masses of 42 small exoplanets using Keck-HIRES, finding many planets that have volatiles and a few planets that might have stony-iron compositions.

The mass measurements listed above allowed the community to probe composition trends within the planet population. Based on the density-radius distribution of 65 exoplanets smaller than Neptune, Weiss & Marcy (2014) found two empirical relations: among planets smaller than 1.5 $R_{\oplus}$, density increases nearly linearly with increasing planet radius in a manner consistent with a stony-iron composition like Earth's. However, bulk density decreases with increasing radius for planets between 1.5-4.0 $R_{\oplus}$, implying an increasing admixture of volatiles above 1.5 $R_{\oplus}$. Rogers (2015) used a hierarchical Bayesian framework to rigorously test the transition from stony-iron planets to planets with a gaseous envelope and found that at and above 1.6 $R_{\oplus}$, the majority of planets have a volatile envelope, while the remaining minority are sufficiently dense to be comprised of iron and silicate only. Dressing et al. (2015) measured the mass of Kepler-93 b ($R_{\rm p} = 1.478 \pm 0.019$, $M_{\rm p} = 4.02 \pm 0.68$) and determined that Kepler-93 b and the other known rocky planets (Kepler-78 b, Kepler-36 b, Kepler-10 b, and Corot-7 b) all have masses and radii that can be explained with an iron-

silicate composition. By contrast, KOI-273 b ($R_{\rm p} = 2.37 \pm 0.13 R_\oplus$, $M_{\rm p} = 6.8 \pm 1.4 M_\oplus$ Gettel et al. 2016) is too big to be rocky and requires a small volatile envelope. Wolfgang & Lopez (2015) used a hierarchical Bayesian model to explore the diversity of planet mass, density, and composition as a function of planet radius. They found that planets smaller than 1.5 $R_\oplus$ are typically rocky, whereas planets larger than 1.5 $R_\oplus$ typically require a small fraction of hydrogen gas or other volatiles to explain their densities. Furthermore, small differences in the mass fraction of hydrogen in the planet's envelope explain the broad range of planet densities at a given radius for planets between 2-4$R_\oplus$.

Although planets smaller than 1.5 $R_\oplus$ tend to be stony-iron and planets larger than 1.5 $R_\oplus$ tend to have at least a small hydrogen envelope, there are exceptions to the pattern. In the Kepler-138 system, which contains three planets smaller than 1.5 $R_\oplus$, at least one planet, Kepler-138 d ($R_{\rm p} = 1.212 \pm 0.075 R_\oplus$, $M_{\rm p} = 0.640^{+0.674}_{-0.387} M_\oplus$, $\rho_{\rm p} = 2.1^{+2.2}_{-1.2} {\rm g\,cm^{-3}}$), has a low enough density to require a volatile envelope (Kipping et al. 2014; Jontof-Hutter et al. 2015). Kepler-138 d is the smallest exoplanet that we know to contain a gaseous envelope.

The Kepler-10 system is a powerful testing ground for our understanding of the compositions of small planets. Kepler-10 is a sun-like star with slow rotation and little stellar activity (Dumusque et al. 2014). It has two planets discovered via transits in the *Kepler* Mission: Kepler-10 b, which has an orbital period of 0.84 days and radius 1.47 $R_\oplus$, and Kepler-10 c, which has an orbital period of 45 days and radius 2.35 $R_\oplus$ (Batalha et al. 2011; Dumusque et al. 2014). Batalha et al. (2011, hereafter B11) measured the mass and bulk density of Kepler-10 b and determined that it was rocky, making this planet the first rocky planet discovered by the *Kepler* Mission, and the second rocky exoplanet discovery. More recently, Dumusque et al. (2014, hereafter D14) reported that Kepler-10 c has a radius of 2.35 $R_\oplus$, a mass of 17.2 ± 1.9 $M_\oplus$, and a density of $7.1 \pm 1.0 {\rm g\,cm^{-3}}$. Based on its position in the mass-radius diagram, D14 interpreted the composition of Kepler-10 c as mostly rock by mass, with the remaining mass in volatiles of high mean-molecular weight (likely water). They noted, however, that compositional degeneracy prevented them from determining the precise water fraction.

Kepler-10 c is unusual in that the mass reported in D14 is large compared to other exoplanets its size. Most exoplanets with radii 2.0-2.5 $R_\oplus$ have much lower masses than 17 $M_\oplus$, with a weighted mean mass of 5.4 $M_\oplus$ (Weiss & Marcy 2014) in that size range. For example, HD 97658 b, a planet discovered in RVs (Howard et al. 2011) that was subsequently observed to transit its star, has a radius of 2.34 ± 0.16 $R_\oplus$ and a mass of 7.87 ± 0.73 $M_\oplus$ (Dragomir et al. 2013). Kepler-68 b has a radius of 2.32 ± 0.02 $R_\oplus$ and a mass of 7.15 ± 2.0 $M_\oplus$ (Marcy et al. 2014; Gilliland et al. 2013). Although there is a large scatter in the observed masses between 2 and 2.5 $R_\oplus$, this scatter results from a few low-mass planets of this size. For example, Kepler-11 f, which has a radius of 2.49 ± 0.06 $R_\oplus$, has a mass of $1.94^{+0.32}_{-0.88}$ $M_\oplus$ (Lissauer et al. 2011; Lissauer et al. 2013, Weiss et al. in prep.). In contrast, the most massive planet in this size range other than Kepler-10 c is Kepler-131 b. The initial mass measurement of Kepler-131 b (Marcy et al. 2014) was $R_{\rm p} = 2.41 \pm 0.20$ $R_\oplus$, $M_{\rm p} = 16.13 \pm 3.50$ $M_\oplus$, resulting in a bulk density of 6.0 ± 1.98 g cm^{-3}, but additional measurements obtained since publication show the mass to be much smaller; the confusion was from astrophysical rather

than instrumental sources (personal communication, H. Isaacson in prep.). Thus, Kepler-10 c seems to be unusual in its high mass for planets between 2-2.5 $R_\oplus$. All of these planets except Kepler-10 c are included in the empirical mass-radius relation to exoplanets between 1.5 and 4 $R_\oplus$ ($M_\mathrm{p}/M_\oplus = 2.69(R_\mathrm{p}/R_\oplus)^{0.93}$; Weiss & Marcy 2014), according to which a planet of size 2.3 $R_\oplus$ should have a mass of 5.8 $M_\oplus$.

In this paper, we build on the data and analysis of D14, adhering to the techniques therein as completely as possible but with the addition of 72 RVs from Keck-HIRES, in an effort to calculate a new and improved two-planet orbital solution for the Kepler-10 system. We also notice that Kepler-10 c exhibits transit timing variations (TTVs), i.e. perturbations to its orbit, as did Kipping et al. (2015). Because Kepler-10 b is dynamically distant from Kepler-10 c ($P_c/P_b = 54$), Kepler-10 b cannot perturb Kepler-10 c sufficiently to reproduce the observed TTVs. Therefore, we infer the existence of a third planet in the system, planet candidate KOI-72.X, which explains the observed TTVs. We explore various dynamic configurations for KOI-72.X that reproduce the observed TTVs and are consistent with the RVs as well. Finally, we comment on the compositions of Kepler-10 b and Kepler-10 c, and how their masses, radii, and densities compare to those of other small transiting planets.

4.2 Radial Velocities of Kepler-10 from HIRES and HARPS-N

HIRES has a long history of achieving precision RVs with an RMS of $\sim 2\ \mathrm{m\,s^{-1}}$ on quiet, sun-like stars over many years of observations (Howard et al. 2010; Howard et al. 2011, Figure 4.1). Our group has used HIRES to measure and place upper limits on the masses of many small planets, especially in the *Kepler* era (e.g. Marcy et al. 2014). Because the planets transit and are vetted through a variety of astrophysical techniques, the burden of confirming the planet does not fall entirely to radial velocities. In this case, Fressin et al. (2011) validated the planetary nature of Kepler-10 c, incorporating the transit shape and depth in multiple passbands, high-resolution imaging and spectroscopy of the host star, and stellar population synthesis to find a conservative false alarm probability of 1.6×10^{-5}. Lissauer et al. (2012) demonstrated the very low probability of having a false alarm planet in a multi-planet system, further reducing the false alarm probability of Kepler-10 c by an order of magnitude. Thus, it is not necessary to determine the mass of Kepler-10 c (or any other statistically validated small planet) with 3σ significance in order to confirm the planet's existence or to make statistically significant claims about the composition of the planet. A mass upper limit might exclude a purely stony-iron composition with 3σ confidence while only being 1σ away from a mass of zero. Such planets provide valuable information about the exoplanet population, and excluding them from population studies on the basis of their large fractional mass uncertainty (σ_m/m) will systematically exclude the low-mass exoplanets. Modern exoplanet mass-radius relations (e.g. Weiss & Marcy 2014; Rogers 2015; Wolfgang & Lopez 2015) incorporate the low-significance mass detections.

Both the HIRES and HARPS-N spectrographs have successfully obtained high-precision

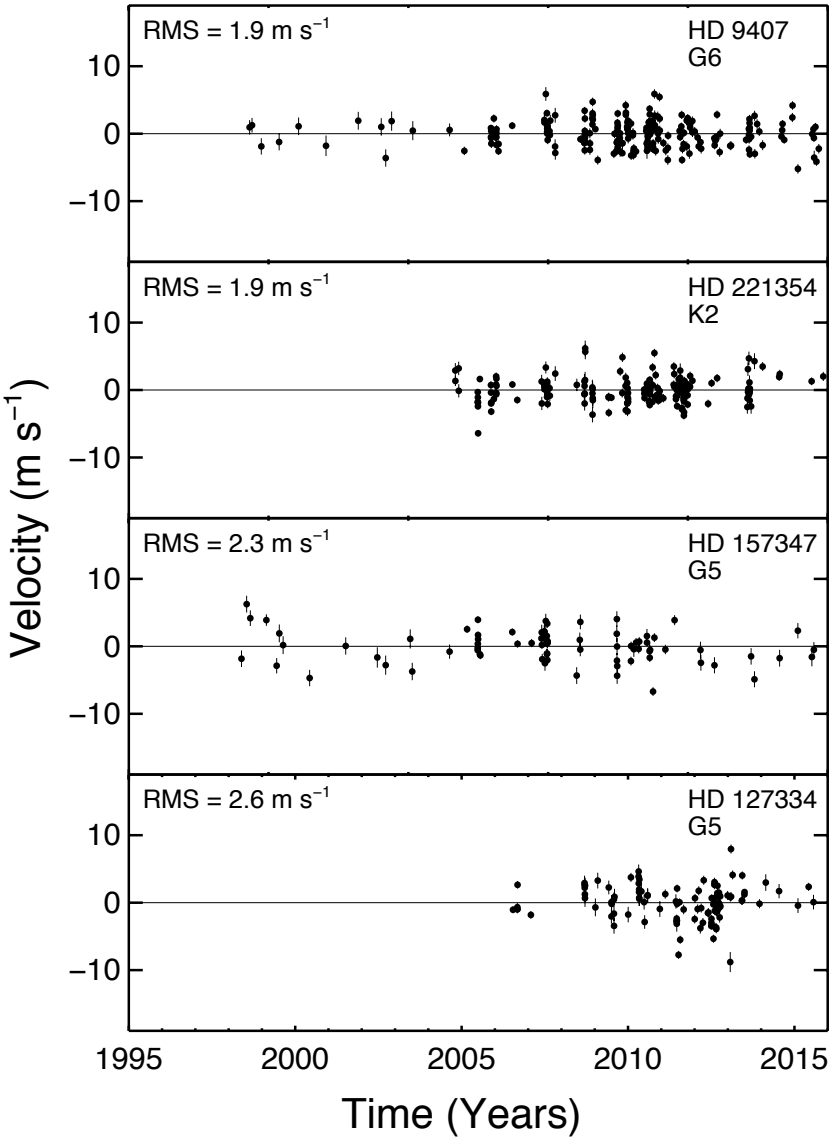

Figure 4.1: RV vs. time for stable stars observed by Keck-HIRES. The RMS of the RVs, stellar name, and stellar spectral type are shown. The typical RMS of ~ 2 m s^{-1} achieved by Keck-HIRES over a decade for stars without planets demonstrates the ability of HIRES as a multi-season, precision-RV instrument.

RVs of *Kepler* stars in the past (Marcy et al. 2014; Dressing et al. 2015). Notably, two teams used each spectrograph to independently measure the RV signal from the low-mass planet Kepler-78 b. Howard et al. (2013) obtained a mass of $1.69 \pm 0.41 M_{\oplus}$ for Kepler-78 b, and Pepe et al. (2013) obtained a mass of 1.86 ± 0.32. The independent detections of the RV signal in both spectrometers, and the agreement in the amplitude of that signal, demonstrate that both the HIRES and HARPS-N spectrometers are capable of accurately and precisely measuring low-amplitude RV signals.

Ground-based RV follow-up of Kepler-10 has been ongoing since Kepler-10 b and Kepler-10 c were discovered. B11 presented 52 RVs obtained on Keck-HIRES in 2009–2010, the first seasons after Kepler-10 b and c were discovered, and D14 presented 148 RVs obtained on TNG-HARPS-N that span the summers of 2012–2013. The early measurements presented in B11 targeted the quadrature times of planet b, whereas the later measurements from D14 targeted the quadrature times of planet c.

We present 20 additional RVs from 2014-2015 which, in combination with all the previous RVs, comprise the largest dataset of Kepler-10 RVs to date of 220 RVs total (Table 1 and Figure 4.2). HARPS-N, which is a fiber-fed, thermally stable spectrometer in a vacuum, achieves better velocity precision at given signal-to-noise than the HIRES spectrometer, but the larger aperture of the Keck telescope (10 m compared to 3.6 m) collects more photons. Thus, both telescope-spectrometer setups achieve a velocity precision of a few $\mathrm{m\,s^{-1}}$ per half hour observing Kepler-10.

Although only 20 RVs were taken since the publication of D14, combining all the data provides several major advantages over either the B11 or D14 data alone. Because the *Kepler* field is best accessible during the summer, the data from both HIRES and HARPS-N are clumped in intervals of 2-3 months, a timescale barely longer than the orbital period of Kepler-10 c (45.3 days). Observing just 1-2 orbits of planet c could be problematic if the stellar rotation period is comparable to the orbital period of planet c and temporarily phases with the orbit of planet c over a few rotation cyles. Furthermore, incomplete observing phase coverage combined with noise can result in additional power in an alias of the planetary signal or a peak resulting from the window function (Dawson & Fabrycky 2010; Rajpaul et al. 2015). The combined data cover observing phase as a function of sidereal day, solar day, and solar year better than either data set does alone (see Figure 6.8), improving our resilience to noise manifesting in monthly and yearly aliases of planet c's orbit. Furthermore, the combined baseline of 6 years (2009-2015) is much longer than the 2-year baseline achieved in either of the previous papers. The long observing baseline helps to average out possible spurious signals that can arise from stellar activity on the timescales of stellar rotation and convection ($\sim$ 1 month). The long baseline also improves our sensitivity to possible long-period signals. These advantages motivate combining all of the reliable data.

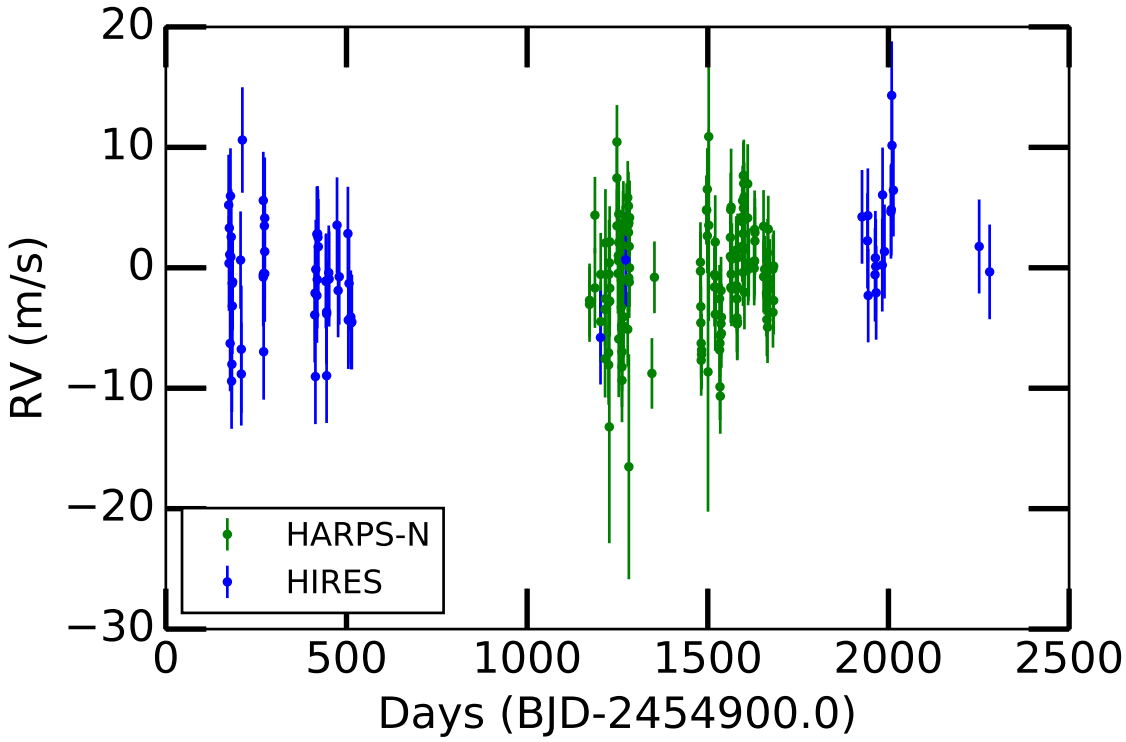

Figure 4.2: Radial velocity measurements of Kepler-10 from the HIRES (blue) and HARPS-N (green) high-resolution echelle spectrometers.

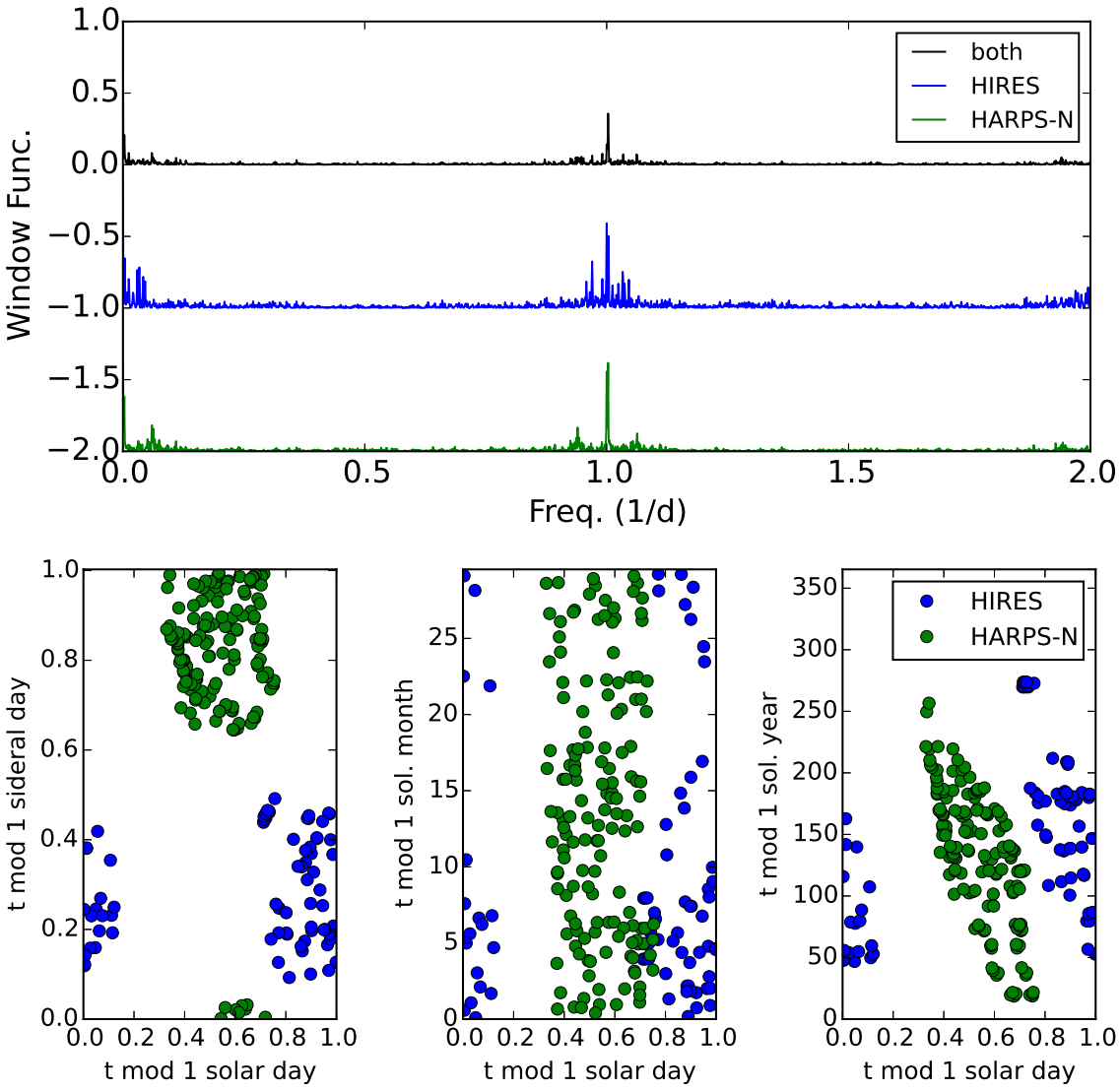

Figure 4.3: Top: window function of the combined RVs, HIRES RVs, and HARPS-N RVs, vertically offset for clarity. The peaks near 1/day indicate the daily alias in each data set, and the peaks near 0.06/day are consistent with a monthly alias. The combined RVs reduce the strength of the daily alias and remove the monthly alias. Bottom left: time of observation modulo the sidereal day versus time of observation modulo the solar day shows the sidereal and solar daily phase coverage of the observations from HIRES (blue) and HARPS-N (green). Bottom center: same as bottom left, but with time modulo the solar month on the dependent axis. Bottom right: same as bottom left, but with time modulo the solar year on the dependent axis.

Table 4.1: RVs of Kepler-10 from HIRES and HARPS-N.

BJD (- 2454900.0)	RV (m/s)	unc. RV (m/s, inc. jitter)	SNR	Instrument
173.900499	5.21	4.18	152.8	HIRES
174.877797	0.37	3.94	217.3	HIRES
175.773348	3.31	3.95	214.6	HIRES
176.862854	1.10	3.96	217.1	HIRES
177.923401	-6.28	3.97	222.3	HIRES
178.922398	5.96	3.96	217.8	HIRES
179.972876	0.90	4.00	217.8	HIRES
180.896063	2.56	3.94	216.3	HIRES
181.969271	-9.41	3.96	217.6	HIRES
182.847887	-8.01	3.97	215.8	HIRES
183.760854	-1.30	3.92	217.0	HIRES
183.945387	-3.17	3.99	218.2	HIRES
184.877994	-1.17	3.93	217.0	HIRES
206.889914	0.64	4.04	220.6	HIRES
208.885123	-8.82	4.28	154.1	HIRES
208.890922	-6.76	5.28	80.0	HIRES
211.830107	10.61	4.38	166.7	HIRES
269.71177	-0.59	4.22	152.7	HIRES
269.720925	-0.77	4.08	202.7	HIRES
269.733899	5.59	4.04	215.5	HIRES
270.715114	-0.47	3.99	214.5	HIRES
270.733655	-6.97	3.98	213.4	HIRES
272.756489	3.48	4.03	157.2	HIRES
273.714025	1.35	3.97	198.7	HIRES
273.720425	4.13	5.03	75.4	HIRES
273.727555	-0.49	4.00	193.4	HIRES
412.04715	-3.91	3.94	217.3	HIRES
413.004124	-2.11	3.94	215.9	HIRES
414.004814	-9.03	3.95	215.3	HIRES
415.111272	-0.13	4.12	205.1	HIRES
417.998478	2.79	3.96	215.8	HIRES
418.121283	-2.30	3.93	215.4	HIRES
419.027179	-0.98	4.06	214.7	HIRES
420.062974	2.83	3.95	218.5	HIRES
421.006521	2.53	3.93	218.1	HIRES
421.969467	1.75	3.97	217.7	HIRES
443.050045	-1.13	3.90	241.1	HIRES
444.031958	-1.08	3.93	242.3	HIRES
444.964655	-3.66	4.34	132.4	HIRES
444.977237	-8.96	3.93	241.4	HIRES
445.068315	-3.82	4.00	218.3	HIRES

Table 4.1 (cont'd): RVs of Kepler-10 from HIRES and HARPS-N.

BJD (- 2454900.0)	RV (m/s)	unc. RV (m/s, inc. jitter)	SNR	Instrument
450.972744	-0.41	3.92	243.6	HIRES
451.987745	-0.93	3.95	242.7	HIRES
473.81361	3.54	3.97	241.1	HIRES
476.86488	-1.89	3.88	313.6	HIRES
479.902118	-0.74	3.98	242.6	HIRES
503.897962	2.84	3.89	313.6	HIRES
505.056086	-4.34	4.06	211.1	HIRES
507.012774	-1.30	3.92	311.8	HIRES
511.985723	-4.08	3.86	314.8	HIRES
512.805268	-4.57	3.86	314.4	HIRES
514.80255	-4.50	3.93	281.8	HIRES
1172.682384	-2.70	3.05	56.2	HARPS-N 1
1172.704768	-3.04	3.11	53.4	HARPS-N 1
1187.57572	-1.67	3.32	45.0	HARPS-N 1
1187.596901	4.37	3.18	48.5	HARPS-N 1
1203.106739	-5.79	3.90	312.2	HIRES
1203.661644	-0.55	3.45	38.7	HARPS-N 1
1203.689793	-4.47	3.32	41.9	HARPS-N 1
1215.691945	-3.45	3.04	60.6	HARPS-N 1
1215.713149	-7.55	3.22	52.5	HARPS-N 1
1216.704755	2.06	4.47	28.4	HARPS-N 1
1216.719003	-2.56	4.77	26.5	HARPS-N 1
1225.568254	-7.06	3.76	35.2	HARPS-N 1
1225.589446	-8.06	3.31	44.2	HARPS-N 1
1226.447899	-2.83	2.94	59.4	HARPS-N 1
1226.664948	-0.54	4.53	28.7	HARPS-N 1
1227.422428	-13.21	9.66	13.9	HARPS-N 1
1227.441641	0.41	2.91	62.7	HARPS-N 1
1228.43499	2.16	2.95	60.1	HARPS-N 1
1228.560476	-2.77	2.94	59.7	HARPS-N 1
1228.662918	-1.70	3.14	49.7	HARPS-N 1
1248.408122	7.45	3.22	43.5	HARPS-N 1
1248.511779	10.45	3.06	48.5	HARPS-N 1
1248.617819	3.48	3.05	53.9	HARPS-N 1
1251.396386	-0.48	3.33	42.5	HARPS-N 1
1252.407893	1.01	2.84	67.9	HARPS-N 1
1252.640275	0.59	3.36	45.4	HARPS-N 1
1253.395106	2.11	2.98	54.3	HARPS-N 1
1253.493404	-5.91	4.83	25.1	HARPS-N 1
1253.647013	4.45	2.97	58.8	HARPS-N 1
1260.473487	-1.01	4.25	31.4	HARPS-N 1

Table 4.1 (cont'd): RVs of Kepler-10 from HIRES and HARPS-N.

BJD (- 2454900.0)	RV (m/s)	unc. RV (m/s, inc. jitter)	SNR	Instrument
1260.626355	-3.28	3.98	34.8	HARPS-N 1
1261.39719	-4.78	3.42	40.7	HARPS-N 1
1261.573183	-5.06	3.65	38.9	HARPS-N 1
1262.394398	-8.23	3.33	43.4	HARPS-N 1
1262.487962	-6.97	3.28	45.2	HARPS-N 1
1262.567972	-9.35	3.47	42.1	HARPS-N 1
1264.385261	1.87	3.27	44.4	HARPS-N 1
1265.380836	3.11	3.27	45.0	HARPS-N 1
1266.384814	3.74	3.45	38.9	HARPS-N 1
1266.534418	-4.07	3.36	42.0	HARPS-N 1
1266.601002	-4.84	3.48	40.9	HARPS-N 1
1272.8013	0.67	3.91	283.2	HIRES
1275.410615	4.18	2.84	67.5	HARPS-N 1
1275.521886	3.13	2.97	58.3	HARPS-N 1
1278.373888	-5.11	3.09	49.5	HARPS-N 1
1278.494638	5.83	3.03	53.7	HARPS-N 1
1279.373462	3.53	2.91	58.8	HARPS-N 1
1279.521052	4.21	3.02	57.6	HARPS-N 1
1280.40035	5.13	2.84	70.7	HARPS-N 1
1280.543831	2.94	2.97	60.5	HARPS-N 1
1281.435709	-0.84	2.81	73.4	HARPS-N 1
1281.529573	-16.52	9.34	16.1	HARPS-N 1
1281.534515	3.71	2.98	61.3	HARPS-N 1
1282.398292	1.78	2.86	64.9	HARPS-N 1
1282.535095	-1.19	2.98	58.3	HARPS-N 1
1283.373536	0.00	3.23	44.7	HARPS-N 1
1283.560153	4.16	3.08	53.2	HARPS-N 1
1345.332519	-8.77	2.93	60.6	HARPS-N 2
1352.34146	-0.79	2.98	66.6	HARPS-N 2
1479.677427	0.46	3.32	53.2	HARPS-N 2
1479.750484	-0.28	3.25	54.8	HARPS-N 2
1480.663449	-3.22	3.18	55.6	HARPS-N 2
1480.739863	-4.57	3.06	61.1	HARPS-N 2
1481.685619	-6.27	2.94	72.1	HARPS-N 2
1481.75076	-7.68	2.94	72.0	HARPS-N 2
1482.671897	-7.20	2.88	75.3	HARPS-N 2
1482.753519	-6.84	3.00	66.5	HARPS-N 2
1496.608742	4.82	2.86	80.9	HARPS-N 2
1496.724487	4.77	2.84	83.1	HARPS-N 2
1498.614845	6.52	3.41	51.1	HARPS-N 2
1498.727696	2.65	3.09	60.7	HARPS-N 2

Table 4.1 (cont'd): RVs of Kepler-10 from HIRES and HARPS-N.

BJD (- 2454900.0)	RV (m/s)	unc. RV (m/s, inc. jitter)	SNR	Instrument
1500.594327	-8.64	11.61	14.9	HARPS-N 2
1502.590476	10.89	5.82	26.6	HARPS-N 2
1502.707713	3.53	7.95	20.0	HARPS-N 2
1518.588709	-1.60	3.27	49.9	HARPS-N 2
1518.689186	-0.56	3.19	50.1	HARPS-N 2
1520.585042	2.13	3.89	37.1	HARPS-N 2
1520.698459	-3.86	3.03	59.1	HARPS-N 2
1521.589725	-1.62	2.92	68.8	HARPS-N 2
1521.686301	-0.71	2.75	90.7	HARPS-N 2
1532.559497	-2.57	2.81	78.4	HARPS-N 2
1532.704814	-6.82	2.78	84.1	HARPS-N 2
1533.562499	-6.26	2.79	83.9	HARPS-N 2
1533.708811	-9.88	2.76	88.1	HARPS-N 2
1534.523174	-10.66	3.12	57.1	HARPS-N 2
1534.689787	-5.63	2.85	73.0	HARPS-N 2
1536.539212	-4.64	2.83	78.5	HARPS-N 2
1536.69836	-1.89	2.80	81.7	HARPS-N 2
1537.537063	-5.45	2.85	75.3	HARPS-N 2
1537.698873	-4.10	2.78	84.5	HARPS-N 2
1562.440914	0.95	3.05	60.9	HARPS-N 2
1562.595327	2.52	3.04	60.7	HARPS-N 2
1563.499671	4.82	3.07	58.3	HARPS-N 2
1563.673401	-1.63	2.94	63.5	HARPS-N 2
1564.515083	5.04	4.85	29.9	HARPS-N 2
1564.675676	-0.53	3.33	49.0	HARPS-N 2
1565.523526	-1.72	3.13	56.4	HARPS-N 2
1566.47765	-1.59	2.94	67.5	HARPS-N 2
1566.698684	0.74	2.96	67.4	HARPS-N 2
1578.422373	-1.78	3.08	59.9	HARPS-N 2
1578.607224	1.29	2.91	71.5	HARPS-N 2
1579.468298	1.48	2.81	83.0	HARPS-N 2
1579.606263	-1.48	2.81	84.3	HARPS-N 2
1580.550925	-2.58	2.78	86.3	HARPS-N 2
1580.702582	-4.15	2.85	79.9	HARPS-N 2
1581.443399	-4.66	2.94	67.5	HARPS-N 2
1581.578226	-4.45	3.23	53.2	HARPS-N 2
1582.444149	-1.68	3.15	56.2	HARPS-N 2
1582.62878	0.83	3.67	42.6	HARPS-N 2
1595.439337	3.83	2.82	82.7	HARPS-N 2
1595.606467	1.79	2.95	68.4	HARPS-N 2
1596.385682	5.56	2.92	71.5	HARPS-N 2

Table 4.1 (cont'd): RVs of Kepler-10 from HIRES and HARPS-N.

BJD (- 2454900.0)	RV (m/s)	unc. RV (m/s, inc. jitter)	SNR	Instrument
1596.639015	4.24	2.87	77.4	HARPS-N 2
1597.498195	-0.38	2.80	85.5	HARPS-N 2
1597.67948	2.83	2.89	75.6	HARPS-N 2
1598.494932	7.64	2.84	81.0	HARPS-N 2
1598.671622	4.95	3.06	62.1	HARPS-N 2
1599.444782	6.99	2.88	75.5	HARPS-N 2
1599.669099	7.67	2.97	69.9	HARPS-N 2
1600.450037	5.89	2.85	79.3	HARPS-N 2
1600.634886	1.53	3.08	62.8	HARPS-N 2
1601.425511	-2.03	3.08	61.1	HARPS-N 2
1601.65852	1.59	3.08	62.6	HARPS-N 2
1610.395668	4.14	3.36	48.7	HARPS-N 2
1610.406339	6.97	3.29	50.2	HARPS-N 2
1611.547768	-0.14	2.97	66.5	HARPS-N 2
1612.49135	0.09	2.84	79.8	HARPS-N 2
1613.483021	0.44	2.83	80.6	HARPS-N 2
1628.459887	-0.04	3.08	60.1	HARPS-N 2
1628.564955	0.51	3.16	58.7	HARPS-N 2
1629.480763	0.57	2.83	83.6	HARPS-N 2
1629.614778	3.18	3.24	57.0	HARPS-N 2
1630.444186	2.22	2.82	84.2	HARPS-N 2
1630.53025	2.92	2.87	77.3	HARPS-N 2
1654.373345	3.44	3.01	56.8	HARPS-N 2
1654.46788	-0.74	2.98	58.8	HARPS-N 2
1657.371082	-0.12	2.77	84.4	HARPS-N 2
1657.503069	-0.78	3.10	58.0	HARPS-N 2
1662.435891	-2.10	3.61	45.0	HARPS-N 2
1663.373238	-2.36	2.89	71.8	HARPS-N 2
1663.472796	-4.30	3.04	62.5	HARPS-N 2
1665.352941	-4.94	2.97	66.8	HARPS-N 2
1665.482578	1.24	2.82	81.1	HARPS-N 2
1667.347572	3.21	2.77	88.3	HARPS-N 2
1671.344738	-1.73	3.37	48.5	HARPS-N 2
1671.455024	-0.97	3.35	49.9	HARPS-N 2
1680.342329	-0.12	2.89	70.8	HARPS-N 2
1680.43589	-3.70	2.93	69.6	HARPS-N 2
1682.32927	-2.72	2.80	81.4	HARPS-N 2
1682.376757	0.14	2.96	66.8	HARPS-N 2
1926.898038	4.23	3.89	283.4	HIRES
1942.001946	2.24	3.95	283.1	HIRES
1942.954468	4.33	3.92	283.4	HIRES

Table 4.1 (cont'd): RVs of Kepler-10 from HIRES and HARPS-N.

BJD (- 2454900.0)	RV (m/s)	unc. RV (m/s, inc. jitter)	SNR	Instrument
1943.951042	-2.30	3.89	284.7	HIRES
1962.874534	-0.57	3.89	286.0	HIRES
1963.860172	0.82	3.90	283.8	HIRES
1964.900473	0.11	3.93	283.4	HIRES
1965.945739	-2.07	3.90	282.6	HIRES
1982.934778	0.23	3.86	281.7	HIRES
1983.770615	6.05	3.93	280.2	HIRES
1989.012469	1.35	3.90	282.4	HIRES
2006.909888	4.64	3.88	280.8	HIRES
2007.77185	4.84	3.81	283.8	HIRES
2008.976767	14.31	4.49	131.4	HIRES
2009.88478	10.16	3.85	280.9	HIRES
2013.741571	6.44	3.84	285.1	HIRES
2251.114854	1.77	3.90	280.9	HIRES
2280.075021	-0.34	3.93	277.9	HIRES

4.2.1 HIRES Doppler Pipeline

We calculate precise radial velocities of Kepler-10 using the standard Doppler code of the CPS group (Howard et al. 2011) with the inclusion of a new de-trending routine. Previoulsy published RVs (B11) were collected during the 2009-2010 observing seasons. Subsequent observations were taken in the 2014 observing season. Long term RV precision spanning 10 years is consistently achieved with HIRES as described in Howard et al. (2011). Exposure times of ∼30 minutes are required to achieve SNR ∼200 in the iodine region, resulting in internal RV errors of 1.5 to 2.0 $\mathrm{m\,s^{-1}}$. Each observation uses a slit with dimensions of 0.87″x 14.″0 yielding a resolving power of 60,000, and allowing for subtraction of night sky emission lines, and scattered moonlight.

During the initial RV extraction we model the instrumental PSF as a sum of 13 Gaussians with positions and widths fixed but their heights free to vary (Butler et al. 1996). Any correlations in the final RVs with the heights of these Gaussians (PSF parameters) likely indicate small inadequacies of our PSF model to completely describe the shape of the instrumental PSF. RV shifts caused by the gravitational influence of orbiting bodies should not be correlated with the shape of the instrumental PSF.

In order to clean the RVs of any possible systematic trends we detrend the final RVs by removing correlations with the instrumental PSF parameters, the magnitude of the RV uncertainty, and the S/N ratio of the spectrum. After masking any 5σ outliers, we search for significant correlations by calculating the Spearman rank correlation coefficient for each of these variables with RV (Spearman1904). We take note of any parameters that show a correlation coefficient greater than 0.1 and include these variables in a multivariate ordinary

least squares linear regression using the STATSMODELS[1] package in Python. This final multidimensional surface is then subtracted from the final RVs. This technique improves the RMS of the RV time series of Kepler-10 from 4.9 $\mathrm{m\,s^{-1}}$ to 4.6 $\mathrm{m\,s^{-1}}$ by detrending against nine PSF parameters and the S/N ratio of the spectra. To check that the detrending algorithm does not accidentally remove the signal of the planets, we calculated a two-planet circular fit to both the detrended and non-detrended RVs. The RMS of the change in RV introduced by the detrending algorithm was 1.2 $\mathrm{m\,s^{-1}}$ (i.e., less than the uncertainty in each RV), and the solutions for all parameters were consistent within 0.1 $\mathrm{m\,s^{-1}}$ (much less than our 1σ uncertainties in the parameters). We do not add the random noise introduced by the detrending algorithm to our error budget because our technique for solving for the jitter (see Equation 4.1) naturally incorporates the uncertainties that arise through this method.

4.2.2 Analysis of the HIRES and HARPS-N RVs

Figure 4.4 shows the Kepler-10 RVs from HIRES and HARPS-N phase-folded to the orbital periods of the two transiting planets, with red diamonds indicating the weighted mean RV in bins of 0.1 orbital phases to guide the eye. Figure 4.5 shows the MCMC posterior distributions of two-planet circular fits to the HIRES RVs alone (blue) and the HARPS-N RVs alone (green). A summary of the best fit parameters to the HIRES RVs alone are given in Table 4.2.2. The HIRES RVs yield $m_c = 5.69^{+3.19}_{-2.90}\ M_\oplus$, a result that disagrees with the best fit to the HARPS-N RVs ($m_c = 17.2 \pm 1.9$) by 3.1 σ.

4.2.3 Analysis of the Discrepancy between HIRES and HARPS-N RVs

What is the source of the discrepancies between K_b and K_c in the HIRES and HARPS-N data? HIRES RVs are stable with an RMS of 2 $\mathrm{m\,s^{-1}}$ for various stars of spectral types without any known planets over decades (Figure 1). Removing 2.5σ outliers outliers changes K_b and K_c by 1%, an insignificant amount compared to our uncertainties. We do not find any significant correlations between the RVs and barycentric correction, or between the RVs and stellar activity indices, in either the HIRES or HARPS-N data.

When we break either the HIRES or HARPS-N data into two epochs (first half vs. second half of the acquired RVs), both spectrometers find significantly different values of K_b and/or K_c in the first versus the second half of their RV data. Using just the first half of the HIRES data, we find $K_{b,1} = 4.07 \pm 0.95 \mathrm{m\,s^{-1}}$, $K_{c,1} < 1.10 \mathrm{m\,s^{-1}}$ (68% confidence). Using just the second half of the HIRES RVs, we get $K_{b,2} = 2.67 \pm 0.88 \mathrm{m\,s^{-1}}$, $K_{c,2} = 1.48 \pm 0.80 \mathrm{m\,s^{-1}}$. For HARPS-N, we divided the RVs into those taken before and after Nov. 12, 2012 (the date of their CCD upgrade, which is a convenient division time). Using just the pre-upgrade HARPS-N data, we find $K_{b,1} = 3.29 \pm 0.62 \mathrm{m\,s^{-1}}$, $K_{c,1} = 2.25 \pm 0.59 \mathrm{m\,s^{-1}}$. Using just the post-upgrade HARPS-N RVs, we get $K_{b,2} = 2.02 \pm 0.37 \mathrm{m\,s^{-1}}$, $K_{c,2} = 3.71 \pm 0.41 \mathrm{m\,s^{-1}}$ (see Figure

[1] https://pypi.python.org/pypi/statsmodels

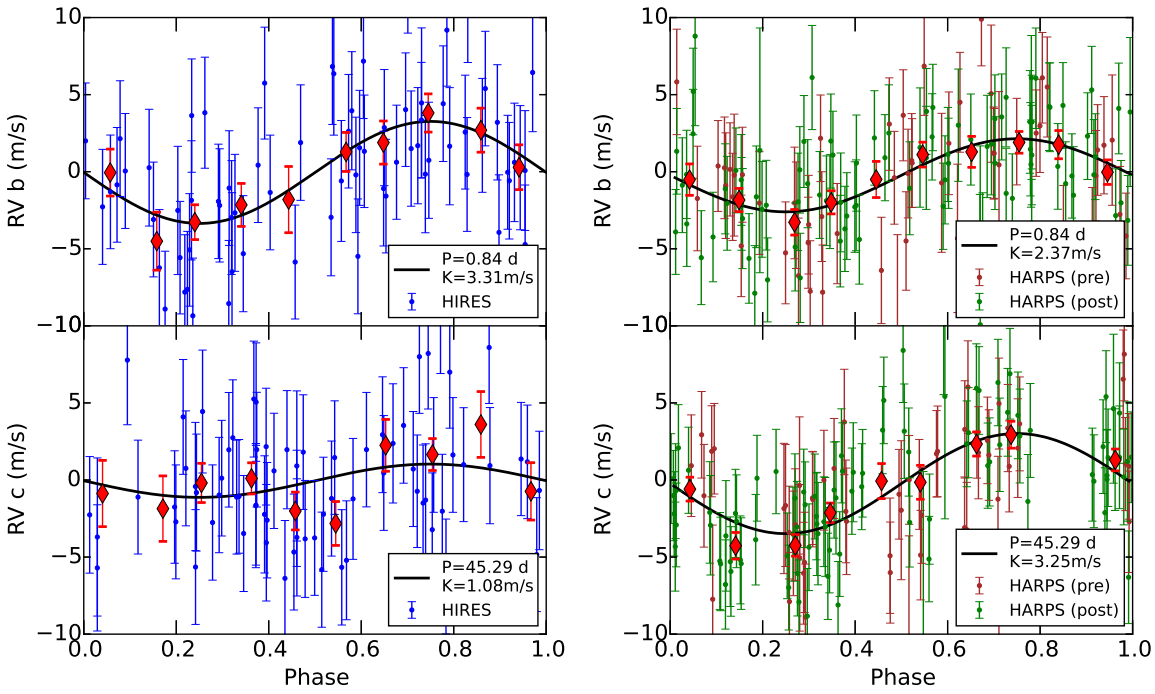

Figure 4.4: Left: the RVs from HIRES phase-folded to the orbital periods of Kepler-10 b (top) and c (bottom). The red diamonds show the weighted mean RV of the HIRES data in bins of 0.1 orbital phase. The black curve shows the best two-planet circular fit: $K_b = 3.31\ \mathrm{m\,s^{-1}}$, $K_c = 1.08\ \mathrm{m\,s^{-1}}$. Right: same as left, but using the pre-CCD upgrade (brown) and post-CCD upgrade (green) HARPS-N RVs. Our best two-planet circular fit yields $K_b = 2.37\ \mathrm{m\,s^{-1}}$, $K_c = 3.25\ \mathrm{m\,s^{-1}}$, in agreement with Dumusque et al. (2014).

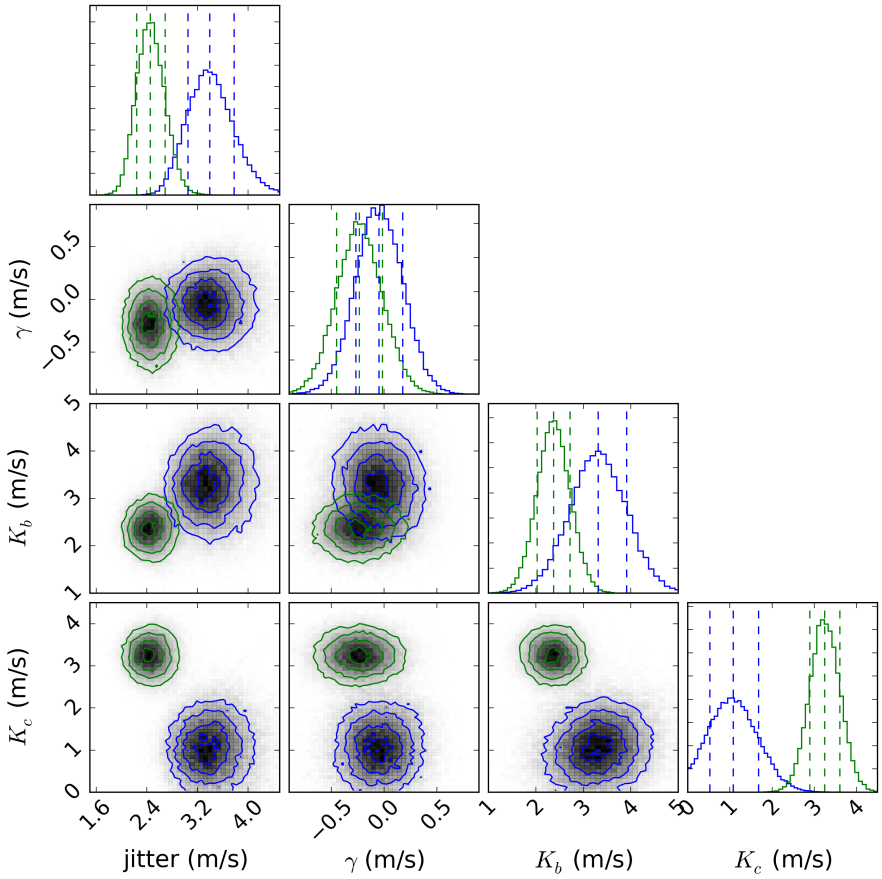

Figure 4.5: The MCMC posterior distributions of two-planet circular fits to the HIRES RVs alone (blue) and the HARPS-N RVs alone (green). The parameters are jitter, the RV zero-point offset γ, and the RV semi-amplitudes from planets b (K_b) and c (K_c). Dashed lines denote the 16^{th}, 50^{th}, and 84^{th} percentiles.

Table 4.2: Two-Planet Circular Fit to Only HIRES RVs

Parameter	Units	Median	$+1\sigma$	-1σ	Ref.
jitter	$\mathrm{m\,s^{-1}}$	3.41	0.39	0.34	A
γ	$\mathrm{m\,s^{-1}}$	-0.05	0.22	0.22	A
K_b	$\mathrm{m\,s^{-1}}$	3.31	0.59	0.59	A
K_c	$\mathrm{m\,s^{-1}}$	1.09	0.61	0.55	A
m_b	$M_\oplus$	4.61	0.83	0.83	A,B
m_c	$M_\oplus$	5.69	3.19	2.9	A,B
r_b	$R_\oplus$	1.47	0.03	0.02	B
r_c	$R_\oplus$	2.35	0.09	0.04	B
ρ_b	$\mathrm{g\,cm^{-3}}$	8.0	1.43	1.44	A,B
ρ_c	$\mathrm{g\,cm^{-3}}$	2.42	1.36	1.24	A,B

Note. — All parameters were explored with uniform priors.

References. — A. This work. B. Dumusque et al. (2014)

4.6. The 1.7σ difference in K_b and 2.0σ difference K_c between the pre- and post-upgrade RVs from HARPS-N is larger than we would expect from statistical fluctuations alone. The apparent change in K_b and K_c suggests that an additional, time-correlated source, possibly from stellar activity or the presence of additional planets, confounds both the HIRES and HARPS-N spectrometers on short timescales.

4.3 K10 Orbital Dynamics: Two-Planet Solutions

The significant discrepancy between the best two-planet fits to the HIRES and HARPS-N data sets motivates a reanalysis of the data. Since we cannot find evidence that either data set is compromised, we choose to combine all the available data from HIRES and HARPS-N to calculate the most up-to-date planet masses. For consistency and relevant comparison to previous findings, we adopt the Kepler-10 stellar properties from D14, which are listed in Table 4.7.

4.3.1 Two-Planet Circular Fit

The RV signals produced by small planets are often too low-amplitude, compared to the typical RV noise, to precisely measure their orbital eccentricities. Thus, the RVs of many

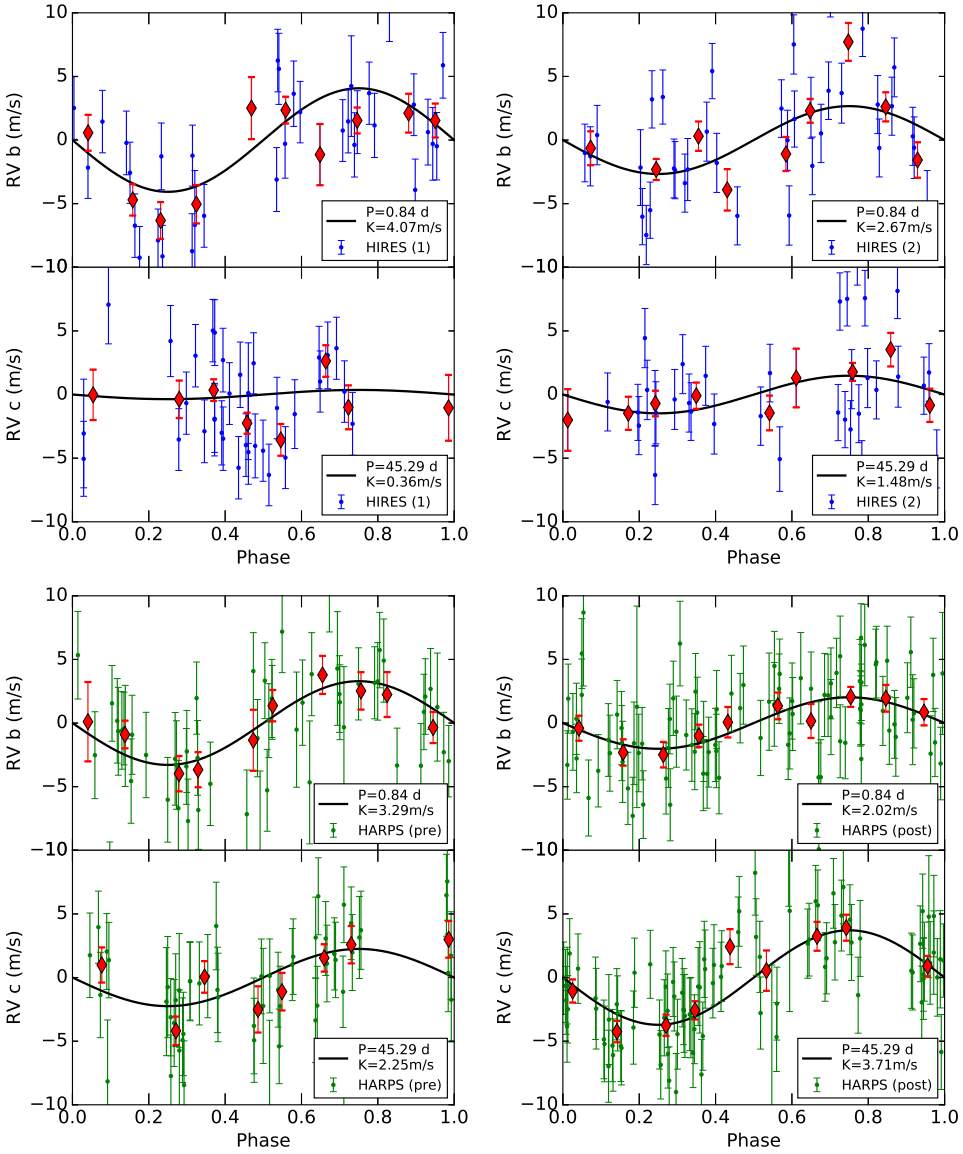

Figure 4.6: The RV curve of Kepler-10 phase-folded to the orbital periods of planets b and c, for four different subsets of the data: the first half of the HIRES data (top left, $K_b = 4.07 \pm 0.95 \mathrm{m\,s^{-1}}$, $K_c = 0.36 \pm 0.7 \mathrm{m\,s^{-1}}$), the second half of the HIRES data (top right, $K_b = 2.67 \pm 0.88 \mathrm{m\,s^{-1}}$, $K_c = 1.48 \pm 0.80 \mathrm{m\,s^{-1}}$), the HARPS-N data from before their CCD upgrade (bottom left, $K_b = 3.29 \pm 0.62 \mathrm{m\,s^{-1}}, \mathrm{K_c} = 2.25 \pm 0.59 \mathrm{m\,s^{-1}}$), and the HARPS-N data from after their CCD upgrade (bottom right, $K_b = 2.02 \pm 0.37 \mathrm{m\,s^{-1}}, \mathrm{K_c} = 3.71 \pm 0.41 \mathrm{m\,s^{-1}}$). The derived values of the RV semi-amplitude, K, for both planets b and c are different by more than $1 \mathrm{m\,s^{-1}} (\sim 30\%)$ from the two halves of the RV data sets from each spectrometer. These inconsistencies within each spectrometer indicate some time-correlated contribution to the RVs, perhaps from stellar activity, additional planets, or systematic RV errors at the level of $\sim 1 \mathrm{m\,s^{-1}}$ in the spectrometers.

of the systems of small planets discovered by *Kepler* and RV surveys (e.g. Eta-Earth) are consistent with planets in circular or nearly circular orbits. We are motivated to explore a two-planet circular orbit because the RVs do not demand eccentric orbits for either Kepler-10 b or Kepler-10 c. Furthermore, B11 and D14 model the Kepler-10 system with circular orbits, so we explore a two-planet circular fit to enable a direct comparison to their results.

The photometrically determined transit times from *Kepler* constrain the orbital ephemerides of Kepler-10 b and c. Specifically, the photometry precisely constrains the time of transit, orbital period, and inclination of each planet. The remaining free dynamical parameter for each planet is the mass. We solve for the mass via the observable semi-amplitude of the RV sinusoid, K.

In addition to the dynamical parameters, fitting RVs from two different spectrographs incurs several nuisance parameters. There is a zero point offset for each set of RVs. Each measured RV has some internal uncertainty, plus error of astrophysical origin (from stellar oscillations, plage, starspots, magnetic activity, etc.), plus additional errors from the spectrometer. For each spectrometer, we report the combined astrophysically-induced error and spectrometer-induced error as a jitter term, $\sigma_{\rm jitter}$, which we add in quadrature with the internal uncertainty in the RV to obtain the total uncertainty of each RV. The internal uncertainty of the RV varies from measurement to measurement, whereas the jitter term is the same for all RVs taken by a single spectrometer.

Therefore, the two-planet circular fit has seven free parameters: the semi-amplitude of the RVs resulting from planet b (K_b), the semi-amplitude of the RVs resulting from planet c (K_c), the velocity zero-point of the RVs (γ), an offset between the RVs taken by the HIRES spectrograph and the RVs taken on the pre-upgrade HARPS-N CCD (offset 1), an offset between the RVs taken by the HIRES spectrograph and the RVs taken on the post-upgrade HARPS-N CCD (offset 2), the jitter of the HIRES spectrograph (j_1) and the the jitter of the HARPS-N spectrograph (j_2). The orbital period, time of transit, and orbital inclination were derived from photometry in D14, and we fix them at the values published therein.

To determine the best circular fit to the data, we adopt the same likelihood function as D14:

$$\mathcal{L} = \prod_i \frac{1}{\sqrt{2\pi(\sigma_i^2 + \sigma_j^2)}} \exp\Big[- \frac{(\mathrm{RV}_i - \mathrm{RV}_{\mathrm{mod},i})^2}{2(\sigma_i^2 + \sigma_j^2)} \Big] \tag{4.1}$$

where RV_i is the $i^{\rm th}$ observed RV, $\mathrm{RV}_{\mathrm{mod},i}$ is the $i^{\rm th}$ modeled RV, σ_i is the uncertainty in the $i^{\rm th}$ observed RV, and σ_j is the jitter term from the instrument on which the observation was made (either HIRES or HARPS). We minimized the negative log-likelihood via the Levenberg-Marquardt method with the Python package lmfit.

We performed a Markov Chain Monte Carlo (MCMC) analysis to understand the full posterior distribution of the dynamical parameters and their covariances. We used the Python package emcee (Foreman-Mackey et al. 2013), an affine-invariant MCMC sampler. We adopted uniform priors in j_1, j_2, γ, offset 1, offset 2, K_b, and K_c, while restricting j_1, $j_2, K_b, K_c > 0$. Our dynamical equations, choice of parameters, and the priors on those parameters were chosen to replicate D14 as closely as possible, while allowing the inclusion

Table 4.3: Two-Planet Circular Fit MCMC Parameters

Parameter	Units	Median	$+1\sigma$	-1σ	Ref.
HIRES jitter	$\mathrm{m\,s^{-1}}$	3.62	0.41	0.37	A
HARPS jitter	$\mathrm{m\,s^{-1}}$	2.49	0.24	0.21	A
γ	$\mathrm{m\,s^{-1}}$	-0.01	0.23	0.23	A
offset 1	$\mathrm{m\,s^{-1}}$	0.44	0.63	0.64	A
offset 2	$\mathrm{m\,s^{-1}}$	-1.21	0.56	0.57	A
K_b	$\mathrm{m\,s^{-1}}$	2.67	0.30	0.30	A
K_c	$\mathrm{m\,s^{-1}}$	2.67	0.34	0.34	A
m_b	$M_\oplus$	3.72	0.42	0.42	A, B
m_c	$M_\oplus$	13.98	1.77	1.80	A, B
r_b	$R_\oplus$	1.47	0.03	0.02	B
r_c	$R_\oplus$	2.35	0.09	0.04	B
ρ_b	$\mathrm{g\,cm^{-3}}$	6.46	0.72	0.74	A,B
ρ_c	$\mathrm{g\,cm^{-3}}$	5.94	0.75	0.77	A,B

Note. — All parameters were explored with uniform priors.

References. — A. This work. B. Dumusque et al. (2014)

of the HIRES RVs.

The posterior of the MCMC sampler is shown in Figure 4.7. The two-planet circular fit using the parameters from the median of the posterior distribution is shown in Figure 4.8. The best two-planet circular fit yields $m_b = 3.72 \pm 0.42\ M_\oplus$, $m_c = 13.98 \pm 1.79\ M_\oplus$, $\rho_b = 6.46 \pm 0.73\ \mathrm{g\,cm^{-3}}$, and $\rho_c = 5.94 \pm 0.76\ \mathrm{g\,cm^{-3}}$. Table 4.3.1 lists the median and 1σ uncertainties of the marginalized parameters and derived planet masses and densities.

We computed the Lomb-Scargle (L-S) periodogram of the combined HIRES and HARPS-N RVs using the fasper algorithm (Press & Rybicki 1989, see Figure 4.9). The most prominent peak was at 0.84 days, the orbital period of planet b. We subtracted the RV component from Kepler-10 b (as determined by our maximum-likelihood model) and computed the periodogram of the residuals, finding a pair of peaks at 44.8 and 51.5 days. The orbital period of planet c is 45.3 days; the peak at 51.5 day is a one-year alias of the orbital period of planet c, intensified by noise in the manner described in Dawson & Fabrycky (2010). We subtracted the model RVs of planet c and computed the periodogram of the residuals, finding a forest of peaks from 13-100 days.

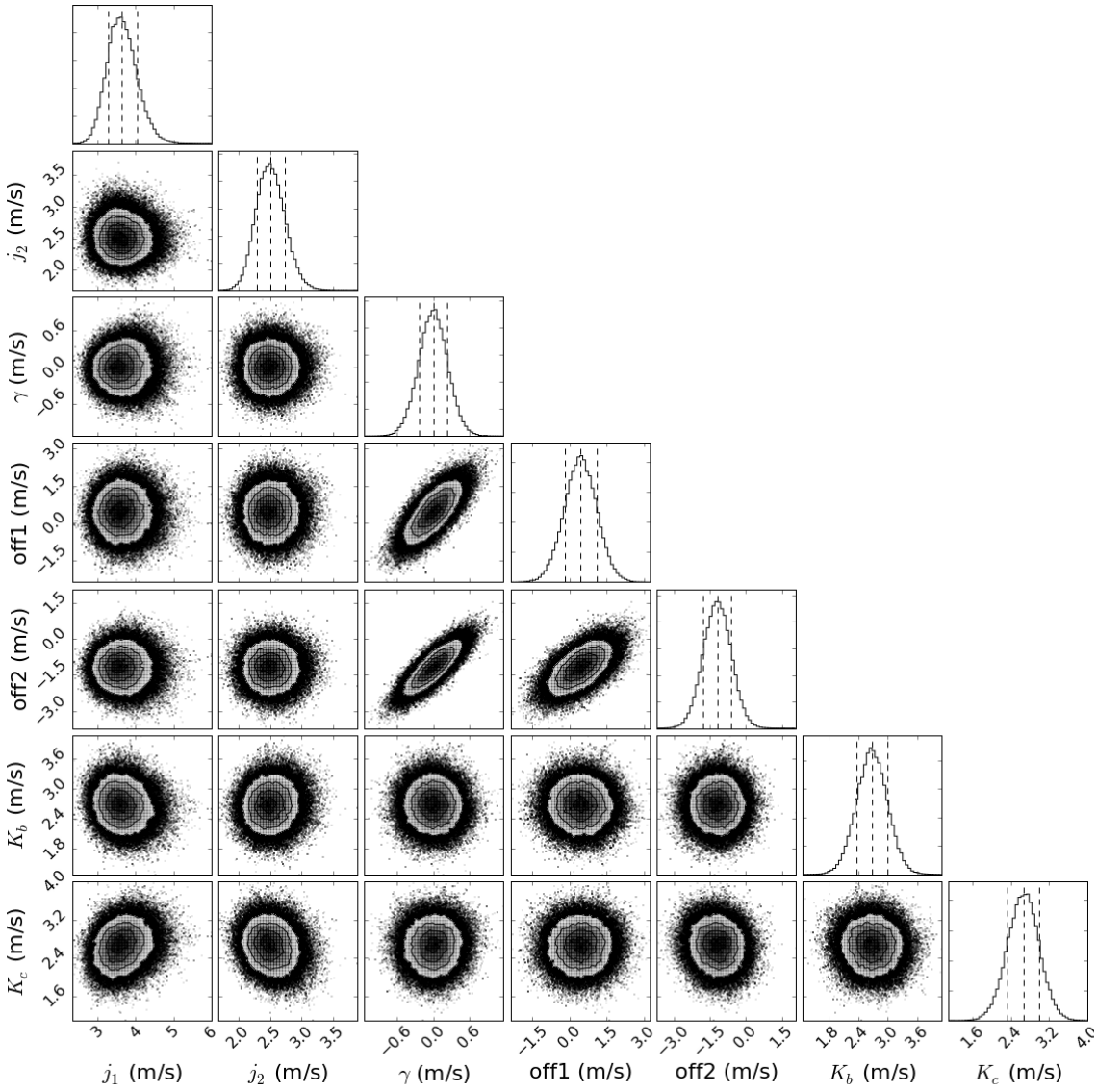

Figure 4.7: Posterior distribution for the two-planet circular fit to Kepler-10 RVs. Variables are the jitter of the HIRES instrument (j_1), jitter of the HARPS-N instrument (j_2), velocity zero point (γ), velocity offset between HIRES and the HARPS-N RVs from before the CCD upgrade (off1), velocity offset between HIRES and the HARPS-N RVs from after the CCD upgrade (off2), and the semi-amplitudes of the RV curve for planets b (K_b) and c (K_c). The dahsed lines indicate the 16^{th}, 50^{th}, and 84^{th} percentiles.

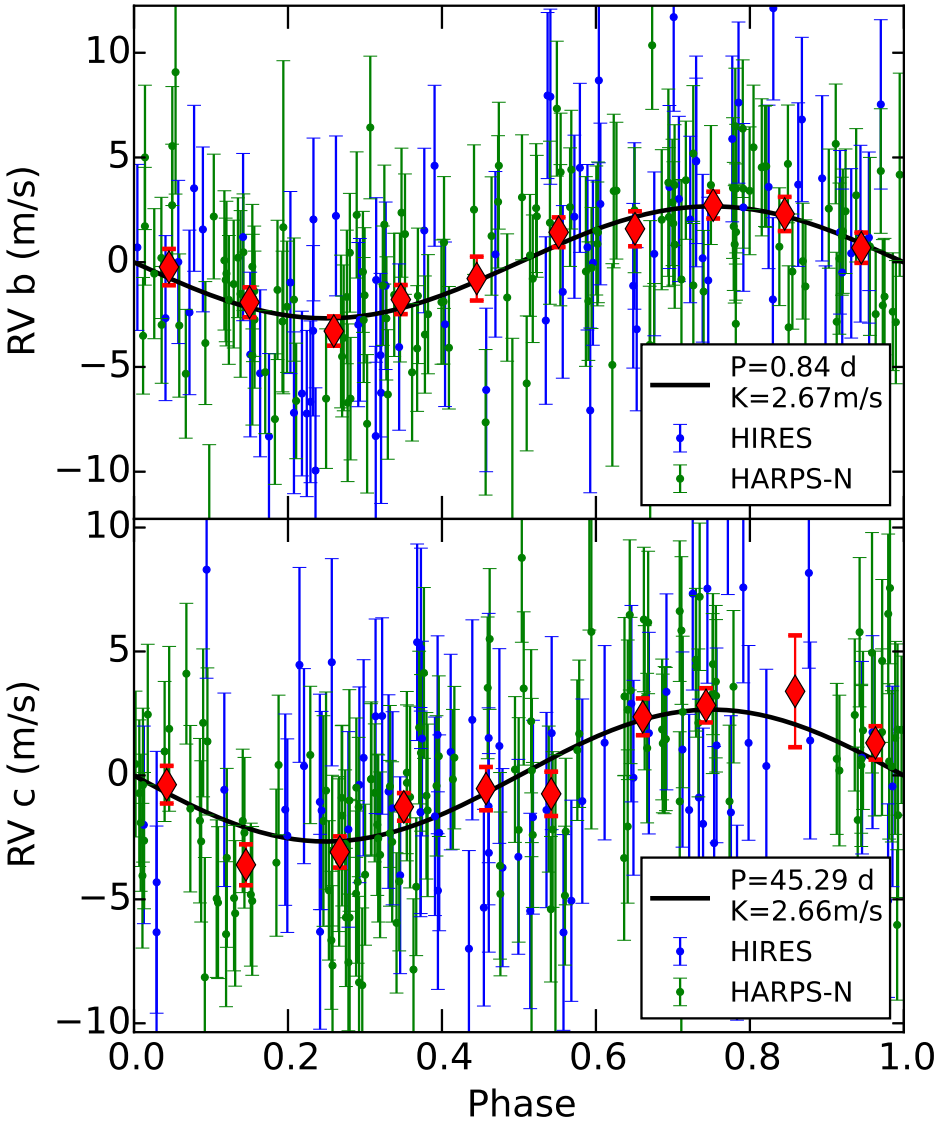

Figure 4.8: The RVs from HIRES (blue) and HARPS-N (green) phase-folded to the periods of Kepler-10 b (top) and c (bottom). The red diamonds show the weighted mean RV of the HIRES and HARPS-N data combined in bins of 0.1 orbital phase. The best two-planet circular fit is shown in black. The orbits of both planets are constrained by the *Kepler*-determined transit times. The best two-planet circular fit yields $m_b = 3.72 \pm 0.42\ M_\oplus$, and $m_c = 13.98 \pm 1.79\ M_\oplus$.

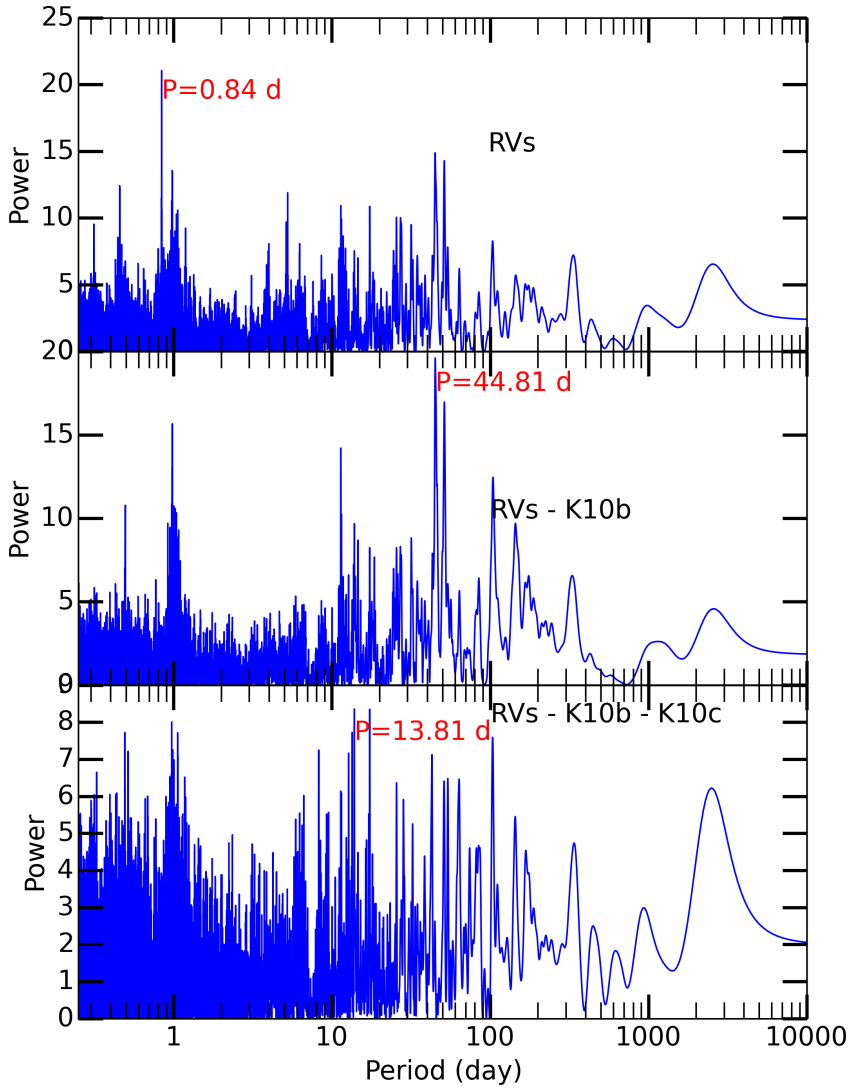

Figure 4.9: Top: L-S periodogram of the combined RVs from HIRES and HARPS-N. Center: L-S periodogram of the RVs after subtracting the model RVs for planet b. Bottom: L-S periodogram of the RVs after subtracting the model RVs for planets b and c.

4.3.2 Two-Planet Fit with Eccentricity for Planet c

Kepler-10 b, which has an ultra-short orbital period of 0.84 days, very likely has a circular orbit because its circularization timescale is much shorter than the stellar age (B11). However, Kepler-10 c has a sufficiently long orbital period (45.3 days) to maintain a moderately eccentric orbit over the system age. Because we cannot rule out a moderately eccentric orbit for Kepler-10 c, we explore possible two-planet fits in which the orbit of planet c (but not planet b) is allowed to be eccentric.

The two-planet fit in which planet c is allowed eccentricity has two free parameters in addition to the free parameters of the circular fit: $\sqrt{e_c}\cos\omega_c$ and $\sqrt{e_c}\sin\omega_c$. These parameters are a combination of the Keplerian orbital parameters e_c (the eccentricity of planet c) and ω_c (the argument of periastron passage of planet c). We adopted a uniform prior on $\sqrt{e_c}\cos\omega_c$ and $\sqrt{e_c}\sin\omega_c$ with the constraint $(\sqrt{e_c}\cos\omega_c)^2 + (\sqrt{e_c}\sin\omega_c)^2 \leq 1$. The time of periastron passage is determined by a combination of the argument of periastron passage (ω_c), the eccentricity (e_c), the time of transit ($T_{t,c}$), and the orbital period (P).

For the parameters j_1, j_2, γ, offset, K_b, and K_c, we adopt uniform priors with the same boundaries as listed for the two-planet circular fit.

We perform an MCMC analysis over j_1, j_2, γ, offset 1, offset 2, K_b, K_c, $\sqrt{e_c}\cos\omega_c$, and $\sqrt{e_c}\sin\omega_c$. The posterior distribution of our sampler is shown in Figure 4.10. The two-planet fit using the parameters from the maximum likelihood of the posterior distribution is shown in Figure 4.11. The best two-planet fit allowing eccentricity for planet c yields $m_b = 3.76 \pm 0.43\ M_\oplus$, $m_c = 14.59 \pm 1.90\ M_\oplus$, $\rho_b = 6.53 \pm 0.75\ \mathrm{g\,cm^{-3}}$, $\rho_c = 6.21 \pm 0.81\ \mathrm{g\,cm^{-3}}$, and $e_c = 0.17 \pm 0.13$. Table 4.4 lists the median and 1σ uncertainties of the marginalized parameters and derived orbital and physical quantities.

4.4 Transit Times of Kepler-10 c

The transit times of Kepler-10 c vary with respect to a linear ephemeris. Kipping et al. (2015) found transit timing variations (TTVs) in the long and short cadence data with 5σ confidence. We independently measure the TTVs and find a solution consistent with the TTVs in Kipping et al. (2015, see Figure 4.12). The TTVs appear to have a sinusoidal period of about 475 days.

4.4.1 Measuring the transit times

From the photometry, we computed the TTVs twice. David Kipping measured the transit times $\mathrm{TT_{Kip}}$, as documented in Kipping et al. (2015), and Eric Agol measured the transit times $\mathrm{TT_{Agol}}$ with the method described here. To include the impact of correlated noise on the transit timing uncertainty measured from the short cadence data, we carried out the following procedure: 1) We did a joint fit to the transits of both planets assuming white noise and polynomial detrending near each transit. Overlapping transits of the two planets were modeled simultaneously. We let the transit times of 10 c vary, but fixed the transit times of

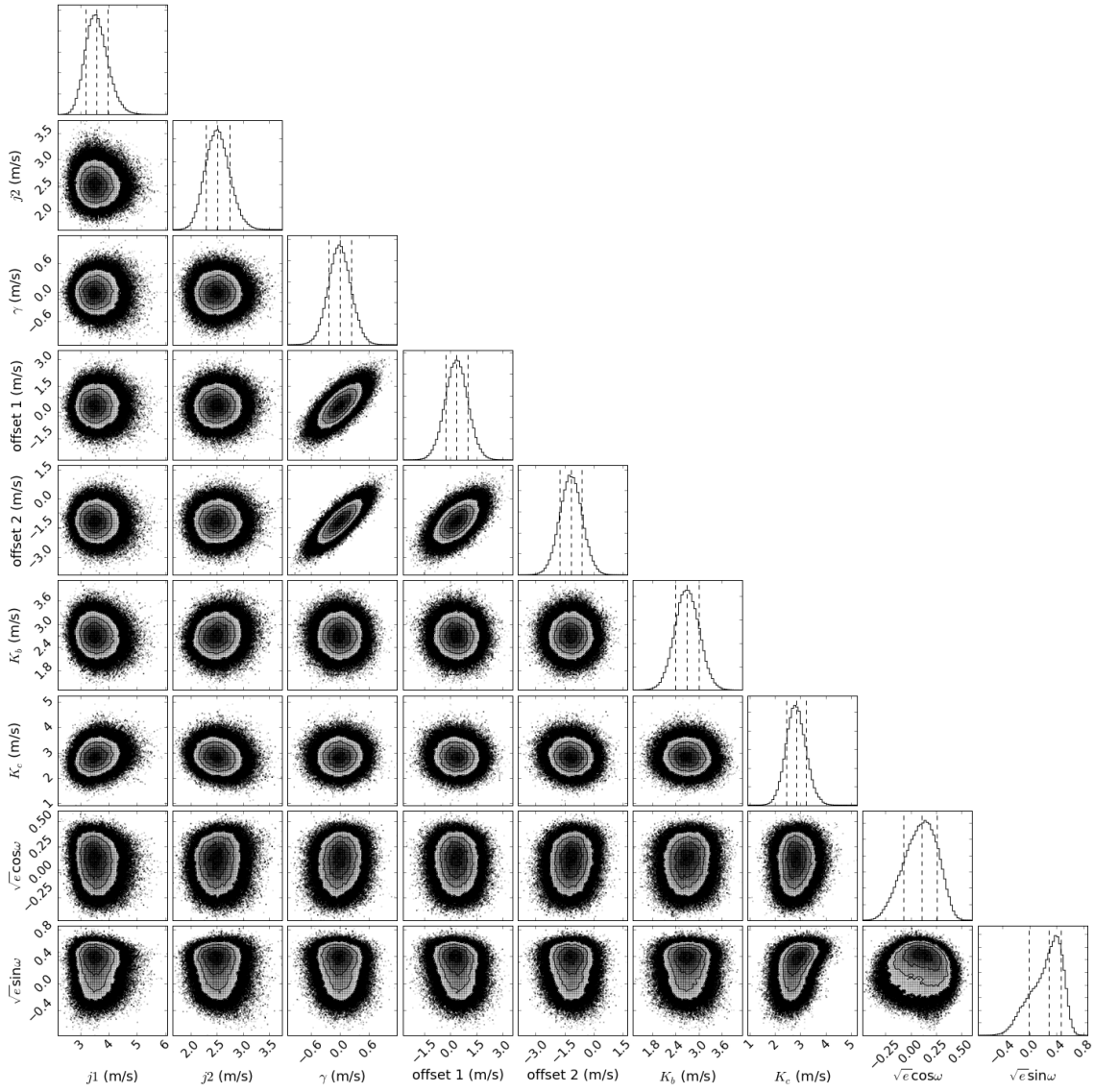

Figure 4.10: Posterior distribution for the two-planet fit to Kepler-10 RVs, allowing eccentricity for planet c. Variables are the jitter of the HIRES instrument (j_1), jitter of the HARPS-N instrument (j_2), velocity zero point (γ), velocity offset between HIRES and pre-upgrade HARPS-N RVs (offset 1), velocity offset between HIRES and post-upgrade HARPS-N RVs (offset 2), the semi-amplitudes of the RV curve for planets b (K_b) and c (K_c), and combinations of the eccentricity and argument of periastron of planet c, $\sqrt{e_c}\cos\omega_c$ and $\sqrt{e_c}\sin\omega_c$. The dahsed lines indicate the 16^{th}, 50^{th}, and 84^{th} percentiles.

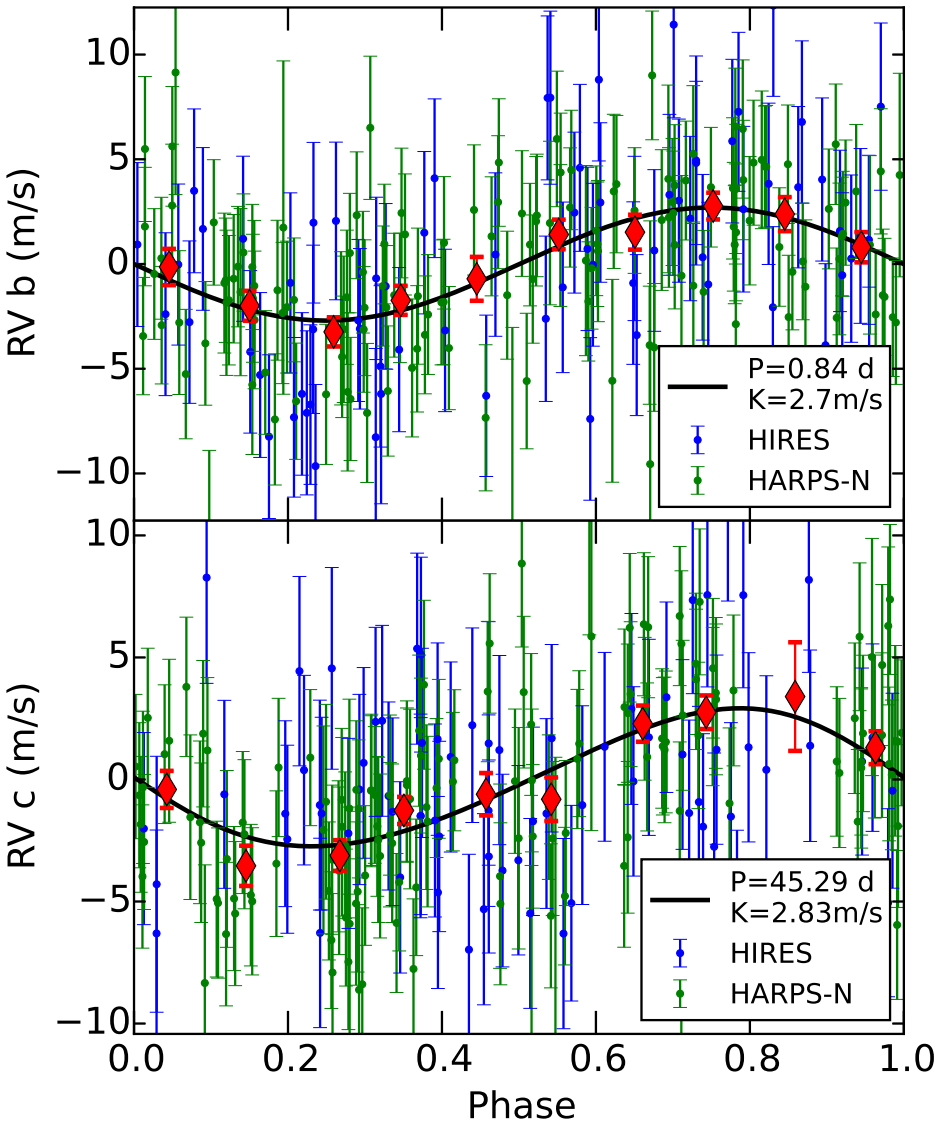

Figure 4.11: The RVs from HIRES (blue) and HARPS-N (green) phase-folded to the periods of Kepler-10 b (top) and c (bottom). The red diamonds show the weighted mean RV of the HIRES and HARPS-N data combined in bins of 0.1 orbital phase. The best two-planet fit in which the orbit of planet c (P = 45.3 d) is allowed to be eccentric is shown in black. The orbits of both planets are constrained by the *Kepler*-determined transit times. The best two-planet fit allowing eccentricity for planet c yields $m_b = 3.76 \pm 0.43\ M_\oplus$, $m_c = 14.59 \pm 1.90\ M_\oplus$, and $e_c = 0.17 \pm 0.13$.

Table 4.4: Two Planet Eccentric MCMC Parameters

Parameter	Units	Median	$+1\sigma$	-1σ	Ref.
HIRES jitter	$\mathrm{m\,s^{-1}}$	3.57	0.41	0.36	A
HARPS jitter	$\mathrm{m\,s^{-1}}$	2.51	0.24	0.22	A
γ	$\mathrm{m\,s^{-1}}$	-0.0	0.23	0.23	A
offset 1	$\mathrm{m\,s^{-1}}$	0.35	0.64	0.64	A
offset 2	$\mathrm{m\,s^{-1}}$	-1.17	0.57	0.57	A
K_b	$\mathrm{m\,s^{-1}}$	2.7	0.31	0.31	A
K_c	$\mathrm{m\,s^{-1}}$	2.83	0.4	0.37	A
$\sqrt{e}\cos\omega$		0.11	0.16	0.18	A
$\sqrt{e}\sin\omega$		0.29	0.18	0.29	A
e_c		0.13	0.12	0.09	A
ω_c	deg.	66.81	31.19	68.51	A
m_b	$M_\oplus$	3.76	0.43	0.42	A,B
m_c	$M_\oplus$	14.59	1.93	1.87	A,B
r_b	$R_\oplus$	1.47	0.03	0.02	B
r_c	$R_\oplus$	2.35	0.09	0.04	B
ρ_b	$\mathrm{g\,cm^{-3}}$	6.53	0.76	0.74	A,B
ρ_c	$\mathrm{g\,cm^{-3}}$	6.21	0.82	0.8	A,B

Note. — The priors on all the parameters were uniform.

References. — A.This work. B.Dumusque et al. (2014)

10 b to a periodic ephemeris. 2) We optimized this fit with a Levenberg-Marquardt model, and then subtracted it from the short cadence data. 3) We computed the autocovariance of the residuals to this initial fit for the short cadence light curve as a function of the number of cadences, $a(n)$, where $a(0)$ is the variance of the data and $a(1)$ is the covariance between residuals separated by one cadence, etc. We concatenated data across gaps when computing the autocovariance as these gaps are a small fraction of the entire dataset. 4) Using the computed autocovariance of the data, we computed the best-fit transit model to Kepler-10 c with the model for Kepler-10 b subtracted. We did not detrend at this stage, but instead used a covariance matrix computed from $a(n)$: $\Sigma_{i,j} = a(|i-j|)$. The likelihood function was $\mathcal{L} \propto \exp\left(-\frac{1}{2}(\mathbf{r}^T\mathbf{\Sigma}^{-1}\mathbf{r})\right)$, where $\mathbf{r}$ is the residual vector for each transit after subtracting off the model component due to Kepler-10 b. We computed the timing uncertainties, $\sigma_{t,i}$, from the covariance of the model parameters at the best-fit value for the ith transit. We then allowed transit time to vary by $\pm 3\sigma_{t,i}$ for each transit, and mapped out the effective chi-square, $\chi^2 = -2\ln\mathcal{L}$, versus timing offset. 5) We found the upper and lower time offsets at which the χ^2 of the fit changed by one, and chose the maximum of these offsets and $\sigma_{t,i}$ to estimate the transit timing uncertainty. The best-fit times of transit and the uncertainty are reported in Table 4.5.

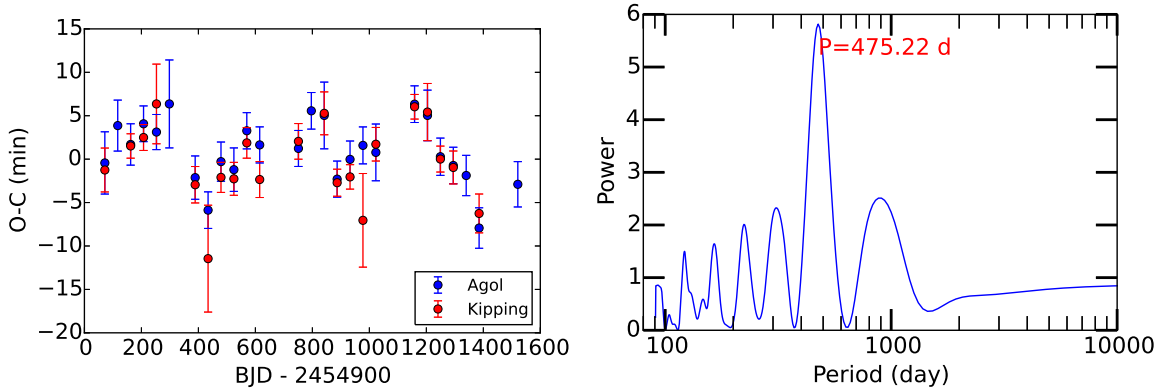

Figure 4.12: Left: the TTVs of Kepler-10 c measured in independent analyses by Eric Agol and David Kipping. The dependent axis (O-C) is the lateness of each observed transit with respect to a linear ephemeris. Right: the periodogram of Eric Agol's TTVs. The peak at 475 days corresponds to the observed sinusoidal period in the TTV time series and is the TTV super-period.

4.5 False Alarm Probability

We used two diagnostics to explore the possibility that the apparent coherent signal of the Kepler-10 c TTVs were due to noise, rather than planetary dynamics. First, we used a bootstrap test, which is a common method in the RV literature to assess whether an

Table 4.5: Transit times of Kepler-10 c

Transit	Time JD-2,455,000	Uncertainty (days)
0	62.2673	0.0017
1	107.5632	0.0014
2	152.8569	0.0014
3	198.1534	0.0436
4	288.7361	0.0014
5	334.0278	0.0015
6	379.3260	0.0016
7	424.6197	0.0016
8	469.9171	0.0014
9	515.2102	0.0014
10	651.0928	0.0014
11	696.3902	0.0015
12	741.6841	0.0015
13	786.9733	0.0014
14	832.2692	0.0015
15	877.5646	0.0015
16	922.8583	0.0015
17	1058.7451	0.0015
18	1104.0385	0.0016
19	1149.3295	0.0015
20	1194.6231	0.0015
21	1239.9166	0.0016
22	1285.2067	0.0016
23	1421.0931	0.0016

Note. — Transit times were measured using short-cadence photometry and a correlated noise analysis.

apparently coherent, sinusoidal signal could be produced by noise. Second, we used a Monte Carlo test. We applied each test to both TT_{Agol} and TT_{Kip}.

4.5.1 Scramble (Bootstrap) Tests

We numbered the observed TTVs (O-C values) from 1-N and produced 10,000 fake data sets of length N. To construct each fake data set, we randomly drew a number j between 1 and N and used the jth observed transit as the first transit in our fake data set. We repeated this procedure (including the possibility of drawing j again) until we had a fake data set of length N. Thus, it would be possible to draw j N times, or to draw each number between 1 and N exactly once, or any other combination from the N^N possibilities.

For each fake data set, we computed the Lomb-Scargle periodogram (Press & Rybicki 1989) of the fake TTVs from the Nyquist period (90.5 days, i.e., twice the orbital period of planet c) to 10,000 days. We found the period with the most power in the periodogram, and recorded this period (the "TTV super period") and its associated power. We then compared the periodogram of the observations to our suite of 10,000 data sets (see Figure 4.13). By counting the number of fake data sets that produce a peak with more power than the observed peak, we can estimate the false alarm probability, i.e., the probability that noise, rather than an astrophysical signal, is responsible for the observed peak. For TT_{Agol}, we get FAP = 3.89%. For TT_{Kip}, we get FAP = 3.71%.

4.5.2 Monte Carlo Tests

We generated 10,000 Monte Carlo fake data sets of transit midpoint times. To construct each fake data set, we drew a fake observation of each transit time from a Normal distribution with a mean of the observed transit time and a variance of the uncertainty in the transit time squared. We computed the false alarm probability in the same manner as for the scramble test, obtaining FAP = 2.6% for TT_{Agol}, and FAP = 1.89% for TT_{Kip} (see Figure 4.13).

The FAP values of 1.9% to 3.9% indicate a 3% probability that the apparent TTV super period is spurious and that the apparent coherence of the TTVs is a chance occurrence due to noise in the TTVs. This result differs from the Bayesian approach in Kipping et al. (2015), which finds the TTVs with 5σ confidence. Possible reasons for the difference between the FAP calculated in this work and the the 5σ confidence found in Kipping et al. (2015) are (1) we look for a sinusoidal signal, whereas Kipping et al. (2015) look for any type of variation from a flat line, and (2) we ignore the error bars (since the errors in TT_{Agol} are of nearly equal values), whereas Kipping et al. (2015) interpret the errors, allowing a few outliers with large errors to be down-weighted.

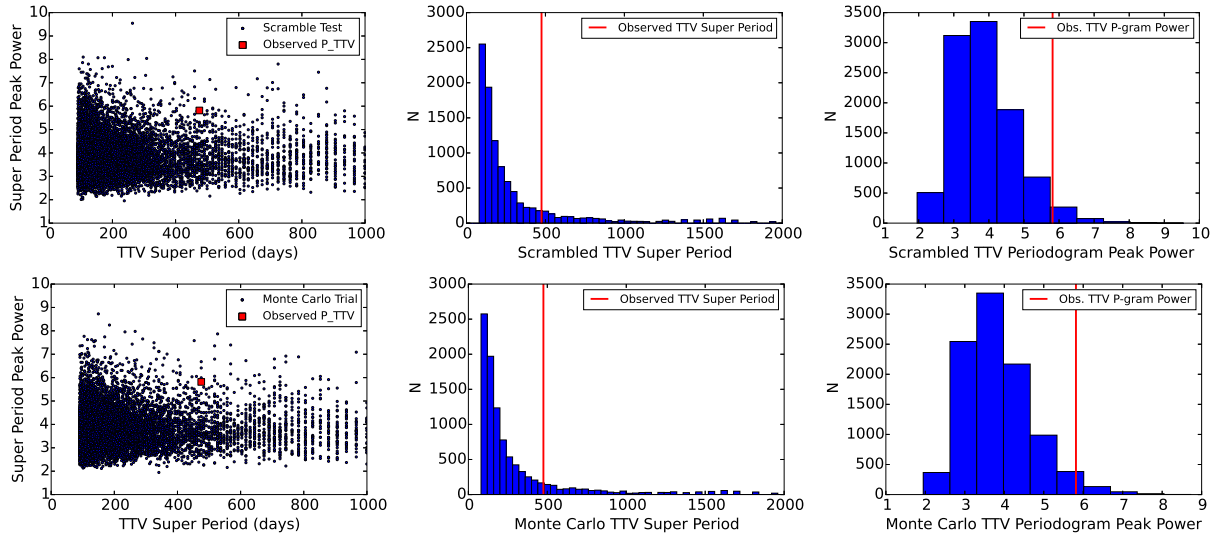

Figure 4.13: False alarm probability tests for the Kepler-10 TTVs. Top left: Peak periodogram power as a function of TTV super-period for 10,000 scramble tests (black), as compared to the observed peak periodogram power and super-period. Top center: Histogram of the super-periods generated from 10,000 scramble tests, compared to the observed TTV super-period. Top right: Histogram of the peak periodogram powers generated from 10,000 scramble tests, compared to the observed peak periodogram power of the TTVs. Bottom row: same as top, but for 10,000 monte carlo tests.

4.6 K10 Orbital Dynamics: Three-Planet Solutions

4.6.1 Analytical Motivation

If the observed coherent TTVs are due to the dynamical interactions of planets in the system, they indicate the presence of a third planet (KOI-72.X). Known planets (b and c) cannot cause the TTVs because planet c cannot be its own perturber, and planet b is too far away in period space ($P_c/P_b = 54$) to perturb planet c at the amplitude observed. Therefore, the best dynamical explanation of the TTVs is the existence of a third planet. The periodogram of the residual RVs after the RVs due to planets b and c are subtracted does not present a strong peak (see Figure 4.9). Therefore we cannot unambiguously identify the orbital period KOI-72.X from the RVs alone.

We use analytic theory to predict the most likely orbital periods of a third planet. Equation 5 from Lithwick et al. (2012), also called the TTV equation, relates the super-period of the TTVs to the orbital periods of the two planets:

$$\frac{1}{P_{\rm TTV}} = \left|\frac{j}{P} - \frac{j-1}{P'}\right| \tag{4.2}$$

where $\rm P_{TTV}$ is the super-period measured from the TTV sinusoid, P is the inner period, P' is the outer period, and the planets are near the $j : j-1$ resonance. Because the perturber can exist just inside or just outside the $j : j-1$ mean motion resonance, and because the perturber can be interior or exterior, there are 4 solutions for each $j : j-1$. Using Equation 4.2, we can predict a series of likely orbital periods for the perturber, planet candidate KOI-72.X, which are enumerated in Table 4.6.

4.6.2 Dynamical Solutions

For each candidate orbital period for KOI-72.X listed in Table 4.6, we perform a series of numerical N-body integrations using TTVFast (Deck et al. 2014). We use the analytically predicted orbital parameters as inputs to the integrator at epoch $T0(BJD - 2454900) = 53.67844$. TTVFast predicts the times of transit of each planet in the N-body simulation, and the RVs of the star at the times of RV observation. To determine the orbital parameters that best reproduce the observed transit times and RVs, we minimize the following statistic:

$$\chi^2 = \sum_k \frac{(\mathrm{TT}_{c,k} - \mathrm{TT}_{c,\mathrm{mod},k})^2}{\sigma^2_{\mathrm{TT},c,k}} + \sum_i \frac{(\mathrm{RV}_i - \mathrm{RV}_{\mathrm{mod},i})^2}{\sigma^2_{\mathrm{RV},i}} \tag{4.3}$$

where the residuals between the observed and modeled transit times and RVs are simultaneously minimized. We fit the TTVs of only planet c, since planet b does not have significant, coherent TTVs. We use a combination of a Nelder-Mead and Levenberg-Marquardt (LM) minimization algorithm to find the orbital parameters and masses for planets c and d that produce a local minimum near the input orbital period. We allow the period (P), eccentricity (e), argument of periastron passage (ω), mean anomaly (M), and mass (m) of planets c

Table 4.6: Tests of Possible Orbits of KOI-72.X.

Analytic $j:j-1$	P_X (predicted, days)	Numerical – Parameters at epoch $T_0 = 53.67844$ (BJD-2454900) P_c (days)	P_X (days)	m_c ($M_\oplus$)	m_X ($M_\oplus$)	ecc$_c$	ω_c (deg.)	ecc$_X$	ω_X (deg.)	M$_c$ (deg.)	M$_X$ (deg.)	$\chi^2_{\rm TT,c}$	$\chi^2_{\rm RV}$	χ^2	ΔBIC[a]
2:1	100	45.295	101.36	13.94	6.84	0.09	79.7	0.19	96.5	225.5	222.9	19	198	217	0.0
2:1	82.7	45.295	80.118	14.13	0.06	0.02	79.3	0.23	89.9	227.1	205.4	46	214	260	43.0
2:1	23.8	45.295	23.761	15.37	0.86	0.28	89.1	0.24	50.8	217.4	8.6	18	212	230	13.0
2:1	21.6	45.296	21.619	14.74	0.54	0.11	89.0	0.26	107.9	217.7	360.0	28	212	240	23.0
3:2	71.3	445.295	71.323	14.15	1.06	0.01	87.4	0.08	182.6	219.5	216.2	17	216	233	16.0
3:2	64.9	45.294	63.56	14.29	0.93	0.06	90.0	0.02	41.0	216.9	116.0	27	213	240	23.0
3:2	31.2	45.296	31.183	14.68	1.38	0.01	89.6	0.02	48.9	217.3	9.7	26	214	240	23.0
3:2	29.7	45.3	28.777	15.83	3.3	0.19	92.5	0.22	89.6	215.3	270.6	42	204	246	29.0
ctrl. 1[b]	90.5	45.296	90.433	13.81	3.21	0.0	79.6	0.07	230.1	227.3	90.2	47	222	269	52.0
ctrl. 2[c]	x	45.295	x	13.98	x	0.00	60.9	x	x	245.9	x	52	215	267	22.5

Note. — [a] The difference in the Bayesian Information Criterion (BIC) with respect to the best solution explored (at P=100 days). According to Kass & Raftery (1995), the favorability for the model with the lower BIC value is "very strong" when $\Delta BIC > 10$, "strong" when $6 < \Delta BIC < 10$, "positive" when $2 < \Delta BIC < 6$, and "not worth more than a bare mention" when $0 < \Delta BIC < 2$.

Note. — [b] KOI-72.X was placed exactly on the 2:1 exterior resonance, halfway between the 82 day and 101 day analytic solutions.

Note. — [c] A two-planet dynamic solution with only Kepler-10 b and c (i.e. no KOI-72.X).

and d to vary. We fix the inclination $i = 90°$ and longitude of ascending node $\Omega = 0°$ for all planets, for simplicity. The orbital parameters and mass of planet b are fixed, since planet b is not interacting with planet c or d. The outcome of the LM minimization for each input orbital period of KOI-72.X in listed in the right half of each row of Table 4.6. Figure 4.14 shows the numerical solutions in which KOI-72.X is near the 2:1 mean motion resonance. For each solution, the predicted TTVs are overlaid on the observed TTVs in the left panel, and the RVs are phase-folded to the orbits of each of the planets in the right panel. Figure 4.15 is the same, but for solutions in which KOI-72.X is near the 3:2 mean motion resonance.

Considering that there are 246 data points (26 transit times plus 220 RVs), the reduced χ^2 statistic is comparatively good for most of the orbital periods for KOI-72.X suggested by the TTV equation (top half of Table 4.6); however, we achieve $\chi^2_\nu \approx 1$ by construction based on how we treat the jitter in Equation 4.1. To convey how much some solutions are favored over others, we consider the change in the Bayesian Information Criterion (ΔBIC) as a way to rank the possible solutions in order of preference. The BIC is defined as:

$$BIC = \chi^2 + k \ln(n) \tag{4.4}$$

where k is the number of free parameters in the model and n is the number of observations (Schwarz 1978). The best solution for P_X is at 101 days ($\chi^2 = 217$). The ΔBIC between the best and second-best model is 13, meaning that our best solution ($P_X = 101$ days) is "very strongly favored" over all the other solutions (Kass & Raftery 1995). However, based on their low values of reduced $\chi^2 \approx 1$, the other solutions describe the data well enough that we cannot rule them out. Furthermore, the solutions listed above do not fully explore the high-dimensional parameter space. At each orbital period, multiple initial locations of KOI-72.X (as defined by ω_X, M_X, and e_X) are possible, and produce comparatively good χ^2 statistics to the values listed in Table 4.6. While the orbital solutions listed represent solutions that produce the lowest values of χ^2 found in our Nelder-Mead algorithm, the parameters ω_X, M_X, and e_X are poorly constrained by the TTVs and RVs, even when a particular orbital period for KOI-72.X is chosen. To fully explore the dynamical parameter space for the putative KOI-72.X would be very computationally intensive and is outside the scope of this paper.

Orbital periods for KOI-72.X that are not near solutions to the TTV equation produce significantly higher χ^2 values than orbital periods that solve the TTV equation. In the bottom half of Table 4.6, the "ctrl. 1" solution, we seed the orbital period for KOI-72.X with a value halfway between two solutions to the TTV equation ($P_X = 90.5$ days). Even after using the Nelder-Mead minimizer to find the best orbital parameters for planets c and d with this initial guess, the lowest value of χ^2 attained is 269, which is significantly worse (according to the BIC) than any of the analytically predicted solutions, with ΔBIC = 52 (i.e. very strongly disfavored) with respect to the best three-planet solution. Thus, we numerically demonstrate that the TTV equation accurately predicts orbital periods for KOI-72.X that best reproduce the observed TTVs.

In the last row of Table 4.6 ("ctrl. 2"), we perform an N-body integration in which we simulate only planet b (which still has fixed orbital properties and a fixed mass) and planet

c (for which the orbital parameters and mass are allowed to vary). The χ^2 statistic for this control test is 267 (ΔBIC = 22.5), demonstrating that the best three-planet solution is strongly favored over the two-planet solution. In particular, the solutions for KOI-72.X at P=101, 24, and 71 days achieve significantly lower BIC values than the two-planet model, suggesting that these orbital periods are strongly favored over a two-planet model.

The transit duration variations (TDVs) of Kepler-10 c are negligible. The various coplanar solutions for KOI-72.X that we examine all produce negligible TDVs as well, and so TDVs do not help break the degeneracy of the orbit for KOI-72.X in this particular system. The absence of TDVs implies that KOI-72.X is not highly inclined with respect to planets b and c.

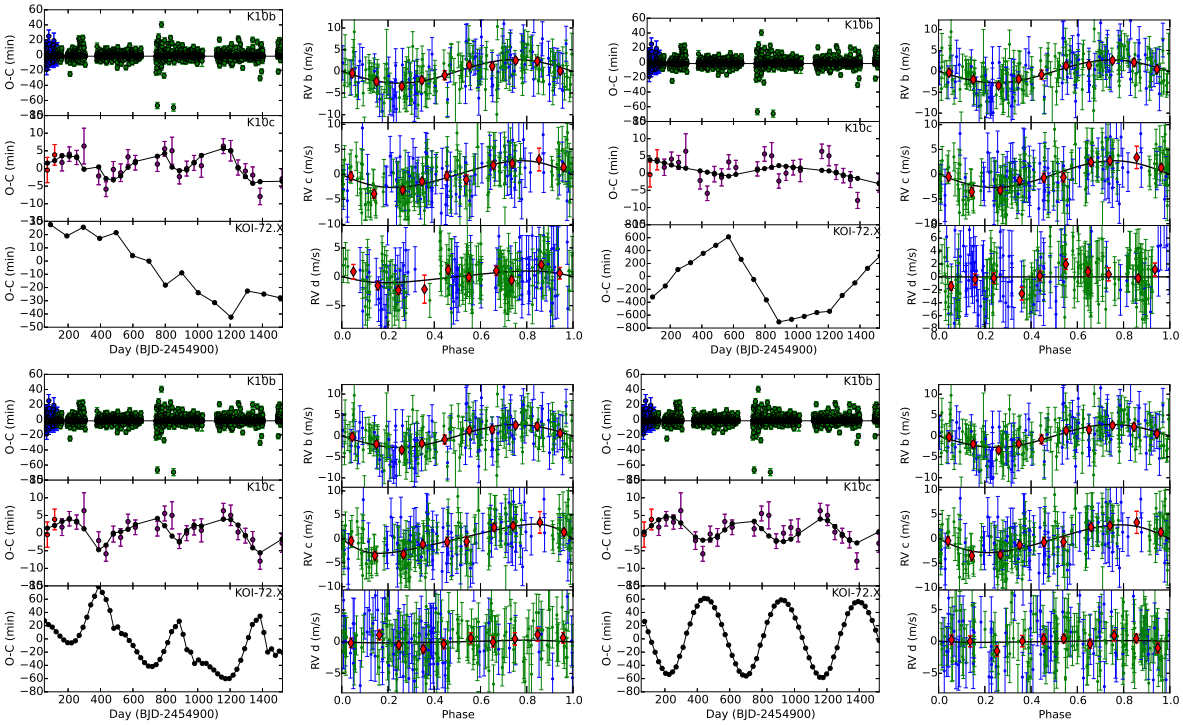

Figure 4.14: Solutions for KOI-72.X near the 2:1 mean motion resonance. Top left: O-C diagram for the solution with P_X =101 days, showing the transit times of planets b, c, and X in the three vertical sub-panels. The colored points are the data; the black dotted line is the model. Top, second from left: RVs of Kepler-10 decomposed into the orbits of planets b, c, and d (top to bottom), where P_X =101 days. The blue points are from HIRES; the green are from HARPS-N, the red diamonds are the weighted mean RV in bins of 0.1 phase, and the black line is the model. Top, second from right, and top right: the same as the top left two panels, but for P=82 days. Bottom left and second from the left: The same as top left two panels, but for P=23 days. Bottom second from right, and right: The same as top left two panels, but for P=21 days.

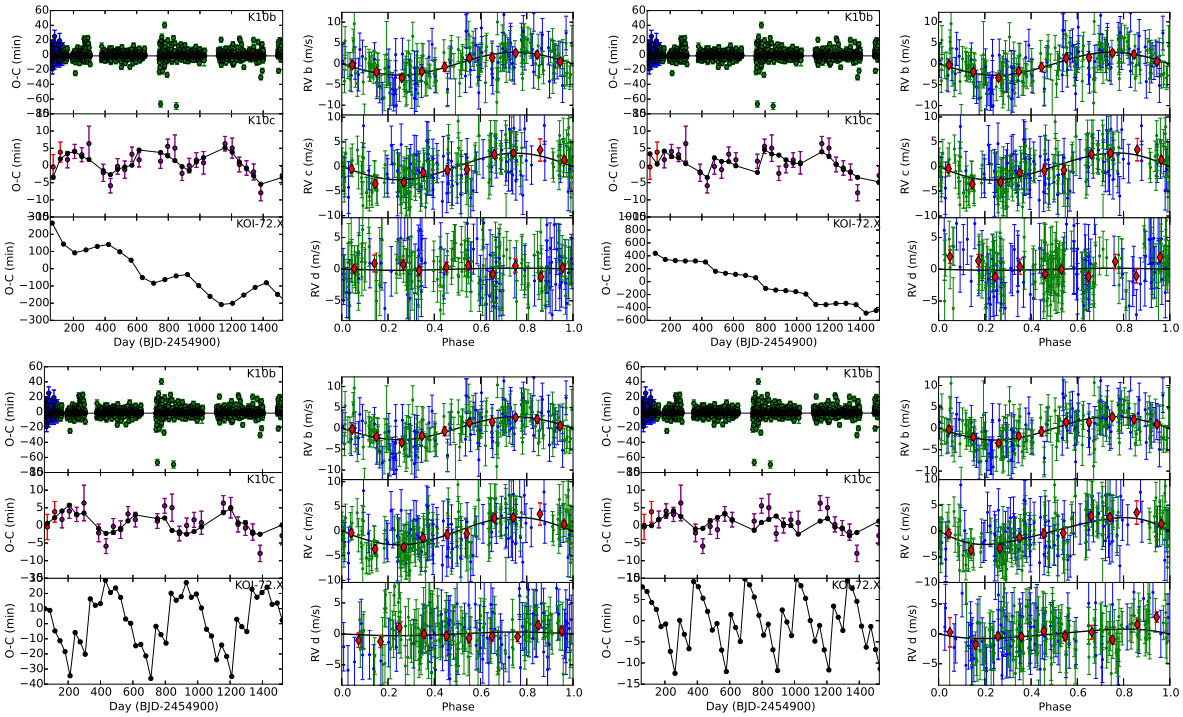

Figure 4.15: Solutions for KOI-72.X near the 3:2 mean motion resonance. The same as Figure 4.14 but with with top left two panels: P_X =71 days; top right two panels: P_X =64 days; bottom left two panels: P_X =31 days; bottom right two panels: P_X =28 days.

The various dynamical solutions for KOI-72.X yield m_X between 1-7$M_\oplus$. Without being able to choose the correct dynamical solution, we cannot pinpoint the mass of non-transiting planet candidate. However, the masses that best fit the TTVs and RVs are consistent with the population of low-mass, small planets discovered by *Kepler* and η-Earth surveys.

The family of solutions for KOI-72.X all yield similar masses for planet c (13.5-15 $M_\oplus$). This is likely because (1) the mass of KOI-72.X is small, meaning that it contributes little to the RVs, (2) planet c cannot create its own TTVs, and so the presence of TTVs should not be correlated with planet mass. For Kepler-10 c, modeling the TTVs with an N-body integrator does not result in an erroneously low planet mass.

4.7 Interior Structure and Composition of K-10 b and c

In this section, we estimate compositions of the planets Kepler-10 b and Kepler-10 c assuming the mass estimates from our formal fits using all available data. However, given the issues discussed in Section 4.2.3, actual uncertainties are larger than we assume for this analysis.

Kepler-10 c falls near the high density extreme among the locus of sub-Neptune-sized planet mass-radius measurements characterized to date. As such, Kepler-10 c presents a valuable test case for planet formation theories and interior structure models. Comparing measured masses and radii to theoretical mass radius relations, which incorporate the behavior of materials at high pressure, reveals insights into the planets' possible bulk compositions. We employ planet interior structure models from Rogers & Seager (2010a,b); Rogers et al. (2011) to provide a mapping from planet mass and composition to radius, and apply the Bayesian approach described in Rogers & Seager (2010a) (and applied in Schmitt et al. 2014) to invert planet composition constraints from the radial velocity and transit observations.

The first point to note about Kepler-10 c's bulk composition is that its transit radius is likely not defined by a "rocky" or "solid" surface. In the vast majority (98.4%) of dynamical solutions to the combined *Kepler* photometry, HIRES spectroscopy, and HARPS-N spectroscopy dataset, Kepler-10 c has a sufficiently low mean density (less dense than a pure magnesium silicate sphere) that the planet must have a substantial complement of volatiles (astrophysical ices and/or H/He) that contribute to the observed transit depth. Only 1.6% of the the Kepler-10 c mass-radius posterior probability corresponds to scenarios in which the planet is sufficiently dense to have a stony-iron composition (comprised of an admixture iron and silicates alone). Since Kepler-10 c's measured density necessitates that the planet contains a volatile complement that contributes to the transit depth, the planetary composition is inconsistent with a "solid" or "rocky" makeup.

The nature of Kepler-10 c's volatiles is ambiguous; the planet could have a H/He envelope contributing less than a fraction of a percent by mass to the planet, or a water envelope contributing a few tens of percent of the planet mass. The measured mass and radius of Kepler-10 c are consistent with a "water-world" composition; less than 0.95% of the Kepler-10 c mass-radius posterior PDF spills into a low density regime wherein an H/He envelope

is required (corresponding to planet configurations that are less dense than even a 100% pure water sphere with $T_{\rm eq} = 550$ K). Assuming a 2-component planet interior structure model, where in the planet consists of an Earth-like stony-iron core (modeled as a 30:70 mix or iron and magnesium silicates) surrounded by a pure water envelope, the water mass fraction is constrained in this scenario to be $M_{\rm env,H_2O}/M_p = 0.280^{+0.119}_{-0.102}$ (where the median, and range between the 16th and 84th percentiles are quoted) (Figure 4.17). At the other extreme, the measured mass and radius of Kepler-10 c are also consistent with a dry (waterless) mixture of stony-iron material and H/He. Coupling the planet mass-radius posterior distribution to a 2-component planet interior structure model wherein the planet consists of a Earth-like stony-iron core surrounded by a 30 times enhanced metalicity solar composition envelope, the H/He envelope mass fraction is constrained to be $M_{\rm env,H/He}/M_p = 0.0023^{+0.0017}_{-0.0012}$ (Figure 4.18). Whether the planet's volatile envelope is dominated by H/He or water, the radial extent of the envelope, $\Delta R_{\rm env}$, accounts for more than one tenth of the planet radius; in the end member scenarios described above, $\Delta R_{\rm env,H_2O}/R_p = 0.285^{+0.077}_{-0.073}$ and $\Delta R_{\rm env,HHe}/R_p = 0.162^{+0.038}_{-0.037}$ (lower panels of Figure 4.17 and 4.18).

In contrast to Kepler-10 c, the measured mass and radius of the smaller inner planet, Kepler-10 b, is consistent with a rocky composition. Only 13.6% of the posterior probability of Kepler-10 b spills into a low-density regime of mass-radius parameter space where volatiles are demanded. Under the assumption of a 2-layer rocky planet model consisting of an iron core and a silicate mantle (having molar magnesium fraction Mg# = 90%), the iron core mass fraction of Kepler-10 b is constrained, $M_{\rm Fe,core}/M_p = 0.169^{+0.115}_{-0.117}$ (Figure 4.19). The measured mass and radius of Kepler-10 b is consistent with an Earth-like bulk composition (32.5% iron core by mass), while an iron-enhanced Mercury composition (70% iron core by mass) is strongly disfavored.

All the composition constraints described above are based upon the combined analysis of the Keck HIRES and HARPS-N radial velocity measurements. The qualitative constraints on Kepler-10 b and c's bulk compositions are largely unchanged when only the Keck HIRES radial velocities are used to derive the planet mass. Omission of the HARPS-N dataset from the analysis leads to a downward shift in the density of Kepler-10 c, an upward shift in the density of Kepler-10 b, and an overall broadening of all the posterior PDFs. The downward shift in the density of Kepler-10 c further strengthens the conclusion that Kepler-10 c has a volatile envelope. Conditioned on the HIRES data alone, there is only a 0.4% posterior probability that Kepler-10 c is more dense than a pure silicate sphere (compared to 4.1% conditioned on both HARPS-N and HIRES). Further, the posterior probability that Kepler-10 c is sufficiently dense to have water envelope (instead of H/He) also decreases to 62% (compared to 99% conditioned on both HARPS-N and HIRES). On the other hand, the shift in Kepler-10 b posterior distribution toward higher masses and densities leads to increased posterior probability at higher Kepler-10 b iron core mass fractions $M_{\rm Fe,core}/M_p = 0.44^{+0.15}_{-0.19}$ (compared to 0.17 ± 0.12 based on both HARPS-N and HIRES).

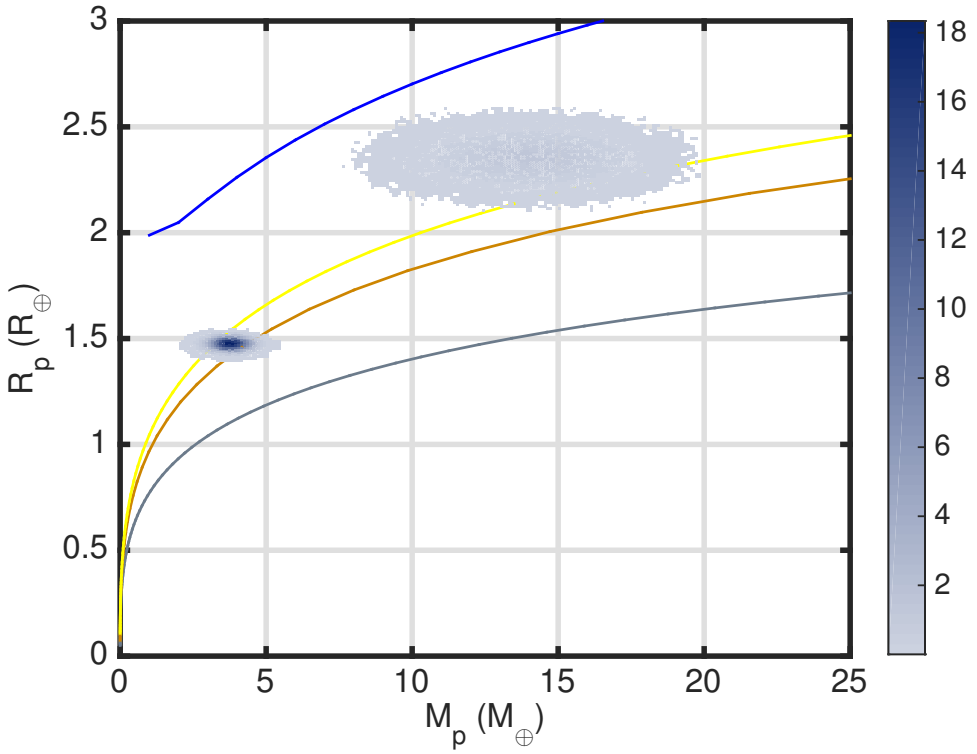

Figure 4.16: Mass-radius posterior distribution for Kepler-10 b and Kepler-10 c, compared to theoretical mass-radius relations. The color bar indicates the mass-radius posterior probability density conditioned on the combined HIRES and HARPS dataset. The solid curves represent theoretical mass-radius relations for notable compositions: pure Fe (grey), Earth-like stony-iron (brown), pure silicate (yellow), pure water (blue). The water planet mass-radius relation includes thermal effects and the presence of a super-critical steam envelope.

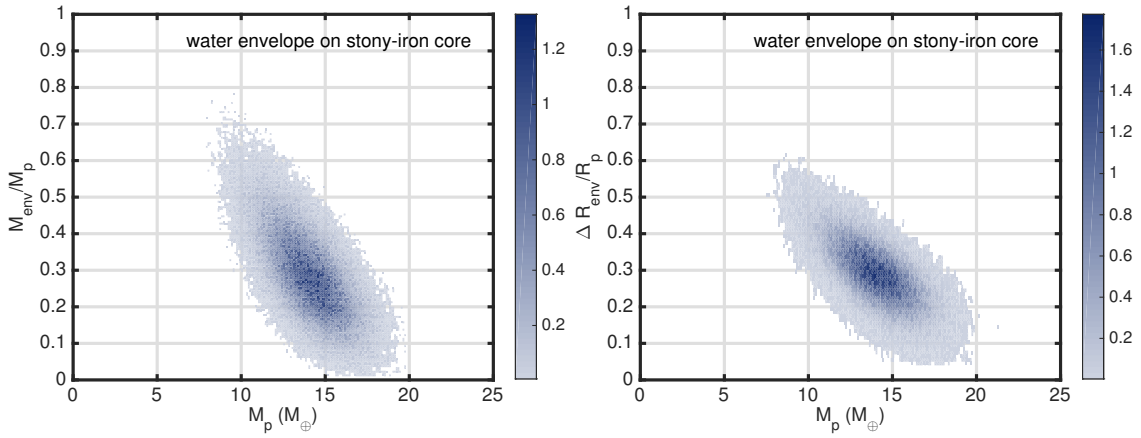

Figure 4.17: Posterior probability density distribution for Kepler-10 c, as a function of planet mass, M_p and the water envelope mass fraction $M_{\mathrm{env,H_2O}}/M_p$ (upper panel), and radius fraction $R_{\mathrm{env,H_2O}}/R_p$ (lower panel). Darker shades of blue represent higher probability. The posterior pdf obtained from the combined analysis of the Keck HIRES and HARPS-N radial velocity measurements is compared to planet interior structure models in which the planet is assumed to consist of an Earth-like stony-iron core (modeled as a 30:70 mix or iron and magnesium silicates) surrounded by a pure water envelope.

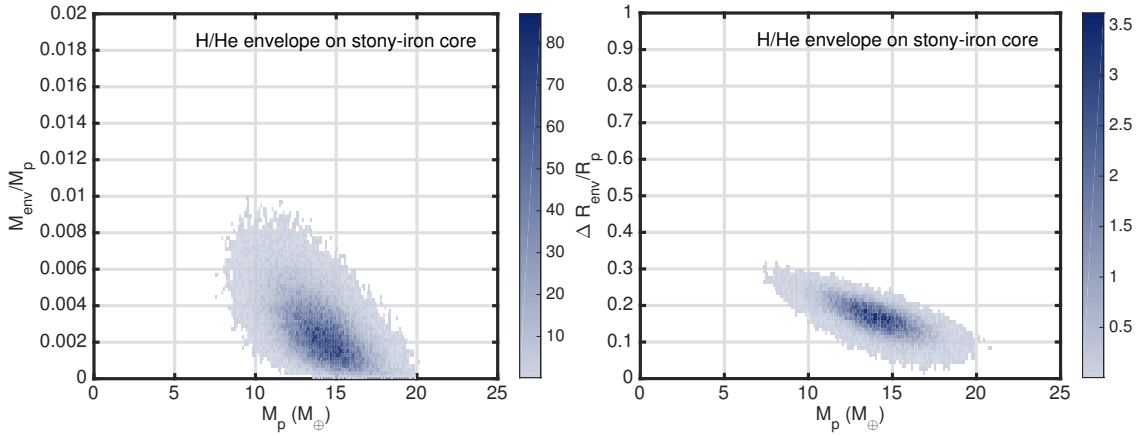

Figure 4.18: Posterior probability density distribution for Kepler-10 c, as a function of planet mass, M_p and the H/He envelope mass fraction $M_{\mathrm{env,HHe}}/M_p$ (upper panel), and radius fraction $R_{\mathrm{env,HHe}}/R_p$ (lower panel). This figure is analogous to Figure 4.17 except a H/He-dominated 30 times enhanced solar metalicity composition is assumed for the planet envelope instead of a pure water composition.

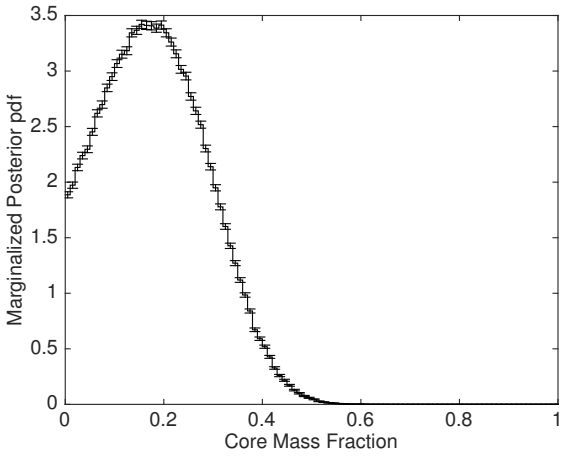

Figure 4.19: Posterior probability distribution on the iron core mass fraction of Kepler-10 b. A 2-layer fully differentiated interior structure model wherein the planet consists of an iron core surrounded by a silicate mantle (Mg# = 90%) is assumed.

4.8 Discussion

4.8.1 Insights on successful observing strategies for Kepler follow-up

The source of the discrepancy between the HIRES and HARPS-N RVs is unknown. However, the apparent time-variability of K_b and K_c on both instruments suggests that a time-correlated noise (or astrophysical signal) confounds both data sets on timescales of a summer observing season. This time-correlated property could be from stellar rotation and the stellar magnetic cycle or from an additional planet in the system. The most effective way to combat this time-correlated noise is to increase the quantity and baseline of observations of this star. This strategy of employing a long observing baseline compared to time-correlated noise influences should be employed on other stars with low-mass planets to avoid confusion in the future.

4.8.2 The masses and densities of the Kepler-10 planets

This paper is the third study of the masses and densities of the Kepler-10 planets. B11 and D14 previously measured the planetary and stellar properties of the Kepler-10 system. The stellar and planetary parameters they found are shown in Table 4.7. The planetary properties obtained in this paper are also shown. We include our solutions to the two-planet circular fit, the two-planet fit in which planet c is allowed eccentricity, and the best three-planet fit.

Table 4.7 reveals how the estimates of the masses of Kepler-10 b and c have changed based on which RVs were included in the analysis. B11 used 52 RVs from Keck HIRES that were

timed at the quadratures of planet b, and spanned 2 seasons (2009-2010). They assumed that both planets had circular orbits. They obtained masses of $m_b = 4.56 \pm 1.23\ M_\oplus$, and an upper limit for planet c, $m_c < 20\ M_\oplus$. D14 used 148 RVs from TNG HARPS-N that were timed at the quadratures of planet c, and spanned 2 seasons (2012–2013). They assumed that both planets had circular orbits. They obtained $m_b = 3.3 \pm 0.49\ M_\oplus$, a measurement 1σ lower than the B11 mass for Kepler-10 b, and a mass measurement for planet c of $M_c = 17.2 \pm 1.9\ M_\oplus$. Analyzing the 52 literature RVs plus 20 new RVs from HIRES, we obtain $m_b = 4.61 \pm 0.83 M_\oplus$ and $m_c = 5.69^{+3.19}_{-2.90} M_\oplus$, which are 1.1σ and 3.1σ away from the values in D14, respectively. We combine the 72 RVs from HIRES with 148 literature RVs from HARPS-N to obtain the best orbital coverage of both planets and the longest baseline. In our two-planet circular fit (the most direct orbital comparison to the previous studies), we obtain $m_b = 3.72 \pm 0.42\ M_\oplus$ and $m_c = 13.98 \pm 1.79\ M_\oplus$. The mass we obtain for Kepler-10 b sits between the two previously published values. Likewise, the mass we obtain for Kepler-10 c represents a compromise between the 2σ detection in the HIRES data and the massive planet obtained in the HARPS-N data.

When we allow the orbit of Kepler-10 c to be eccentric, or when we add a third planet to the system, the mass of Kepler-10 c does not change significantly. The mass for Kepler-10 c obtained in the eccentric fit ($m_c = 14.59 \pm 1.90\ M_\oplus$) is consistent with our circular fit. Likewise, the masses for planet c obtained for various orbital solutions of candidate KOI-72.X all resulted in $m_c = 13\text{-}14.5 M_\oplus$, i.e., all within 1σ of the mass we obtained in the two-planet circular fit. Therefore, allowing the orbit of planet c to be eccentric, or including a third planet at a variety of orbital periods, does not significantly affect the mass computed for Kepler-10 c.

4.8.3 Updated mass-radius and density-radius relations

We incorporate our newly derived mass measurements of the Kepler-10 planets, as well as several new planet discoveries, in an updated mass-radius relation. The planets are the same as those in Weiss & Marcy (2014), with the inclusion of planets listed in Table 4.8. Figure 4.20 shows how the weighted mean density and weighted mean mass of planets changes from 0-4 Earth radii.

Figure 4.20 shows where Kepler-10 b and c sit in the density-radius and mass-radius diagrams for planets smaller than 4 $R_\oplus$. As one of the first rocky exoplanet discoveries, Kepler-10 b has shaped our expectations for rocky exoplanets. Like Kepler-10 b, most of the rocky exoplanets discovered so far are larger than the Earth. This is because larger planets are easier to detect in transit, and because the masses of large, rocky planets are easier to measure than the masses of small, possibly rocky planets.

Kepler-10 b, at 1.47 $R_\oplus$, sits very close to the peak of the density-radius diagram (at 1.5 $R_\oplus$). Planet density increases with planet radius for $R_\mathrm{p} < 1.5 R_\oplus$, not only in the solar system terrestrial planets, but also among the few exoplanets with measured masses in this radius range (Kepler-78 b, Kepler-10 b, Kepler-36 b, Corot-7 b, Kepler-93 b). We attribute the empirical linear increase in planet density with radius to the slight compressibility of

Table 4.7: Kepler-10 Parameters in different studies

Parameter	units	B11[a]	D14[b]	This Work HIRES only	2 pl. circ.	2 pl. ecc.	Best 3 pl.
Stellar							
$T_{\rm eff}$	K	5627 ± 44	5708 ± 28	same as D14			
$\log g$	cgs	4.341 ± 0.012	4.344 ± 0.004	.	.	.	
$M_\star$	$M_\odot$	0.895 ± 0.060	0.910 ± 0.0214	.	.	.	
$R_\star$	$R_\odot$	1.056 ± 0.021	1.065 ± 0.009	.	.	.	
$L_\star$	$L_\odot$	1.004 ± 0.059	1.004 ± 0.059	.	.	.	
[Fe/H]	dex	-0.15 ± 0.04	-0.15 ± 0.04	.	.	.	
$v \sin i$	$\mathrm{m\,s^{-1}}$	0.5 ± 0.5	$0.6 \pm 0.5 - 2.04 \pm 0.34$	.	.	.	
age	Gyr	11.9 ± 4.5	10.6 ± 1.4	.	.	.	
Kepler-10 b							
Period	days	0.837495±4E-6	0.8374907±2E-7	fixed, same as D14			
TT	BJD - 2,454,900	64.57375 ± 0.0007	134.08687±0.00018	fixed, same as D14			
K	$\mathrm{m\,s^{-1}}$	3.3 ± 0.9	2.38±0.35	3.31±0.59	2.67±0.3	2.70±0.31	2.67 (fixed)
a	AU	0.01684±0.00033	0.01685±0.00013	fixed, same as D14			
$M_{\rm p}$	$M_\oplus$	4.56 ± 1.23	3.33±0.49	4.61±0.83	3.72±0.42	3.76 ± 0.43 $M_\oplus$	3.70 (fixed)
$R_{\rm p}$	$R_\oplus$	1.416 ± 0.034	1.47±0.03	fixed, same as D14			
$\rho_{\rm p}$	$\mathrm{g\,cm^{-3}}$	8.8 ± 2.5	5.8±0.8	8.0±1.43	6.46± 0.72	6.53±0.75	6.46 (fixed)
Kepler-10 c							
Period	days	45.29485±0.0007	45.294301±4.8E-5	fixed, same as D14			45.295
TT	BJD - 2,454,900	71.6761±0.0022	162.26648±0.00081	fixed, same as D14			71.67
K	$\mathrm{m\,s^{-1}}$	x	3.26±0.36	1.09±0.58	2.67±0.34	2.83 ±0.38	2.66
a	AU	0.2407 ± 0.0048	0.2410±0.0019	fixed, same as D14			0.24
e		0 (fixed)	0 (fixed)	0 (fixed)	0 (fixed)	0.17±0.13	0.09
ω_c	$^\circ$	.	.	.	.	71±20	79.7
$M_{\rm p}$	$M_\oplus$	< 20	17.2±1.9	$5.69^{+3.19}_{-2.90}$	13.98±1.79	14.59±1.90	13.94
$R_{\rm p}$	$R_\oplus$	2.277±0.054	2.35±0.06	fixed, same as D14			
$\rho_{\rm p}$	$\mathrm{g\,cm^{-3}}$	< 10	7.1±1.0	$2.42^{+1.36}_{-1.24}$	5.94±0.75	6.21±0.81	6.20
KOI-72.X							
Period	days	.	.	.	.	.	101.360[c]
e		.	.	.	.	.	0.19[c]
$M_{\rm p}$	$M_\oplus$	.	.	.	.	.	6.84[c]

Note. — [a] B11–Batalha et al. (2011). [b] D14–Dumusque et al. (2014). [c] The variety of orbital solutions with similar goodness of fit for planet candidate KOI-72.X prevents an accurate characterization of the planet's true orbital parameters and mass. The numbers shown here reflect the best three-planet solution, which is strongly preferred over the two-planet solution and over other three-planet solutions based on the BIC.

Table 4.8: Planetary Mass & Radius Measurements from 2014-2015

Name	Period (d)	Mass ($M_\oplus$)	Radius ($R_\oplus$)	Insolation ($S_\oplus$)	First Ref.	Orbital Ref.
Kepler-138 b	10.3126	0.066 ± 0.048	0.522 ± 0.032	6.90	Borucki et al. (2011)	Jontof-Hutter et al. (2015)
Kepler-138 c	13.7813	1.97 ± 1.5	1.197 ± 0.070	4.75	Borucki et al. (2011)	Jontof-Hutter et al. (2015)
Kepler-138 d	23.0881	0.640 ± 0.520	1.212 ± 0.075	2.35	Borucki et al. (2011)	Jontof-Hutter et al. (2015)
HIP 116454 b	9.120500	11.82 ± 1.33	2.530 ± 0.180	43.2	Vanderburg et al. (2015)	Vanderburg et al. (2015)
Kepler-93 b	4.726740	4.02 ± 0.68	1.478 ± 0.019	278	Borucki et al. (2011)	Dressing et al. (2015)
KOI-273 b	10.573753	6.8 ± 1.4	2.37 ± 0.13	119	Borucki et al. (2011)	Gettel et al. (2016)
Wasp-47 e	0.789597	< 22	1.829 ± 0.070	3998	Becker et al. (2015)	Becker et al. (2015)
Wasp-47 d	9.03081	15.2 ± 7	3.63 ± 0.14	155	Becker et al. (2015)	Becker et al. (2015)

rock. The density of rock changes gradually with increasing planet mass or radius, and so the first-order (linear) Taylor expansion of the true density-radius relation of rock is sufficient to describe the observed terrestrial planets and exoplanets smaller than 1.5 $R_\oplus$. Kepler-10 b (R_p= 1.47 $R_\oplus$, ρ_p= 6.68 g cm^{-3}) sits exactly on the linear density-radius relation that describes the terrestrial planets. Kepler-10 b also achieves a density consistent with an Earth-like composition (67.5% $MgSiO_3$, 32.5% Fe, Seager et al. 2007).

Kepler-10 c, at 2.35 $R_\oplus$, sits to the right of the peak of the density-radius diagram. Its density (5.74 g cm^{-3}) is among the highest for planets between 2.0 and 2.5 $R_\oplus$. However, its density is still lower than the density of Kepler-10 b. Neither the empirical density-radius relation for rocky planets, nor the Seager et al. (2007) prediction for the densities of rocky planets, intersects with Kepler-10 c's position on the mass-radius diagram. Extrapolating from both of these relations, we would expect the density of a 2.35 $R_\oplus$ Earth-composition planet to be 11 g cm^{-3}, nearly twice the observed density for Kepler-10 c. The mass and radius of Kepler-10 c are inconsistent with a stony-iron planet.

Composition modeling for Kepler-10 c strongly disfavors a rocky interpretation. Less than 2% of the posterior distribution on the planet's mass and radius permits a planet denser than pure perovskite. A stony-iron composition like the Earth and other known rocky exoplanets is excluded with high confidence. Kepler-10 c may have a stony-iron interior overlaid with a 0.2% mass (16% radius) hydrogen-helium envelope. Alternatively, Kepler-10 c may be a stony-iron interior covered with super-ionic water and a steam envelope.

Planet candidate KOI-72.X cannot be shown on the mass-radius diagram because it does not transit, and so its radius cannot be measured.

4.9 Conclusions

In this paper, we present the revised masses and densities of Kepler-10 b and c based on 220 RVs from two telescopes, 1.5 times as many RVs as were used in the most recent analysis of this planetary system. The combined RVs yield a baseline 3 times as long as any previous RV publication for this system. We find Kepler-10 b has $m_b = 3.72 \pm 0.42$ $M_\oplus$ and $\rho_b = 6.46 \pm 0.73$ g cm^{-3}, and Kepler-10 c has $m_c = 13.98 \pm 1.79$ $M_\oplus$ and $\rho_c = 5.94 \pm 0.76$ g cm^{-3}. However, we note that analysis of only HIRES data yields a higher mass for planet b and a lower mass for planet c than does analysis of the HARPS-N data alone, with the mass estimates for Kepler-10 c being formally inconsistent at the 3σ level. While we cannot identify the source of the disagreement between the HIRES and HARPS-N RVs, we note that the apparent time-variability of K_b and K_c in both instruments suggests that time-correlated noise, in the form of either stellar activity or an additional planet, is responsible for the apparent discrepancy. The time-correlated noise indicates that the uncertainties in the masses of the planets (especially planet c) likely exceed our formal estimates. More RVs and/or better priors on the stellar rotation period are needed to adequately model the time-correlated noise without compromising our analysis of the planetary signal of Kepler-10 c. We jointly analyze the TTVs and RVs of the Kepler-10 system to find planet candidate KOI-

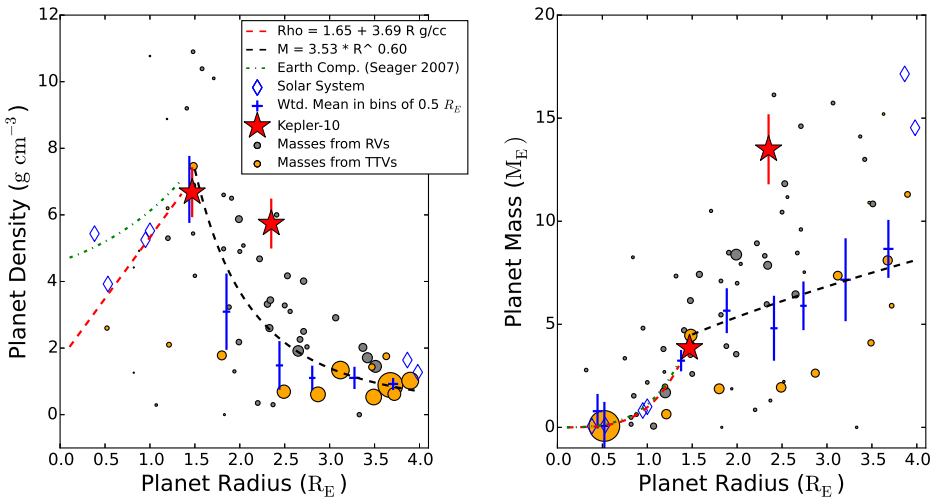

Figure 4.20: Left: planet density as a function of planet radius for planets smaller than 4 $R_\oplus$, updated from Weiss & Marcy (2014). Planets with mass measurements from RVs are in gray; planets with mass measurements from TTVs are in gold. The size of the dot corresponds to $1/\sigma_\rho^2$. Kepler-10 b and c are shown as large red stars. The solar system planets are shown as blue diamonds. The blue crosses show the weighted mean density in bins of 0.5 $R_\oplus$ to guide the eye, and their vertical error bars represent the RMS scatter of planet densities in that bin. The green line is the predicted bulk density for a 32.5% Fe, 67.5% $MgSiO_3$ planet (like Earth) as a function of radius (Seager et al. 2007). The red line is an empirical linear fit to planet density as a function of radius for $R_\mathrm{p} < 1.5R_\oplus$. The black line is an empirical power law fit to planet mass as a function of radius for $R_\mathrm{p} > 1.5R_\oplus$. Right: planet mass as a function of planet radius for $R_\mathrm{p} < 4R_\oplus$. The symbols and lines are the same as to the left, but the sizes of the dots corresponds to $1/\sigma_m^2$.

72.X. Several possible orbital solutions exist for KOI-72.X, with orbital periods ranging from 21-100 days, and masses ranging from 1-7$M_\oplus$. The existence of KOI-72.X has a negligible effect on the mass solutions for Kepler-10 b and Kepler-10 c.

4.9.1 Compositions of Kepler-10 b and Kepler-10 c

Kepler-10 b is very likely a planet with a rocky surface. Its density is consistent with a stony-iron composition (90.8% of the posterior distribution is denser than $MgSiO_3$). Assuming a 2-layer model with an iron core and silicate mantle, the iron core mass fraction of Kepler-10 b is constrained at 0.17 ± 0.12. Kepler-10 c is inconsistent with a purely rocky composition (only 1.6% of its posterior distribution is denser than pure $MgSiO_3$). Kepler-10 c may be a stony-iron interior overlaid with a 0.2% mass (16% radius) hydrogen-helium envelope. Alternatively, Kepler-10 c may be a stony-iron interior covered with a 28% mass (29% radius) super-ionic water envelope.

4.9.2 Non-transiting planet candidate KOI-72.X

From the coherent TTVs of Kepler-10 c, we identify a third, non-transiting planet candidate KOI-72.X. There is a 3% probability that the coherent TTVs are due to noise rather than a third planet. We explore possible solutions for the third planet, especially solutions that satisfy the TTV equation for the observed super-period of the TTVs, by running numerical N-body simulations over the duration of the *Kepler* observations. We demonstrate that orbital periods for the third planet that satisfy the TTV equation better reproduce the observed TTVs than other orbital periods do. Some orbital solutions for the third planet are interior to Kepler-10 c, while others are exterior. The most likely orbital periods for the non-transiting planet are 101 days, 24 days, and 71 days, which are near the 2:1, 1:2, or 3:2 mean motion resonance with planet c. The mass for the non-transiting planet candidate ranges from $1 - 7M_\oplus$.

Acknowledgements

LMW gratefully acknowledges support from Kenneth and Gloria Levy. This research was supported in part by the National Science Foundation under Grant No. NSF PHY11-25915 via the Dynamics of Exoplanets workshop at the Kavli Institute for Theoretical Physics in Santa Barbara, CA. We thank Tsevi Mazeh for informative discussions regarding time-correlated noise. The authors wish to extend special thanks to those of Hawaiian ancestry on whose sacred mountain of Maunakea we are privileged to be guests. Without their generous hospitality, the Keck observations presented herein would not have been possible.

5

Constraining the Masses of the Kepler-11 Planets with Radial Velocities

A version of the material in this chapter will be submitted for publication.

Kepler-11 is a sun-like star with 6 transiting planets discovered by the *Kepler* Mission. Five of the six planets have been found to have very-low densities through an N-body dynamical analysis of their transit timing variations (TTVs). Numerically reproducing TTVs has become a new method for solving the masses of planets, but this method is susceptible to dynamical degeneracies: planet eccentricity is degenerate with planet mass, and perturbations caused by non-transiting planets could be misattributed to the transiting planets. Furthermore, the masses of planets characterized by TTV analysis are systematically $2\times$ lower than the masses (including non-detections) reported by radial velocity (RV) analysis for planets of the same radius. In the first part of this paper, we address the discrepancy between the TTV- and RV- determined planet masses by measuring the RVs of Kepler-11 at strategic times, as determined by the ephemerides of the transiting planets. We obtained 27 RVs of Kepler-11 system with Keck/HIRES from 2011-2015. This four-year baseline excludes a Jupiter-mass planet interior to 1 AU in the Kepler-11 system. From our RVs only, we place a 3σ upper limit on the masses of the Kepler-11 planets of $2\times$ their nominal masses. Thus, we demonstrate that the RVs are consistent with the very-low mass scenario determined by the TTVs. In the second part of this paper, we analyze, for the first time, the Q1-Q17 TTVs of Kepler-11 to obtain the most precise constraints on the planet masses and orbital properties published yet. We use the simplectic N-body integrator TTVFast to (1) model the TTVs alone, and (2) jointly model the RVs and TTVs of Kepler-11. We derive new planet masses and densities for the five inner planets: $m_b = 2.0 \pm 0.7 M_\oplus$, $m_c = 2.6 \pm 0.8 M_\oplus$, $m_d = 6.3 \pm 0.7 M_\oplus$, $m_e = 8.3 \pm 0.8 M_\oplus$, and $m_f = 2.0 \pm 0.4 M_\oplus$. Our re-analysis of the TTVs provides new constraints on the mass of the outermost planet: $m_g < 25 M_\oplus$ with 2σ confidence. The consistency of the TTVs and RVs in the Kepler-11 system bodes well for N-body simulations of TTVs for other Kepler systems that are too faint for RV follow-up.

5.1 Introduction

The *Kepler* Mission (Borucki et al. 2011; Batalha et al. 2013; Burke et al. 2014; Mullally et al. 2015) has revealed that planets between the size of Earth and Neptune, though absent from our own solar system, are extremely common around other stars, occurring around at least half of all stars (Petigura et al. 2013a; Fressin et al. 2013; Petigura et al. 2013b). Determining the compositions of these so-called sub-Neptunes has been a major effort in the wake of the *Kepler* Mission. Marcy et al. (2014) obtained masses and mass upper limits of 42 transiting sub-Neptunes by measuring the radial velocity (RV) time-series of their host stars. Further analyses of *Kepler*'s small planets by Weiss & Marcy (2014), Rogers (2015), and Wolfgang & Lopez (2015) determined that many of these sub-Neptunes, especially those larger than $1.5R_{\oplus}$, require a of layer gaseous volatiles comprising $> 0.1\%$ of the planet's total mass to explain their low densities.

In addition to being numerous, many super-Earths inhabit compact, multi-planet systems. An exemplary compact system is Kepler-11, a sun-like star with six transiting planets between 1.8 and 4.2 Earth radii. Five of the planets reside within the equivalent orbital distance of Mercury. The sixth planet is dynamically decoupled from the others but is still within the equivalent orbital distance of Venus (Lissauer et al. 2011, hereafter L2011). How and where did these planets assemble from the materials of the proto-planetary disk, and what forces (if any) arranged the planets in the compact configuration we find them in today? Is a special mechanism required to create Kepler-11, or can Kepler-11 be formed in the same way as less compact systems with one or more sub-Neptunes? Accurately determining the compositions of planets in compact systems like Kepler-11 will allow us to constrain possible formation and evolution scenarios.

Because Kepler-11 was discovered early in the *Kepler* Mission, many studies have been conducted about the dynamics and formation of the Kepler-11 system (e.g., L2011, Lissauer et al. 2013; Mahajan & Wu 2014; Hands et al. 2014; Lee et al. 2014). Mahajan & Wu (2014) test the dynamical stability of the system and to what extent the orbital parameters of the planets need to be perturbed to induce chaos or dynamical instability. They find that the system is dynamically stable, but that altering the semi-major axis or eccentricity of either of the innermost planets by a few percent renders the system dynamically unstable. Hands et al. (2014) perform an N-body integration of the planets within a gaseous disk to model possible migration scenarios, concluding that the Kepler-11 planets could have migrated en masse though the disk on timescales of 10^5 years if the eccentricity damping was sufficiently high. Chiang & Laughlin (2013) consider the possibility of forming compact systems like Kepler-11 from proto-planetary disks an order of magnitude more massive than the minimum mass solar nebula (MMSN). Lopez et al. (2012) examine how the history of X-ray and UV radiation from the star could have photo-evaporated the outermost layers of the planets, sculpting their atmospheres to result in the densities and compositions we see today. All of these formation and evolution mechanisms are tuned to reproduce the observed masses and compositions of the Kepler-11 planets.

In an analysis of *Kepler*'s photometrically determined transit times from Q1-Q14, Lis-

sauer et al. (2013, hereafter L2013) model how gravitational interactions between the planets alter the transit times. This N-body analysis enables a precise determination of the planet masses. The L2013 analysis finds that the Kepler-11 planets have very low densities, from 0.59 - 1.72 g cm^{-3}(0.7 g cm^{-3} on average). Their average density is equal to that of Saturn, but Saturn is a gas giant. Compared to other planets of their sizes, the Kepler-11 planets have densities a factor of 2-3 lower. However, even within the family of solutions from TTVs, the individual masses of the planets, especially b and c, vary by a factor of 2 between the solutions drafted by Eric Agol (E.A.), Jason Rowe (J.R.), and Donald Short (D.S.) due to the mass/eccentricity degeneracy and choices about how to handle planet g (L2013). These inconsistencies motivate an alternate measurement of the Kepler-11 planet masses.

TTVs have been used to characterize the orbital dynamics of many compact systems since the discovery of Kepler-11. Kepler-36, which has two sub-Neptunes at orbital periods of 14 and 16 days in the 6:7 mean motion resonance, demonstrated that TTV analyses can achieve planet mass measurements with only 5% uncertainty in resonant systems (Carter et al. 2012). Kepler-30 is a system of three transiting planets at orbital periods of 29, 60, and 143 days, of which only the innermost planet is sub-Neptune sized (3.9 $R_\oplus$). The TTVs of the other two planets constrain the mass of the sub-Neptune at $11.3 \pm 1.4 M_\oplus$, about half the mass of Neptune (Sanchis-Ojeda et al. 2012). Kepler-51 is a system of three sub-Saturn sized planets near a 1:2:3 resonance chain, all of which have densities lower than 0.05g cm^{-3} based on an analysis of their TTVs (Masuda 2014). The Kepler-79 planets (KOI-152) are all very-low density, and this system includes a sub-Saturn size planet of density 0.09 g cm^{-3} (Jontof-Hutter et al. 2014). Kepler-138 d (formerly KOI-314 c) is a 1.2 Earth-radius planet that has a mass, as measured by TTVs, of only 0.64 $M_\oplus$, resulting in a density of 2.1 g cm^{-3} (Jontof-Hutter et al. 2015; Kipping et al. 2014). Typically, planets of this size have densities closer to 6 g cm^{-3} consistent with rocky or nearly rocky compositions; Kepler-138 d is the only planet smaller than 1.5 $R_\oplus$ that is inconsistent with a rocky composition. The two defining features of the systems described above are (1) they are all compact multi-transiting systems, and (2) they all have TTVs.

The handful of very low density planets characterized by TTVs have densities that, for their radii, are statistically distinct from the densities of planets characterized by the more established radial velocity (RV) technique (Weiss & Marcy 2014). Why are the TTV mass determinations yielding significantly lower densities than the RV mass determinations? At least four possible explanations exist: (1) the reported RV masses are systematically too high, (2) the reported TTV masses are systematically too low, (3) detection/selection biases in TTVs result in the preferential characterization of compact systems of low-density planets, or (4) the TTV method is characterizing a distinct population of planets that, due to some yet-to-be-determined formation mechanism, have compact architectures and low densities. Although scientists are historically biased in reporting RV detections over non-detections, Weiss & Marcy (2014) included the RV non-detections at all planet radii, and so it is unlikely that the distinction between RV and TTV planets results solely from a bias toward high masses from RVs. Even if there is a slight bias toward more massive planets with the RV technique, the very-low densities of planets determined from TTVs (e.g. 0.1

g cm^{-3} Jontof-Hutter et al. 2014), if accurate, require a physical explanation. Therefore, we are interested in determining whether the ultra-low density planets characterized by TTVs are indeed ultra-low density.

Direct comparisons between TTVs and RVs have been attempted in a few systems for which both measurement techniques are feasible, but the mass determinations were all for giant planets rather than sub-Neptune sized planets. In the Kepler-9 system, the RVs (Holman et al. 2010) and TTVs (Borsato et al. 2014) result in planet masses that differ by a factor of 2, with the TTVs yielding the lower masses. However, the spectra obtained in Holman et al. (2010) were contaminated by moonlight, making the resulting RVs unreliable. In Kepler-89 (KOI-94), a compact system containing a warm, Jupiter-sized planet, the RV-determined masses (Weiss et al. 2013) and TTV-determined masses (Masuda et al. 2013) differ by a factor of 2, with the TTVs finding the lower planet mass. In the Kepler-88 system (KOI-142, the "King of TTVs"), Nesvorný et al. (2013) used the gargantuan TTV signature (which has an amplitude of half a day) of KOI-142 b to predict a Saturn-mass non-transiting planet in an exterior 2:1 mean motion resonance. Barros et al. (2014) detected KOI-142 c with RVs in the predicted orbital period and within 1σ of the predicted mass. It is worth noting that the TTVs predicted a slightly lower mass than what was detected with RVs. In K2-19, a system containing two large planets in a 3:2 mean motion resonance, there is tension between the mass determinations from TTVs and RVs. While the masses determined by Narita et al. (2015, TTVs) and Barros et al. (2015, TTVs and RVs) agree, later RVs taken by Nespral et al. (2016) determine a much higher mass for K2-19 b. In all of these systems, the masses determined from TTVs are lower than the masses determined from RVs. The source of the mass discrepancies for individual planets is unclear.

In this chapter, we make a direct comparison between the TTV-determined and RV-determined planet masses for a single system with claimed very-low density planets, Kepler-11. This is the first comparison between RVs and TTVs for sub-Neptune size planets.

5.2 Radial Velocities

5.2.1 Observing Strategy

We employ a novel technique in obtaining radial velocities of Kepler-11. If the planets are indeed low-mass (as expected from their TTV-determined masses), the RV signals they produce have amplitudes of $\sim 1\,\mathrm{m\,s^{-1}}$ that are too difficult to disentangle using traditional RV observing techniques. Although the expected signals from the individual planets are small, at certain opportune times, the planets roughly align at one quadrature phase or the other, inducing a cohesive, maximal RV kick on the star. At such times, the expected change in the RV of the star is 6 $\mathrm{m\,s^{-1}}$ (see Figure 5.1), which is comparable to the detection capabilities of Keck/HIRES for very faint stars ($V > 13$). If the planets have masses consistent with the typical masses for planets their size (about 2-3$\times$ as massive as in L2013), they should produce a proportionally larger kick that would be easily detectable and distinguishable from

the 6 $\mathrm{m\,s^{-1}}$ kick.

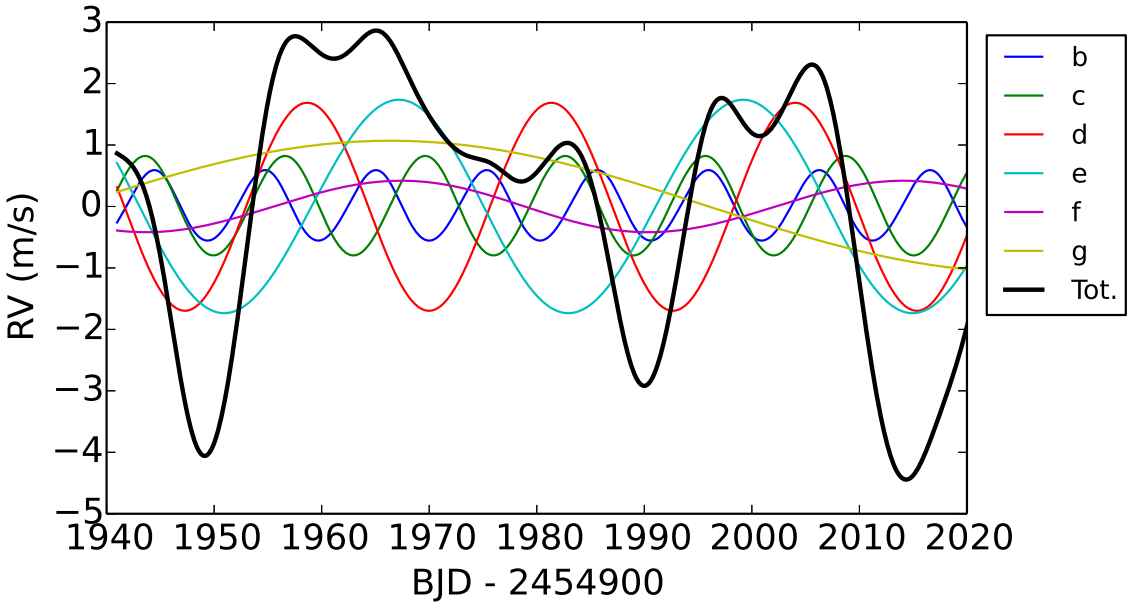

Figure 5.1: The predicted RVs of the Kepler-11 system during the summer of 2014, based on the orbital ephemerides derived in L2013. The thin colored lines correspond to the stellar velocity reflex from each of the individual planets; the thick black line is the total predicted stellar RV.

This careful prediction of the RV extrema requires a precise knowledge of the planets' orbital ephemerides. Since all of the planets have been observed in transit at least 12 times by *Kepler*, their orbital periods and times of transit are precisely known, enabling us to forward-model the RV curve. The planet orbits are nearly circular (as measured by L2013 and as required for dynamical stability), and their very low eccentricities have negligible impact on the predicted RV curve. Likewise, their non-Keplerian interactions are small over long time-scales, causing only slight deviations from a Keplerian prediction (Section 5.3.1). Finally, the TTV analysis, which is most sensitive to the interactions of pairs of planets, is very good at constraining the mass ratios between adjacent pairs of planets, so we have no reason to believe that a single planet might spuriously have a much higher mass than what was determined by TTVs, if all the other planets have masses comparable to their TTV-determined masses. Thus, the only parameters that could reasonably be varied by a factor of a few are the sum of the planet masses, which we call the mass scale factor, and the RV zero point.

5.2.2 Measurements with HIRES

We obtained 27 spectra of Kepler-11 through an iodine absorption cell on Keck/HIRES from 2011-2015, including 17 carefully timed measurements between July 1, 2014 and September 12, 2014, and an additional 3 targeted measurements in July 2015. For a stellar template, we obtained an iodine-free spectrum of the star on UT 12 July 2014. To enable deconvolution of the stellar template with the PSF, we obtained spectra of two rapidly rotating B stars, HR 7457 and HR 7543, immediately before and after our measurement of the stellar template.

5.2.3 Doppler Pipeline

We calculate precise radial velocities of Kepler-11 using the standard Doppler code of the CPS group (Howard et al. 2011) with the inclusion of a new de-trending routine (see below). Each observation uses a slit with dimensions of 0.87″x 14.″0 yielding a resolving power of 60,000, and allowing for subtraction of night sky emission lines and scattered moonlight. During the initial RV extraction we model the instrumental PSF as a sum of 13 Gaussians with positions and widths fixed but their heights free to vary (Butler et al. 1996). Any correlations in the final RVs with the heights of these Gaussians (PSF parameters) likely indicate small inadequacies of our PSF model to completely describe the shape of the instrumental PSF. RV shifts caused by the gravitational influence of orbiting bodies should not be correlated with the shape of the instrumental PSF.

5.2.4 Velocity Error Determination

At V=14, Kepler-11 is one of the faintest stars for which we have attempted to measure precision velocities. The typical signal to noise (S/N) we obtained in each 45-minute iodine spectrum is 60 (30k counts on the HIRES exposure meter), which is a lower S/N than we typically use to determine RVs. In particular, modeling the PSF for such low S/N is challenging, as the 13-dimensional PSF description often ends up describing noise instead of the PSF shape.

To quantify the extent to which the low S/N spectra incurred additional errors, we calibrated against a bright RV standard star of the same spectral type, HD 12846. We obtained 27 iodine spectra and one iodine-free spectrum of HD 12846 at S/N=60. Fifteen years of historical RVs of this star at S/N=250 on Keck/HIRES exhibit an RMS scatter of 2.5 $\mathrm{m\,s^{-1}}$, but when the exposure time is reduced to make S/N=60 (typically a 3-second exposure), the RMS of the resulting RVs is 5.07 $\mathrm{m\,s^{-1}}$. Therefore, we attribute a 5.07 $\mathrm{m\,s^{-1}}$ error penalty to the poor PSF fitting for spectra of G0 type stars with S/N=60, and add this error in quadrature to the internal velocity errors ($\sim$2.5 $\mathrm{m\,s^{-1}}$) for Kepler-11.

5.2.5 Detrending Algorithm and Test

In order to clean the RVs of possible systematic trends we detrend the final RVs by removing correlations with the instrumental PSF parameters, the magnitude of the RV uncertainty, and the S/N ratio of the spectrum. After masking any 5-σ outliers, we search for significant correlations by calculating the Spearman rank correlation coefficient for each of these variables with RV (Spearman1904). We take note of any parameters that show a correlation coefficient greater than 0.1 and include these variables in a multivariate ordinary least squares linear regression using the STATSMODELS[1] package in Python. This final multidimensional surface is then subtracted from the final RVs. This technique improves the RMS of the RV time series of Kepler-11 from 8.25 $\mathrm{m\,s^{-1}}$ to 6.65 $\mathrm{m\,s^{-1}}$. Since the stellar motion has no way of knowing how the starlight enters the spectrometer, the RVs should not be correlated with PSF parameters, and removing the RV-PSF correlation should result in more accurate (as well as more precise) RVs.

To check that the detrending algorithm does not accidentally remove the signal of the planets or generate spurious signals, we subjected the raw and detrended RVs to a rigorous test. We asked how slight fluctuations in the determination of the PSF parameters altered the raw RVs, and whether the decorrelation process helped correct for the changes in the PSF parameters. We constructed 4 distinct deconvolved stellar spectral templates (DSSTs), each of which relied on different observations of rapidly rotating B stars (cosmic lightbulbs) to determine the PSF parameters. For each DSST, we computed a set of velocities which we called trial 1, trial 2, trial 3, and trial 4. We then ran the decorrelation algorithm on each set of velocities. The raw and decorrelated RV curves are shown in Figure 5.2

By comparing the RMS of the velocities across the 4 trials before and after detrending, we can test whether the detrending algorithm makes each RV more resilient to how we determine the PSF. Table 5.1 summarizes the scatter in each RV without and with the decorrelation technique. Overall, both the RMS scatter of the RVs and the χ^2 goodness of fit to the predicted RV curve improved in each trial as a result of the decorrelation algorithm. We adopt the mean of the four decorrelated trials as our RV time series.

We report the Barycentric Julian Date (BJD) of each iodine spectrum's flux-weighted midpoint, the RV of that spectrum, and the RV uncertainty after correcting for the low S/N systematics in Table 5.2.

5.2.6 Limits on the Kepler-11 Planet Masses from RVs Only

By measuring the RV extrema of Kepler-11 when all the planets are on one side of the star or the other, we effectively constrain the sum of the planet masses. Because over a dozen transits of each planet were observed in the Kepler-11 photometry, the orbital ephemerides of the planets were extremely well determined. Even though the mass uncertainties from the Lissauer et al. (2013) analysis were large (50%), the TTVs constrain the mass ratios of the planet pairs b-c, and the triple d-e-f, very tightly. If the planets were indeed more

[1] https://pypi.python.org/pypi/statsmodels

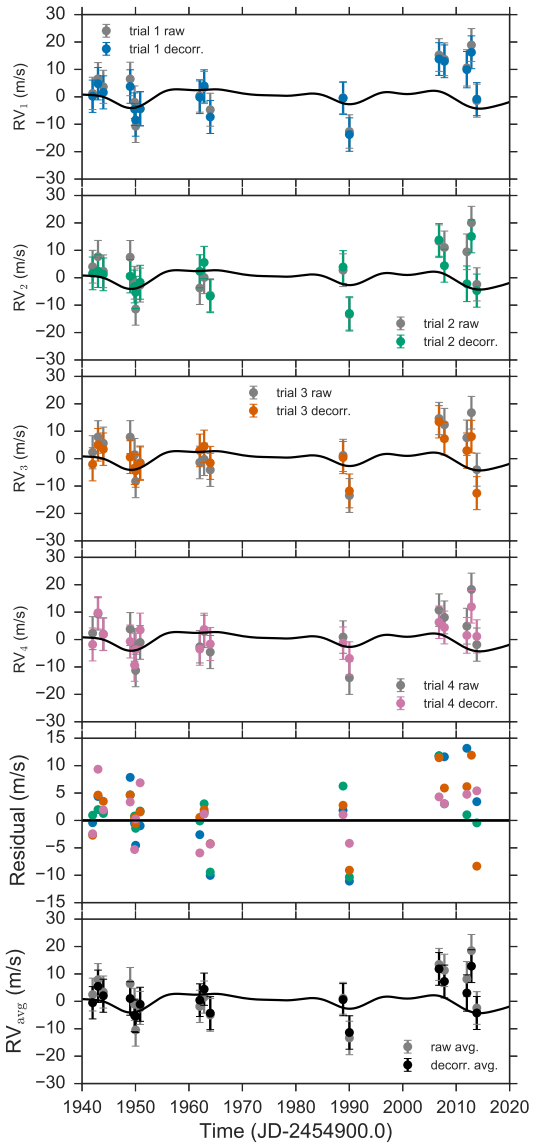

Figure 5.2: RV time series of Kepler-11 using 4 different PSF descriptions to construct the DSST (trials 1-4), and the raw or decorrelated RVs. Top 4 panels: the raw and decorrelated RVs from trials 1, 2, 3, 4 vs. time. The differences between the raw and decorrelated RVs are less than the individual uncertainties, demonstrating that the decorrelation algorithm produces believable RVs. Furthermore, the decorrelated RVs hug the model better than the raw RVs and appear to remove time-correlated noise at BJD−2454900 ≈2010. Second from bottom: the residual decorrelated RVs from all 4 trials. Bottom: The average raw (gray circles) and decorrelated (colored circles) RVs compared to the nominal model RV curve predicted from TTVs (black line).

Table 5.1: Results of Decorrelation Algorithm Tests

	Trial	RMS ($m\,s^{-1}$)	Residual to model ($m\,s^{-1}$)
raw RVs:			
	trial 1	8.86	8.99
	trial 2	8.54	8.89
	trial 3	8.87	9.06
	trial 4	7.38	7.63
	avg.	8.25	8.48
decorrelated RVs:			
	trial 1	8.23	8.54
	trial 2	7.19	7.00
	trial 3	7.84	7.26
	trial 4	5.98	6.06
	avg.	6.65	6.55

massive than determined in the TTV analysis, their mass ratios should still be consistent (see Section 5.3.1). Assuming that the mass ratios between pairs of planets are well-constrained by the TTVs, we use a single, multiplicative scale factor on the TTV-determined masses to reproduce the observed RVs. Figure 5.3 shows the predicted RV curve for Kepler-11 for several mass scalings.

Examining the RVs and models with different mass scalings by eye, we can immediately rule out large mass scalings. If the planets were 4 times as massive as determined from TTVs, we should have seen a change in RV of 25 $m\,s^{-1}$ between BJD$-2454900 = 1950$ and 1960. The comparative flatness of the RVs favors low masses for the planets.

We calculate the χ^2 goodness of fit for various mass scalings and compute the natural logarithm of the likelihood function

$$\ln \mathcal{L}(\Delta\chi^2) = \frac{-\Delta\chi^2}{2} \tag{5.1}$$

where $\Delta\chi^2$ is the difference in χ^2 between the model we are considering and the minimum value of χ^2. Using Equation 5.1, we determine the relative likelihood of each mass scaling compared to the best fit model. Figure 5.3 shows that the RVs alone rule out large mass scalings. A model with a mass scaling of 2.0 has a likelihood of less than 0.01. *Thus, the RVs independently confirm that the Kepler-11 planets have low densities for their sizes.*

Table 5.2: Radial Velocities of Kepler-11

BJD - 2454900.0	RV ($m\,s^{-1}$)	Unc. RV ($m\,s^{-1}$)
541.000944	-8.9	7.1
600.843062	-12.0	9.5
642.727971	-3.4	7.3
890.965581	6.9	7.2
1200.034440	4.1	7.4
1296.782722	6.0	6.4
1633.933555	-3.4	6.7
1941.976352	-0.5	6.0
1942.983959	5.5	5.9
1943.978104	2.1	6.0
1949.006796	1.0	6.0
1949.828734	-5.1	5.9
1950.025521	-5.5	5.9
1950.868813	-1.1	6.2
1962.028919	0.4	6.0
1962.842492	4.4	5.9
1963.984970	-4.3	6.0
1988.834208	0.6	5.9
1990.017309	-11.4	6.1
2006.790933	11.8	5.9
2007.794057	7.3	6.0
2011.995698	3.0	6.5
2012.848556	12.8	6.0
2013.854327	-4.2	6.0
2322.005642	0.4	5.9
2322.984348	-5.1	5.7
2329.832163	-13.4	5.9

Note. — All RVs obtained with the W.M. Keck telescope and HIRES instrument, 2011-2015.

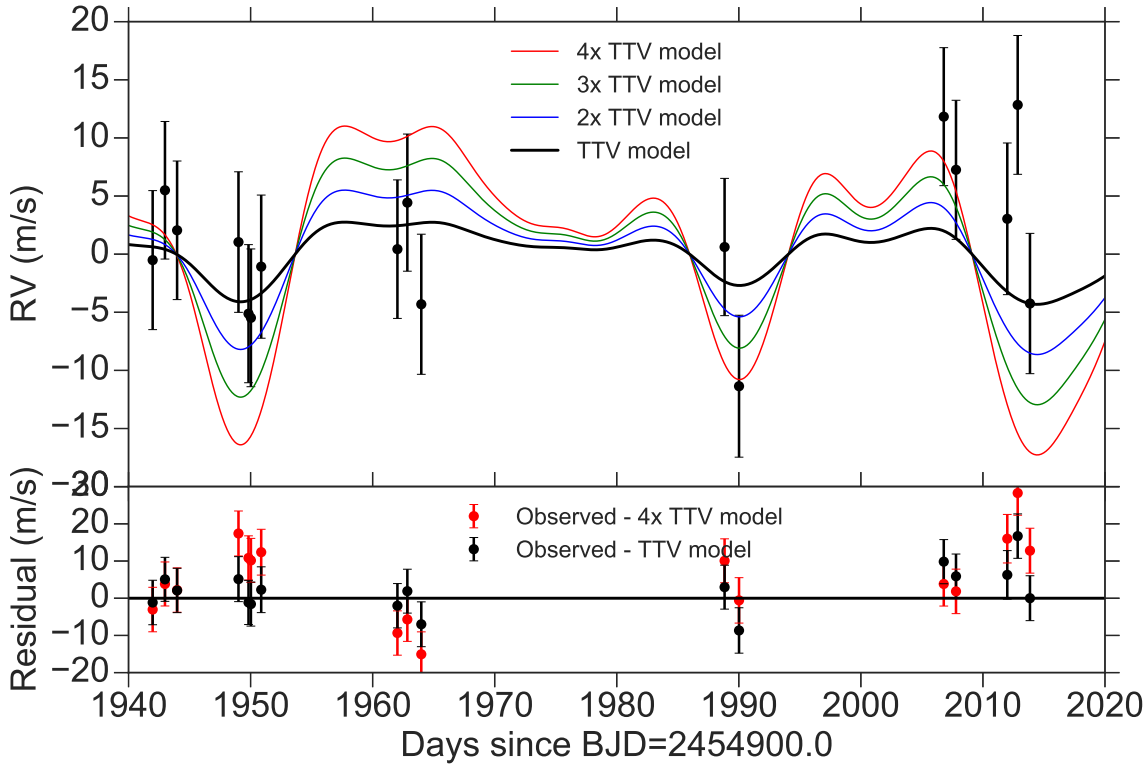

Figure 5.3: Top: The observed RVs of Kepler-11 and their uncertainties versus time (black bars). Overlaid are the RV curve predicted from the L2013 parameters (black line) and the RV curves predicted from the L2013 orbital parameters but with the planet masses multiplied by a common scale factor of 2 (blue), 3 (green), and 4 (red). Bottom: The residual RVs with respect to the nominal model from TTVs (black bars) and the model with masses enhanced by a factor of 4 (red bars). The superiority of the nominal model demonstrates that the RVs favor low masses for the Kepler-11 planets.

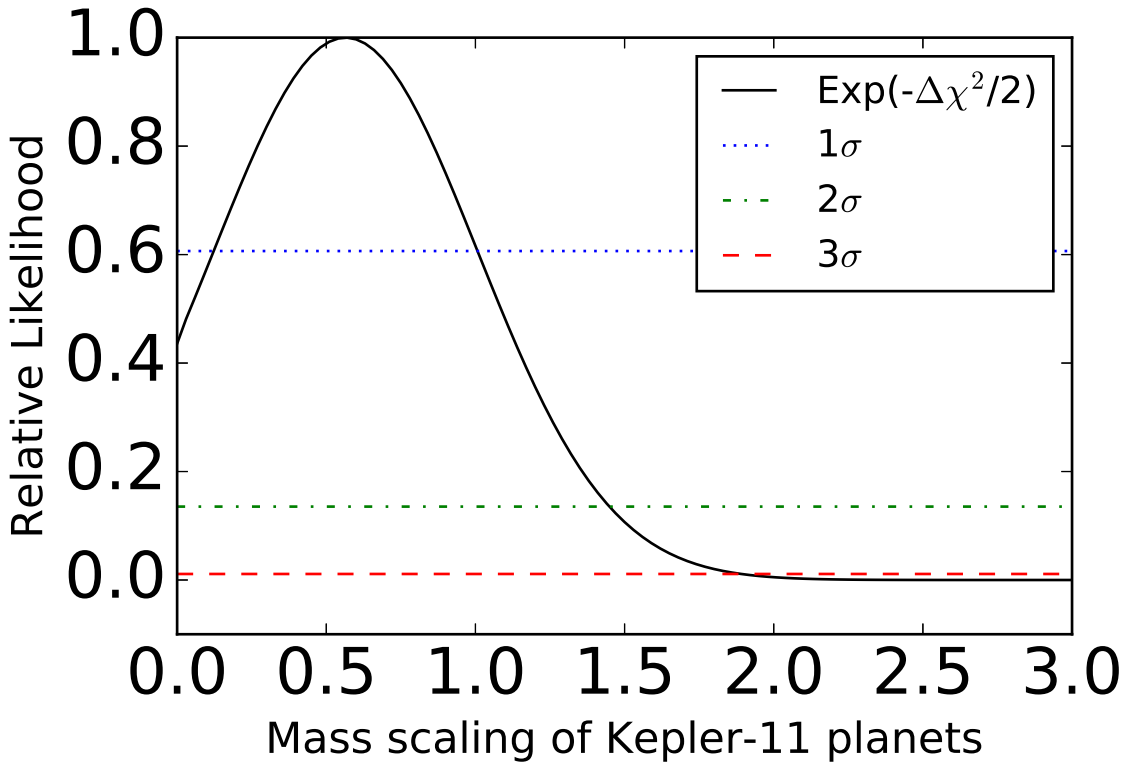

Figure 5.4: The relative likelihoods of various scale factors for the masses of the Kepler-11 planets. The nominal model (mass scaling = 1) is consistent with the RVs. A model with a mass scaling of 1.6 becomes discrepant with the RVs with 2σ significance, and a model with a mass scaling of 2.0 is more than 3σ discrepant from the RVs. Therefore, the RVs alone rule out scenarios in which the masses of the Kepler-11 planets are more than twice the masses determined by TTVs, ruling out rocky compositions for most of these planets.

5.2.7 A Search for Non-Transiting Planets around Kepler-11 using RVs

The Kepler-11 system is compact, leaving few possibilities for non-transiting planets. However, there is enough room for a stable planet in 3 places: interior to planet b, between planets f and g, or exterior to planet g. The long baseline (2011-2015) of the RVs, including a high-cadence streak of 17 RVs in the summer of 2014, helps explore and rule out scenarios of non-transiting planets. The window function of the RVs is shown in Figure 5.5.

To look for non-transiting planets, we inspect the residual RVs (after subtracting the best N-body ephemeris) and their periodogram (Figure 5.5). There is no significant peak in the periodogram, and so we do not detect any additional planets in the system.

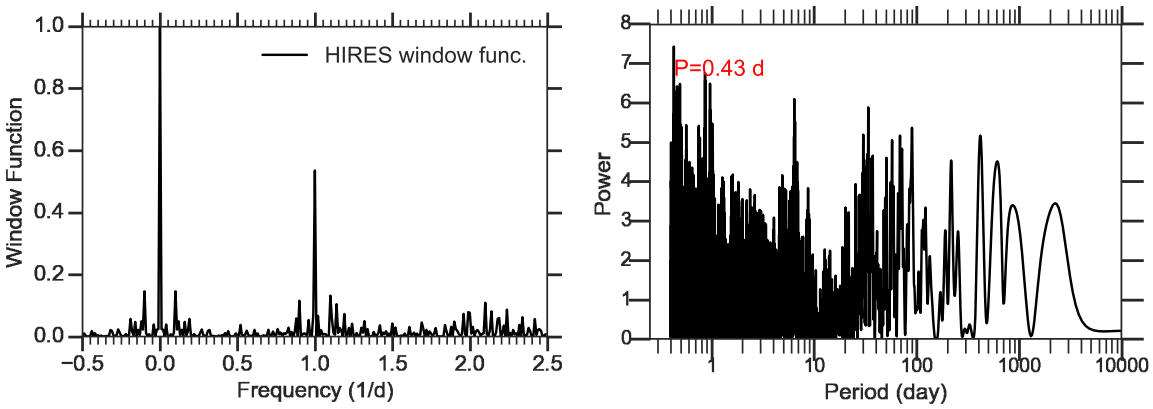

Figure 5.5: Left: Window function of the Kepler-11 RVs. Insufficient coverage of frequencies near 1/day and low frequencies (long periods) obscures our search for additional planets. Right: Periodogram of the Kepler-11 RV residuals (observations minus best N-body ephemeris). No high-fidelity peak stands out, illustrating that no additional planets are detected in the system.

To test whether additional non-transiting planets might exist in the Kepler-11 system near our detection threshold, we perform a suite of injection-recovery tests. In each injection-recovery test, we construct a sine wave from three random variables: semi-amplitude K (uniform on [0,26] $\mathrm{m\,s^{-1}}$), the logarithm of the orbital period P (uniform on [0,4]), and orbital phase ϕ (uniform on [0,2π]). From these variables, we generate a sine wave of the form

$$\text{Signal} = K\sin(2\pi t/P + \phi) \tag{5.2}$$

where t is the time of observation. The procedure for one injection-recovery test is:

1. Generate the signal,
2. add this signal to the residual RVs to make a trial observation,
3. run a Python version of fasper (Press & Rybicki 1989) to generate the Lomb-Scargle periodogram of the trial observation, and

4. find the peak power of the periodogram.

5. If the recovered period matches the input orbital period (to within 10%), we consider this a recovery of the injected orbital period. Otherwise, the trial results in a non-recovery.

We perform 10,000 independent injection-recovery trials. Figure 5.6 shows the outcome of which K, P pairs are recovered and which are not. The fraction of trials that are recovered in each bin are shown as a black percentage. We rule out the following planets with 50% confidence: $m\sin i = 1 M_{\rm J}$ at 1000 days, $m \sin i = 100 M_\oplus$ at 100 days, $m \sin i = 30 M_\oplus$ at 4 days. We need a longer baseline and more RV measurements to detect or rule out a Jupiter analog at 5 A.U. in the Kepler-11 system. With $6 \mathrm{m\,s^{-1}}$ uncertainty in our RVs, we would need hundreds of measurements to reach the detection threshold of Earth-mass planets. Future precision RV instruments on large telescopes might be capable of measuring the masses of the individual planets in Kepler-11 and searching for non-transiting planets in the dynamically stable regions between the known planets.

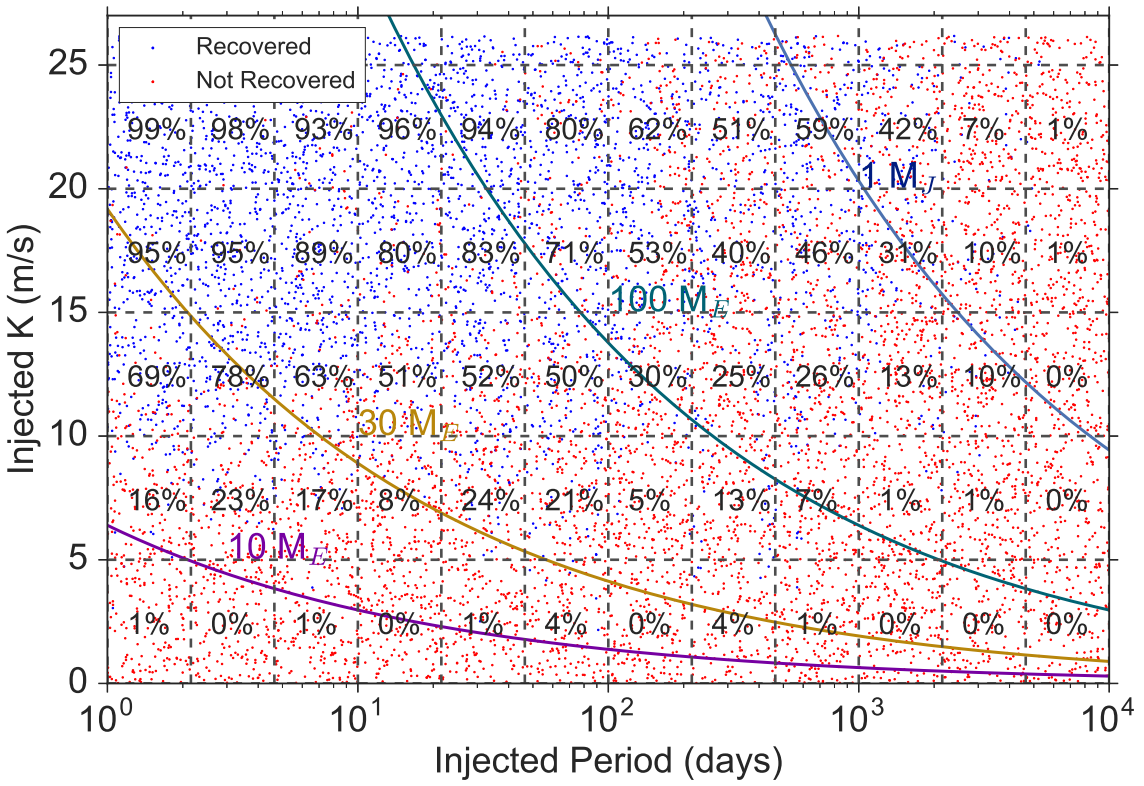

Figure 5.6: Results of injection-recovery tests of sine-wave signals with amplitude K and period P added to the RV residuals. The phase angle of each sine wave was randomized. Curves describing the signals created by planets of 10 Earth masses (magenta), 30 Earth masses (mustard), 100 Earth masses (turquoise), and 1 Jupiter mass (blue) illustrate the regions of parameter space in which each of these planet masses would be detectable. For instance, approximately half of possible signals from a 100 Earth mass planets at 100 days would be detectable. Nearly 100% of the signals from 100 Earth-mass planets within 10 days would be detectable.

5.3 N-Body Analysis of Transit Timing Variations and Radial Velocities

In this section, we re-analyze the Kepler-11 TTVs and then jointly analyze the TTVs and RVs. A re-analysis of the TTVs alone is valuable because new photometry and analysis techniques have become available since the publication of L2013. L2013 analyzed *Kepler* photometry from quarters Q1-Q14; here, we use photometry from Q1-Q17, the entire duration of the primary *Kepler* Mission. We use TTVFast, a simplectic N-body integrator (Deck et al. 2014), to dynamically forward-model the initial orbital elements and masses of the Kepler-11 planets. TTVFast models (1) the transit times of all the planets in the system, and (2) the RV of the star at specified times of observation. Thus, we can simultaneously compare the models generated by TTVFast to the observed TTVs and RVs. We explore (1) what we can learn from the updated TTVs alone, (2) what additional information the RVs provide.

5.3.1 Testing TTVFast

Benchmarking against RVs

To ensure that TTVFast predicts sensible RVs, we first simulated the RVs of a small, low-mass planet in an eccentric orbit with both a Keplerian equation and TTVFast. TTVFast and the Keplerian prescriptions agreed within $10^{-8}\mathrm{m\,s^{-1}}$ at all epochs, showing that TTVFast indeed produces Keplerian results in a purely Keplerian limit. TTVFast also reproduced the Keplerian result for a two-planet system with circular orbits.

We forward-modeled the Kepler-11 planet ephemerides with both TTVFast and a simpler model consisting of 6 Keplerian orbits. At the time of the majority of our RV observations (summer 2014, just over a year after our last *Kepler* photometry measurement), the RVs predicted by TTVFast and the Keplerian model differ by no more than $0.4\ \mathrm{m\,s^{-1}}$, a distinction too small to discern given our typical velocity errors of $5\ \mathrm{m\,s^{-1}}$. The fractional energy loss during the 4-year integration is 10^{-15}, a loss too small to explain the growing discrepancy between the N-body and Keplerian curves. Furthermore, the difference between the N-body and Keplerian curves oscillates. The times of maximal discrepancy between the N-body and Keplerian curves occur when the planets align at quadrature and exert the strongest gravitational perturbations on the star. The timing of the discrepancies between the N-body simulation and Keplerian prediction supports that the discrepancy is physical and not the result of machine errors. A direct comparison of the RVs predicted by Keplerian orbits and TTVFast for the Kepler-11 system is shown in Figure 5.7.

Benchmarking against TTVs

We compared the transit times predicted by TTVFast to the transit times observed in L2013. As L2013 did, we discard two outlier transit times that are each more than 5σ

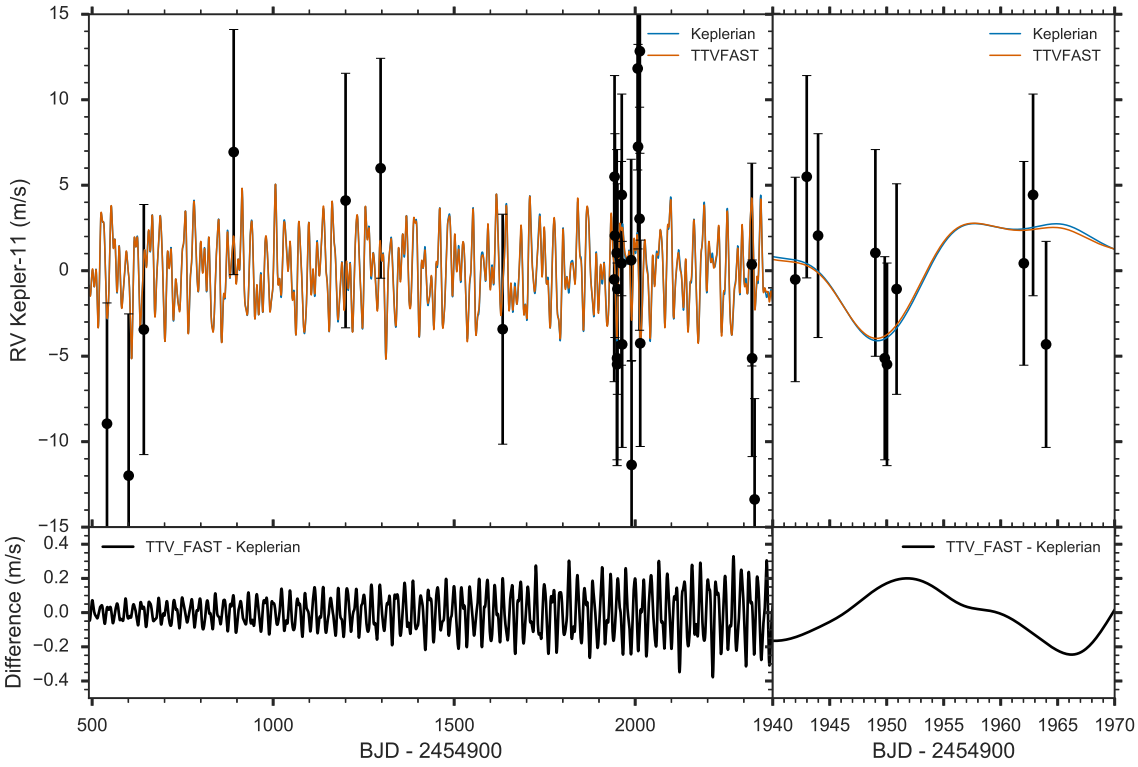

Figure 5.7: Top: Radial velocity versus time computed with TTVFast (red) and a six-planet Keplerian (blue). Both models use the osculating orbital elements and planet masses derived from the best joint fit to the TTVs and RVs. The observed RVs of the Kepler-11 system and their uncertainties versus time (black) are shown for reference. Bottom: The difference between the TTVFast and Keplerian solutions versus time illustrates that the TTVFast and 6-planet Keplerian algorithms differ by no more than 0.4 $\mathrm{m\,s^{-1}}$, validating TTVFast as an excellent predictor of RVs. Note that the times at which the TTVFast and RV solutions differ most are near RV maxima and minima, which correspond to alignments of the planets, during which we expect the planet-planet interactions to cause deviations from strictly Keplerian RVs.

away from the model transit times and are likely corrupted due to simultaneous transits or incomplete coverage of a transit. Using the best orbital parameters and masses determined in L2013, we obtained $\chi^2 = 486$, which is comparable to the 365 transit times we considered (reduced $\chi^2 = 1.3$).

5.3.2 Analysis of the Q1-Q17 Transit times of Kepler-11

From the full Q1-Q17 *Kepler* photometry, Jason Rowe determined the midpoint transit times and their uncertainties. The long- and short-cadence photometric data were detrended using Jason Rowe's algorithm for detrending *Kepler* photometry (Rowe et al. 2014). In brief, this algorithm applies a polynomial fit to the light curve within a pre-determined window of several days to remove low-frequency variability in the light curve. This analysis does not significantly affect the transits, which have durations of minutes to hours. Wherever short-cadence data (1 minute cadence) were available (from BJD-2454900=189 onward), we used it; before this time, the transit times were determined from the long cadence photometry (30 minute cadence). Correlated noise was not considered in this analysis. The transit times TT, their uncertainties σ_T, and their photometric cadence are given in Table 5.6, which is at the bottom of this chapter due to its length.

5.3.3 The Kepler-11 Parameters from TTVs Alone

The additional quarters of *Kepler* data motivate a re-analysis of the best orbital parameters and their uncertainties from the TTVs alone (without considering the RVs). We performed a Levenberg-Marquardt minimization of χ^2 between a variety of N-body models generated with TTVFast and the observed Q1-Q17 transit times. Our fit has 30 free parameters: mass (m), the initial orbital period (P), eccentricity vector components $e\cos\omega$ and $e\sin\omega$, and the initial time of transit (TT) for each planet. The result of the L-M minimization is that none of the orbital osculating elements differ substantially from the L2013 parameters. The masses are consistent with the L2013 values, typically differing by only 6% (Table 5.3).

5.3.4 Error Analysis of Planet Masses (TTVs Alone)

To characterize the uncertainties in the planet masses in detail, we explore all 30 free orbital parameters with a Markov Chain Monte Carlo (MCMC) sampling algorithm. First we consider the uncertainties in the planet masses from the TTVs alone. We wrap ttvfaster (Agol & Deck 2016) with emcee (Foreman-Mackey et al. 2013) to efficiently explore this complex parameter space. In the spirit of understanding which large planet masses we can rule out, we initialize our walkers with uniform distributions in planet mass from [0,50] $M_\oplus$ (but for planet g, we use the range [0,200] $M_\oplus$). We run 4000 walkers 2000 steps (Figures 5.8 and 5.9) to arrive at the mass distributions reported in Table 5.3 and shown in Figure 5.10. We find masses of $m_b = 2.0 \pm 0.7$ $M_\oplus$, $m_c = 2.3 \pm 0.8$ $M_\oplus$, $m_d = 7.2 \pm 0.7$ $M_\oplus$,

$m_e = 8.0 \pm 0.8\ M_\oplus$, $m_f = 1.9 \pm 0.4\ M_\oplus$, and $m_g < 25\ M_\oplus$ with 2σ confidence. For comparison, L2013 found $m_{b,2013} = 1.9^{+1.4}_{-1.0}\ M_\oplus$, $m_{c,2013} = 2.9^{+2.9}_{-1.6}\ M_\oplus$, $m_{d,2013} = 7.3^{+0.8}_{-1.5}\ M_\oplus$, $m_{e,2013} = 8.0^{+1.5}_{-2.1}\ M_\oplus$, $m_{f,2013} = 2.0^{+0.8}_{-0.9}\ M_\oplus$, $m_{g,2013} < 25\ M_\oplus$ with 2σ confidence. Our new Q1-Q17 results (1) are consistent with the results from L2013, (2) place tighter constraints on the allowed masses of the planets than those reported in L2013, (3) demonstrate that large planet masses cannot reproduce the observed TTVs.

The analytic expression for TTVs reveals that the masses and the eccentricity vector difference between a pair of planets can be covariant (Wu & Lithwick 2013; Lithwick et al. 2012). The eccentricity vector difference is

$$\vec{e}_{12} = \sqrt{(e_1 \sin\omega_1 - e_2 \sin\omega_2)^2 + (e_1 \cos\omega_1 - e_2 \cos\omega_2)^2} \tag{5.3}$$

where the subscript 1 corresponds to the inner planet and the subscript 2 corresponds to the outer planet. We inspect the covariances between the masses and eccentricity vector differences of the Kepler-11 planets. We find some covariance between the masses of planets b and c and their eccentricity vector difference (Figure 5.11). The other planets do not exhibit any significant correlation between mass and eccentricity.

5.3.5 The Kepler-11 Parameters from TTVs and RVs Combined

Although we only obtained 27 RVs, increasing the number of data points from 364 transit times (TTs) to 391 total measurements, the RVs result from an independent measurement technique and therefore constrain the planetary dynamics in ways that the TTVs do not. We investigate the extent to which the RVs tighten the constraints on the planet masses in this section. We repeat the L-M minimization described in the previous section, but compare the N-body model TTs and RVs to the observed TTs and RVs. We obtained a minimum $\chi^2 = 334$ to 391 independent measurements (reduced $\chi^2 = 0.86$, reduced $\chi^2_{\rm RV} = 1.0$, reduced $\chi^2_{\rm TT} = 0.85$). The initial osculating elements for our fit, as well as other derived orbital parameters, and the best fit planet masses, are given in Table 5.4. Figure 5.7 shows the observed and modeled RVs, and Figure 5.12 shows the observed and modeled TTVs.

We attempted an MCMC analysis to the combined RV + TTV data set to obtain a complete understanding of the benefits of RVs, but doing so required using TTVFast (rather than TTVFaster), which is too slow to converge on useful timescales. To quickly compare the benefits of the RVs in addition to the TTVs in constraining the planet masses, we apply the following technique:

1. Start with the best fit parameters determined by the Levenberg-Marquardt minimization to the data (RVs + TTs).

2. Fix the mass of the planet of interest at some value m, letting all the other parameters vary.

3. Minimize χ^2 with the Levenberg-Marquardt algorithm.

Table 5.3: MCMC Analysis of Kepler-11 TTVs Only

Parameter	Units	Median	1σ	2σ
m_b	$M_\oplus$	2.0	0.7	1.2
P_b	days	10.30406	0.00001	0.000019
$\sqrt{e_b}\cos\omega_b$		0.11	0.08	0.20
$\sqrt{e_b}\sin\omega_b$		0.07	0.09	0.20
TT_b	days	71.4993	0.0007	0.0016
m_c	$M_\oplus$	2.3	0.8	1.6
P_c	days	13.024934	0.000009	0.000018
$\sqrt{e_c}\cos\omega_c$		0.03	0.11	0.21
$\sqrt{e_c}\sin\omega_c$		0.02	0.10	0.20
TT_c	days	71.1760	0.0005	0.001
m_d	$M_\oplus$	7.2	0.7	1.3
P_d	days	22.68712	0.00001	0.00003
$\sqrt{e_d}\cos\omega_d$		-0.06	0.10	0.19
$\sqrt{e_d}\sin\omega_d$		0.08	0.09	0.19
TT_d	days	81.4557	0.0005	0.001
m_e	$M_\oplus$	8.0	0.8	1.6
P_e	days	31.99544	0.00002	0.00005
$\sqrt{e_e}\cos\omega_e$		-0.13	0.05	0.16
$\sqrt{e_e}\sin\omega_e$		-0.02	0.08	0.17
TT_e	days	87.16237	0.0006	0.0010
m_f	$M_\oplus$	1.9	0.4	0.8
P_f	days	46.68586	0.00006	0.00012
$\sqrt{e_f}\cos\omega_f$		0.04	0.09	0.16
$\sqrt{e_f}\sin\omega_f$		-0.03	0.08	0.16
TT_f	days	64.6708	0.0008	0.0016
m_g	$M_\oplus$	12	12	25
P_g	days	118.3787	0.0002	0.0003
$\sqrt{e_g}\cos\omega_g$		0.1	0.2	0.4
$\sqrt{e_g}\sin\omega_g$		-0.03	0.2	0.4
TT_g	days	101.9069	0.0008	0.0019

Note. — The solution to the TTVs alone was computed with TTVFaster. The orbital elements are the average orbital elements over the time of integration (BJD$-2454900.0 = [0, 1600]$). Uncertainties are computed based on the 16th and 84th (1σ) and 2nd and 98th (2σ) percentiles.

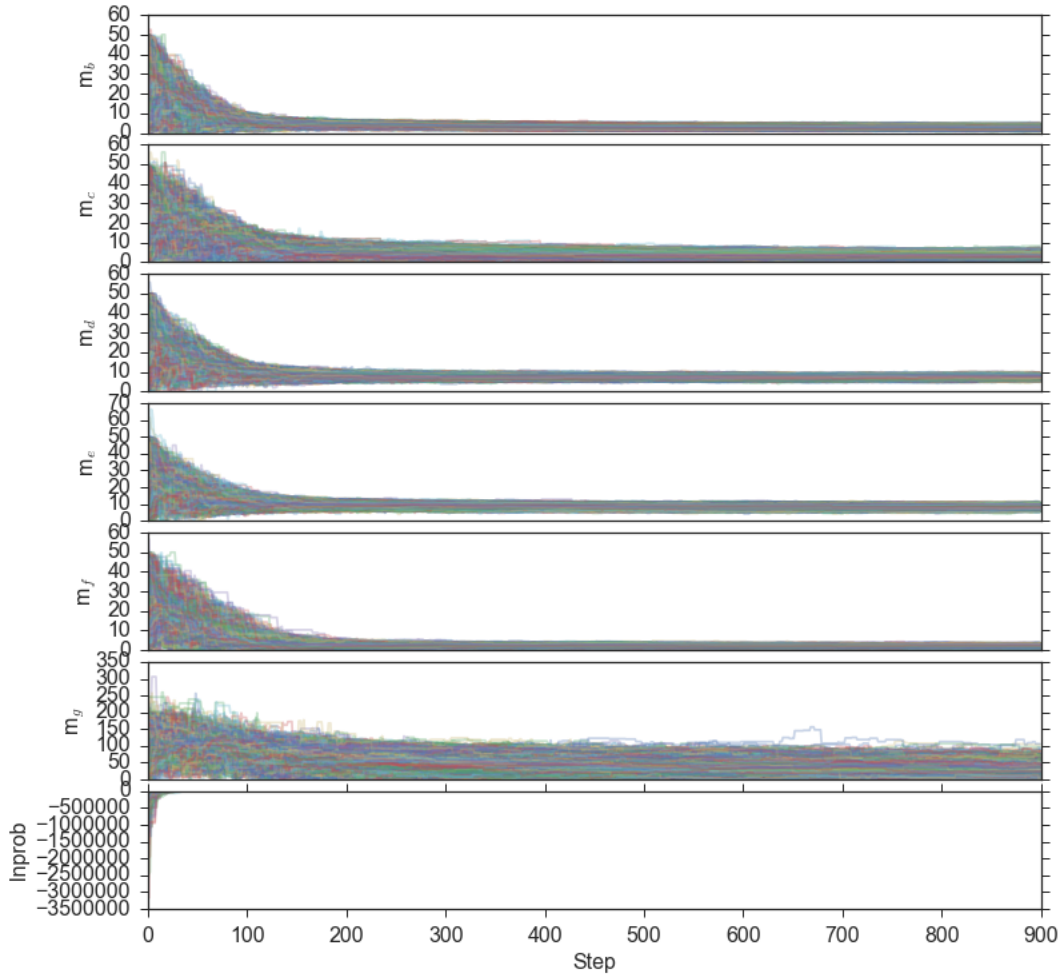

Figure 5.8: The MCMC chains show the positions of the walkers as a function of step number for m_b, m_c, m_d, m_e, m_f, m_g, and the natural logarithm of the probability, lnprob. Each colored line corresponds to a unique walker. The algorithm was initialized (step = 0) with 4000 walkers. For the five inner planets, the 4000 initial masses were drawn from a uniform distributions from [0,50] Earth masses. For planet g, the 4000 initial masses were drawn from a uniform distribution from [0,200] Earth masses. The variance in the distribution of masses and lnprob of the walkers decreases dramatically in the first 100 steps.

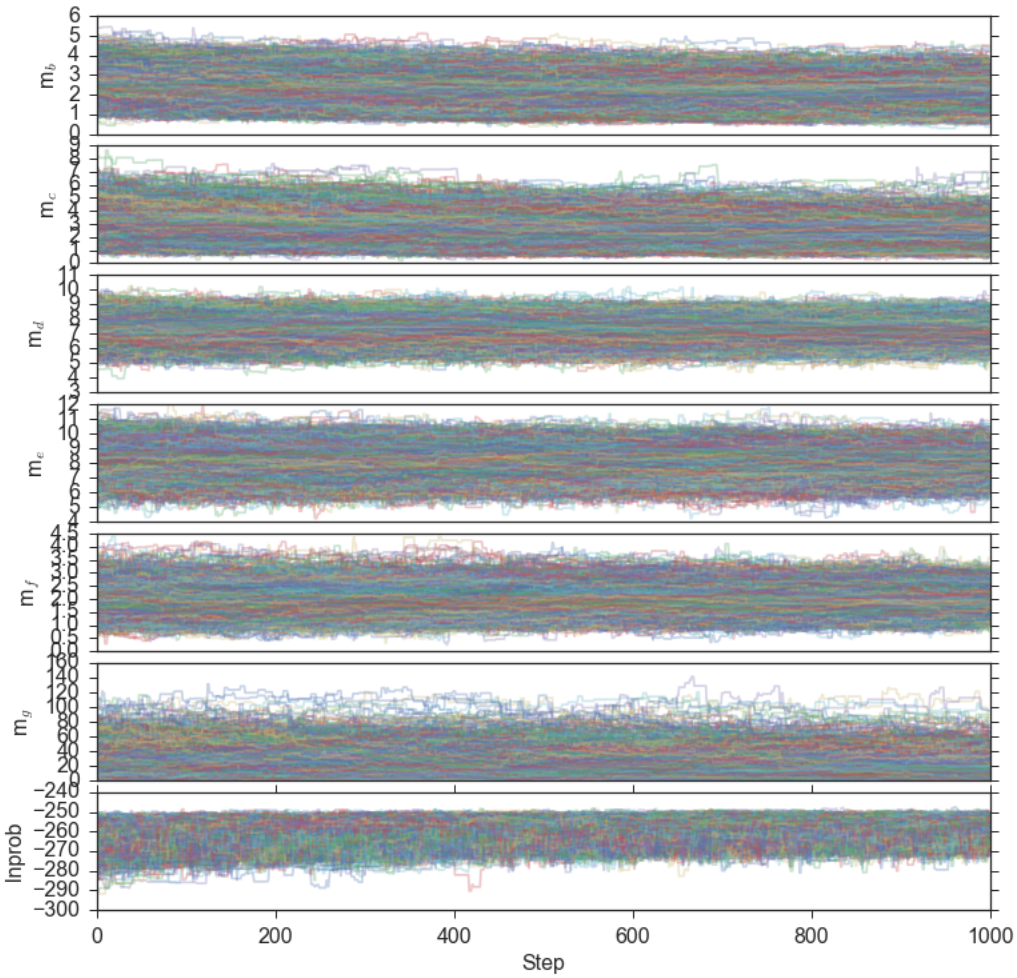

Figure 5.9: The continuation of the chains in 5.8 for another 1000 steps. In these steps, the walkers appear to converge to a steady-state posterior distribution.

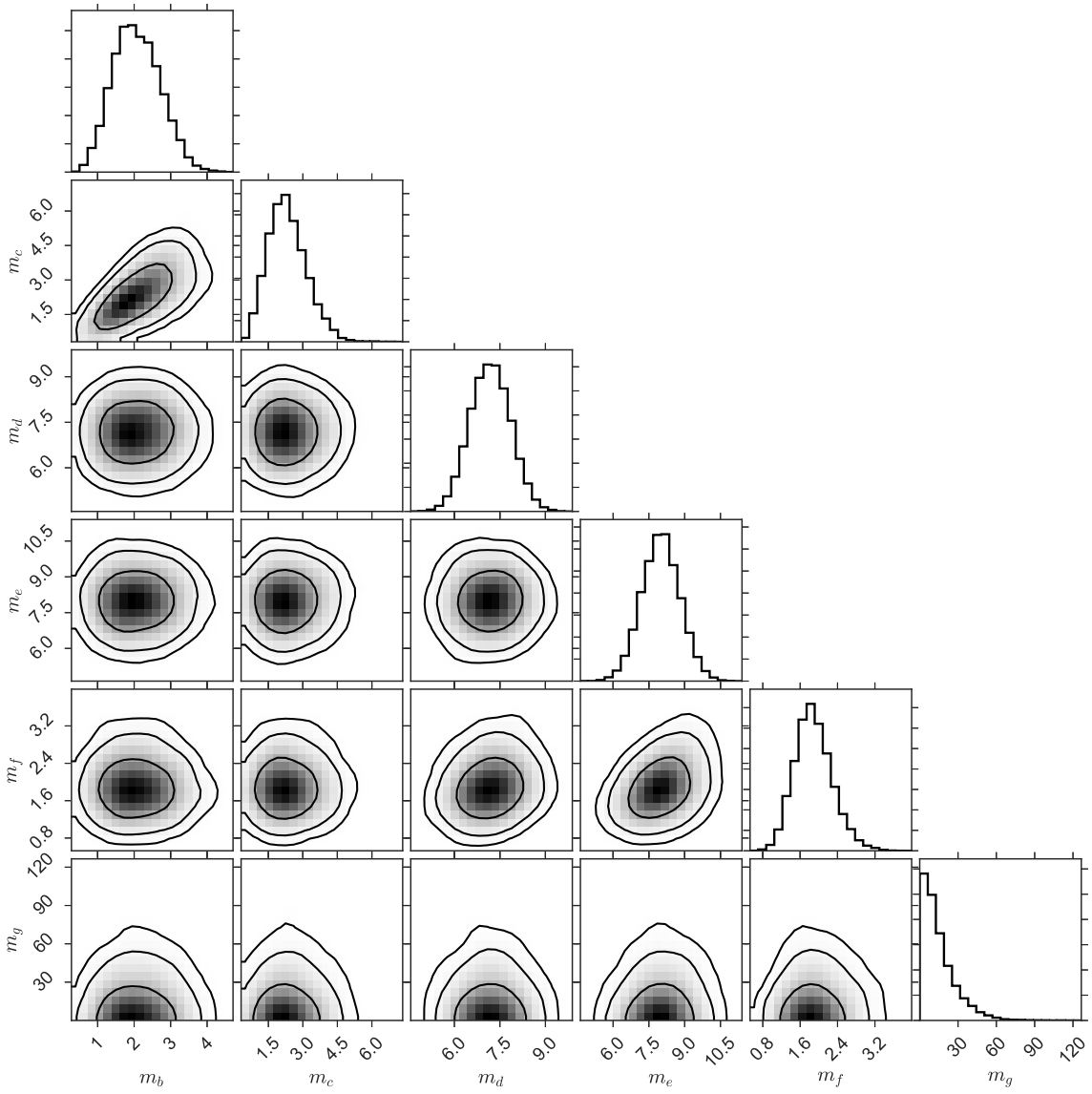

Figure 5.10: Triangle plot of the posteriors and covariances of the planet masses in Kepler-11. The panels on the diagonal show histograms of the posteriors of the planet masses. The off-diagonal panels show the covariance between the masses of a pair of planets. In the covariance plots, the contours correspond to the 68%, 95%, and 99% intervals. Only planets b and c have covariate masses.

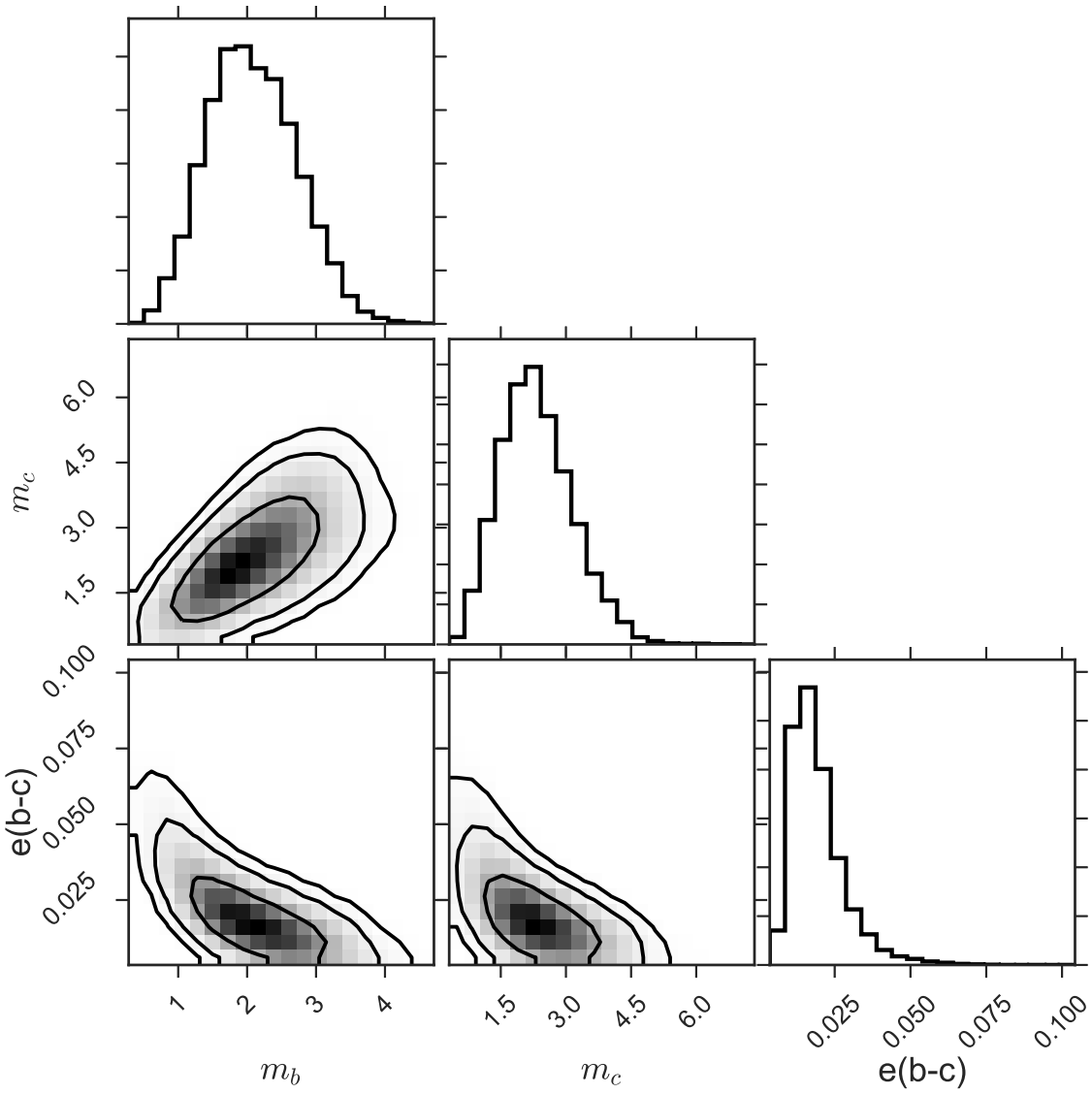

Figure 5.11: Triangle plot of the posteriors and covariances of the masses of Kepler-11 b, Kepler-11 c, and the difference between their eccentricity vectors, $\vec{e}_{12}$. The planet masses are positively correlated with each other, and negatively correlated with the difference between their eccentricity vectors. If the planets are not apsidally aligned and their eccentricities are moderate, lower planet masses are favored. If the eccentricities are low and/or the planets are apsidally aligned, larger planet masses are favored.

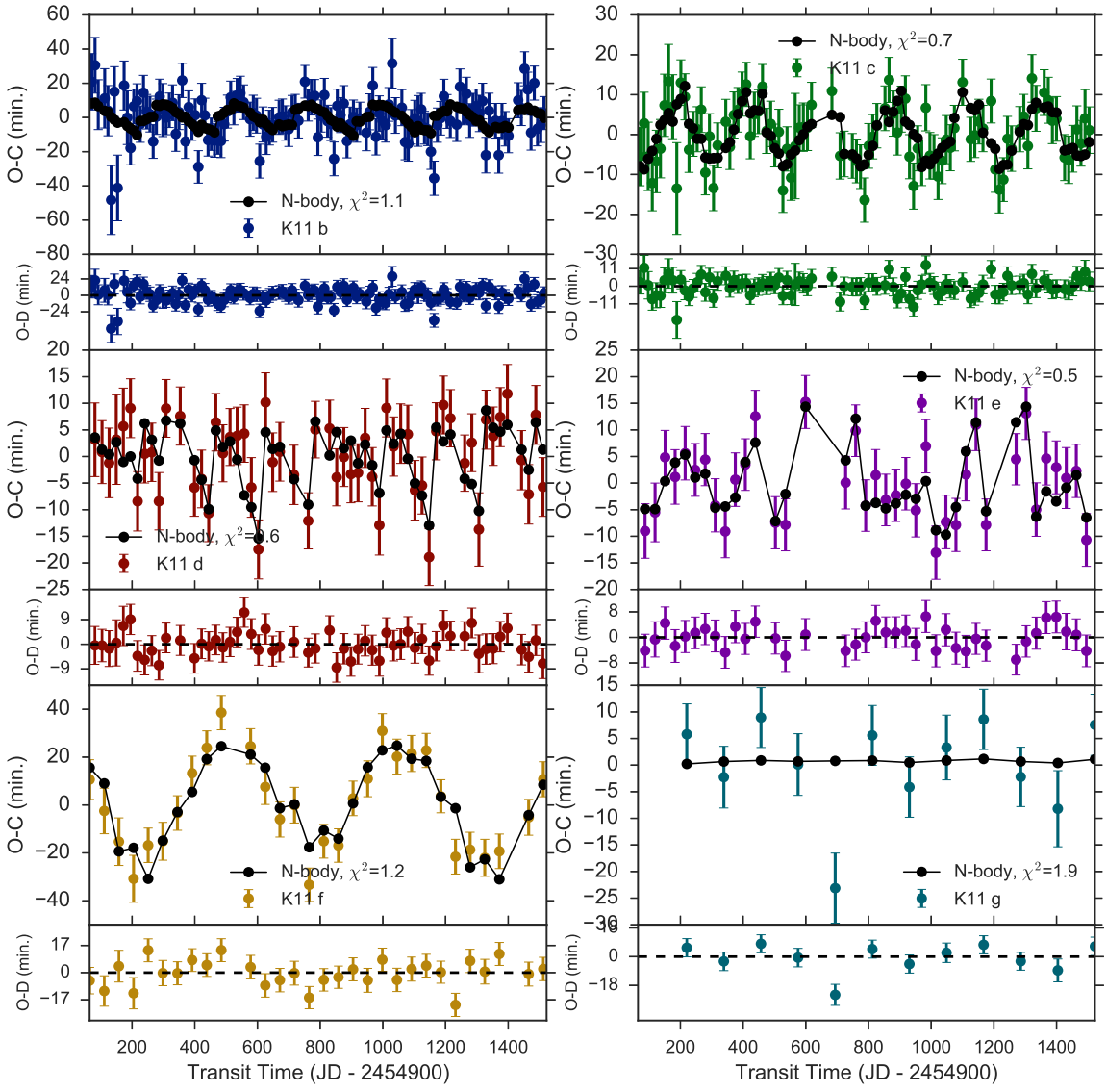

Figure 5.12: A comparison of the observed TTVs to the best-fit model of TTVFast using both the RV and TTV data sets. The six large panels show the observed minus linear-ephemeris calculated (O-C) transit times versus time for planets b (upper left, blue), c (upper right, green), d (central left, rust), e (central right, purple), f (lower left, mustard), and g (lower right, turquoise). The TTVFast N-body dynamical prediction of the O-C for that same planet is overlaid as black circles connected by a line. The residuals between the observed and dynamically modeled transit times (O-D) are shown in the smaller inset plots at the bottom of each large panel. The reduced χ^2 goodness of fit to the TTVs of each individual planet is shown in the respective panel. Overall, reduced $\chi^2_{\rm TT} = 0.85$, and reduced $\chi^2_{\rm RV} = 1.0$.

Table 5.4: Kepler-11 Best Fit Dynamical Properties

Planet	Period (days)	Ecc.	Inc. (°, fixed)	ω (°)	TT_0 (days*)	Mass[A] ($M_\oplus$)	Radius[B] ($R_\oplus$)	Density (g/cc)
Kepler-11 b	10.30458	0.045	89.64	45.0	195.15089927	2.0 ± 0.7	1.8 ± 0.04	1.9 ± 0.7
Kepler-11 c	13.02410	0.026	89.59	51.34	201.424543717	2.6 ± 0.8	2.87 ± 0.05	0.6 ± 0.2
Kepler-11 d	22.69165	0.004	89.67	146.31	194.890778584	6.3 ± 0.7	3.12 ± 0.06	1.1 ± 0.1
Kepler-11 e	31.99503	0.012	88.89	228.37	215.143945985	8.3 ± 0.8	4.19 ± 0.07	0.6 ± 0.1
Kepler-11 f	46.69327	0.012	89.47	335.56	204.728267767	2.0 ± 0.4	2.49 ± 0.05	0.7 ± 0.1
Kepler-11 g	118.39681	0.039	89.87	34.51	220.28292865	$< 25^C$	3.33 ± 0.06	$< 3.7^B$

[A]Masses computed from RVs and TTVs, uncertainties computed from TTVs only.
[B]Values from Lissauer et al. (2013)
[C]2σ upper limit.

Note. — *Osculating Elements determined at epoch BJD−2454900 = 63.67

4. Repeat steps 2-3 with different values of m.
5. Do a cubic interpolation to χ^2 as a function of m.
6. Calculate the relative likelihood as a function of m, using Equation 2.
7. Repeat steps 1-6, but only using the TTs as data.

The results of this exploration of parameter space are shown in Figure 5.13. Comparing the relative likelihoods with or without the RVs allows us to ascertain the extent to which the RVs help constrain the planet masses. Figure 5.13 shows that the RVs provide little additional information about planets b-f, but rule out massive scenarios for planet g. Using the TTVs and RVs, we calculate a 2σ upper limit on the mass of planet g of 10 $M_\oplus$. With the TTVs only, the 2σ upper limit on the mass of planet g is 40 $M_\oplus$. (Note that our MCMC analysis found a 2σ upper limit of 25 $M_\oplus$, demonstrating that our quick exploration does not sufficiently explore parameter space. In reality, the RVs might place a stronger constraint on the mass of planet g than what is determined here.)

5.4 Summary and Discussion

In the first part of this chapter, we presented 27 RVs of Kepler-11 obtained on Keck/HIRES. The RVs alone confirm that the Kepler-11 planets have low densities. Having sizes of 2-4 Earth radii and densities of 0.59 - 1.72 g cm^{-3}, the Kepler-11 planets are among the lowest-density planets discovered for their sizes. In the second part of this chapter, we analyzed updated TTVs of the Kepler-11 planets. We used photometry from Q1-Q17 to obtain 364 TTV measurements. We applied the N-body integrator TTVFast to these TTVs, obtaining updated masses, mass uncertainties, and orbital parameters of the Kepler-11 planets. We repeated our analysis including the RVs to determine what new information the RVs provide.

How do the confirmed very-low planet densities affect our understanding of the Kepler-11 system? We discuss a few topics of interest below.

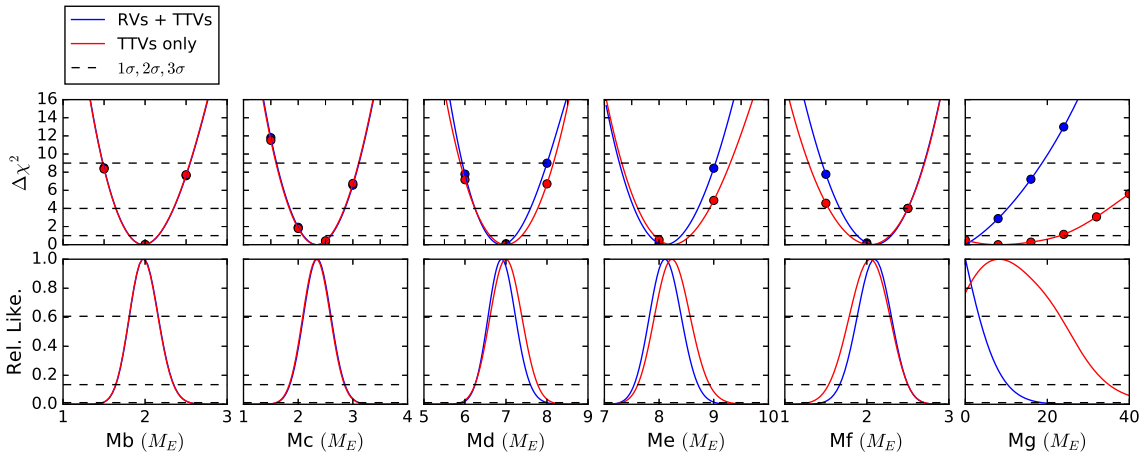

Figure 5.13: Contribution to the Planet Mass Determinations from RVs. Upper left: $\Delta\chi^2$ goodness of fit to the RVs + TTVs (blue) and to the TTVs only (red) as a function of the mass of Kepler-11 b. Lower left: The relative likelihood of various masses for Kepler-11 b, given the RVs + TTVs (blue) or the TTVs only (red). The other panels, from left to right, are the corresponding plots for planets c, d, e, f, and g. For planet g, the RVs assist the TTVs in in constraining the low mass of the planet.

5.4.1 The Kepler-11 planets are not rocky.

Of particular interest are small planets that might be rocky. Weiss & Marcy (2014), Rogers (2015), and Dressing et al. (2015) have explored the transition from rocky to non-rocky planets. These studies all find that planets smaller than about 1.5 $R_\oplus$ can have densities consistent with a rocky composition, whereas planets larger than about 1.5 $R_\oplus$ require a layer of lightweight volatiles to explain their low densities. The five inner planets in the Kepler-11 system are larger than 1.5 $R_\oplus$ (the smallest is 1.8 $R_\oplus$), and their densities range from 0.6-1.9 g cm^{-3}. These low densities are inconsistent with purely rocky compositions and require significant volumes of hydrogen. The interior models suggest these planets have mass in hydrogen and helium ranging from 0.5-15 percent of the total mass (L2013).

5.4.2 How did the Kepler-11 planets arrive in their current orbital configuration and obtain their modest gaseous envelopes?

The low densities of the Kepler-11 planets imply that the proto-planetary disk must have contained significant amounts of gas, with a mass of at least a few percent that of the non-volatile dust, when these planets formed. The presence of gas necessitates a different model from the standard formation model for terrestrial planets, in which the planets form after all of the gas has left the sun's proto-planetary disk. The challenges of a formation model for the Kepler-11 planets are that it must (1) reproduce the compact architecture of

low-mass planets, (2) reproduce compositions that are primarily iron/silicate/ice with a few percent mass in hydrogen and helium. Moreover, *Kepler* discovered hundreds of compact, non-resonant planetary systems, so Kepler-11 is not a fluke but a predictable outcome of multi-planet formation physics. The formation mechanism for Kepler-11 should be generally applicable to compact, non-resonant systems of multiple low-mass planets.

The compact configuration of the Kepler-11 planets can be explained if they formed at large orbital distances and migrated inward. Migration while the gas disk is still present has been proposed to explain the existence of Jovian-mass planets at orbital periods of 3 days and the abundance of sub-Neptune sized planets at orbital periods of 10-100 days. Migration in a gas disk might explain how the Kepler-11 cores accreted their thick atmospheres from nebular material. Migration can also occur in the absence of a gas disk. Planet-planet scattering presents a way for planets to migrate inward. However, migration associated with Lidov-Kozai oscillations in particular requires large mutual inclinations ($> 40°$) between the planets, and therefore is unsuitable for transporting the coplanar Kepler-11 system inward (Kozai 1962; Lidov 1962). Regardless of the mechanism, if the Kepler-11 system migrated inward, all six planets must have avoided (or escaped from) entrapment in mean motion resonances (Fabrycky et al. 2014). Furthermore, some eccentricity damping mechanism (i.e., a gas disk) was necessary to produce the near-circular orbits the Kepler-11 planets have today. Hands et al. (2014) successfully simulated the present-day Kepler-11 system by migrating the planets inward in a gas disk, but they found that the migration rates of the planets had to be finely tuned to escape entrapment in mean motion resonances, and the eccentricity damping from the gas disk had to be high. The requirement for strong eccentricity damping suggests that the only viable type of migration for Kepler-11 is migration in a gas-rich disk, and even that scenario must be finely tuned.

Alternatively, in situ formation has been proposed as a potentially viable way to make super-Earths in compact planetary systems (Chiang & Laughlin 2013). Such a formation mechanism requires the proto-planetary disks to be much more massive than the minimum mass solar nebula (MMSN). Lee et al. (2014) find that during the formation of small planets, high opacity from atmospheric dust can drastically slow the cooling of the gas layer. The long cooling time prevents the forming planets from accreting additional gas from the nebula. This mechanism allows the in situ formation of small planets with low gas content, such as the Kepler-11 planets and the hundreds of other compact systems of gas-poor planets discovered by *Kepler*. However, either the metallicity of the disk or the time at which the gas disk dissipates must be finely tuned.

A third option that combines elements of migration theory and in situ formation is inside-out planet formation. Chatterjee & Tan (2014) propose that solid material migrating inward could accumulate at the pressure maximum between the region of the active magneto-rotational instability (MRI-zone) and the inactive MRI "dead zone." This solid material could accrete to form a planetary isolation mass on the timescale that the MRI boundary moves outward. As the MRI boundary and associated pressure maximum moves outward, pebbles accumulate in successive annuli from the inside out. This mechanism potentially results in the in situ formation of compactly spaced planets while the gas disk is still present.

In situ formation and inside-out planet formation more readily reproduce Kepler-11 and similar systems than large-scale disk migration does. To assemble the Kepler-11 system through migration requires fine tuning of the migration rates of all six planets to avoid entrapment in mean-motion resonances. Therefore, we would expect to see many six-planet systems like Kepler-11, but in mean motion resonances, if gas migration were responsible for the current architecture of Kepler-11. On the other hand, in situ planet formation requires fine tuning of the time that the gas disk dissipates. This can be explained if the dissipation of the gas disk is responsible for increased eccentricities of solids in the disk, allowing the solids to coagulate to form the rocky interiors of the Kepler-11 planets (Lee et al. 2014). In inside-out planet formation, the only requirement is that the MRI boundary moves outward sufficiently slowly to form planetary isolation masses of $\sim 2\ M_\oplus$, but not so slowly that the isolation masses grow beyond $\sim 2\ M_\oplus$. The Kepler-11 planetary cores most likely formed nearly in situ, followed by modest migration at most. The planetary cores likely assembled when the gas disk around them was dissipating, allowing them to accrete only small amounts of gas. If the Kepler-11 planets formed nearly in situ (i.e. inside the snow line), they probably do not contain a significant water layer in their interior structures.

5.4.3 Updated mass-radius and density-radius relations.

We incorporate our newly derived mass measurements of the Kepler-11 planets, as well as several new planet discoveries, in an updated mass-radius relation. The planets are the same as those in Weiss & Marcy (2014), with the inclusion of planets listed in Table 5.5. Figure 5.14 shows how the weighted mean density and weighted mean mass vary among planets smaller than 4 Earth radii.

The result from Weiss & Marcy (2014) holds; we identify a peak in planet density at 1.5 $R_\oplus$. Planets up to 1.5 $R_\oplus$ can have densities consistent with a rocky composition analogous to that of Mars, Venus, and Earth (primarily silicates by volume), whereas planets larger than 1.5 $R_\oplus$ require a large fraction of volatiles by volume to explain their low densities. The improved mass measurements of the Kepler-11 planets and the inclusion of Kepler-11 g further support the idea that planets larger than 1.5 $R_\oplus$ have thick gaseous layers. To explain their very-low densities, the Kepler-11 planets require gaseous layers with low mean molecular weight, i.e. hydrogen/helium envelopes.

Acknowledgments

The authors would like to acknowledge Simon Walker, who developed the python wrapper for TTVFast. L.M.W. thanks Björn Benneke and Matt Holman for helpful conversations. The authors wish to extend special thanks to those of Hawai'ian ancestry on whose sacred mountain of Maunakea we are privileged to be guests. Without their generous hospitality, the Keck observations presented herein would not have been possible.

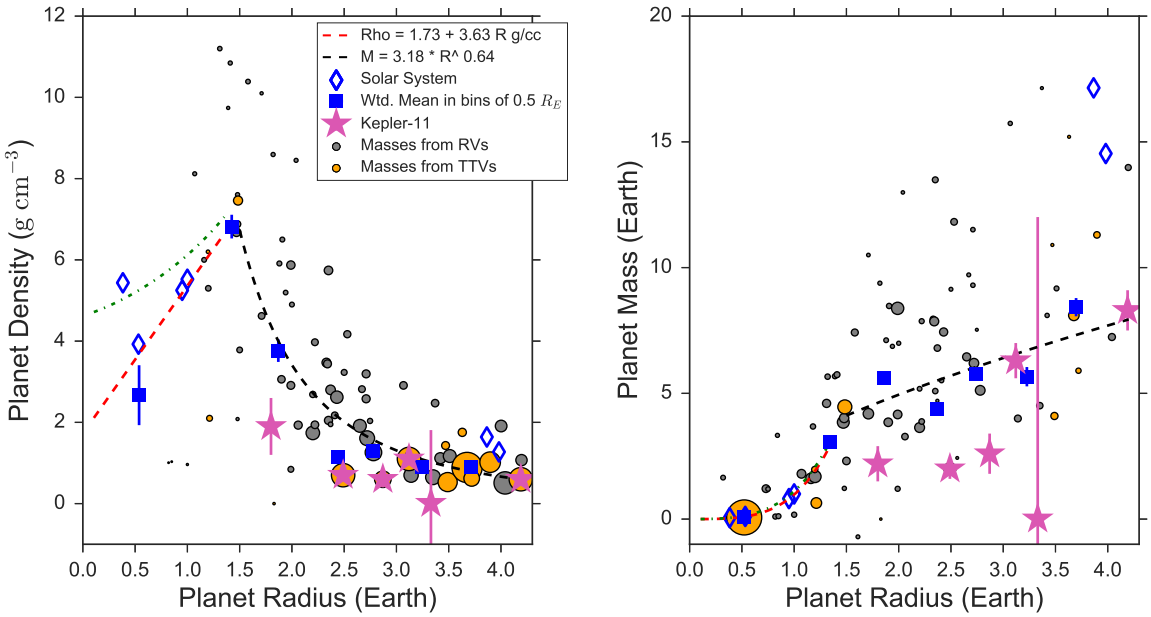

Figure 5.14: Left: planet density as a function of planet radius for exoplanets smaller than 4.2 Earth radii that have measured masses or mass upper limits. This is an update of the work in Weiss & Marcy (2014), but with the the masses of the Kepler-11 planets measured in this paper and several newly discovered planets (see Table 5.5 for a list of recent additions to the census). Planets with mass measurements from RVs are in gray; planets with mass measurements from TTVs are in gold. The size of the dot corresponds to $1/\sigma_\rho^2$. The Kepler-11 planets are shown as large pink stars. The red line is a linear empirical fit to the $1/\sigma^2$-weighted planet density as a function of radius for $R_\mathrm{p} < 1.5R_\oplus$. The black line is a power-law empirical fit to the $1/\sigma^2$-weighted planet mass as a function of radius for $1.5R_\oplus < R_\mathrm{p} < 4R_\oplus$. The green line shows the Seager et al. (2007) predicted density as a function of radius for a differentiated planet with 32.5% Fe and 67.5% $MgSiO_3$ based on a polytropic equation of state. The solar system planets are shown as blue diamonds; the terrestrial planets were included in the fit to density versus radius for $R_\mathrm{p} < 1.5R_\oplus$ but with their density uncertainties artificially inflated to 20% to allow the handful of exoplanets in that size range (Kepler-78 b, Kepler-36 b, Kepler-10 b, Kepler-93 b, Corot-7 b) to contribute to the fit. Uranus and Neptune were not included in the fit for exoplanets with $1.5R_\oplus < R_\mathrm{p} < 4R_\oplus$ because the orbits of Uranus and Neptune (10,000 days) are much longer than the orbits of the exoplanets considered in this sample (up to 100 days), and so Uranus and Neptune might represent substantially different formation and evolution pathways than the super-Earths we are trying to characterize. The blue squares show the weighted mean density in bins of 0.5 $R_\oplus$, and are to guide the eye only. The blue squares and diamonds trace the peak in planet density at 1.5 $R_\oplus$. Right: planet mass as a function of planet radius for the same planets. The symbols and lines are the same as to the left, but the sizes of the dots corresponds to $1/\sigma_m^2$.

Table 5.5: Planetary Mass & Radius Measurements from 2015-2016

Name	Period (d)	Mass ($M_\oplus$)	Radius ($R_\oplus$)	Insolation ($S_\oplus$)	First Ref.	Orbital Ref.
KOI-273 b	10.573753	6.8 ± 1.4	2.37 ± 0.13	119	Borucki et al. (2011)	Gettel et al. (2016)
Kepler-10 b	0.8374907	3.72±0.42	1.47±0.03	3805	Batalha et al. (2011)	Weiss et al. (2016)
Kepler-10 c	45.294301	13.98±1.79	2.35±0.09	18.6	Dumusque et al. (2014)	Weiss et al. (2016)
Kepler-26 b	12.2796	5.12 ± 0.63	2.78±0.11	7.60	Steffen et al. (2012)	Jontof-Hutter et al. (2016)
Kepler-26 c	17.2559	6.20 ± 0.65	2.72±0.12	4.82	Steffen et al. (2012)	Jontof-Hutter et al. (2016)
Kepler-29 b	10.3393	4.51 ± 1.45	3.35±0.22	96	Fabrycky et al. (2012)	Jontof-Hutter et al. (2016)
Kepler-29 c	13.2869	4.00 ± 1.26	3.14±0.20	69	Fabrycky et al. (2012)	Jontof-Hutter et al. (2016)
Kepler-60 b	7.1334	4.19 ± 0.54	1.71±0.13	318	Batalha et al. (2013)	Jontof-Hutter et al. (2016)
Kepler-60 c	8.9187	3.85 ± 0.81	1.90±0.15	236	Batalha et al. (2013)	Jontof-Hutter et al. (2016)
Kepler-60 d	11.8981	4.16 ± 0.80	1.99±0.16	161	Batalha et al. (2013)	Jontof-Hutter et al. (2016)
Kepler-105 c	7.1262	4.60 ± 0.89	1.31±0.07	161	Rowe et al. (2014)	Jontof-Hutter et al. (2016)
Kepler-307 b	10.4208	7.44 ± 0.89	2.43 ± 0.09	59.7	Rowe et al. (2014)	Jontof-Hutter et al. (2016)
Kepler-307 c	13.0729	3.64 ± 0.61	2.20±0.07	44.0	Rowe et al. (2014)	Jontof-Hutter et al. (2016)
Kepler-11 b	10.30458	2.0 ± 0.7	1.8 ± 0.04	114	Lissauer et al. (2011)	This work
Kepler-11 c	13.02410	2.6 ± 0.8	2.87 ± 0.05	83	Lissauer et al. (2011)	This work
Kepler-11 d	22.69165	6.3 ± 0.7	3.12 ± 0.06	40	Lissauer et al. (2011)	This work
Kepler-11 e	31.99503	8.3 ± 0.8	4.19 ± 0.07	25	Lissauer et al. (2011)	This work
Kepler-11 f	46.69327	2.0 ± 0.4	2.49 ± 0.05	15	Lissauer et al. (2011)	This work
Kepler-11 g	118.39681	< 25	3.33 ± 0.06	4.4	Lissauer et al. (2011)	This work

Table 5.6: Kepler-11 Q1-Q17 TTVs

Planet	Epoch	TT (days*)	σ_T (days)	Cadence
f	0	64.67428313	0.005042239989	lc
c	0	71.17179568	0.004251779939	lc
b	0	71.51404847	0.01109132208	lc
d	0	81.45826742	0.003923903877	lc
b	1	81.82481561	0.01095757331	lc
c	1	84.20251958	0.0046333987	lc
e	0	87.15581918	0.002223498459	lc
b	2	92.11287671	0.009725995047	lc
c	2	97.22168367	0.005255342602	lc
d	1	104.1437648	0.003027173683	lc
c	3	110.2419818	0.003948594996	lc
f	1	111.3511494	0.006001644397	lc
b	4	112.7235653	0.01172211618	lc
e	1	119.1537177	0.00263478478	lc
b	5	123.0226197	0.009812612331	lc
c	4	123.2706653	0.004668829281	lc
d	2	126.8294718	0.003594226893	lc
b	6	133.2903986	0.01373022325	lc
c	5	136.297827	0.004256329454	lc
b	7	143.6384781	0.0097422532	lc
c	6	149.330309	0.004648377885	lc
d	3	149.5196218	0.005149120208	lc
e	2	151.1563849	0.002144741902	lc
b	8	153.9034277	0.01304127919	lc
f	2	158.0282008	0.006314777471	lc
c	7	162.3594223	0.005792038294	lc
d	4	172.2084728	0.004136619678	lc
b	10	174.553152	0.009550424393	lc
c	8	175.3799245	0.00482294443	lc
e	3	183.1492939	0.002226512988	lc
b	11	184.8441465	0.01053580054	lc
c	9	188.390617	0.007490424699	lc
d	5	194.8979423	0.00265675745	sc

Table 5.6 (cont'd): Kepler-11 Q1-Q17 TTVs

Planet	Epoch	TT (days*)	σ_T (days)	Cadence
b	12	195.1358781	0.006203204537	sc
c	10	201.433986	0.002830744022	sc
f	3	204.703404	0.00621251174	sc
b	13	205.4568912	0.006457319096	sc
c	11	214.4564436	0.002894399743	sc
e	4	215.1478624	0.002115380391	sc
b	14	215.7630763	0.006444298492	sc
d	6	217.5729033	0.002701682274	sc
g	1	220.2885682	0.002831729793	sc
b	15	226.0577627	0.006833985318	sc
c	12	227.4721637	0.002787967756	sc
b	16	236.3745981	0.006464835785	sc
d	7	240.2662138	0.002605182846	sc
c	13	240.4998637	0.002747359449	sc
b	17	246.6709324	0.006429843692	sc
e	5	247.1411588	0.002037454401	sc
f	4	251.3990797	0.004137326387	sc
c	14	253.5256024	0.002765039016	sc
b	18	256.9740225	0.0067093179	sc
d	8	262.9535216	0.002601831938	sc
c	15	266.5539405	0.002846051358	sc
b	19	267.2669456	0.00623710243	sc
b	20	277.5810736	0.006611648317	sc
e	6	279.1379737	0.00196132631	sc
c	16	279.5679197	0.002707825832	sc
d	9	285.6342451	0.002513142687	sc
b	21	287.8933542	0.006465541267	sc
c	17	292.5991528	0.002818077811	sc
f	5	298.0862174	0.004732516088	sc
b	22	298.1918992	0.01039213953	sc
c	18	305.6150942	0.002794450097	sc
d	10	308.3334784	0.002548356663	sc
b	23	308.4929117	0.006380088035	sc

Table 5.6 (cont'd): Kepler-11 Q1-Q17 TTVs

Planet	Epoch	TT (days*)	σ_T (days)	Cadence
e	7	311.1274805	0.002080677121	sc
c	19	318.6474506	0.0027489726	sc
b	24	318.7999335	0.0064278657	sc
b	25	329.1070697	0.006703920536	sc
g	2	338.6616587	0.002915155902	sc
b	26	339.3984588	0.006494784996	sc
e	8	343.119544	0.002024261897	sc
c	21	344.7014279	0.002746154663	sc
f	6	344.7803755	0.004165072418	sc
b	27	349.7113689	0.006514279158	sc
d	12	353.7067008	0.002589222913	sc
c	22	357.7219791	0.002769041933	sc
b	28	360.02831	0.00636795308	sc
b	29	370.3075763	0.006301284312	sc
c	23	370.7524687	0.002898012294	sc
e	9	375.1217798	0.002114015317	sc
b	30	380.6255852	0.006006269087	sc
c	24	383.7783065	0.002710081497	sc
b	31	390.923021	0.006271049739	sc
f	7	391.4778937	0.004084747349	sc
c	25	396.8059717	0.002650676023	sc
d	14	399.0715869	0.002509830515	sc
b	32	401.2304577	0.00597958691	sc
e	10	407.1192161	0.001909691855	sc
c	26	409.8325904	0.002653863914	sc
b	33	411.5134942	0.00597815776	sc
d	15	421.7598238	0.002540353635	sc
b	34	421.8446297	0.006283117181	sc
c	27	422.8484832	0.002751274397	sc
b	35	432.1425709	0.006352345252	sc
c	28	435.8772581	0.002651113818	sc
f	8	438.1712165	0.004058688418	sc
e	11	439.1209881	0.001952730858	sc

Table 5.6 (cont'd): Kepler-11 Q1-Q17 TTVs

Planet	Epoch	TT (days*)	σ_T (days)	Cadence
b	36	442.4365775	0.005881275023	sc
d	16	444.4424654	0.00246196123	sc
c	29	448.9026419	0.00262847563	sc
b	37	452.7430068	0.005949492564	sc
g	3	457.0481381	0.002753874073	sc
c	30	461.9319378	0.002666133852	sc
b	38	463.0444883	0.006183984308	sc
d	17	467.1414513	0.00252683886	sc
b	39	473.3495902	0.005968878263	sc
c	31	474.9491601	0.002771918986	sc
b	40	483.6524484	0.006158696227	sc
f	9	484.8673911	0.00413485357	sc
c	32	487.9753146	0.002808477384	sc
d	18	489.8245116	0.002479562679	sc
b	41	493.9633351	0.006266423064	sc
c	33	500.9964774	0.00248260436	sc
e	13	503.0980431	0.001968951323	sc
b	42	504.2725029	0.00609407095	sc
d	19	512.5137451	0.002472431882	sc
c	34	514.0237868	0.002795977611	sc
b	43	514.5823389	0.005990607752	sc
b	44	524.8820296	0.006194903895	sc
c	35	527.0385303	0.002636796445	sc
e	14	535.0932437	0.001951656294	sc
b	45	535.1913031	0.006236556374	sc
d	20	535.2010101	0.002515148638	sc
c	36	540.0706838	0.002670399243	sc
b	46	545.496194	0.006338540954	sc
c	37	553.0906027	0.002781123866	sc
b	47	555.7966158	0.006463453417	sc
d	21	557.8884212	0.002518477705	sc
c	38	566.1210447	0.008742137106	sc
g	4	575.4206936	0.002912724535	sc

Table 5.6 (cont'd): Kepler-11 Q1-Q17 TTVs

Planet	Epoch	TT (days*)	σ_T (days)	Cadence
b	49	576.3978477	0.00633254528	sc
f	11	578.2295529	0.004285850089	sc
c	39	579.1491801	0.002836404826	sc
d	22	580.568502	0.002725307476	sc
b	50	586.7044802	0.006594222755	sc
c	40	592.174203	0.003165494386	sc
b	51	597.0073926	0.006492988735	sc
e	16	599.1002293	0.002063475265	sc
d	23	603.247517	0.00267215381	sc
c	41	605.1990382	0.00284129644	sc
b	52	607.2929988	0.006305286177	sc
b	53	617.6119424	0.006562046454	sc
c	42	618.2279484	0.002767552607	sc
f	12	624.9037527	0.004280471112	sc
d	24	625.9538309	0.002660483155	sc
b	54	627.911054	0.006684449589	sc
b	55	638.2187833	0.006496241644	sc
b	56	648.5239987	0.006488207352	sc
d	25	648.6331306	0.002628046079	sc
b	58	669.1351527	0.006358025693	sc
d	26	671.3215982	0.002634248684	sc
f	13	671.5802719	0.004279708864	sc
b	59	679.4396228	0.006451185323	sc
c	47	683.3550072	0.00288510033	sc
b	60	689.7409679	0.006419466184	sc
g	5	693.7832543	0.003632644167	sc
b	61	700.042531	0.00645680055	sc
c	49	709.3935837	0.002919471602	sc
b	62	710.353384	0.006312305414	sc
d	28	716.6928084	0.002698233703	sc
f	14	718.2703663	0.004368927098	sc
b	63	720.6577478	0.006453223201	sc
c	50	722.4188594	0.002826845348	sc

Table 5.6 (cont'd): Kepler-11 Q1-Q17 TTVs

Planet	Epoch	TT (days*)	σ_T (days)	Cadence
e	20	727.0715803	0.002011930722	sc
b	64	730.9581596	0.006462559555	sc
c	52	748.468391	0.002721417093	sc
b	66	751.5820831	0.006013801973	sc
e	21	759.0738378	0.001907838904	sc
c	53	761.4924388	0.002604642914	sc
b	67	761.8766191	0.005811198582	sc
d	30	762.0610341	0.002389403706	sc
f	15	764.9332526	0.003960649294	sc
b	68	772.1839154	0.006663894411	sc
c	54	774.5163765	0.002599501224	sc
b	69	782.4885662	0.005990152321	sc
d	31	784.7600504	0.002433544833	sc
c	55	787.5354944	0.002666380189	sc
e	22	791.0595368	0.001897598597	sc
b	70	792.7757794	0.00684015693	sc
c	56	800.5698527	0.002722954047	sc
b	71	803.0884919	0.005917274962	sc
f	16	811.631839	0.004021559504	sc
g	6	812.1818824	0.002745066989	sc
b	72	813.4010523	0.006167099783	sc
c	57	813.5963822	0.002677260742	sc
e	23	823.0589757	0.001866419201	sc
b	73	823.6944865	0.005873291922	sc
c	58	826.6232339	0.002684893645	sc
d	33	830.1344296	0.002433551678	sc
b	74	833.9973767	0.006069421517	sc
b	75	844.2872985	0.00626614413	sc
c	60	852.6761339	0.002726417438	sc
d	34	852.8151617	0.002486895206	sc
b	76	854.6129101	0.006175080907	sc
e	24	855.0512101	0.001904274954	sc
f	17	858.316556	0.003963612731	sc

Table 5.6 (cont'd): Kepler-11 Q1-Q17 TTVs

Planet	Epoch	TT (days*)	σ_T (days)	Cadence
b	77	864.9132168	0.006530620962	sc
c	61	865.7060016	0.002772811653	sc
b	78	875.2219896	0.006701212516	sc
d	35	875.5049182	0.002662129929	sc
c	62	878.7250712	0.002780435867	sc
b	79	885.5108014	0.00624528354	sc
e	25	887.0472977	0.001988890133	sc
c	63	891.7467008	0.002757301656	sc
b	80	895.8217143	0.006356792045	sc
d	36	898.1897979	0.002504278818	sc
c	64	904.7757193	0.002885549753	sc
f	18	905.0161998	0.004166898298	sc
b	81	906.1287699	0.006216398152	sc
b	82	916.4294295	0.006341708651	sc
c	65	917.802475	0.002834862592	sc
e	26	919.044279	0.002000641294	sc
d	37	920.8770817	0.002573587584	sc
b	83	926.7362749	0.005940662401	sc
g	7	930.5538311	0.002798652526	sc
c	66	930.8172957	0.002646221432	sc
d	38	943.5687479	0.002669860604	sc
c	67	943.837117	0.002896278676	sc
b	85	947.3385599	0.006783288831	sc
e	27	951.0362795	0.002093726438	sc
f	19	951.7078516	0.004401524607	sc
c	68	956.868617	0.002768179	sc
b	86	957.6510918	0.006761735663	sc
d	39	966.2507885	0.002605050109	sc
b	87	967.9658381	0.006786519641	sc
c	69	969.8910359	0.002834699912	sc
b	88	978.2490438	0.006810963552	sc
c	70	982.9255445	0.002913950671	sc
e	28	983.0401094	0.002089395601	sc

Table 5.6 (cont'd): Kepler-11 Q1-Q17 TTVs

Planet	Epoch	TT (days*)	σ_T (days)	Cadence
b	89	988.5625193	0.006679508958	sc
d	40	988.9315872	0.002743456614	sc
c	71	995.9421262	0.002935981552	sc
f	20	998.407693	0.004186539026	sc
b	90	998.8636676	0.006846047006	sc
c	72	1008.966857	0.002695261977	sc
b	91	1009.165985	0.006307582298	sc
d	41	1011.633994	0.002566289948	sc
e	29	1015.021698	0.00210036912	sc
b	92	1019.478462	0.006267219348	sc
c	73	1021.988365	0.002857892263	sc
b	93	1029.799187	0.009621018717	sc
d	42	1034.316072	0.002690631748	sc
c	74	1035.016053	0.00286494297	sc
b	94	1040.082092	0.006684853621	sc
f	21	1045.086207	0.004241246774	sc
e	30	1047.021181	0.002124971579	sc
c	75	1048.044659	0.003135289276	sc
g	8	1048.937691	0.00318828535	sc
d	43	1057.004866	0.002714157756	sc
b	96	1060.693386	0.006779287936	sc
c	76	1061.068173	0.002887181164	sc
b	97	1070.983471	0.006628013487	sc
c	77	1074.096535	0.002822118634	sc
e	31	1079.01626	0.002073312453	sc
d	44	1079.691898	0.002581501511	sc
b	98	1081.286833	0.006484636205	sc
b	99	1091.597794	0.006443266297	sc
f	22	1091.773093	0.004428228286	sc
c	79	1100.154371	0.002894211547	sc
b	100	1101.905345	0.006725734677	sc
d	45	1102.371698	0.002722507961	sc
e	32	1111.018325	0.002046729697	sc

Table 5.6 (cont'd): Kepler-11 Q1-Q17 TTVs

Planet	Epoch	TT (days*)	σ_T (days)	Cadence
b	101	1112.208305	0.009919473853	sc
b	102	1122.517053	0.005920301576	sc
d	46	1125.059431	0.002476632937	sc
c	81	1126.194305	0.00264127676	sc
b	103	1132.813679	0.006045605692	sc
f	23	1138.459934	0.00409447279	sc
c	82	1139.219944	0.002715145382	sc
e	33	1143.020277	0.001899805845	sc
b	104	1143.117113	0.006033114649	sc
d	47	1147.737192	0.00245454296	sc
c	83	1152.24725	0.002727480745	sc
b	105	1153.41205	0.006606635802	sc
b	106	1163.705321	0.006369737904	sc
c	84	1165.270982	0.002923669329	sc
g	9	1167.320055	0.002790267149	sc
d	48	1170.44073	0.002486422069	sc
b	107	1174.030964	0.006378899954	sc
e	34	1175.002685	0.001927631727	sc
b	108	1184.337826	0.006226195189	sc
f	24	1185.132604	0.003910299185	sc
c	86	1191.325634	0.002627724922	sc
d	49	1193.131275	0.00256538292	sc
b	109	1194.650836	0.006295687055	sc
c	87	1204.33863	0.002811264173	sc
b	110	1204.948698	0.006280844976	sc
b	111	1215.248903	0.006114696089	sc
d	50	1215.816653	0.00250440412	sc
c	88	1217.360065	0.002943900821	sc
c	89	1230.386757	0.002604991044	sc
f	25	1231.801047	0.004205429519	sc
b	113	1235.855524	0.006227449588	sc
c	90	1243.418788	0.002738052523	sc
b	114	1246.174996	0.006645907711	sc

Table 5.6 (cont'd): Kepler-11 Q1-Q17 TTVs

Planet	Epoch	TT (days*)	σ_T (days)	Cadence
c	91	1256.44201	0.002813751147	sc
b	115	1256.470547	0.006386834073	sc
d	52	1261.185021	0.002401119914	sc
b	116	1266.780246	0.006110673707	sc
e	37	1270.997669	0.001866909458	sc
b	117	1277.073432	0.006251072421	sc
f	26	1278.489032	0.004236537985	sc
c	93	1282.495259	0.002788465107	sc
d	53	1283.874797	0.002558946037	sc
g	10	1285.691238	0.002704044212	sc
b	118	1287.381889	0.006048446842	sc
c	94	1295.5224	0.002666961405	sc
b	119	1297.68742	0.006344753237	sc
e	38	1302.999126	0.001967102201	sc
d	54	1306.550585	0.003895171295	sc
b	120	1307.988507	0.006844693215	sc
c	95	1308.542176	0.002824681807	sc
b	121	1318.297572	0.006698033991	sc
c	96	1321.578896	0.003077406546	sc
f	27	1325.172644	0.004594162053	sc
b	122	1328.579676	0.006678600553	sc
d	55	1329.252026	0.002673372036	sc
c	97	1334.59861	0.002864560215	sc
e	39	1334.982048	0.002116296464	sc
b	123	1338.901794	0.006556511173	sc
d	56	1351.936982	0.002610171501	sc
b	125	1359.505833	0.006466712044	sc
c	99	1360.651214	0.002850483091	sc
e	40	1366.984191	0.002071721824	sc
b	126	1369.795938	0.006777229278	sc
f	28	1371.860501	0.004162081606	sc
c	100	1373.674816	0.002873448171	sc
d	57	1374.626584	0.002675539896	sc

Table 5.6 (cont'd): Kepler-11 Q1-Q17 TTVs

Planet	Epoch	TT (days*)	σ_T (days)	Cadence
b	127	1380.113869	0.006574121106	sc
c	101	1386.696178	0.002853367711	sc
b	128	1390.414761	0.0064167448	sc
d	58	1397.316739	0.002632885837	sc
e	41	1398.978508	0.002048035407	sc
c	102	1399.721438	0.002715236109	sc
b	129	1400.716002	0.006336838853	sc
g	11	1404.065772	0.004120021625	sc
c	104	1425.76457	0.002872991656	sc
e	42	1430.972586	0.002838676363	sc
b	132	1431.64258	0.006571104264	sc
c	105	1438.789115	0.003048456328	sc
b	133	1441.943508	0.006586703815	sc
d	60	1442.682294	0.002687239112	sc
c	106	1451.815969	0.002971342012	sc
b	134	1452.263491	0.006329018991	sc
b	135	1462.559161	0.006442804827	sc
e	43	1462.968989	0.002087951854	sc
c	107	1464.844256	0.003031704593	sc
f	30	1465.242292	0.004392080267	sc
d	61	1465.364951	0.002709482851	sc
b	136	1472.845695	0.006550811011	sc
c	108	1477.866788	0.002847067948	sc
b	137	1483.169867	0.006318393969	sc
d	62	1488.062435	0.002650157134	sc
c	109	1490.896061	0.004146010914	sc
b	138	1493.455373	0.006368392769	sc
e	44	1494.955449	0.002033138872	sc
b	139	1503.760941	0.006490594837	sc
c	110	1503.918941	0.002940486703	sc
d	63	1510.740133	0.002638861003	sc
f	31	1511.939297	0.004249366311	sc
b	140	1514.069872	0.006101746304	sc

Table 5.6 (cont'd): Kepler-11 Q1-Q17 TTVs

Planet	Epoch	TT (days*)	σ_T (days)	Cadence
g	12	1522.455423	0.002873205139	sc

Note. — *Reference time is BJD 2454900.0. Cadences "sc" and "lc" correspond to short and long cadence data.

6

Automated Planet Finder

6.1 Introduction

Hundreds of Doppler observations of a single star are necessary to find a small planet orbiting it. A telescope specialized for the Doppler-method planet hunting rapidly increases the rate of planet detection. The Automated Planet Finder (APF) is a mid-size telescope dedicated to discovering new planets and measuring planet masses via the Doppler technique. After just two years of operation, the number and quality of APF science observations rival a decade of Keck observations from the California Planet Search (Fulton et al. 2015).

The APF is located at Lick Observatory on Mt. Hamilton, CA, at 4,220 ft. elevation, above most of the weather and some of the light pollution of the San Jose metropolitan area (Figure 6.1). The diameter of the primary mirror is 2.4 meters. The sole instrument onboard the APF is the high-resolution, slit-fed, echelle Levy spectrometer, which sits at one of the two Nasmyth foci. The Levy spectrometer has formats capable of resolution $R = 120,000$ and spans 3743-9800 Angstroms in wavelength. The removable molecular iodine gas cell provides a precise wavelength calibration source, enabling a velocity precision of $2 \mathrm{m\,s^{-1}}$ for bright, sun-like stars.

The automation of the APF, which primarily occurred from 2013-2014, was a major project in which over a dozen people made significant contributions. Vogt et al. (2014), Radovan et al. (2014), and Burt et al. (2014) detail the construction, commissioning, and roboticization of the APF. This chapter focuses on my scientific program on the APF and my technical contributions to the automatic pipeline.

6.2 Searching for New Planets in Multi-planet Systems

Using the APF, I am leading a survey for additional planets in known multi-planet systems. The motivation for this survey is that many RVs are needed to correctly identify the orbital properties of all of the planets in a multi-planet system. Systems that are already known to have at least two planets might have additional planets that cannot yet be dis-

Figure 6.1: The APF and Venus at sunset, Lick Observatory, CA. Copyright Laurie Hatch.

tinguished from the noise. *Kepler* has demonstrated that multi-planet systems are common (Lissauer et al. 2012, 2014; Rowe et al. 2014) and usually coplanar (Fang & Margot 2012; Fabrycky et al. 2014). If the nearby multi-planet systems discovered with RVs are similar to the *Kepler* multi-planet systems, they are likely to have additional, coplanar planets, making them good targets in which to search for additional planets.

6.2.1 Advantages of the APF for this Survey

Intensive, high-cadence RV measurements are especially needed to find and characterize new planets in multi-planet systems. The stellar motion is the sum of the motion induced by each of the planets. The perturbation from each planet can be broken down into the orbital period P, velocity semi-amplitude K, eccentricity e, argument of periastron ω, and time of periastron passage, T_p. Thus, the number of free parameters necessary to find and characterize N planets in a single system is $5\times N+1$ (one for a velocity zero-point). Typically 50-100 RVs are needed to uniquely identify the orbit of one planet; resolving an entire multi-planet system can require hundreds of measurements. Using the highly competitive W. M. Keck Observatory, it took the California Planet Search team over a decade to acquire ∼500 measurements of a handful of the nearest and brightest stars, revealing multiple planets. The dedicated APF has made an additional ∼100 measurements of those same stars in the past year alone. These bountiful new measurements will likely reveal additional planets.

For compact non-transiting planets, identifying the correct orbital periods of the planets can be a major challenge. This is because confusing aliases can arise when observations are infrequent and too widely spaced. For example, after taking just two velocity measurements, it is impossible to tell whether the planet went the short way around the star, the long way around the star, or more than once around the star during the time between the observations. This ambiguity persists until there are enough observations at different times during the planet's orbit to resolve the orbit completely.

Confusing aliases were a major problem in the system 55 Cancri. In this system, the innermost planet (55 Cnc e) has an orbital period of 0.7365 days Dawson & Fabrycky (2010). However, earlier characterizations of the planetary system mistakenly identified the orbital period of 55 Cnc e at 2.817 days (McArthur et al. 2004; Fischer et al. 2008). Identifying the correct orbital period of 55 Cnc e improved the accuracies of the orbital characterizations of all the planets in the system. The corrected minimum mass of 55 Cnc e is $m \sin i = 8.3\pm0.3$ $M_\oplus$(Dragomir et al. 2013). The new ephemeris of 55 Cnc e resulted in a new predicted transit time (von Braun et al. 2011), and a transit was detected (Endl et al. 2012). The transit properties for 55 Cnc e result in a radius measurement of $R_\mathrm{p} = 1.99\pm0.084$ $R_\oplus$, a mass measurement of $M_\mathrm{p} = 8.3\pm0.39$ $M_\oplus$, and a computed bulk density of $\rho_\mathrm{p} = 5.87\pm0.79$ $\mathrm{g\,cm^{-3}}$. This density is too low for 55 Cnc e to have a purely rocky composition. Because the planet's orbital period is extremely short, the amount of radiation it receives from the star would photo-evaporate a hydrogen atmosphere on a very short timescale. Water and other species with high mean molecular weight might stay bound to the planet despite the extreme radiation, and so a steam atmosphere might explain the radius and density of 55

Table 6.1: APF Survey of Bright Stars with Multiple Planets

Name	RA (h:m:s)	Dec. (d:m:s)	m_V	N pla.	N obs.	Last Obs. (days)	First Ref.	Orbit Ref.
HD 7924	01:21:59.1	+76:42:37.0	7.19	3	167	35.6	Howard et al. (2009)	Fulton et al. (2015)
HD 9826	01:36:47.8	+41:24:19.6	4.10	3	89	153.5	Butler et al. (1997)	Wright et al. (2009)
HD 11964a	01:57:09.6	−10:14:32.7	6.42	2	64	113.6	Butler et al. (2006)	Wright et al. (2009)
HD 12661	02:04:34.3	+25:24:51.5	7.44	2	37	138.5	Fischer et al. (2001)	Wright et al. (2009)
HD 13908	02:18:14.6	+65:35:39.7	7.51	2	6	261.5	Moutou et al. (2013)	Moutou et al. (2013)
HD 37124	05:37:02.5	+20:43:50.8	7.68	3	31	554.4	Vogt et al. (2000)	Wright et al. (2011)
HD 38529	05:46:34.9	+01:10:05.5	5.94	2	76	51.6	Fischer et al. (2001)	Wright et al. (2009)
HD 69830	08:18:23.9	−12:37:55.8	5.95	3	90	5.6	Lovis et al. (2006)	Lovis et al. (2006)
HD 74156	08:42:25.1	+04:34:41.2	7.61	2	29	188.3	Naef et al. (2004)	Meschiari et al. (2011)
HD 75732	08:52:35.8	+28:19:51.0	5.95	5	102	43.5	Butler et al. (1997)	Endl et al. (2012)
HD 82943	09:34:50.7	−12:07:46.4	6.53	2	6	351.6	Mayor et al. (2004)	Tan et al. (2013)
HD 90043	10:23:28.4	−00:54:08.1	6.44	2	20	5.5	Johnson et al. (2011)	Johnson et al. (2011)
HD 95128	10:59:28.0	+40:25:48.9	5.04	2	77	5.5	Butler et al. (1996)	Gregory & Fischer (2010)
HD 155358	17:09:34.6	+33:21:21.1	7.27	2	5	308.5	Cochran et al. (2007)	Robertson et al. (2012)
HD 168443	18:20:03.9	−09:35:44.6	6.92	2	48	261.5	Marcy et al. (1999)	Pilyavsky et al. (2011)
HD 183263	19:28:24.6	+08:21:29.0	7.86	2	116	134.7	Marcy et al. (2005)	Wright et al. (2009)
HD 187123	19:46:58.1	+34:25:10.3	7.83	2	48	343.4	Butler et al. (1998)	Wright et al. (2009)
HD 190360	20:03:37.4	+29:53:48.5	5.71	2	121	0.4	Naef et al. (2003)	Wright et al. (2009)
HD 200964	21:06:39.8	+03:48:11.2	6.49	2	101	186.6	Johnson et al. (2011)	Johnson et al. (2011)
HD 217107	22:58:15.5	−02:23:43.4	6.18	2	87	120.6	Fischer et al. (1999)	Wright et al. (2009)
Total	20 stars,	47 planets			1219			

Note. — Stars selected for this survey have at least 2 planets, $m_V < 8$, and Dec. $> -15°$. The selection was made based on querying exoplanets.org (Wright et al. 2011; Han et al. 2014). Observation counts are as of 2016 April 05.

Cnc e. While the exact composition of the planet is still unknown, identifying the correct orbital period and mass of the planet were essential steps in the characterization of this iconic planet.

6.2.2 Target Selection and Progress Report

The APF multi-planet survey began in fall 2013 and is still ongoing. The survey is following 21 stars that are listed in table 6.1. The survey criteria are: (1) the star hosts at least 2 planets detected with radial velocities, (2) the star is bright ($m_V < 8$), (3) the star is accessible from the latitude of the APF (declination $> -15°$).

So far, this survey has accomplished 1219 total observations from the APF with 65 observations per target on average. Combining these new, high-cadence APF RVs with the long baseline of RVs from Keck will characterize the orbits of the planets with the highest precision and accuracy yet. Furthermore, the survey might find new planets. Whether or not any new planets are identified, upper limits will be placed on the possible orbits and masses of additional planets in each of the multi-planet systems.

6.3 Technical Contributions

From June 2013-January 2014, I was one of the commissioners of the APF. My major contribution was to observe with the telescope and to work with engineers to gradually automate my tasks. I oversaw the robotic operations for six months, ensuring that the automatic script performed the correct functions in the correct order at the correct times. Basic human tasks that were challenging to roboticize include the sequences for opening and closing the

telescope and dome, focusing the telescope, using the weather and seeing conditions to alter the planned observations, and correctly responding to bad weather triggers. During commissioning, whenever the robot performed a task incorrectly, I would take over the operations until the problem was resolved and communicated to the appropriate engineers (Figure 6.2).

Figure 6.2: Comssioning the APF, UC Berkeley, CA. Copyright Laurie Hatch.

In addition to participating in the direct efforts to roboticize the telescope, I automated some of the reduction tasks that an observer would traditionally do at the end of the night. I developed an automatic end-of-night routine that stitches together a few basic tasks. The routine fetches the raw data files from the Mt. Hamilton data archive, records the observations in a log sheet, performs the raw reduction on the data, calculates barycentric corrections for the observations, and sends an end-of-night email summarizing the observations (Table 6.3).

I customized the California Planet Search automatic raw reduction pipeline for the APF (Figure 6.3). This algorithm transforms the raw, CCD image of the spectrum into a measurement of intensity as a function of pixel number, which corresponds to wavelength. The raw image (Figure 6.4) is bias-subtracted and flat-fielded. Polynomial fits to the locations of the spectral orders on the CCD are determined (Figure 6.5). Diffuse scattered light inside the spectrometer is measured and subtracted (Figure 6.6). The spatial widths of the spectral orders are determined, and the spatial-dimension information from the slit is collapsed to

increase the signal-to-noise per wavelength bin. The spectrum is extracted, and some cosmic rays are removed (Figure 6.7). Use of our previously determined wavelength calibration provides intensity as a function of wavelength.

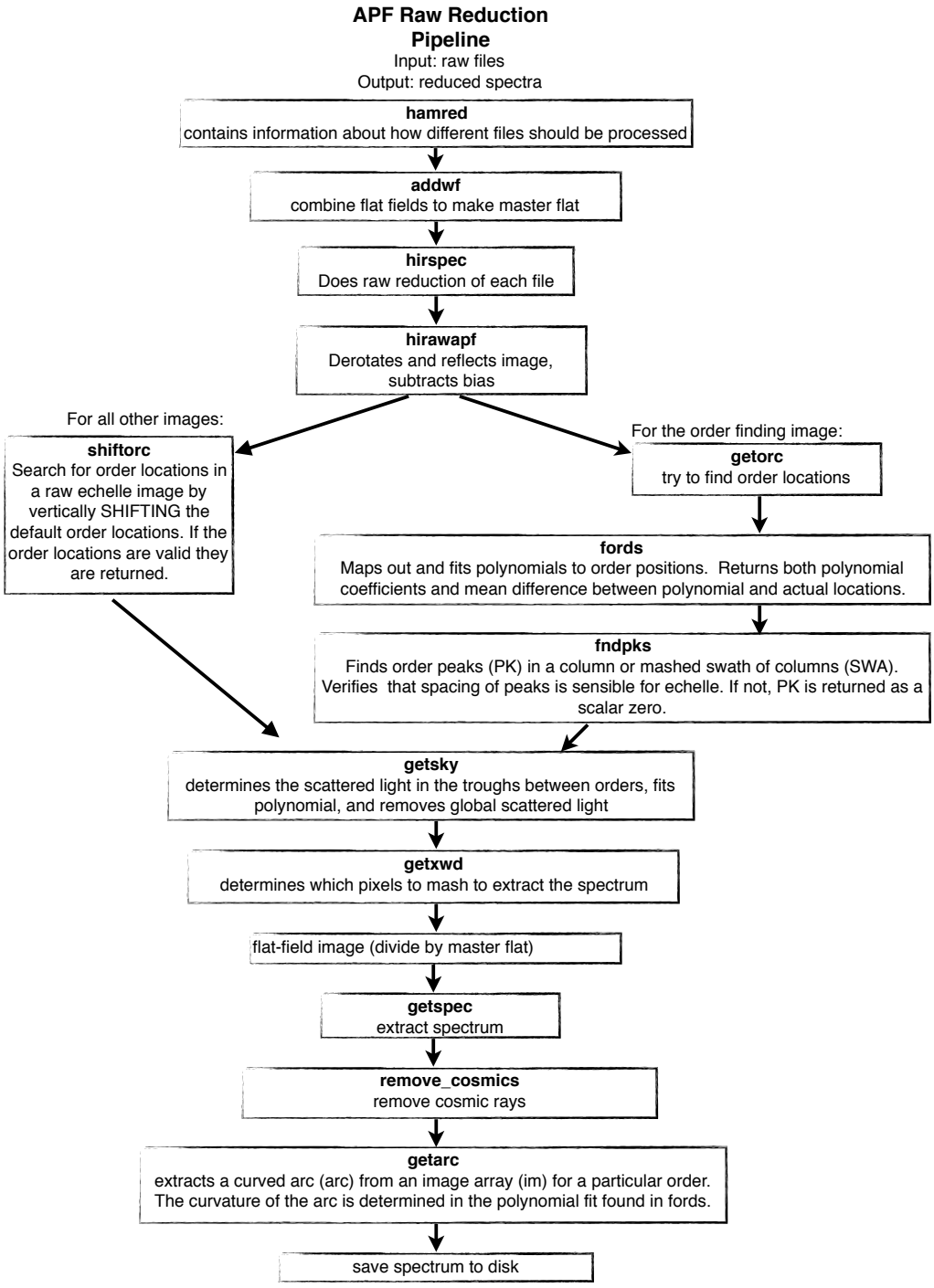

Figure 6.3: The APF raw reduction flowchart.

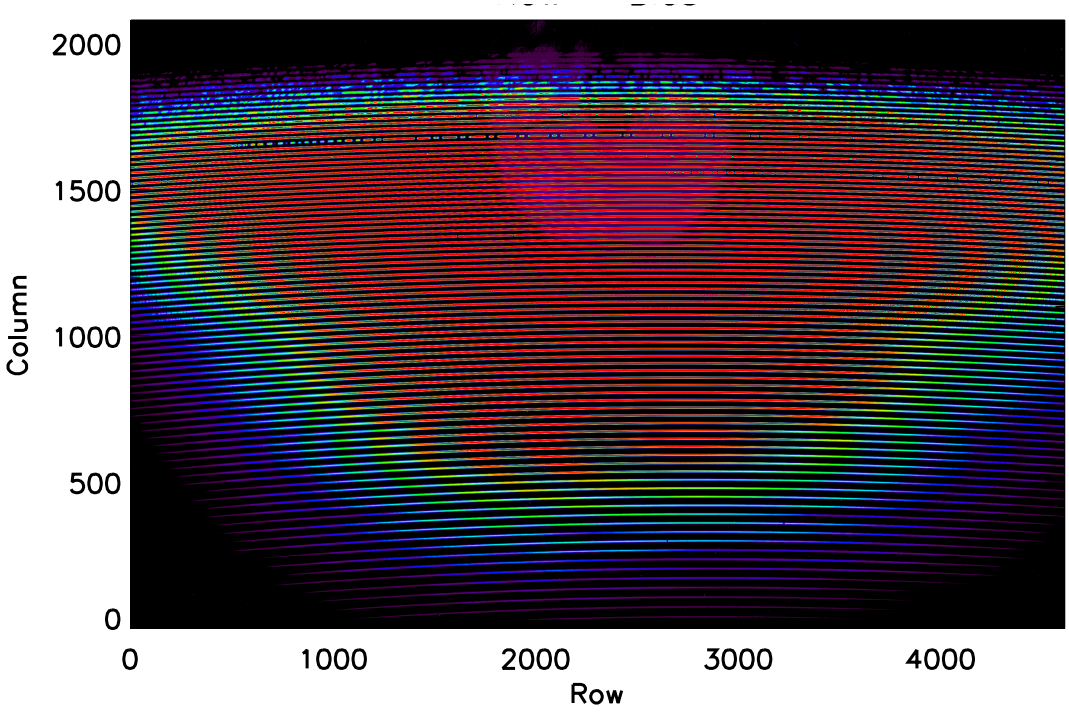

Figure 6.4: The raw CCD image of a spectrum from the APF. The CCD is 4608×2080 pixels. This is the spectrum of a bright, rapidly rotating B star used for pixel positioning calibrations. The spectral orders are the bright arcs that span the rows. In this colormap, the black regions are dark and the red regions are bright. Deep absorption features from telluric lines, especially molecular oxygen, are visible from columns 1500-1700. The bright feature between rows 2000-3000 and columns 1500-1700 is from internal reflection. Some fringing is apparent throughout.

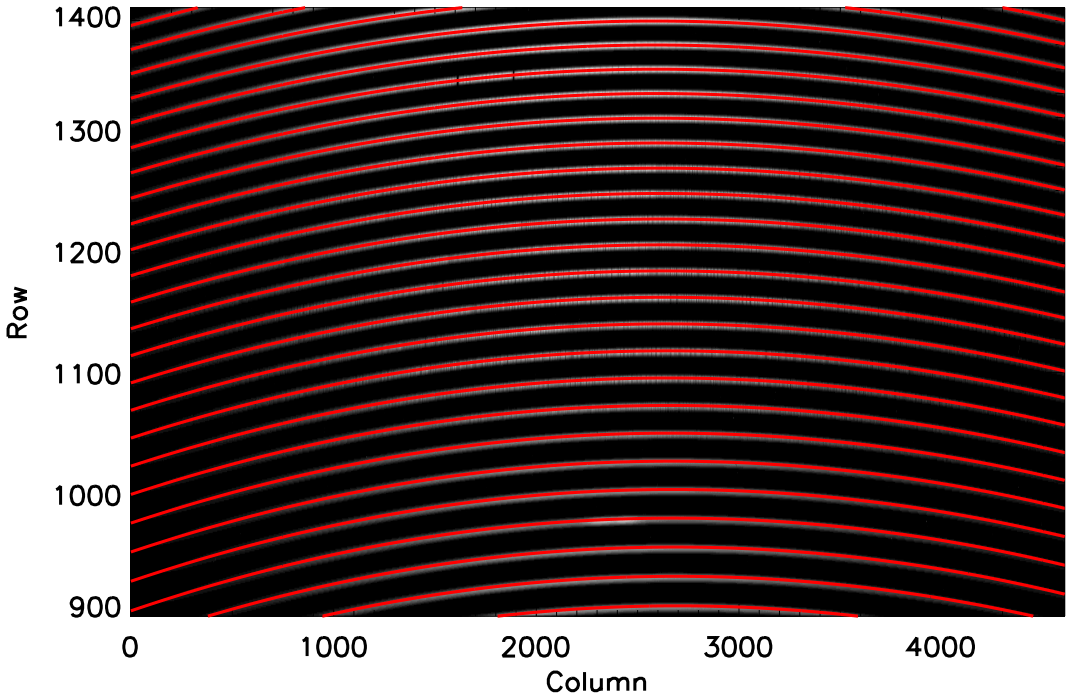

Figure 6.5: A zoomed in region of the flat-fielded spectrum (grayscale) and the polynomial determination of the spectral orders (red). The polynomial order determinations are used to extract the wavelength-dependent 1D spectrum.

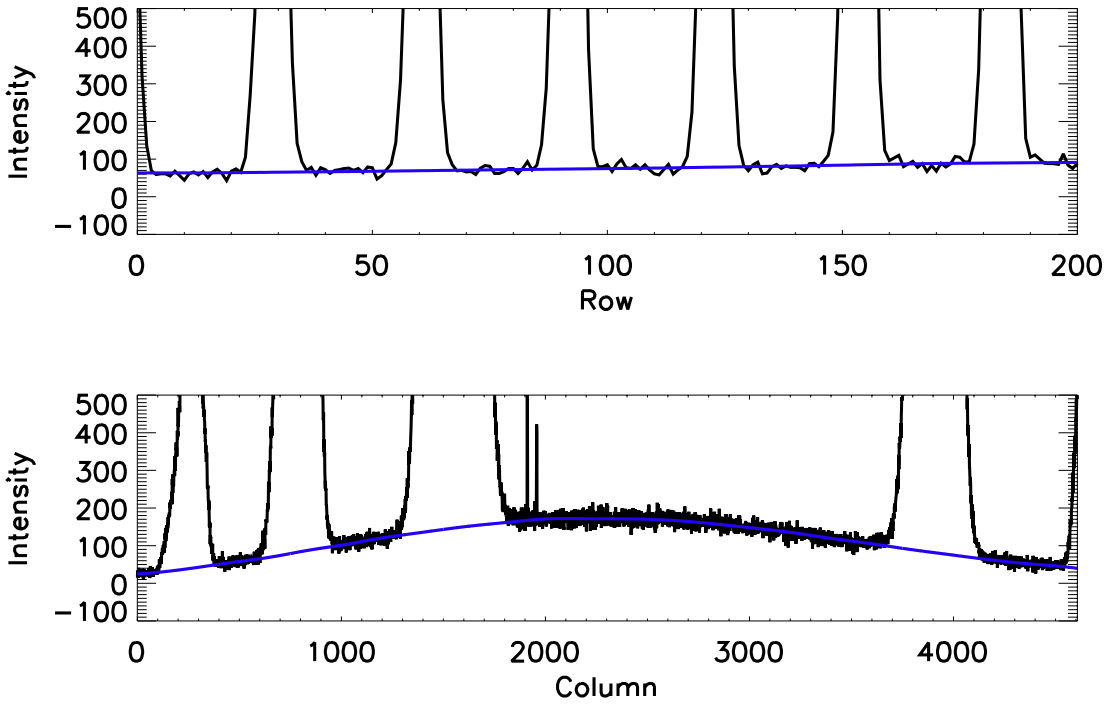

Figure 6.6: Top: A cross section of the light in the orders in the row direction. Bottom: A cross section of the light in the orders in the column direction. The blue line shows a 2D polynomial fit to the contribution of scattered light within the spectrometer.

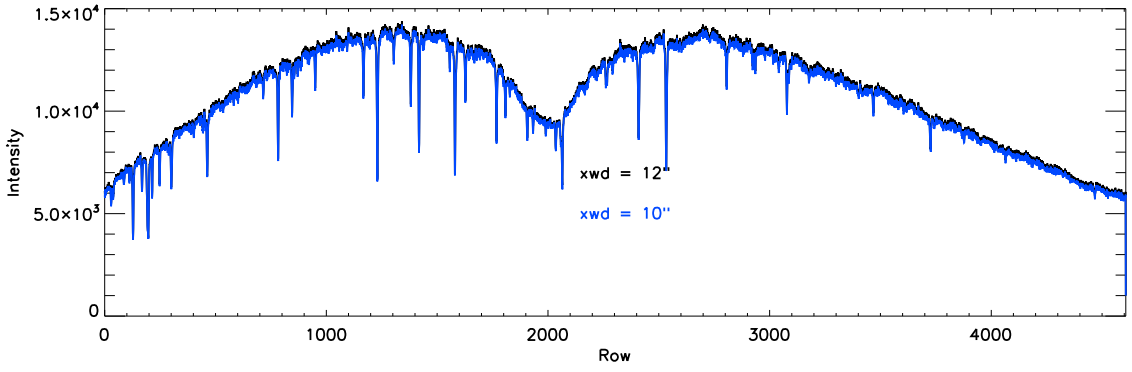

Figure 6.7: The extracted 1D spectrum. This is the order containing the Hα transition at 6563Å(2000 pixels). This absorption feature is broad because the target is a rapidly rotating ($v \sin i > 100 \mathrm{km\,s^{-1}}$) B star, which causes extreme Doppler broadening of the spectral features. The narrow absorption lines are telluric lines.

Table 6.2: APF Logsheet "aou" from UT 2016 March 26

1 Obs (num)	2 Object Name	3 I2 (y/n)	4 Flux Wtd. Midpoint	5 Exposure Time (s)	6 Decker	7 Counts	8 HA	9 Az/El (deg.)	10 Spec Temp (C)	11 Dome Temp (C)	12 Seeing ($''$)
100-120	Focus	n	21:40:28	10	P	0.00G	5.08	90/175	15.	12.	
121-170	WideFlat	n	22:52:45	40	B	0.00G	6.13	101/189	15.	13.	
171	ThAr	n	22:54:15	20	W	0.00G	6.15	101/189	13.	13.	
172	ThAr	n	22:55:20	20	W	0.00G	7.00	102/189	15.	13.	
173	ThAr	n	22:56:34	40	N	0.00G	7.03	102/190	16.	13.	
174	ThAr	n	22:57:59	40	N	0.00G	7.05	102/190	16.	13.	
175	Iodine	y	23:00:45	150	N	0.00G	7.11	103/191	13.	13.	
176	Iodine	y	23:04:00	150	N	0.00G	7.00	103/191	17.	13.	
177	Iodine	y	23:06:37	75	W	0.00G	7.03	103/192	16.	13.	
178	Iodine	y	23:08:37	75	W	0.00G	7.06	104/192	18.	13.	
179	twil-hr2198	y	02:31:02	263	W	2.01G	0.15	199/67	12.	11.	3.15
180	twil-hr2198	y	02:36:24	299	W	2.00G	0.08	202/67	12.	10.	2.63
181	twil-hr2198	y	02:42:10	300	W	1.88G	0.01	205/66	13.	10.	2.41
182	twil-hr2198	y	02:47:57	300	W	1.81G	0.10	209/66	11.	10.	2.34
183	twil-hr2198	y	02:55:10	300	W	1.85G	0.06	212/65	11.	9.8	2.22
184	hr2198	y	03:08:01	300	W	1.65G	1.10	219/64	11.	9.3	2.43
185	HIP32349	y	03:11:57	2	W	2.28G	0.08	190/35	12.	9.2	
186	82885	y	03:14:32	52	W	1.01G	2.20	83/63	11.	9.0	1.62
187	89269	y	03:17:16	175	W	0.50G	2.86	64/57	13.	9.1	1.62
188	89269	y	03:21:04	193	W	0.50G	2.79	64/57	11.	9.1	2.04
189	52711	y	03:26:21	240	W	1.00G	0.05	223/79	13	9.1	1.77
190	52711	y	03:31:11	251	W	1.00G	0.13	227/78	12.	9.0	1.90
191	185144	y	03:36:19	61	W	0.35G	11.7	1/17	11.	8.7	2.38
192	185144	y	03:38:04	57	W	0.36G	11.7	1/17	9.3	8.7	2.13
193	185144	y	03:39:52	81	W	0.35G	11.7	1/17	12.	8.8	3.18
194	65583	y	03:44:58	205	W	0.50G	0.08	171/81	12.	8.8	1.87
195	65583	y	03:49:07	202	W	0.50G	0.02	178/81	13.	8.6	1.84
196	38858	y	03:56:10	288	W	1.00G	2.13	225/37	12.	8.6	2.16
197	84737	y	04:00:51	50	W	1.02G	1.64	57/69	11.	8.5	1.67
198	42618	y	04:04:48	223	W	0.50G	2.05	230/48	14.	8.3	2.55
199	42618	y	04:09:12	204	W	0.50G	2.11	231/47	12.	8.6	1.95
200	86728	y	04:13:44	155	W	1.00G	1.62	98/69	12.	8.5	1.62
201	32923	y	04:17:12	46	W	1.00G	3.13	260/42	11.	8.5	1.63
202	69830	y	04:21:10	282	W	1.00G	0.05	184/39	12	8.3	2.16
203	73752	y	04:27:21	187	W	1.00G	0.01	179/29	12.	8.4	2.50
204	95128	y	04:31:03	51	W	1.01G	2.32	72/62	11.	8.4	1.93
205	97101	y	04:42:58	1222	W	0.50G	2.16	94/62	11.	8.1	1.65
206	97101	y	05:03:25	1191	W	0.50G	1.81	99/66	10.	8.0	1.61
207	95735	y	05:17:41	169	W	0.50G	1.59	87/70	12.	8.1	1.29
208	2M0659-0405	n	05:38:56	1800	B	0.04G	3.05	236/30	12.	8.3	1.73
209	hr4468	y	05:58:34	215	N	1.00G	1.45	152/38	12.	8.2	1.49
210	hr4468	y	06:02:56	209	N	1.01G	1.38	153/38	9.3	8.3	1.56
211	hr4468	y	06:07:04	203	N	1.00G	1.31	154/39	10.	8.3	1.39
212	90043	n	06:13:20	451	N	0.60G	0.03	181/51	12.	8.1	1.27
213	90043	n	06:21:56	485	N	0.60G	0.01	184/51	9.6	8.0	1.38
214	90043	n	06:31:02	496	N	0.60G	0.00	188/51	9.8	8.1	1.43
215	90043	n	06:39:39	460	N	0.60G	0.15	191/51	10.	8.1	1.32
216	90043	n	06:47:51	434	N	0.60G	0.11	194/50	9.8	8.2	1.23
217	hr4828	y	06:54:22	213	N	1.00G	1.60	135/55	9.5	8.3	1.26
218	hr4828	y	06:58:29	197	N	1.00G	1.54	136/55	10.	8.3	1.11
219	hr4828	y	07:02:30	201	N	1.00G	1.47	138/56	12	8.3	1.24
220	97101	y	07:14:12	832	W	0.50G	0.15	211/81	9.1	8.1	1.06
221	97101	y	07:28:28	790	W	0.50G	0.05	226/80	11.	8.0	1.03
222	95735	y	07:39:23	306	W	1.00G	0.11	264/80	8.6	8.2	1.14
223	97658	y	07:54:57	1392	W	1.00G	1.00	232/72	12.	8.5	1.17
224	168009	y	08:10:11	137	W	0.35G	5.90	51/26	12.	8.5	2.53
225	168009	y	08:13:19	141	W	0.35G	5.85	52/26	10.	8.4	2.61
226	168009	y	08:16:27	149	W	0.35G	5.80	52/27	9.6	8.4	2.67
227	166620	y	08:19:39	146	W	0.35G	5.65	59/25	10.	8.4	2.76
228	166620	y	08:22:45	131	W	0.35G	5.60	60/26	8.3	8.5	2.36
229	166620	y	08:25:34	121	W	0.35G	5.55	60/26	11.	8.4	2.02
230	161797	y	08:27:38	27	W	1.01G	5.14	73/25	12.	8.4	1.60
231	161797	y	08:28:51	28	W	1.01G	5.12	73/26	10.	8.4	2.08
232	161797	y	08:30:03	29	W	1.01G	5.10	74/26	11.	8.3	2.11
233	101501	y	08:32:36	32	W	0.61G	1.01	-100/77	8.8	8.4	1.04
234	101501	y	08:33:53	29	W	0.61G	1.03	-99/76	10.	8.3	1.15
235	101501	y	08:35:07	31	W	0.62G	1.05	-99/76	10.	8.3	1.09
236	95128	y	08:36:33	35	W	0.83G	1.10	-73/69	10.	8.3	1.04
237	95128	y	08:37:51	33	W	0.83G	1.13	-73/68	10.	8.3	0.97
238	95128	y	08:39:09	33	W	0.81G	1.15	-73/68	11	8.4	1.02
239	164922	y	08:46:11	582	W	1.00G	5.03	76/26	9.5	8.4	1.76
240	115383	y	08:52:58	53	W	1.01G	0.23	172/61	11.	8.2	1.12

Table 6.2 (cont'd): APF Logsheet "aou" from UT 2016 March 26

1 Obs (num)	2 Object Name	3 I2 (y/n)	4 Flux Wtd. Midpoint	5 Exposure Time (s)	6 Decker	7 Counts	8 HA	9 Az/El (deg.)	10 Spec Temp (C)	11 Dome Temp (C)	12 Seeing ($''$)
241	HIP56445	y	08:55:55	181	W	1.00G	1.03	217/49	11.	8.3	1.11
242	117043	y	09:01:27	249	W	1.00G	0.21	3/64	12.	8.3	0.94
243	117176	y	09:05:31	34	W	0.85G	0.21	172/66	11.	8.2	0.98
244	117176	y	09:06:50	35	W	0.85G	0.19	172/66	12.	8.3	0.92
245	117176	y	09:08:10	36	W	0.86G	0.17	173/66	10	8.2	1.11
246	110897	y	09:13:08	87	W	0.36G	0.13	286/82	12.	8.2	0.99
247	110897	y	09:15:23	94	W	0.35G	0.00	286/81	11.	8.2	1.01
248	110897	y	09:17:42	92	W	0.35G	0.05	285/81	10.	8.2	0.99
249	186408	y	09:21:36	96	W	0.35G	6.15	45/26	9.3	8.2	1.74
250	186408	y	09:27:43	108	W	0.35G	6.05	45/27	10.	8.2	2.17
251	186408	y	09:30:14	105	W	0.35G	6.01	45/27	9.6	8.2	2.10
252	122064	y	09:35:24	270	W	1.00G	0.16	2/65	11	8.2	1.45
253	122742	y	09:41:30	254	W	1.00G	0.17	174/63	10.	8.1	1.46
254	110315	y	09:56:53	1508	W	1.00G	1.13	231/59	9.8	7.9	1.27
255	126053	y	10:11:33	101	W	0.35G	0.01	179/53	10.	7.8	1.76
256	126053	y	10:14:07	115	W	0.35G	0.01	180/53	11.	7.9	2.07
257	126053	y	10:16:44	109	W	0.35G	0.06	181/53	7.6	7.8	1.74
258	182488	y	10:20:06	121	W	0.35G	4.87	70/31	12.	7.8	2.07
259	182488	y	10:22:56	130	W	0.35G	4.82	70/32	11.	7.7	2.17
260	182488	y	10:27:02	276	W	0.69G	4.73	71/33	11.	7.6	2.39
261	130948	y	10:33:30	216	W	1.00G	0.08	174/76	10.	7.6	1.56
262	164507	y	10:37:53	162	W	0.50G	3.19	104/42	8.1	7.7	1.97
263	168723	y	10:40:30	31	W	1.03G	3.51	117/26	9.3	7.7	2.82
264	168723	y	10:41:44	26	W	1.01G	3.49	117/27	9.8	7.8	2.31
265	168723	y	10:42:58	34	W	1.03G	3.47	117/27	8.3	7.8	3.13
266	HIP88404	y	10:45:52	225	W	1.00G	3.09	126/27	9.5	7.8	3.39
267	HIP73695	n	10:50:42	44	W	1.02G	0.04	2/79	10.	7.6	1.70
268	132142	y	11:05:33	1680	W	0.95G	0.06	-17/72	7.4	7.5	1.50
269	131156	y	11:22:45	40	W	1.01G	0.01	209/69	10.	7.5	1.51
270	131156	y	11:24:12	41	W	1.01G	0.05	210/69	8.8	7.4	1.57
271	131156	y	11:25:38	41	W	1.00G	0.06	211/69	8.8	7.5	1.49
272	115617	y	11:29:06	191	W	1.00G	2.03	217/24	9.1	7.6	2.99
273	115617	y	11:33:29	222	W	1.01G	2.10	218/24	7.3	7.6	3.51
274	115617	y	11:37:34	191	W	1.00G	2.00	219/23	10.	7.6	2.80
275	182572	y	11:42:01	164	W	0.70G	3.52	103/36	10	7.4	3.05
276	182572	y	11:45:40	182	W	0.70G	3.46	104/37	10.	7.4	3.25
277	182572	y	11:49:26	172	W	0.70G	3.40	105/37	10	7.4	3.29
278	HIP77655	n	11:54:39	97	W	1.01G	0.06	240/86	8.5	7.4	1.73
279	141004	y	11:56:53	42	W	1.00G	0.00	190/59	9.3	7.4	2.07
280	141004	y	11:58:21	45	W	1.00G	0.03	190/59	10.	7.3	2.66
281	141004	y	11:59:51	46	W	1.02G	0.05	191/59	10.	7.3	2.28
282	188512	y	12:03:24	41	W	1.01G	3.69	107/31	10.	7.4	3.15
283	188512	y	12:04:54	47	W	1.01G	3.66	107/31	11	7.3	3.79
284	188512	y	12:06:21	40	W	1.03G	3.64	107/31	9.3	7.3	3.18
285	HIP75379	y	12:09:39	199	W	1.00G	0.10	198/40	9.5	7.3	2.90
286	145675	y	12:17:08	345	W	1.00G	0.15	-28/82	8.8	7.4	2.02
287	139323	y	12:30:08	1083	W	1.00G	1.05	-74/75	10.	7.1	1.89
288	HIP80179	n	12:43:28	157	W	1.00G	0.03	193/52	8.3	7.1	2.62
289	201091	y	12:48:21	118	W	0.70G	4.12	68/42	8.6	7.1	2.35
290	201091	y	12:51:00	103	W	0.71G	4.08	68/42	11.	7.2	2.11
291	201091	y	12:53:34	119	W	0.71G	4.03	68/43	8.6	7.0	2.43
292	HIP82020	n	12:56:15	46	W	1.01G	0.03	-8/70	10.	7.3	1.79
293	144579	y	13:00:29	328	W	1.00G	1.13	-77/76	8.8	7.3	1.70
294	143761	y	13:04:57	84	W	0.55G	1.06	-99/74	10.	7.1	1.72
295	143761	y	13:07:07	89	W	0.55G	1.11	-98/73	9.3	7.1	1.71
296	143761	y	13:09:23	95	W	0.55G	1.15	-98/73	9.3	7.0	1.86
297	141004	y	13:13:10	45	W	1.01G	1.11	222/52	10.	7.0	2.52
298	141004	y	13:14:40	45	W	1.02G	1.13	222/52	8.8	7.0	2.20
299	141004	y	13:16:09	44	W	1.00G	1.00	223/52	9.3	7.0	2.16
300	190360	y	13:18:50	105	W	0.45G	2.55	91/57	7.9	7.0	2.08

Note. — Columns are (1) Observation number, (2) Object name (HD number unless specified otherwise), (3) Iodine gas cell in light path (yes or no), (4) Flux-weighted midpoint time of the observation, (5) duration of the observation in seconds, (6) the decker used, (7) counts achieved on the exposure meter [1.0G correponds to a signal-to-noise of > 250 per pixel], (8) Hour angle, (9) Azimuth/elevation coordinates of the telescope, (10) spectrometer temperature, (11) dome temperature, (12) seeing convolved with guiding errors (in arcseconds).

6.4 Early Results

A version of the material in this section has been published in the Astrophysical Journal (Fulton, B. J., Weiss, L. M., Sinukoff, E., et al. 2015, The Astrophysical Journal, 805, 175).

The discovery and characterization of the multi-planet system around HD 7924 illustrates an early success of the APF multi-planet survey (Fulton et al. 2015). Howard et al. (2009) discovered the innermost planet, HD 7924 b, at an orbital period of 5.4 days and a mass of $m\sin i = 9.26 \pm 1.72 M_\oplus$, using RVs from the W.M. Keck Observatory. 599 additional RVs from Keck and 109 RVs from the APF identified two more planets and refined the orbital properties of planet b. Fulton et al. (2015) found that HD 7924 b has an orbital period of 5.4 days and a mass of $m\sin i = 8.68 \pm 0.51 M_\oplus$, HD 7924 c has an orbital period of 15.3 days and a mass of $m\sin i = 7.9 \pm 0.72 M_\oplus$, and HD 7924 d has an orbital period of 24.5 days and a mass of $m\sin i = 6.4 \pm 0.78 M_\oplus$.

The high cadence of the APF data of HD 7924 allows us to explore short-period orbital solutions. Traditional observations on large telescopes such as Keck often yield only a few nights of data per year, making it difficult to determine whether a short orbital period is an alias of a longer period, or a true physical signal. Although planets with orbital periods shorter than one day are uncommon in the galaxy (around 0.83 ± 0.18 % of K dwarfs; Sanchis-Ojeda et al. 2014), eleven ultra-short period planets have been found[1] due to their high detectability. We search for short period signals using 797 RVs from Keck and 109 RVs from the APF.

Dawson & Fabrycky (2010) outline a rigorous procedure to distinguish between physical and alias periods. Our method for finding the orbital periods and distinguishing aliases draws from their experience and is as follows:

1. Determine the window function of the data to understand which aliases are likely to appear.
2. Compute the periodogram of the data, determining the power and phase at each input frequency.
3. If there is a strong peak in the periodogram, fit an N-planet Keplerian (starting with N=1), using the periodogram peak as the trial period.
4. Subtract the N-planet Keplerian from the data.
5. Compute the periodogram of the Nth planet in the model and compare it to the periodogram of the Nth planet in the data minus the model of the other planets.
6. If a second peak in the periodogram has similar height to the tallest peak and is located at an alias period, repeat steps 3-5 using that trial period.

[1] Based on a 2014 Nov 20 query of exoplanets.org (Wright et al. 2011; Han et al. 2014)

7. If you explored an alias period, choose the model that minimizes χ^2 and best reproduces the observed periodogram. Subtract this model from the RVs.

8. Treat the residuals as the new data set and go back to step 2. Examine the residuals from the N-planet fit for additional planets, and continue until there are no more signals in the periodogram.

The window functions of the individual and combined Keck and APF RV time series are shown in Figure 6.8. The window function is given by

$$W(\nu) = \frac{1}{N} \sum_{j=1}^{N} \exp(-2\pi i \nu t_j), \tag{6.1}$$

where ν is the frequency in units of days^{-1} and t_j is the time of the jth observation. The data sets are complementary: 109 RVs from APF over the past year are well-distributed over the months and the year, and so are only susceptible to the daily aliases, whereas the 797 RVs from Keck over the last decade are distributed in a way that gives some power to daily aliases as well as longer-period aliases. The power in the combined window function illustrates that we might be susceptible to daily aliases, and weak signals in the periodogram might even be susceptible to monthly or yearly aliases.

To take the periodogram of the time series, we use a version of `fasper` (Press & Rybicki 1989) written for Python. We find peaks in the periodogram of the data and residuals at 5.4, 15.3, and 24.5 days that we interpret as planets. We recover a fourth peak at 2500 days that we attribute to long-term stellar magnetic cycle due to the correlation between the RVs and the activity indicator $S_{\rm HK}$ values. The RV time series is shown in Figure 6.9, and the same RVs phase-folded to the orbital periods of the planets and activity signal are shown in Figure 6.10. The derived planet parameters are shown in Table 6.3. The periodograms of the data and periodograms of the Keplerian models associated with these periods are shown in Figure 6.11. We find a fifth peak at 40.8 days, which is also prominent in the periodogram $S_{\rm HK}$ and is likely the rotation period of the star. The 40.8-day signal has a strong alias at 17.1 days and so we test Keplerian models at both 40.8 days and 17.1 days to discriminate which is the true signal and which is the alias (see Figure 6.12). We find that the periodogram of the model 40.8 day signal better matches the alias structure in the periodogram of the data, and so we prefer 40.8 days as a candidate stellar rotation period.

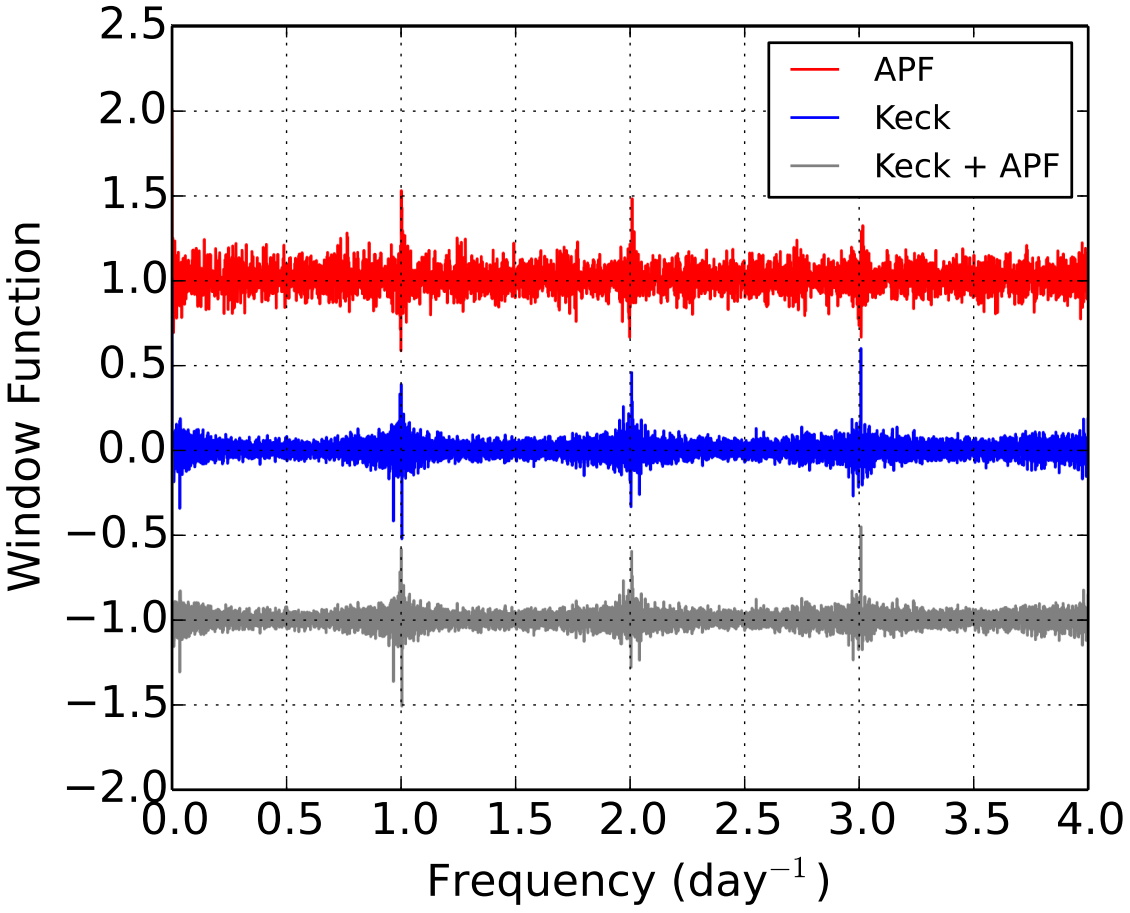

Figure 6.8: The window function of the Keck and APF RV time series. While the APF window function has some power at frequency multiples of one day, it is flat otherwise, whereas the Keck window function has power at low frequencies (corresponding to long-period aliases) and power in broader swaths around the frequency multiples of one day.

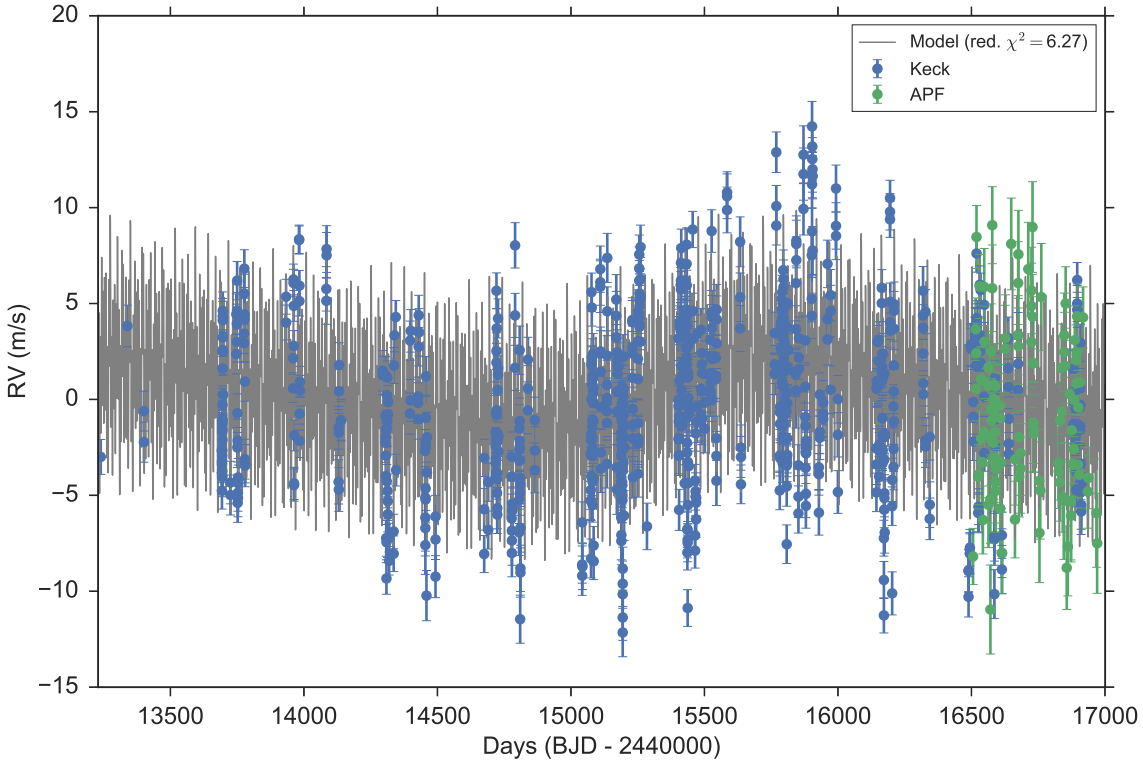

Figure 6.9: The RV time series of HD 7924. The velocities from Keck (blue) and APF (green) are simultaneously fit with a 4-Keplerian model, including a zeropoint offset between the datasets (gray line).

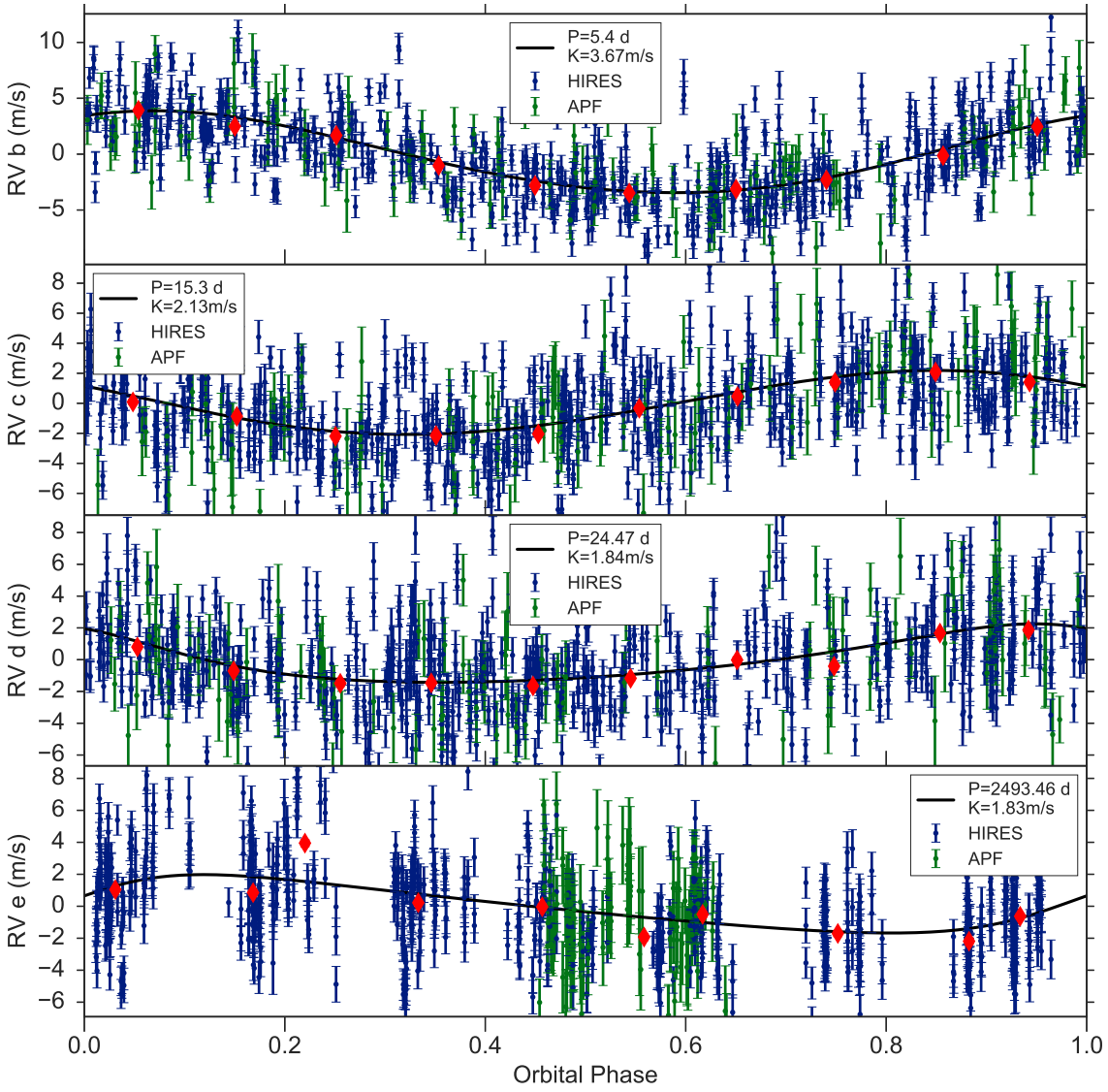

Figure 6.10: The RVs of HD 7924 phase-folded to the orbital periods of the 3 planets (b-d) and a stellar magnetic activity cycle signal ("e"). The blue points are from Keck-HIRES, the green are from the APF-Levy.

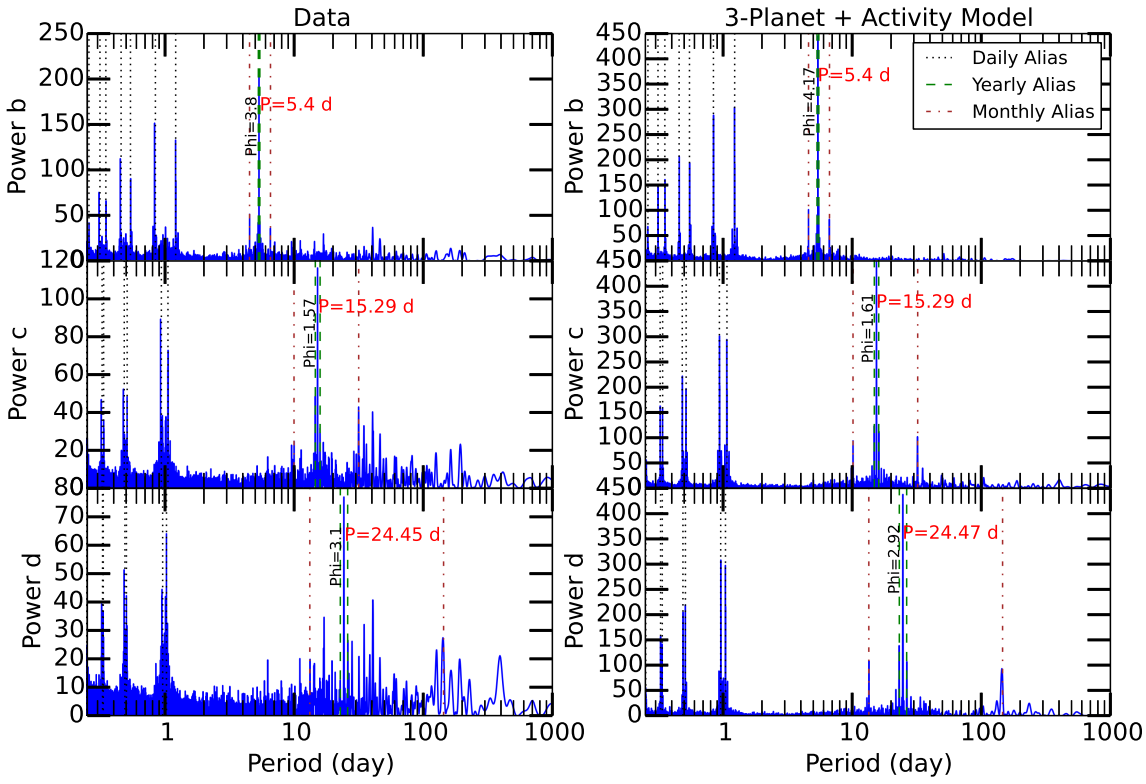

Figure 6.11: Left: Lomb-Scargle periodograms of the data associated with each planet identified, from top to bottom: planet b, planet c, and planet d. In each panel, signals from the other planets and stellar magnetic cycle have been subtracted. The phase of the frequency associated with the peak is given in radians. Right: LS periodograms of the best Keplerian model for each of the planets, from top to bottom, planets b, c, and d. The periodogram of each Keplerian model reproduces the peak period and alias structure of the data.

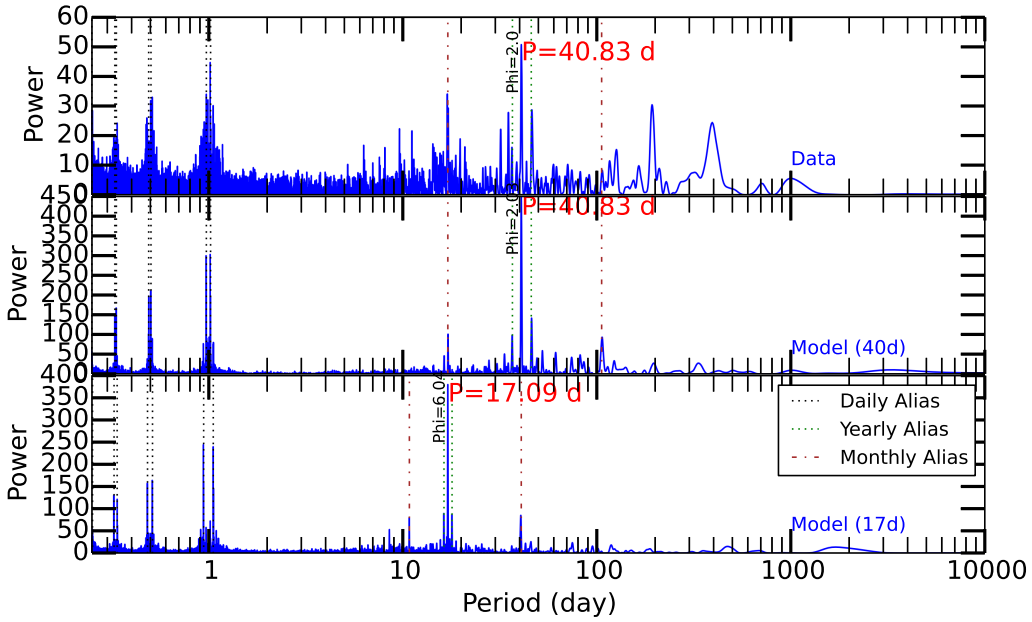

Figure 6.12: Top: a candidate periodic signal at 40.8 or 17.1 days emerges in the periodogram of the residuals to the 3-planet plus long-term stellar magnetic cycle model. These two periods are related to each other by the one synodic month alias. Either 40.8 days or 17.1 days could correspond to the rotation period of the star, although the 40.8 day period is more prominent in the periodogram of the $S_{\rm HK}$ values. To test both periods, we model the best-fit Keplerian at 40.83 days (center) and 17.1 days (bottom) and show their periodograms, complete with phase information.

Table 6.3: HD 7924 Planet Properties

Parameter	Value	Units
P_b	5.3977	days
K_b	3.67	$\mathrm{m\,s^{-1}}$
$M_b \sin i_b$*	$8.68\ ^{+0.52}_{-0.51}$	$M_\oplus$
e_b	0.07	
ω_b	331.5	deg.
P_c	15.295	days
K_c	2.13	$\mathrm{m\,s^{-1}}$
$M_c \sin i_c$*	$7.86\ ^{+0.73}_{-0.71}$	$M_\oplus$
e_c	0.05	
ω_c	59.0	deg.
P_d	24.47	days
K_d	1.84	$\mathrm{m\,s^{-1}}$
$M_d \sin i_d$*	$6.44\ ^{+0.79}_{-0.78}$	$M_\oplus$
e_d	0.27	
ω_d	33.0	deg.
P_{mag}	2493	days
K_{mag}	1.83	$\mathrm{m\,s^{-1}}$
e_{mag}	0.30	
ω_{mag}	285.8	deg.

*Uncertainties in the mass computed by BJ Fulton using a DE-MCMC algorithm described in Fulton et al. (2015).

6.5 Next Steps

The multi-planet survey will continue to obtain RVs of known bright, multi-planet host stars on the APF. To ascertain the value of our decade of RVs on Keck plus APF, we will develop an injection-recovery pipeline. This pipeline will establish upper limits on combinations of $m \sin i$ and orbital period for planets in the system that remain uncharacterized in the style of Figure 5.6. We might also detect additional low-mass planets in known multi-planet systems, enriching our knowledge of the architectures and dynamics of individual planetary systems.

Acknowledgments

Thank you to Ken and Glora Levy for two years of support (Figure 6.13). Thank you also to the California tax payers, the University of California, and Google for supporting Lick Observatory.

Figure 6.13: Left to right: Gloria Levy, Lauren Weiss, and Ken Levy at the Lick Observatory gala on Oct. 4, 2014.

Bibliography

Adams, E. R., Ciardi, D. R., Dupree, a. K., et al. 2012, The Astronomical Journal, 144, 42
Agol, E., & Deck, K. 2016, ApJ, 818, 177
Agol, E., Steffen, J., Sari, R., & Clarkson, W. 2005, Monthly Notices of the Royal Astronomical Society, 359, 567
Aigrain, S., Collier Cameron, A., Ollivier, M., et al. 2008, A&A, 488, L43
Albrecht, S., Winn, J. N., Marcy, G. W., et al. 2013, ApJ, 771, 11
Alonso, R., Brown, T. M., Torres, G., et al. 2004, ApJ, 613, L153
Alonso, R., Auvergne, M., Baglin, A., et al. 2008, A&A, 482, L21
Alsubai, K. A., Parley, N. R., Bramich, D. M., et al. 2011, MNRAS, 417, 709
Anderson, D. R., Gillon, M., Hellier, C., et al. 2008, MNRAS, 387, L4
Anderson, D. R., Hellier, C., Gillon, M., et al. 2010, ApJ, 709, 159
Anderson, D. R., Collier Cameron, A., Hellier, C., et al. 2011a, A&A, 531, A60
Anderson, D. R., Barros, S. C. C., Boisse, I., et al. 2011b, PASP, 123, 555
Arras, P., & Socrates, A. 2010, ApJ, 714, 1
Bakos, G. A., Noyes, R. W., Kovács, G., et al. 2007a, ApJ, 656, 552
Bakos, G. A., Shporer, A., Pál, A., et al. 2007b, ApJ, 671, L173
Bakos, G. A., Kovács, G., Torres, G., et al. 2007c, ApJ, 670, 826
Bakos, G. A., Pál, A., Torres, G., et al. 2009, ApJ, 696, 446
Bakos, G. Á., Pál, A., Torres, G., et al. 2009, ApJ, 696, 1950
Bakos, G. A., Torres, G., Pál, A., et al. 2010, ApJ, 710, 1724
Bakos, G. A., Hartman, J., Torres, G., et al. 2011, ApJ, 742, 116
Bakos, G. A., Hartman, J. D., Torres, G., et al. 2012, AJ, 144, 19
Baraffe, I., Alibert, Y., Chabrier, G., & Benz, W. 2006, A&A, 450, 1221
Baraffe, I., Chabrier, G., & Barman, T. 2010, Reports on Progress in Physics, 73, 016901
Baraffe, I., Selsis, F., Chabrier, G., et al. 2004, A&A, 419, L13
Barbieri, M., Alonso, R., Desidera, S., et al. 2009, A&A, 503, 601
Barge, P., Baglin, A., Auvergne, M., et al. 2008, A&A, 482, L17
Barros, S. C. C., Faedi, F., Collier Cameron, A., et al. 2011, A&A, 525, A54
Barros, S. C. C., Díaz, R. F., Santerne, A., et al. 2014, A&A, 1, 1
Barros, S. C. C., Almenara, J. M., Demangeon, O., et al. 2015, MNRAS, 454, 4267
Batalha, N. M., Borucki, W. J., Bryson, S. T., et al. 2011, ApJ, 729, 27
Batalha, N. M., Rowe, J. F., Bryson, S. T., et al. 2013, The Astrophysical Journal Supple-

ment Series, 204, 24
Batygin, K., & Stevenson, D. J. 2010, ApJ, 714, L238
Becker, J. C., Vanderburg, A., Adams, F. C., Rappaport, S. A., & Schwengeler, H. M. 2015, ApJ, 812, L18
Bodenheimer, P., Lin, D. C. N., & Mardling, R. A. 2001, ApJ, 10, 466
Bonomo, A. S., Santerne, A., Alonso, R., et al. 2010, A&A, 520, A65
Bonomo, A. S., Hébrard, G., Santerne, A., et al. 2012, A&A, 538, A96
Bordé, P., Bouchy, F., Deleuil, M., et al. 2010, A&A, 520, A97
Borsato, L., Marzari, F., Nascimbeni, V., et al. 2014, Astronomy & Astrophysics, 1
Borucki, W. J., Koch, D. G., Brown, T. M., et al. 2010, ApJ, 713, L126
Borucki, W. J., Koch, D. G., Basri, G., et al. 2011, ApJ, 736, 19
Borucki, W. J., Koch, D. G., Batalha, N., et al. 2012, ApJ, 745, 120
Bouchy, F., Udry, S., Mayor, M., et al. 2005, A&A, 444, L15
Bouchy, F., Hebb, L., Skillen, I., et al. 2010, A&A, 519, A98
Bruntt, H., Deleuil, M., Fridlund, M., et al. 2010, Astronomy & Astrophysics, 519, A51
Buchhave, L. A., Bakos, G. A., Hartman, J. D., et al. 2010, ApJ, 720, 1118
—. 2011a, ApJ, 733, 116
Buchhave, L. A., Latham, D. W., Carter, J. A., et al. 2011b, ApJS, 197, 3
Burke, C. J., McCullough, P. R., Valenti, J. A., et al. 2007, ApJ, 671, 2115
—. 2008, ApJ, 686, 1331
Burke, C. J., Bryson, S. T., Mullally, F., et al. 2014, The Astrophysical Journal Supplement Series, 210, 19
Burke, C. J., Christiansen, J. L., Mullally, F., et al. 2015, ApJ, 809, 8
Burrows, A., Hubeny, I., Budaj, J., & Hubbard, W. B. 2007, ApJ, 661, 502
Burt, J., Hanson, R., Rivera, E., et al. 2014, in Proc. SPIE, Vol. 9152, Software and Cyberinfrastructure for Astronomy III, 915211
Butler, R. P., Marcy, G. W., Fischer, D. A., et al. 1999, ApJ, 526, 916
Butler, R. P., Marcy, G. W., Vogt, S. S., & Apps, K. 1998, PASP, 110, 1389
Butler, R. P., Marcy, G. W., Williams, E., Hauser, H., & Shirts, P. 1997, ApJ, 474, L115
Butler, R. P., Marcy, G. W., Williams, E., Mccarthy, C., & Vogt, S. S. 1996, PASP, 500
Butler, R. P., Vogt, S. S., Marcy, G. W., et al. 2004, ApJ, 617, 580
Butler, R. P., Wright, J. T., Marcy, G. W., et al. 2006, The Astrophysical Journal, 646, 505
Cabrera, J., Bruntt, H., Ollivier, M., et al. 2010, A&A, 522, A110
Carter, J. A., Winn, J. N., Gilliland, R., & Holman, M. J. 2009, ApJ, 696, 241
Carter, J. A., Winn, J. N., Holman, M. J., et al. 2011, ApJ, 730, 82
Carter, J. A., Agol, E., Chaplin, W. J., et al. 2012, Science, 337, 556
Chabrier, G., & Baraffe, I. 2007, ApJ, 661, L81
Chambers, J. E. 1999, MNRAS, 304, 793
Charbonneau, D., Brown, T. M., Latham, D. W., & Mayor, M. 2000, ApJ, 529, L45
Charbonneau, D., Winn, J. N., Everett, M. E., et al. 2007, ApJ, 658, 1322
Charbonneau, D., Berta, Z. K., Irwin, J., et al. 2009, Nature, 462, 891
Chatterjee, S., & Tan, J. C. 2014, ApJ, 780, 53

Chiang, E., & Laughlin, G. 2013, Monthly Notices of the Royal Astronomical Society, 431, 3444
Christian, D. J., Gibson, N. P., Simpson, E. K., et al. 2009, MNRAS, 392, 1585
Claret, A., & Bloemen, S. 2011, A&A, 529, A75
Cochran, W. D., Endl, M., Wittenmyer, R. A., & Bean, J. L. 2007, ApJ, 665, 1407
Cochran, W. D., Fabrycky, D. C., Torres, G., et al. 2011, ApJS, 197, 7
Collier Cameron, A., Bouchy, F., Hébrard, G., et al. 2007, MNRAS, 375, 951
Dawson, R. I., & Fabrycky, D. C. 2010, The Astrophysical Journal, 722, 937
Deck, K. M., Agol, E., Holman, M. J., & Nesvorný, D. 2014, The Astrophysical Journal, 787, 132
Deeg, H. J., Moutou, C., Erikson, A., et al. 2010, Nature, 464, 384
Demory, B.-O., & Seager, S. 2011, ApJS, 197, 12
Demory, B.-O., Gillon, M., Deming, D., et al. 2011, A&A, 533, A114
Désert, J.-M., Charbonneau, D., Demory, B.-O., et al. 2011, ApJS, 197, 14
Doyle, L. R., Carter, J. A., Fabrycky, D. C., et al. 2011, Science, 333, 1602
Dragomir, D., Matthews, J. M., Winn, J. N., & Rowe, J. F. 2014, in IAU Symposium, Vol. 293, Formation, Detection, and Characterization of Extrasolar Habitable Planets, ed. N. Haghighipour, 52
Dragomir, D., Matthews, J. M., Eastman, J. D., et al. 2013, ApJ, 772, L2
Dressing, C. D., Charbonneau, D., Dumusque, X., et al. 2015, The Astrophysical Journal, 800, 135
Dumusque, X., Bonomo, A. S., Haywood, R. D., et al. 2014, ApJ, 789, 154
Dunham, E. W., Borucki, W. J., Koch, D. G., et al. 2010, ApJ, 713, L136
Endl, M., MacQueen, P. J., Cochran, W. D., et al. 2011, ApJS, 197, 13
Endl, M., Robertson, P., Cochran, W. D., et al. 2012, The Astrophysical Journal, 759, 19
Enoch, B., Collier Cameron, A., Horne, K., & Cameron, A. C. 2012, A&A, 540, A99
Enoch, B., Cameron, A. C., Anderson, D. R., et al. 2011, MNRAS, 410, 1631
Erkaev, N. V., Kulikov, Y. N., Lammer, H., et al. 2007, A&A, 472, 329
Fabrycky, D. C., & Kepler Science Team. 2012, in AAS/Division of Dynamical Astronomy Meeting, Vol. 43, AAS/Division of Dynamical Astronomy Meeting, 01.03
Fabrycky, D. C., Ford, E. B., Steffen, J. H., et al. 2012, ApJ, 750, 114
Fabrycky, D. C., Lissauer, J. J., Ragozzine, D., et al. 2014, ApJ, 790, 146
Faedi, F., Barros, S. C. C., Anderson, D. R., et al. 2011, A&A, 531, A40
Fang, J., & Margot, J.-L. 2012, ApJ, 761, 92
Fischer, D. A., Marcy, G. W., Butler, R. P., Vogt, S. S., & Apps, K. 1999, PASP, 111, 50
Fischer, D. A., Marcy, G. W., Butler, R. P., et al. 2001, ApJ, 551, 1107
Fischer, D. A., Vogt, S. S., Marcy, G. W., et al. 2007, ApJ, 669, 1336
Fischer, D. A., Marcy, G. W., Butler, R. P., et al. 2008, ApJ, 675, 790
Foreman-Mackey, D., Hogg, D. W., Lang, D., & Goodman, J. 2013, PASP, 125, 306
Fortney, J. J., Marley, M. S., & Barnes, J. W. 2007, ApJ, 659, 1661
Fortney, J. J., & Nettelmann, N. 2010, Space Sci. Rev., 152, 423
Fortney, J. J., Demory, B.-O., Désert, J.-M., et al. 2011, ApJS, 197, 9

Fressin, F., Torres, G., Désert, J.-M., et al. 2011, The Astrophysical Journal Supplement Series, 197, 5
Fressin, F., Torres, G., Charbonneau, D., et al. 2013, The Astrophysical Journal, 766, 81
Fridlund, M., Hébrard, G., Alonso, R., et al. 2010, A&A, 512, A14
Fulton, B. J., Weiss, L. M., Sinukoff, E., et al. 2015, The Astrophysical Journal, 805, 175
Gandolfi, D., Hébrard, G., Alonso, R., et al. 2010, A&A, 524, A55
Gautier, III, T. N., Charbonneau, D., Rowe, J. F., et al. 2012, ApJ, 749, 15
Gautier III, T. N., Charbonneau, D., Rowe, J. F. J. F., et al. 2012, ApJ, 749, 15
Gettel, S., Charbonneau, D., Dressing, C. D., et al. 2016, ApJ, 816, 95
Gilliland, R. L., Marcy, G. W., Rowe, J. F., et al. 2013, ApJ, 766, 40
Gillon, M., Anderson, D. R., Triaud, A. H. M. J., et al. 2009, A&A, 501, 785
Gillon, M., Hatzes, A., Csizmadia, S., et al. 2010, A&A, 520, A97
Gillon, M., Doyle, A. P., Lendl, M., et al. 2011, A&A, 533, A88
Goldreich, P., Lithwick, Y., & Sari, R. 2004, Annual Review of Astronomy and Astrophysics, 42, 549
Gregory, P. C., & Fischer, D. A. 2010, MNRAS, 403, 731
Grunblatt, S. K., Howard, A. W., & Haywood, R. D. 2015, ApJ, 808, 127
Gu, P.-G., Lin, D. N. C., & Bodenheimer, P. H. 2003, ApJ, 588, 509
Guenther, E. W., Díaz, R. F., Gazzano, J.-C., et al. 2012, A&A, 537, A136
Han, E., Wang, S. X., Wright, J. T., et al. 2014, PASP, 126, 827
Hands, T. O., Alexander, R. D., & Dehnen, W. 2014, MNRAS, 12, 1
Hartman, J. D., Bakos, G. A., Torres, G., et al. 2009, ApJ, 706, 785
Hartman, J. D., Bakos, G. A., Sato, B., et al. 2011a, ApJ, 726, 52
Hartman, J. D., Bakos, G. A., Torres, G., et al. 2011b, ApJ, 742, 59
Hartman, J. D. D., Bakos, G. A. A., Kipping, D. M. M., et al. 2011c, ApJ, 728, 138
Hatzes, A. P., Fridlund, M., Nachmani, G., et al. 2011, ApJ, 743, 75
Haywood, R. D., Collier Cameron, A., Queloz, D., et al. 2014, MNRAS, 443, 2517
Hebb, L., Collier-Cameron, A., Loeillet, B., et al. 2009, ApJ, 693, 1920
Hebb, L., Collier-Cameron, A., Triaud, A. H. M. J., et al. 2010, ApJ, 708, 224
Hébrard, G., Evans, T. M., Alonso, R., et al. 2011, A&A, 533, A130
Hellier, C., Anderson, D. R., Collier Cameron, A., et al. 2009a, Nature, 460, 1098
Hellier, C., Anderson, D. R., Gillon, M., et al. 2009b, ApJ, 690, L89
Hellier, C., Anderson, D. R., Collier Cameron, A., et al. 2010, ApJ, 723, L60
—. 2011, A&A, 535, L7
Henry, G. W., Marcy, G. W., Butler, R. P., & Vogt, S. S. 2000, ApJ, 529, L41
Hirano, T., Narita, N., Sato, B., et al. 2012, The Astrophysical Journal, 759, L36
Holman, M. J., Fabrycky, D. C., Ragozzine, D., et al. 2010, Science (New York, N.Y.), 330, 51
Howard, A. W., Johnson, J. A., Marcy, G. W., et al. 2009, ApJ, 696, 75
Howard, A. W., Johnson, J. A., Marcy, G. W., et al. 2010, ApJ, 721, 1467
Howard, A. W., Johnson, J. A., Marcy, G. W., et al. 2011, ApJ, 726, 73
Howard, A. W., Johnson, J. A., Marcy, G. W., et al. 2011, ApJ, 730, 10

Howard, A. W., Marcy, G. W., Bryson, S. T., et al. 2012, ApJS, 201, 15
Howard, A. W., Sanchis-Ojeda, R., Marcy, G. W., et al. 2013, Nature, 503, 381
Howell, S. B., Everett, M. E., Sherry, W., Horch, E., & Ciardi, D. R. 2011, The Astronomical Journal, 142, 19
Hubbard, W. B., Hattori, M. F., Burrows, A., Hubeny, I., & Sudarsky, D. 2007, Icarus, 187, 358
Ibgui, L., & Burrows, A. 2009, ApJ, 700, 1921
Ibgui, L., Burrows, A., & Spiegel, D. S. 2010, ApJ, 713, 751
Ida, S., & Lin, D. N. C. 2004, ApJ, 604, 388
Jenkins, J. M. J. M., Borucki, W. J. W. J., Koch, D. G. D. G., et al. 2010, ApJ, 724, 1108
Johnson, J. A., Winn, J. N., Bakos, G. A., et al. 2011, ApJ, 735, 24
Johnson, J. A., Gazak, J. Z., Apps, K., et al. 2012, AJ, 143, 111
Jontof-Hutter, D., Lissauer, J. J., Rowe, J. F., & Fabrycky, D. C. 2014, The Astrophysical Journal, 785, 15
Jontof-Hutter, D., Rowe, J. F., Lissauer, J. J., Fabrycky, D. C., & Ford, E. B. 2015, Nature, 522, 321
Jontof-Hutter, D., Ford, E., Rowe, J., et al. 2016, ApJ, 820, 39
Joshi, Y. C., Pollacco, D., Collier Cameron, A., et al. 2009, MNRAS, 392, 1532
Kane, S. R., & Gelino, D. M. 2012, PASP, 124, 323
Kass, R. E., & Raftery, A. E. 1995, Journal of the American Statistical Association, 90, 773
Kipping, D. M., Nesvorný, D., Buchhave, L. A., et al. 2014, The Astrophysical Journal, 784, 28
Kipping, D. M., Schmitt, A. R., Huang, X., et al. 2015, The Astrophysical Journal, 813, 14
Kipping, D. M., Bakos, G. A., Hartman, J., et al. 2010, ApJ, 725, 2017
Kipping, D. M., Hartman, J., Bakos, G. A., et al. 2011, AJ, 142, 95
Koch, D. G., Borucki, W. J., Rowe, J. F., et al. 2010, ApJ, 713, L131
Kovács, G., Bakos, G. A., Torres, G., et al. 2007, ApJ, 670, L41
Kovács, G., Bakos, G. A., Hartman, J. D., et al. 2010, ApJ, 724, 866
Kozai, Y. 1962, AJ, 67, 591
Latham, D. W., Bakos, G. A., Torres, G., et al. 2009, ApJ, 704, 1107
Latham, D. W., Borucki, W. J., Koch, D. G., et al. 2010, ApJ, 713, L131
Leconte, J., Chabrier, G., Baraffe, I., & Levrard, B. 2010, A&A, 516, A64
Lee, E. J., Chiang, E., & Ormel, C. W. 2014, ApJ, 797, 95
Léger, A., Rouan, D., Schneider, J., et al. 2009, A&A, 506, 287
Lidov, M. L. 1962, Planet. Space Sci., 9, 719
Lissauer, J. J., & Stewart, G. R. 1993, in Astronomical Society of the Pacific Conference Series, Vol. 36, Planets Around Pulsars, ed. J. A. Phillips, S. E. Thorsett, & S. R. Kulkarni, 217
Lissauer, J. J., Fabrycky, D. C., Ford, E. B., et al. 2011, Nature, 470, 53
Lissauer, J. J., Marcy, G. W., Rowe, J. F., et al. 2012, ApJ, 750, 112
Lissauer, J. J., Jontof-Hutter, D., Rowe, J. F., et al. 2013, The Astrophysical Journal, 770, 131

Lissauer, J. J., Marcy, G. W., Bryson, S. T., et al. 2014, ApJ, 784, 44
Lister, T. A., Anderson, D. R., Gillon, M., et al. 2009, ApJ, 703, 752
Lithwick, Y., Xie, J., & Wu, Y. 2012, The Astrophysical Journal, 761, 122
Lopez, E. D., & Fortney, J. J. 2014, ApJ, 792, 1
Lopez, E. D., Fortney, J. J., & Miller, N. 2012, ApJ, 761, 59
Lovis, C., Mayor, M., Pepe, F., et al. 2006, Nature, 441, 305
Maciejewski, G., Errmann, R., Raetz, S., et al. 2011, A&A, 528, A65
Mahajan, N., & Wu, Y. 2014, ApJ, 795, 32
Mandel, K., & Agol, E. 2002, ApJ, 580, L171
Mandushev, G., O'Donovan, F. T., Charbonneau, D., et al. 2007, ApJ, 667, L195
Mandushev, G., Quinn, S. N., Buchhave, L. A., et al. 2011, ApJ, 741, 114
Maness, H. L., Marcy, G. W., Ford, E. B., et al. 2007, PASP, 119, 90
Marcy, G. W., & Butler, R. P. 1995, in Bulletin of the American Astronomical Society, Vol. 27, American Astronomical Society Meeting Abstracts, 1379
Marcy, G. W., & Butler, R. P. 1996, ApJ, 464, L147
Marcy, G. W., Butler, R. P., Fischer, D., et al. 2001, ApJ, 556, 296
Marcy, G. W., Butler, R. P., & Vogt, S. S. 2000, ApJ, 536, L43
Marcy, G. W., Butler, R. P., Vogt, S. S., Fischer, D., & Liu, M. C. 1999, ApJ, 520, 239
Marcy, G. W., Butler, R. P., Vogt, S. S., et al. 2005, ApJ, 619, 570
Marcy, G. W., Isaacson, H., Howard, A. W., et al. 2014, The Astrophysical Journal Supplement Series, 210, 20
Masuda, K. 2014, The Astrophysical Journal, 783, 53
Masuda, K., Hirano, T., Taruya, A., Nagasawa, M., & Suto, Y. 2013, The Astrophysical Journal, 778, 185
Maxted, P. F. L., Anderson, D. R., Gillon, M., et al. 2010a, AJ, 140, 2007
Maxted, P. F. L., Anderson, D. R., Collier Cameron, A., et al. 2010b, PASP, 122, 1465
—. 2011, PASP, 123, 547
Mayor, M., & Queloz, D. 1995, Nature, 378, 355
Mayor, M., Udry, S., Naef, D., et al. 2004, A&A, 415, 391
McArthur, B. E., Endl, M., Cochran, W. D., et al. 2004, ApJ, 614, L81
McCullough, P. R., Stys, J. E., Valenti, J. A., et al. 2006, ApJ, 648, 1228
Meschiari, S., Laughlin, G., Vogt, S. S., et al. 2011, ApJ, 727, 117
Miller, N., & Fortney, J. J. 2011, ApJ, 736, L29
Miller, N., Fortney, J. J., & Jackson, B. 2009, ApJ, 702, 1413
Morton, T. D., & Johnson, J. A. 2011, The Astrophysical Journal, 738, 170
Morton, T. D., & Johnson, J. A. 2011, ApJ, 738, 170
Moutou, C., Bruntt, H., Guillot, T., et al. 2008, A&A, 488, L47
Moutou, C., Hébrard, G., Bouchy, F., et al. 2009, A&A, 498, L5
Moutou, C., Deleuil, M., Guillot, T., et al. 2013, Icarus, 226, 1625
Mullally, F., Coughlin, J. L., Thompson, S. E., et al. 2015, The Astrophysical Journal Supplement Series, 217, 31
Murray, C. D., & Dermott, S. F. 2000, in Solar System Dynamics (Cambridge University

Press), 321, cambridge Books Online
Naef, D., Mayor, M., Beuzit, J. L., et al. 2004, A&A, 414, 351
Naef, D., Latham, D. W., Mayor, M., et al. 2001, A&A, 375, L27
Naef, D., Mayor, M., Korzennik, S. G., et al. 2003, A&A, 410, 1051
Narita, N., Hirano, T., Fukui, A., et al. 2015, ApJ, 815, 47
Nespral, D., Gandolfi, D., Deeg, H., et al. 2016, Astronomy & Astrophysics (in press)
Nesvorný, D., Kipping, D., Terrell, D., et al. 2013, The Astrophysical Journal, 777, 3
Noyes, R. W., Bakos, G. A., Torres, G., et al. 2008, ApJ, 673, L79
O'Donovan, F. T., Charbonneau, D., Mandushev, G., et al. 2006, ApJ, 651, L61
Pál, A., Bakos, G. A., Torres, G., et al. 2008, ApJ, 680, 1450
—. 2010, MNRAS, 401, 2665
Pepe, F., Cameron, A. C., Latham, D. W., et al. 2013, Nature, 503, 377
Perna, R., Menou, K., & Rauscher, E. 2010, ApJ, 724, 313
Petigura, E. A., Howard, A. W., & Marcy, G. W. 2013a, Proceedings of the National Academy of Sciences, 110, 19273
Petigura, E. A., Marcy, G. W., & Howard, A. W. 2013b, ApJ, 770, 69
Pilyavsky, G., Mahadevan, S., Kane, S. R., et al. 2011, ApJ, 743, 162
Pollacco, D., Skillen, I., Collier Cameron, A., et al. 2008, MNRAS, 385, 1576
Pollack, J. B., Hubickyj, O., Bodenheimer, P., et al. 1996, Icarus, 124, 62
Pont, F., Tamuz, O., Udalski, A., et al. 2008, A&A, 487, 749
Press, W., & Rybicki, G. 1989, ApJ, 277
Queloz, D., Bouchy, F., Moutou, C., et al. 2009, A&A, 506, 303
Queloz, D., Anderson, D., Collier Cameron, A., et al. 2010, A&A, 517, L1
Radovan, M. V., Lanclos, K., Holden, B. P., et al. 2014, in Proc. SPIE, Vol. 9145, Ground-based and Airborne Telescopes V, 91452B
Rajpaul, V., Aigrain, S., & Roberts, S. J. 2015, MNRAS, 10, 6
Rauer, H., Queloz, D., Csizmadia, S., et al. 2009, A&A, 506, 281
Robertson, P., Endl, M., Cochran, W. D., et al. 2012, ApJ, 749, 39
Rogers, L. a. 2015, ApJ, 801, 41
Rogers, L. A., Bodenheimer, P., Lissauer, J. J., & Seager, S. 2011, ApJ, 738, 59
Rogers, L. A., & Seager, S. 2010a, ApJ, 712, 974
—. 2010b, ApJ, 716, 1208
Rowe, J. F., Bryson, S. T., Marcy, G. W., et al. 2014, ApJ, 784, 45
Sanchis-Ojeda, R., Rappaport, S., Winn, J. N., et al. 2014, ApJ, 787, 47
Sanchis-Ojeda, R., Rappaport, S., Winn, J. N., et al. 2013, The Astrophysical Journal, 774, 54
Sanchis-Ojeda, R., Fabrycky, D. C., Winn, J. N., et al. 2012, Nature, 487, 449
Santerne, A., Díaz, R. F., Bouchy, F., et al. 2011, A&A, 528, A63
Sato, B., Fischer, D. A., Henry, G. W., et al. 2005, ApJ, 633, 465
Saumon, D., & Guillot, T. 2004, ApJ, 609, 1170
Schmitt, J. R., Agol, E., Deck, K. M., et al. 2014, ApJ, 795, 167
Schwarz, G. 1978, Ann. Stat., 6, 461

Seager, S., Kuchner, M., HierâĂŘMajumder, C. a., & Militzer, B. 2007, The Astrophysical Journal, 669, 1279
Showman, A. P., & Guillot, T. 2002, A&A, 385, 166
Showman, A. P., & Guillot, T. 2002, A&A, 385, 166
Shporer, A., Bakos, G. A., Bouchy, F., et al. 2009, ApJ, 690, 1393
Simpson, E. K., Pollacco, D., Cameron, A. C., et al. 2011a, MNRAS, 414, 3023
Simpson, E. K., Faedi, F., Barros, S. C. C., et al. 2011b, AJ, 141, 8
Skillen, I., Pollacco, D., Collier Cameron, A., et al. 2009, A&A, 502, 391
Smalley, B., Anderson, D. R., Collier Cameron, A., et al. 2010, A&A, 520, A56
—. 2011, A&A, 526, A130
Smith, A. M. S., Anderson, D. R., Collier Cameron, A., et al. 2012, AJ, 143, 81
Snellen, I. A. G., Koppenhoefer, J., van der Burg, R. F. J., et al. 2009, A&A, 497, 545
Steffen, J. H., Fabrycky, D. C., Ford, E. B., et al. 2012, MNRAS, 421, 2342
Street, R. A., Simpson, E., Barros, S. C. C., et al. 2010, ApJ, 720, 337
Tan, X., Payne, M. J., Lee, M. H., et al. 2013, ApJ, 777, 101
Tingley, B., Endl, M., Gazzano, J.-C., et al. 2011, A&A, 528, A97
Tingley, B., Endl, M., Gazzano, J.-C., et al. 2011, A&A, 531, A41
Torres, G., Winn, J. N., & Holman, M. J. 2008, ApJ, 677, 1324
Torres, G., Bakos, G. A., Kovács, G., et al. 2007, ApJ, 666, L121
Torres, G., Bakos, G. A., Hartman, J., et al. 2010, ApJ, 715, 458
Triaud, A. H. M. J., Queloz, D., Hellier, C., et al. 2011, A&A, 531, A24
Tripathi, A., Winn, J. N., Johnson, J. A., et al. 2010, ApJ, 715, 421
Udalski, A., Pont, F., Naef, D., et al. 2008, A&A, 487, 299
Valenti, J. A. J., & Piskunov, N. 1996, Astronomy & Astrophysics Supplement Series, 118, 595
Vanderburg, A., Montet, B. T., Johnson, J. A., et al. 2015, ApJ, 800, 59
Vogt, S. S., Marcy, G. W., Butler, R. P., & Apps, K. 2000, ApJ, 536, 902
Vogt, S. S., Radovan, M., Kibrick, R., et al. 2014, PASP, 126, 359
von Braun, K., Tabetha, S. B., ten Brummelaar, T. a., et al. 2011, The Astrophysical Journal, 740, 49
Weiss, L. M., & Marcy, G. W. 2014, ApJ, 783, L6
Weiss, L. M., Marcy, G. W., Rowe, J. F., et al. 2013, The Astrophysical Journal, 768, 14
Weiss, L. M., Rogers, L. A., Isaacson, H. T., et al. 2016, ApJ, 819, 83
West, R. G., Collier Cameron, A., Hebb, L., et al. 2009a, A&A, 502, 395
West, R. G., Anderson, D. R., Gillon, M., et al. 2009b, AJ, 137, 4834
Wilson, D. M., Gillon, M., Hellier, C., et al. 2008, ApJ, 675, L113
Winn, J. N., Johnson, J. A., Albrecht, S., et al. 2009, ApJ, 703, L99
Winn, J. N., Johnson, J. A., Howard, A. W., et al. 2010, ApJ, 718, 575
Wolfgang, A., & Lopez, E. 2015, ApJ, 806, 183
Wright, J. T., Upadhyay, S., Marcy, G. W., et al. 2009, The Astrophysical Journal, 693, 1084
Wright, J. T., Fakhouri, O., Marcy, G. W., et al. 2011, PASP, 123, 412

Wu, Y., & Lithwick, Y. 2013, The Astrophysical Journal, 772, 74
Yi, S., Kim, Y.-c., Lee, Y.-w., Ree, C. H., & Barnes, S. 2001, ApJSupplement Series
Youdin, A. N., & Mitchell, J. L. 2010, ApJ, 721, 1113
Yu, Q., & Tremaine, S. 2001, AJ, 121, 1736
Zapolsky, H. S., & Salpeter, E. E. 1969, The Astrophysical Journal, 158, 809